NON-CONTACT SURFACE INSPECTION.

Raymond Y. M. Chung B.Sc., M.Sc.

A thesis submitted as part of
the requirements for the degree
of Doctor of Philosophy of
Liverpool John Moores University.

School of Engineering and
Technology Management,
Liverpool John Moores University.

October 1992

ACKNOWLEDGEMENTS

The author would like to express his gratitude to Dr. D. R. Burton and Professor M. J. Lalor for their help, support and encouragement, without which the completion of this thesis would not have been possible.

The author would also like to thank colleagues within the Coherent and Electro-optics Research Group particularly Dr. G. Halsall, A. Malcolm, P. O'Donovan, P. Stephenson, P. Barton and Dr. J. Atkinson.

Thanks must also go to the technicians in the Metrology and Engineering workshop laboratories, and the NAB for funding and making this research possible.

Thank goes also to Jenny O'Farrell for the excellent typing of this thesis.

Finally the author would like to thank his mother, father and brother for their continual support and encouragement throughout his academic career, and also to Shirley Ko for her added patience.

ABSTRACT

NON-CONTACT SURFACE INSPECTION

Raymond Y.M. Chung

This thesis descibes the development of a non-contact inspection system, used in providing a comparative method for gauging a surface. The purpose of this system is not to measure the 3-D shape of a part. The volume difference between the part to be inspected and a master, is merely part of the decision criteria, where if this difference exceeds a certain threshold value, then the component under inspection is deemed to have failed.

The technique involves a combination of fringe projection and image subtraction. The system comprises two sub-systems, a low-cost pc based image processor and a white light, square wave fringe projector. A camera provides the interface between the two sub-systems. Validation of the technique is provided by the simulation of mathematically generated defects, and by means of experiments on samples of known volume. In addition, the effect of the variation of particular set-up constants, on the technique's accuracy are also illustrated.

The problems and subsequent solutions associated with the practical inspection, result in an improved method of gauging. The system provides reliable results (within 4%) for surfaces of nominally similar form and reflectivity. Additional results (within 10%) are illustrated, where the images and fringe patterns are mis-aligned. As a result of a selective filtering scheme, precise relocation of the surfaces (used in the comparison) is unnecessary. This is conditional upon the fringes on each surface, being identical in orientation with each other.

Further consideration of the technique (within an error analysis) indicates the necessity of an accurate determination of all the set-up constants.The error results cannot be taken too literally, since the worst case values are presented. However, the trends of the effects of these errors are useful.

An adapted alternative method is also described that may prove to be (in certain applications) an interesting real-time solution.

CONTENTS

CHAPTER ONE

INTRODUCTION

1.1 Introduction

The objective of this thesis is to describe the research work carried out in the development of a non-contact surface inspection system, using a PC-based low cost image processor and a simple optical fringe projection set-up. The system provides a method of comparing one surface with another to give a figure for the volume of any surface difference, and thus the ability to pass or fail the item being inspected.

This ability is of great importance (particularly in the manufacturing industry), where maintaining quality is essential. As a surface comparator the main objective is to ensure that each inspected component surface is nominally of similar surface form or surface condition (or both). This would depend upon the type of application. For instance, in the case of a bar of soap, ensuring the surface is defect free is of significant importance (for aesthetic purposes), as compared to a car panel, where both shape and surface condition are critical. For this reason, surface inspection is of great importance within industry.

The system developed provides reliable results for surfaces of nominally similar surface form and reflectivity, which other conventional techniques are incapable of producing with similar accuracy and speed. This is achieved by the use of the Imaging Technology Incorporated (ITI) Series 100 Image processor.

Together with the theory behind the technique for volume estimation, simulation and practical validation results are presented, to illustrate the success of the system, and the effects of certain set-up constants on the final results. The problems associated with the basic technique and the solutions related to these problems are also presented to provide a more improved and flexible method of inspection. An adaption of this improved version provides an interesting option which can be developed further into a real-time inspection system without the relocation problems associated with the basic technique.

This chapter outlines the objective of the research project, the applications of non-contact inspection and the equipment used in this research work. The chapter concludes with a breakdown of the structural organisation of this thesis.

1.2 Non-Contact Inspection

Product inspection within industry continues to play an important role in the improvement of quality and reduction of scrap. Non-contact inspection systems offer the speed, accuracy and flexibility that conventional methods cannot. Non-contacting sensors provide long term unattended use, due to the lack of sensor wear, and in some cases provide the only option for measurement, where conventional contact techniques may damage and geometrically alter the part to be inspected.

A variety of different inspection systems have been described in the past by a number of researchers [1.1 to 1.3], giving an indication of the problems associated with this method of inspection. The method of illumination, in particular at an angle to the direction of observation, enables topographical information to be obtained. This ensures that surface features that otherwise are difficult to detect, can be observed.

Harding [1.4] discusses the current contouring techniques in the manufacturing industry, with descriptions of the basic approaches adopted with 3-D machine vision. A popular approach involves the illumination of the surface examined, with a fringe pattern, observing the effect from an angle. This method of non-contact measurement has been adopted by a number of researchers including Burton and Lalor [1.5, 1.6], Halsall et al [1.7, 1.8], Malcolm et al [1.9] and Chung [1.10]. These authors describe methods for determining certain features of the surface examined, with the fringe period and angle known. The effect of projecting a fringe pattern onto a surface is the modulation of the pattern to the surface shape (see Figure 1.1).

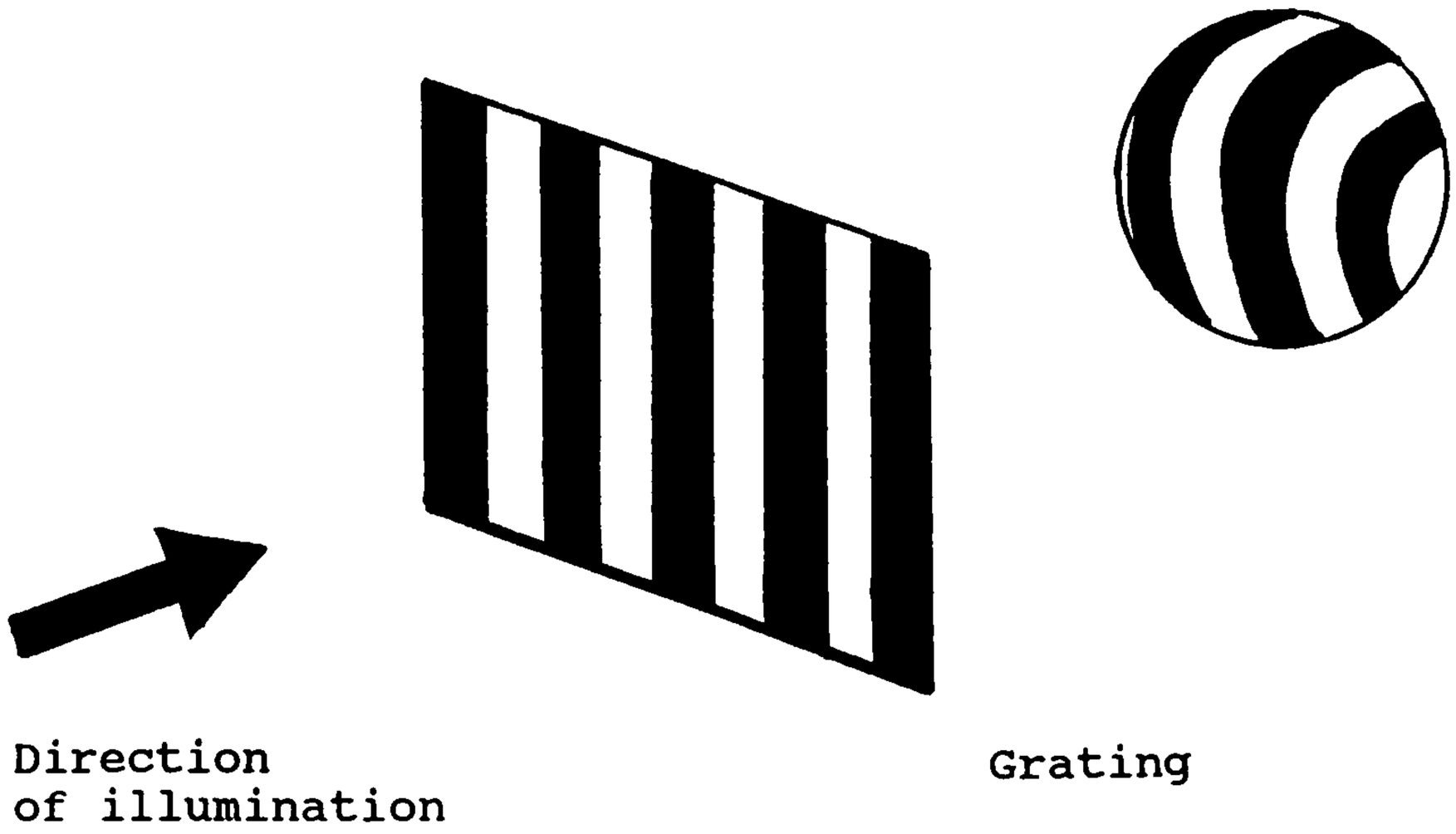

Figure 1.1 Projection of a fringe grating onto surface.

The applications of non-contact measurement systems are numerous and varied. The following section comprises a brief summary of some of the applications to which these techniques may be applied, giving an indication of the potential of the system discussed in this thesis.

1.3 Applications of Non-Contact Inspection

Engineering Industry [1.11 to 1.14]

A large number of applications of non-contact measurement lie within the industrial engineering field. These include a range of applications such as those within the automotive and sheet metal industry, where the repeated inspection to maintain the quality of the product is of significant importance. The effective use of an automated inspection system will ensure incorrect, damaged or defective items will not be passed through the system.

In addition, many other mass produced components made within the manufacturing industry may be inspected in this manner. Too numerous to mention, these include the inspection of glass bottles and light bulbs, where the recognition of cracks or dirt on the glass, and faults in the uncut wires or unsoldered contacts with reference to the light bulb application, are equally important.

Microelectronic Industry [1.15 to 1.17]

Traditional methods of measurement, such as plug gauges and 3-axis co-ordinate measuring machines, are not practical in the case of printed circuit boards (PCB's). Such methods are slow. Only non-contact inspection systems offer the speed, accuracy and flexibility required to make these types of measurements possible.

Medical Applications [1.18 to 1.21]

The measurement of the human body, for a variety of medical and screening applications, such as the early detection of the spinal disease scoliosis is another application of non-contact measurement. In addition, the measurement of wear in different designs of replacement knee and hip joints, and the wear in dental restorations.

The Food Industry [1.22]

The inspection of fruit, (e.g. Apples), for surface defects such as bruise damage, is another application for a non-contact inspection system. Currently when apples are purchased from the grower, their overall quality is assessed by random sampling. The ability to economically detect and sort out bruised fruit, would enable an improved quality and a better value product to be supplied to the consumer.

1.4 Expansion of the Objectives of this Research

The objective of this research work was to develop a simple, low-cost, non-contact surface comparator. The purpose of which is not to accurately measure the volumetric difference, but to gauge the acceptability of a component. The volume difference is merely a decision criteria, where if this difference exceeds a certain threshold, then the component under inspection is deemed to have failed. Therefore, the absolute accuracy in the volume measurement is not critical. The device is a comparator and not a measuring instrument.

It is envisaged that this system would be of most value in the inspection of high volume products such as : plastic bottles, containers, packaging, metal panels, etc.

All components will exhibit some difference, with the most important features including the magnitude (with respect to some threshold), and the distribution of this difference over the object surface. The latter point is particularly important. For example, a difference of 50 mm^3 in volume is not significant over an area of 3000 mm^2, but it is over an area of 50 mm^2.

1.5 System Equipment

The system developed consists of two sub-systems, one digital and the other optical. The digital sub-system consists of a PC based image processor and the optical sub-system of a white light fringe projector. A camera provides the interface between the two sub-systems. A brief description of each sub-system is provided below.

The Image Processor

The image processing system incorporates the Imaging Technology Incorporated (ITI) Series 100 Image Processor. The processor enables complex digital image processing functions such as image averaging, image subtraction and edge enhancement to be performed. Included also, as an object code, is a software library of image processing and graphic functions designed for use with the image processor. The library is a set of more than 200 predefined functions and macros designed for use in C programs.

The Series 100 is a single-board image processing sub-system that captures television standard video signals at video rates of 25 frames / second . It stores an image in the frame memory and simultaneously displays the image on an external monitor in monochrome or colour. Using one of the four look-up tables available (RED,GREEN,BLUE and INPUT LUTs), real-time operations , such as recursive frame averaging and subtraction may be performed on live and stored images.

The frame memory , where ultimately the images are stored, is of size 1024 x 1024 pixels. Each pixel contains a maximum of 12-bits, with a display resolution of 512 by 480, allowing 4 pages of storage to be possible. It has dual scan capability and a pixel buffer for accelerated access and block moves. Access to the frame memory may be software selectable or indirect, with the use of pan and scroll on a pixel by pixel basis, enabling the ability to analyse any area of interest (AOI) of the frame memory at any time. This permits the comparison of various images in the different AOI to be possible,

before any function such as image subtraction is performed.

To use a C library routine, the library header files must be included in the program. The C library functions are stored in compiled form in the library files that accompany the C compiler software, and at link time, the program may be linked with the appropriate functions and provide the code for the called library functions.

Optical Set-up

The method of illumination comprises the use of a MP-1000 (Newport) Moiré projector. The purpose of which is not to produce Moiré fringes, but to project square wave fringes (with white light) onto the surface of the component to be inspected. As a consequence, of the use of this projector, the surface to be inspected is illuminated with a square wave fringe pattern of equal amplitude.

1.6 The Structure of the Thesis

The following section comprises a brief description of the contents of each chapter and the structure of the thesis.

Chapter 1 : This present chapter introduces the research problem undertaken and its solution. Background information on non-contact measurement and its applications are also included, with in addition a brief description of the system used. The structure of the whole thesis is also outlined, with each chapter briefly discussed.

Chapter 2 : The content of this chapter is concerned with a review of some of the past work within the field of surface measurement. Within the context of the technique developed in this thesis, the fields of fringe analysis and image subtraction are discussed, with the specific areas of fringe projection and Moiré contouring discussed in detail. Various analysis techniques are also covered which include skeletonisation and an important area of recent years, Fourier fringe analysis. In addition, the problems associated with image subtraction of printed circuit boards (where it is most often applied), are also discussed. A final section covering surface inspection by subtraction is then included.

Chapter 3 : Discusses the theory involved in modelling a fringe pattern for a previously known height distribution. The theory is developed with a flat plane as the example for ease of explanation, although any shape is applicable.

Chapter 4 : This is an important chapter in that it describes the basic theory for the technique for volume estimation. Again, for ease of explanation for the development of the

theory, a flat plane is used although any shape may be applicable. Also included is a description of the simulation tests, essential in validating the theory, with additional simulation results of the effect of varying a number of the parameters used in the theory.

Chapter 5 : Having discussed the basic theory of the system in the previous chapter, this chapter describes the practical application of the technique and the problems associated with this experimental validation. These problems are listed, with some of the practical solutions investigated and discussed in detail, to enable a more robust system of measurement to be possible. Included also is a description of the procedure for obtaining the parameters essential for an accurate comparative measurement to be made. An interesting alternative, adapting the method of fringe contouring is also described, that may provide a successful real-time solution.

Chapter 6 : This chapter illustrates the system in action in analysing a series of fringe patterns obtained on a variety of different sized surface imperfections. Only a number of particular examples are presented to illustrate certain features of the method of measurement and also to provide an indication of its limitations. The inspection of soap bars is used to demonstrate the feasibility of the technique on an example (and its associated problems). However, it is only one application that the technique could be applied to, many other examples may be chosen.

Chapter 7 : This chapter describes an uncertainty analysis for the possible sources of error, to provide an indication of the

effect of errors in the viewing angle, fringe period and magnification factors.

Chapter 8 : Comprises a discussion of all the topics covered, and lists the major conclusions drawn from the work. The chapter concludes with a discussion of future work proposals and outlines the possible improvements that may be made.

1.7 References

1.1 P. TREPAGNIER, "**Recent developments of visual gaging**", SME VISION 85, p3-12 to 3-23, 1985.

1.2 R. L. THOMASON, "**High speed machine vision inspection for surface flaws, textures and contours**", SME VISION 86, p5-51 to 5-61, 1986.

1.3 G. W. SCHURR, "**Applying a low cost single dimension vision system for surface flaw and package inspection**", SME VISION 86, p1-15 to 1-27, 1986.

1.4 K. G. HARDING, "**Current state-of-the-art of contouring techniques in manufacturing**", ICALEO 1989, Vol 70, p1-11, 1989.

1.5 D. R. BURTON, M. J. LALOR, "**Software techniques for the analysis of contour maps of manufactured components**", Proc SPIE, Vol 952, 1987.

1.6 D. R. BURTON, M. J. LALOR, "**The Precision measurement of engineering form by computer analysis of optically generated contours**", Proc SPIE, Vol 1010, 1988.

1.7 G. R. HALSALL, D. R. BURTON, M. J. LALOR, C. A. HOBSON, "**A Novel real-time opto-electronic profilometer using FFT Processing**", IEEE ICASSP 1989, Vol 3, p1634-1637, 1989.

1.8 G. R. HALSALL, D. R. BURTON, M. J. LALOR, C. A. HOBSON, "**Surface Profile determination by real-time signal processing of interferometric contour fringe data**", FASIG 90, Nottingham, p303-304, 1990.

1.9 A. A. MALCOLM, D. R. BURTON, M. J. LALOR, "**A study of the effects of windowing on the accuracy of surface measurements obtained from the Fourier analysis of fringe patterns**", Fringe Analysis 89, FASIG 89, Loughborough, 1989.

1.10 R. Y. M. CHUNG, "**Surface Flaw Detection**" MSc Dissertation, Liverpool Polytechnic, 1988.

1.11 D. GERMAN, "**Vision aided inspection techniques for the automotive industry**", SME VISION 85, p23-28, 1985.

1.12 A. W. LEWIS, "**Non-Contact inspection of sheet metal fabrication**", SME VISION 86, p9-57 to 9-65, 1986.

1.13 A. McLEOD, O. DAHLE, S. DALE, "**Automatic visual inspection of light bulbs**", SME VISION 89, p1-25 to 1-48, 1989.

1.14 H. GIEBEL, H. GUTSCHALE, F. WAHL, "**A system for automatic inspection of glass bottles using texture analysis procedures**", IEEE Proc. Conf. PR, p1068-1070, 1982.

1.15 F. L. SKAGGS, "**Machine vision system speeds PCB inspection and increases measurement efficiency**", Reprinted SME VISION 85, p123-128, 1985.

1.16 R. T. CHIN, "**Automated Visual Inspection : A Survey**", TPAMI, Vol 4, p557-573, 1982.

1.17 K. S. FU, "**Pattern recognition for automated visual inspection**", Computer, Vol 15, Part 12, p34-40, 1982.

1.18 H. TAKASAKI, **"Moiré topography from it's birth to practical application"**, Optics and Lasers in Engineering, No 3, p3-14, 1982.

1.19 M. J. LALOR, D. GROVES, J. T. ATKINSON, **"Holographic studies in wear in implant materials and devices"**, Springer Series in Optical Sciences - Holography in Medicine and Biology, p20-26, 1979.

1.20 J. T. ATKINSON, D. R. BURTON, M. J. LALOR, P. C. O'DONOVAN, **"Opto/Computer methods applied to the evaluation of a range of acetabular cups"**, MEP Ltd, Vol 17, No 3, p105-110, 1988.

1.21 M. KOUKASH ET AL, **"The measurement of wear in dental restoration using digital image processing techniques"**, 2nd Int Conf Image Processing and its Applications, IEE, p63-67, 1986.

1.22 R. W. TAYLOR, G. E. REHKUGLER, **"Development of a system for automated detection of apple bruises"**, SME VISION 85, p6-55 to 6-65, 1985.

CHAPTER TWO

REVIEW OF PAST WORK IN SURFACE MEASUREMENT

2.1 Introduction

The content of this chapter is concerned with a review of some of the past work within the field of surface measurement. The development of an automated surface measuring system has been well documented, but within the context of the technique developed in this thesis, involving the combination of fringe analysis and image subtraction, the review is divided into two parts. The first in the field of fringe analysis and the second in image subtraction.

A number of different techniques have been developed, including fringe contouring methods [2.1], such as fringe projection and moiré contouring. With a series of fringes projected onto a surface, the shape of the fringes alter according to the topography of the surface. By comparing and measuring the shape of a distorted series of fringes with those that would be formed if the surface were flat, it is possible to calculate the surface topology of the object.

Various methods of analysis of optically generated contour maps including fringe tracking and the important development of phase measurement with the fourier transform analysis are also discussed.

The application of image subtraction is well established in the field of printed circuit board inspection, with the associated problems well documented and demonstrated. The combination of image subtraction and fringe projection is an obvious development, with other similar developments also discussed.

2.2 Fringe Contouring Methods

Fringe contouring methods have been used to measure surface form. There have been several techniques developed to enable the production of contour maps to be possible, with the principal ways of generating contour maps listed below:-

i) Fringe Projection Contouring
ii) Moiré Contouring
iii) Holographic Contouring

A thorough review of the contouring methods is described by Atkinson [2.2], but for the purposes of this research work, a brief summary of the available techniques are listed in Table 1. Because of their relevance, fringe projection and moiré contouring are discussed in more detail.

TABLE 1: FRINGE CONTOURING METHODS (SUMMARY)

Technique	Authors	Description
1. Fringe Projection Contouring	Porter and Mundy [2.3, 2.4]	Development of a non-contact profilometer for industry using pattern projection.
2. Moiré Contouring	Yatagai et al [2.5]	Analysis of Moiré patterns used in spinal deformity analysis.
3. Holographic Contouring	Steinbichler [2.6] Rottenkolber [2.7]	Description and the development of holographic interferometry for use in industry.

2.2.1 Fringe Projection and Pattern Analysis

This section gives an overview of a variety of surface measurement techniques using projected fringes. A number of techniques have been employed to analyse fringe patterns, some of which are described in the following section.

An early approach to automatic fringe pattern analysis by Indebetouw [2.8] proposed in 1978 a method of measuring the profile of an object using projected fringes continually translated across the object. The phase of the signal, picked up at selected points on the surface, is converted to profile heights. (Figure 2.1)

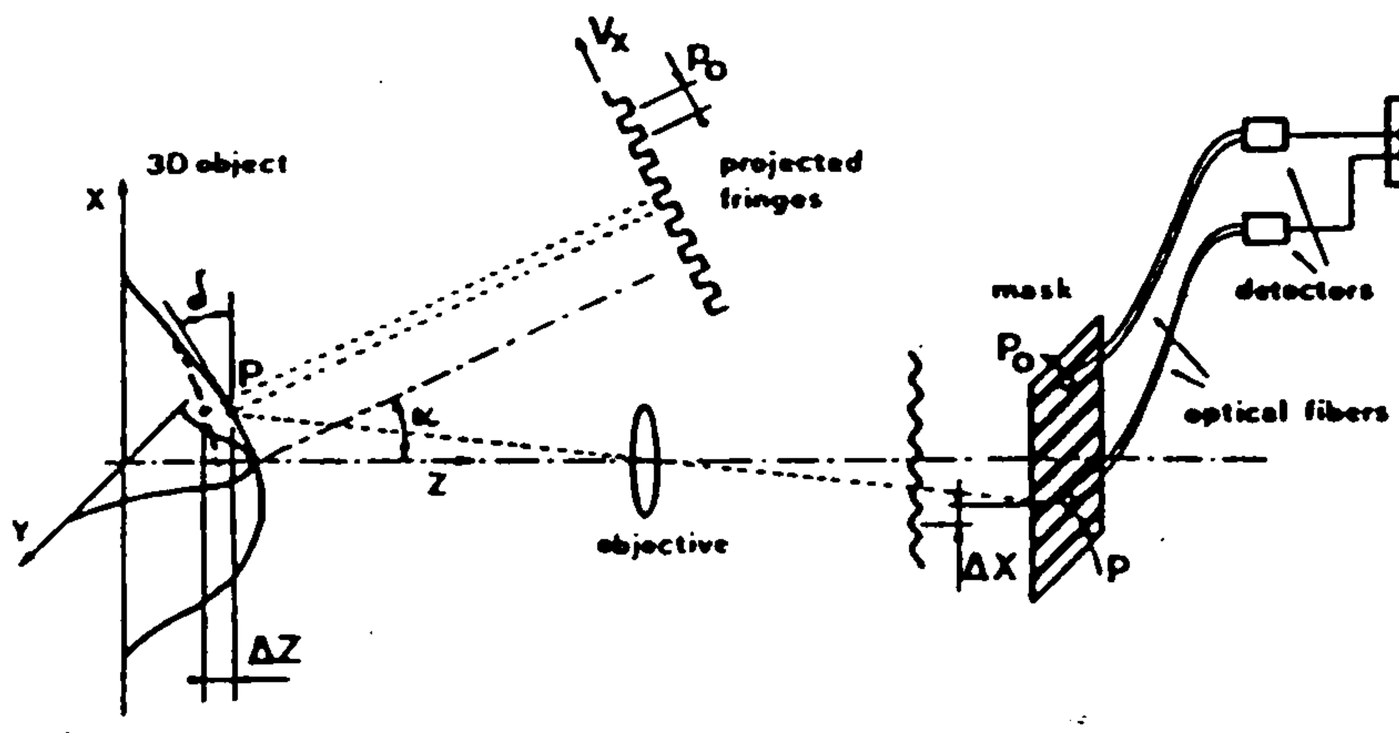

Figure 2.1 Schematic Diagram of fringe projection and measurement through a mask by Indebetouw [2.8].

There are however limitations to the method. To avoid an indeterminate phase measurement, a range of 2π cannot be exceeded. This implies that one must stay within one moiré fringe between the projected pattern and the mask, i.e. the projected fringe pattern cannot be too fine. Also, local variations of reflectivity within a fringe can lead to strong phase errors due to the appearance of an odd part of the electric signal. This would occur if the tool grooves or scratches of a machined part are comparable in size to the fringe period. This source of error limiting the type of surface finish suitable for the methods of fringe projection.

In 1982 Becker et al [2.9] developed a method for the automatic evaluation of interferograms. The system involved digitising the interferograms with a television digitiser, performing different image enhancements on the image. The fringes are numbered using a special scheme with the object reconstructed by a local polynomial least squares approximation. The time for this system to process and analyse a 512 x 512 hologram image was 5-10 minutes.

At a similar time, Robinson [2.10, 2.11] developed a technique which again, brought together the technology of an image processing system and the knowledge to be able to analyse fringe patterns. A schematic diagram of the image processing computer system may be observed in figure 2.2, illustrating the method of image capture, storage and display.

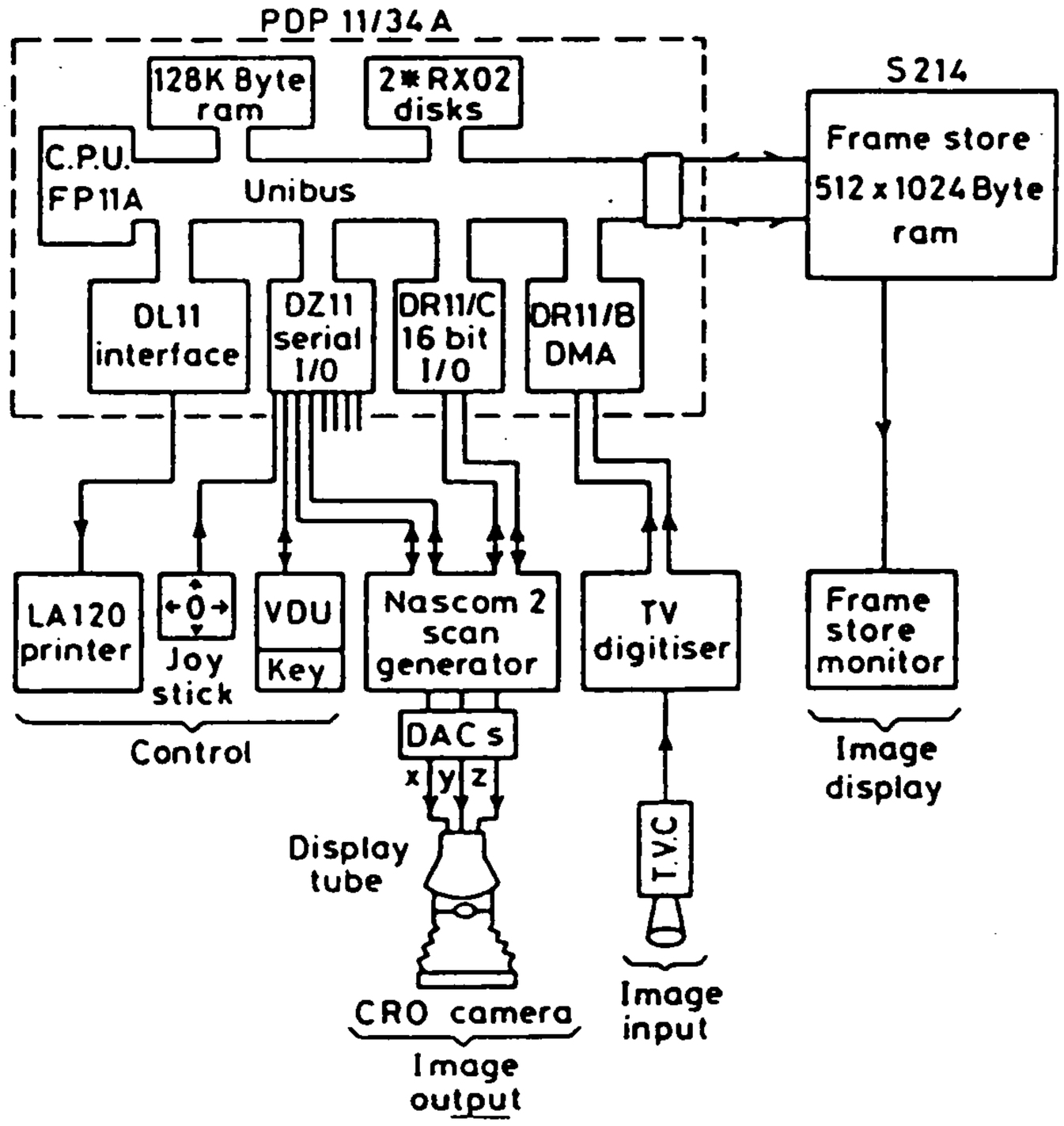

Figure 2.2 **Image Processing Computer System for the automatic analysis of fringe patterns by Robinson [2.10, 2.11].**

Robinson applied his system to a variety of applications:

i) Strain Measurement

ii) 3-D Positional Measurement

iii) Fault detection in Holographic Non-destructive Testing

iv) Moiré fringe analysis in a scanning electron microscope

The potential for development of these techniques are highlighted in two main areas.

a) Where accurate dimensional measurement of complex but noisy fringe data is required, the processing time is significantly longer, due to the processing necessary of which a large proportion of grey level data on such a simple computer architecture.

b) When a qualitative analysis or accept-reject decision is satisfactory, and where binary thresholding is possible, processing times are considerably reduced.

With such a wide number of examples, the versatility of both the computer system and fringe analysis technique are emphasised.

The previous approaches in fringe pattern analysis proposed by Indebetouw, Becket et al and Robinson are categorised as fringe tracking techniques. A number of fringe tracking methods have been developed, Reid [2.1], with the basic fringe tracking procedure described below:

a) Filtering the fringes

b) Fitting curves to the intensity data with a view to interpolating between the fringe centres.

c) Identifying and tracking the intensity maxima and/or minima with a view to skeletonising the pattern and thereby minimising the amount of data which must be subsequently processed.

d) Numbering the fringes automatically or interactively.

This approach however has problems in that although skeletonisation is useful in minimising the data to be subsequently processed (aiding the speed of analysis), a significant amount of useful data is lost. The fact that only a few lines of data, dispersed across the image, are analysed will result in a poor overall impression of this image. Similarly, in the analysis of each line of data (containing the sinusoidal intensity data values), the manner in which information is extracted at specific points (i.e. at each maxima or similarly each minima), again a significant amount of (phase) data is discarded between these points. A method of analysing all of this phase data, of each point throughout the image, would be of more an advantage in providing a more accurate measurement. This is a significant change in approach in the field of fringe analysis in the analysis of phase data.

A variety of techniques have been developed to measure the phase of a fringe pattern at individual points. An interesting method for extracting phase information, which has been used by a number of researchers in the past, is the Fourier Transform technique [2.12 - 2.15].

Takeda describes the analysis of a fringe pattern that may be represented in the form of the equation :

$$g(x,y) = a(x,y) + b(x,y) \cos [\phi(x,y)]$$

where the phase $\phi(x,y)$ contains the desired information and $a(x,y)$ and $b(x,y)$ represent the unwanted irradiance variations arising from the non-uniform light reflection or transmission by a test object.

Taking the Fourier Transform with respect to x, as Takeda [2.12] describes, by the use of a fast Fourier transform (FFT) algorithm gives,

$$G(f,y) = A(f,y) + C(f+f_0,y) + C^*(f+f_0,y)$$

where the capital letters denote the Fourier spectra and f the spatial frequency in the x direction. Since the spatial variation of $a(x,y)$, $b(x,y)$ and

$\phi(x,y)$ are slow compared with the spatial frequency f_0, the fourier spectra are separated by the carrier frequency f_0, as shown in Figure 2.3 below.

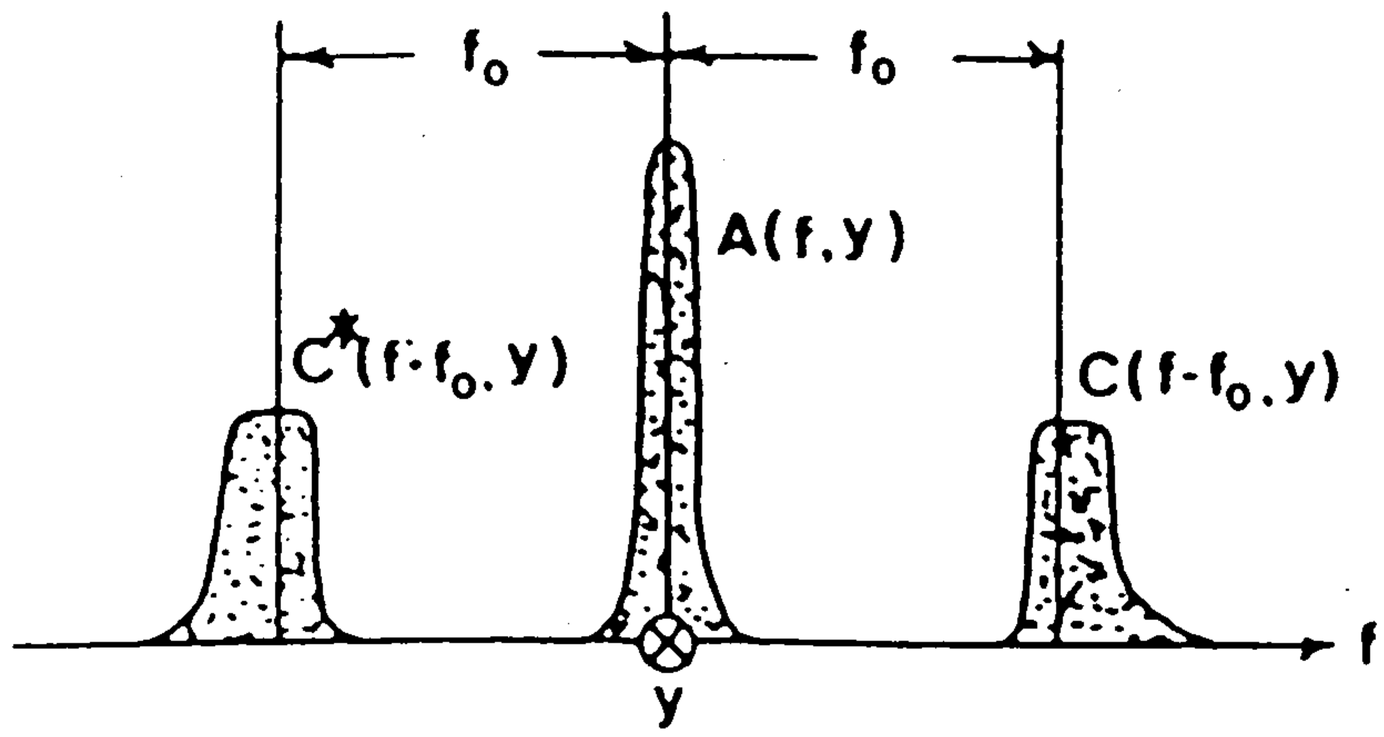

Figure 2.3 Separated fourier spectra of a non-contour type of fringe pattern by Takeda et al [2.12]

The function $C(f+f_0,y)$ can then be isolated by a filter and then translated to the origin of Figure 2.3.

Taking the inverse Fourier Transform of C(f,y) with respect to f, c(x,y) is obtained. The phase $\phi(x,y)$ can then be determined using the expression;

$$\phi(x,y) = \arctan\left[\frac{\mathrm{Im}[c(x,y)]}{\mathrm{Re}[c(x,y)]}\right]$$

where Re[c(x,y)] and Im[c(x,y)] represent the real and imaginery parts of c(x,y).

Similarly, Halsall et al, Malcolm et al and Burton et al [2.16 - 2.20], developed a phase measuring technique using the FFT, producing precision non-contact measurement devices, using image processors in two cases and a digital signal processing chip in the other.

Malcolm et al and Burton et al, have developed their method on image processing systems, analysing 512 x 512 images of 256 grey level resolutions. Over a quarter of a million pieces of information are analysed at any one time, requiring an enormous amount of processing power from the computer hardware for the analysis to be made in a suitable amount of time. Thus the high cost of the computing hardware required.

This is compared to the technique by Halsall et al, where the FFT method is used on the analysis of a line of data from a line scan camera, through a digital signal processor (as compared to the previous more expensive image processing systems). Relatively quick and accurate results may be obtained, on much less expensive equipment, to provide an efficient means of a profile measurement. However, this again is a very computational intensive method (typical for the FFT), although it has great potential is further development of a real-time profilometer.

The basis behind the technique involves the illumination of a surface with a fringe pattern of sinusoidal intensity and viewed at an angle by a camera. The optical setup comprises the use of a laser, beam expander with a collimator, and a wedge, to produce $\cos^2$ intensity interference fringes. By the analysis of these observed fringe patterns, in the computer hardware of the setup, where any deviation from a flat surface will result in the fringe patterns suffering a phase modulation, the fourier transform analysis operation may be performed.

It can be shown that the intensity profile of the illuminating fringes as seen by the camera is given by:

$$I(i,j) = \frac{I_{max}}{2} \cos\left[\frac{2\pi\cos\theta}{p_0}\, j + \frac{2\pi\sin\theta}{p_0}\, h(i,j)\right] + \frac{I_{max}}{2}$$

Expression 3.5 developed in Chapter 3, for a modulated $\cos^2$ pattern, with the phase shift at any point in terms of height at any point i.e.

$$\phi(i,j) = \frac{2\pi \sin\theta}{p_0} h(i,j)$$

or since θ and p_0 are constant.

$$\phi(i,j) = Kp\ h(i,j)$$

where $\phi(i,j)$ is the phase shift at any pixel location (i,j).
h(i,j) is the height and any pixel location (i,j).
Kp is known as the phase constant.

Taking the Fourier Transform of a function such as equation 3.5, a power spectrum (i.e. the previous Figure 2.3) would be produced.

Again, once the inverse Fourier Transform has been applied, the phase of the original fringe pattern may be calculated by:

$$\phi(x,y) = \arctan \left[\frac{Im[(x,y)]}{Re[(x,y)]} \right]$$

The phase distribution is modulo 2π, and must be unwrapped to give a continuous phase distribution, from which it is a simple matter to use expression 3.5 to calculate the range map. Requiring only the geometric properties of the set-up, i.e. Angle θ and fringe period p, the phase constant Kp may then be determined, and so height h(i,j) at any point.

The FFT used by these researchers gives an absolute measure of the fringe pattern being analysed. However, there are problems encountered, namely the fact that it is very numerically and computationally intensive, and also provides an absolute measurement as opposed to the comparative method developed ultimately by this author.

Three problem areas [2.18] are also encountered when the FFT is used as an analysis tool in this fashion. These sources of errors include:

i) Aliasing where high frequency components of a time or spatial function can translate into low frequencies if the sampling frequency is too low. This problem can be alleviated by increasing the sampling frequency, but again may be present even if the highest frequency component is less than half the sampling frequency.

ii) The picket fence effect is corruption to the frequency spectrum. This occurs if the analysed waveform includes a frequency which is not an exact multiple of the number of points in the transform. For example, all frequencies should be of value N/r, where N is the number of points in the transform and r is an integer, if this effect is to be avoided.

iii) Leakage refers to the apparent spreading of energy from one frequency into adjacent ones. This arises due to the truncation of the time sequence such that a fraction of a cycle exists in the waveform that is subjected to the FFT.

Other researchers Halioua et al [2.21] developed a phase measuring system of a similar approach, with a sinusoidal grating structure projected onto an object. The resulting effect is observed by a camera offset at an angle and analysed by a microcomputer using phase measuring algorithms Figure 2.4. Two systems were developed, one that yields range measurements from a single point of view over a two-dimensional array of points, and a second that permits full 360° measurement.

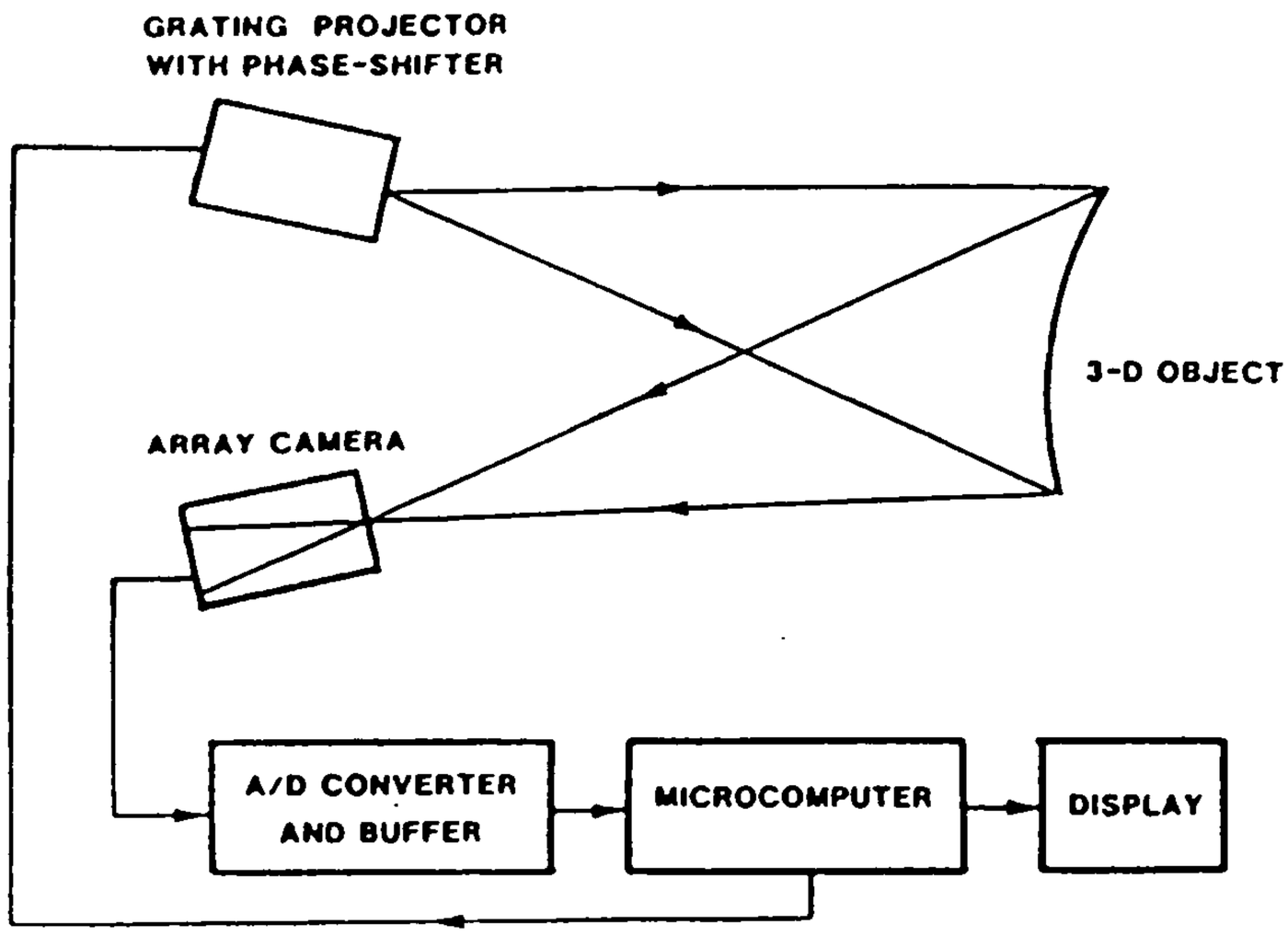

Figure 2.4 Block diagram of complete system by Halioua [2.21]

The first system incorporates the projection of a parallel sinusoidal pattern produced from a complex optical set-up comprising a laser source. This interferometer is compact, stable and insensitive to external disturbances, but like other laser based interferometers restricts the size of object able to be measured.

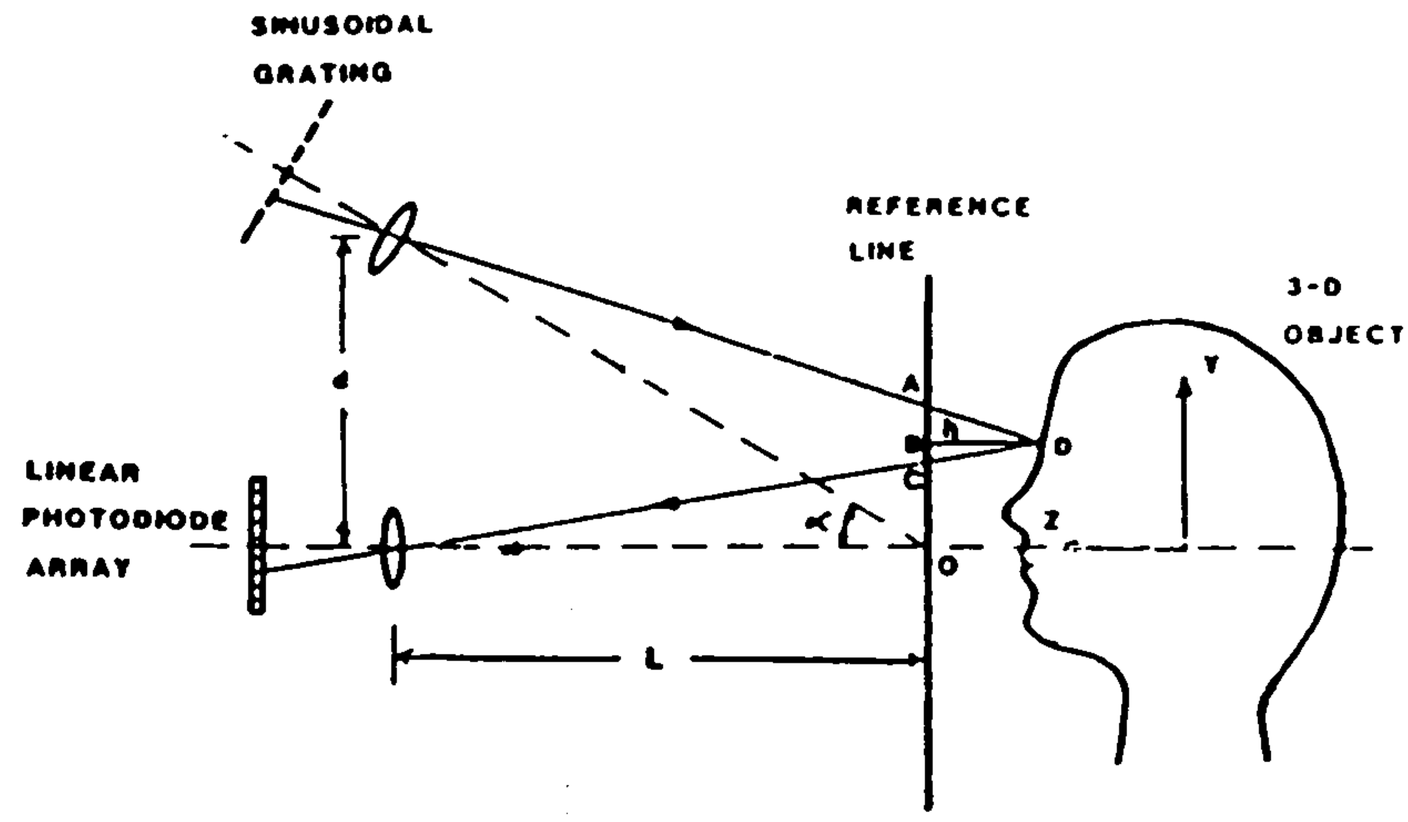

Figure 2.5 Optical geometry for 360° measurement with diverging white light illumination by Halioua [2.21]

The second system Figure 2.5 however is more practical in handling large objects, using a diverging, white light illuminated, sinusoidal grating. The object is placed on a rotation stage, which is rotated by discrete angles between each recording, enabling 360° reconstruction to be possible. Since illumination is of a diverging nature, the analysis is more complicated than the previous case, a different approach requiring a different phase mapping algorithm is developed.

Both systems produce good results (accuracy within 0.1mm), but the complexity of the optical end of the first system is a major disadvantage. The added restriction in the size measurable by this method, led to a more practical, white light system. However, this complete system is computationally very intensive (typically when analysing the phase of a whole image), but in this case for a 360° measurement, considerably more data. Also, in the application of the projection of sinusoidal fringes in the phase measuring technique, the fringes must be ideally sinusoidal. Producing sinusoidal fringe gratings is difficult for the white light projection application.

2.2.2 Moiré Contouring

Moiré fringe patterns are formed when two similar but not identical patterns are superimposed upon one another. The majority of moiré patterns are generated by the interference of straight line fringes, although curved lines have also been used in the past. A moiré pattern is made by forming a fringe pattern on a subject, produced either by projecting or shadowing, and comparing this pattern with some reference pattern by overlaying the two fringe images. The fringes produced illustrated in Figure 2.6 below.

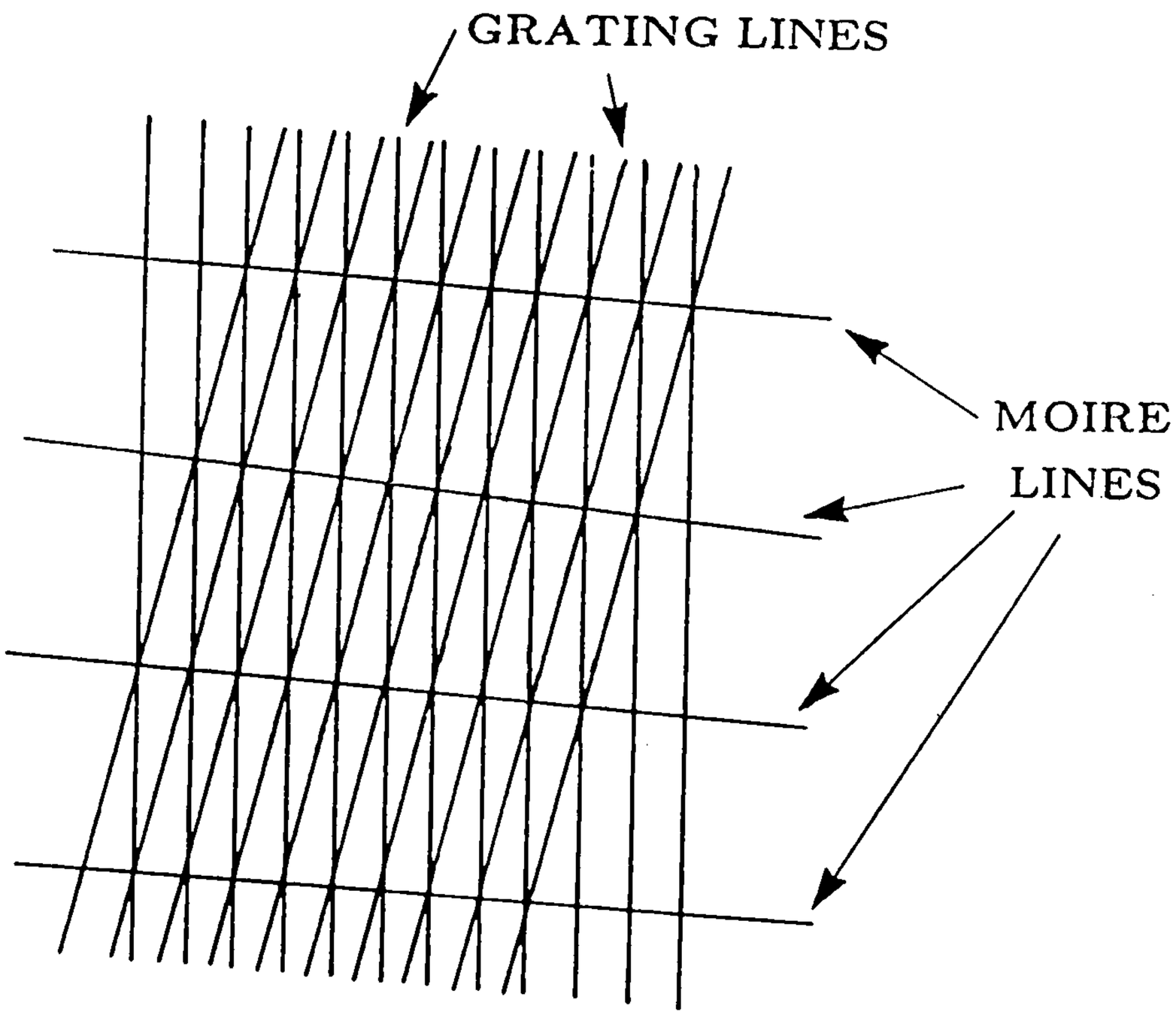

Figure 2.6 Illustration of the beat Moiré fringes created by overlaying two gratings by Harding et al [2.22]

If the reference set of fringes are straight lines, the beat pattern between the two images will form a contour map of the object's surface in the same manner as a topographic map illustrates the contours of the land. Each fringe line follows along the surface of the part at a constant depth range from the viewing system. This meant that every point along a fringe line

is at the same height. As the slope of the surface increases, the fringe lines will get closer together. If the surface slopes a different way, the fringe lines will change accordingly.

As stated by Harding et al [2.22] the pattern produced is a function of the surface shape, and, as such, moves with the part without changing its character. Wherever the part is and whatever orientation the part is in, within the field of view of the system, the moiré fringe pattern on the part will look the same.

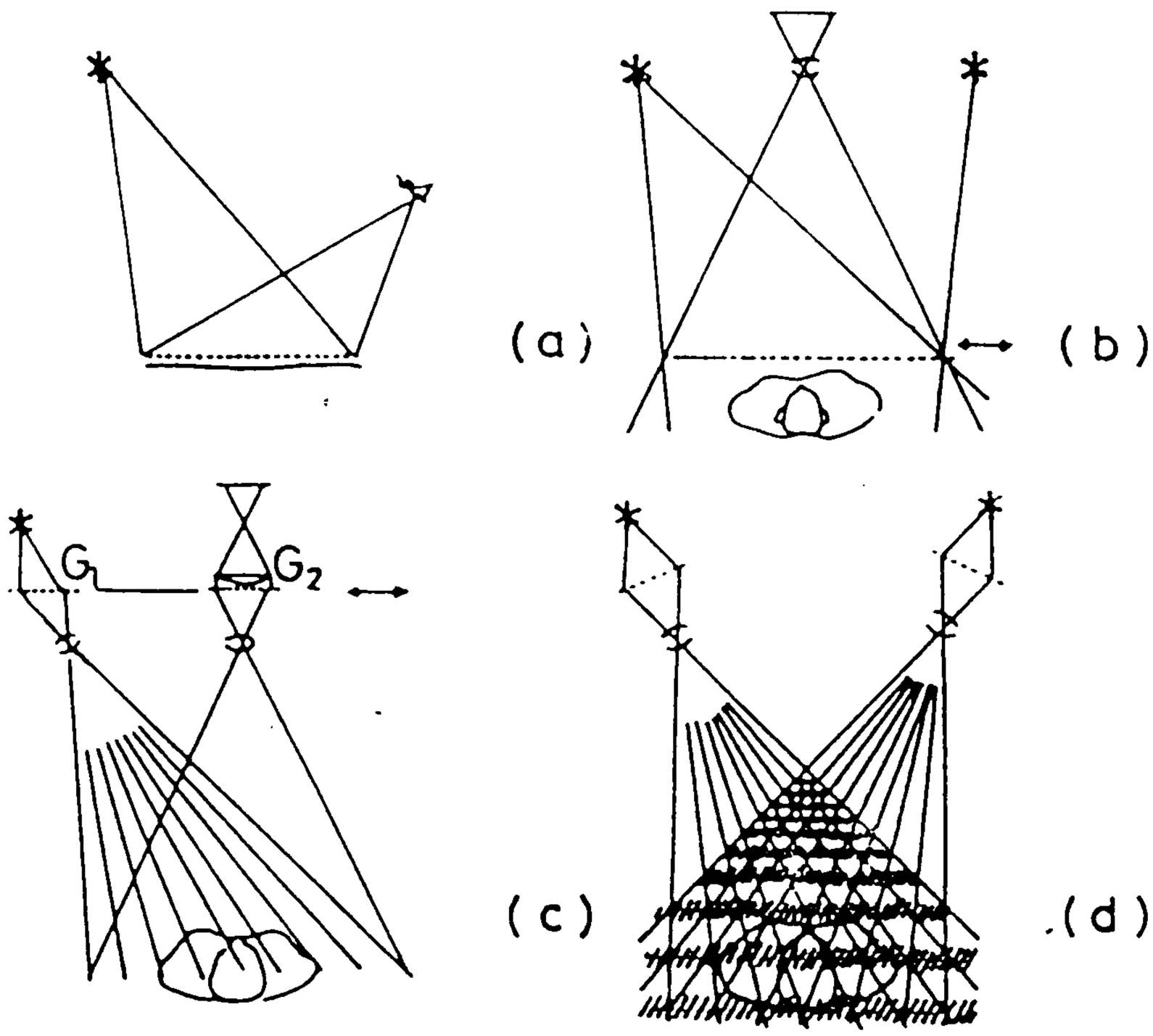

Figure 2.7 Development of modern Moiré topography by Takasaki [2.23].
a) Oblique Shadow b) Basic Type
c) Projection Type d) Additive Projection

The classical oblique shadow method, as shown in Figure 2.7 (a), was perhaps the initial starting point in the development of modern moiré topography [2.23]. When this technique was used, the object was required to be almost flat. This limitation was removed by adjusting the distances from the grating to the light source, and to the viewpoint equally, as shown

in Figure 2.7 (b). From this point, it now becomes possible to show equal height contours by moiré fringes on a large object, although, when the curvature of the object is high, the fringes become diffuse. The two types of noise produced are due as a result to diffusion of the shadow of the grating, and the moiré fringes formed by the higher harmonic components of the grating and its shadow. Both types of noise may be eliminated by the movement of the grating in its plane, since the noise moves and change shape with this movement, even though the fringes showing the contour lines of equal height do not.

With the errors of the grating averaged over the extent of the movement, the accuracy has improved significantly. Employing the moving grating technique is both simple and accurate. However, a grating of the same size as the test object must be placed to its surface, thus limiting the free movement of the test object. A modified type of moiré topography which solves this problem is shown in Figure 2.7 (c). The grating is projected onto the surface, and viewed through an identical grating. Again, the moving grating technique can also be applied. This moiré projection technique has been investigated extensively in the past, with another adaption to the technique, resulting in the additive projection type. In this technique, the moiré fringes are produced by projecting two gratings with different angles onto a test object using two projectors, as show in Figure 2.7 (d). The moiré fringes are generated as a result of the non-linear responses of an observer's eyes. This technique has the advantage in that is permits in situ observation of the fringes, although the fringe visibility is low.

Traditionally, moiré patterns have been generated in two ways:

i) Projection moiré, in which a grating is projected upon a surface, which is subsequently viewed through an optical system which contains an identical grating (Figure 2.8(a)).

ii) Shadow moiré, where light illuminates a grating placed close above the object, casting shadows on the object which are

subsequently viewed through the same grating, but at an angle to the projected light (Figure 2.8(b)).

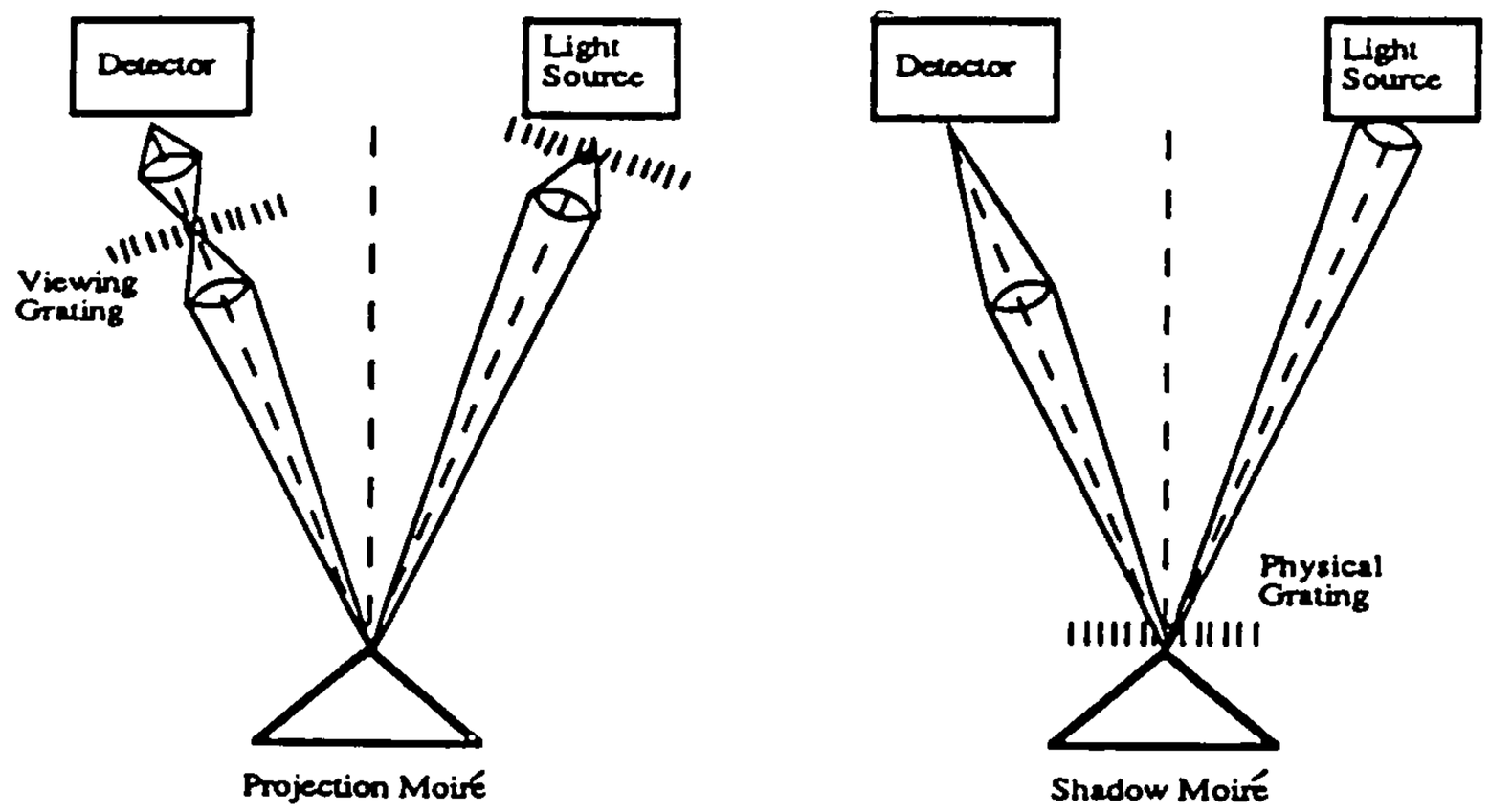

Figure 2.8 (a) Projection moiré (b) Shadow moiré by J. H. Blatt [2.29]

In the case where the part cannot be close enough to the grating for a clear shadow of the grating to be formed on the part, a projection approach can be used where the master grating is imaged onto the surface. Then the surface is imaged back to a reference plane, from an angle different from the illumination angle. The resulting image is viewed through the submaster reference grating.

If the reference grating is made by recording the image of the object grating, then the moiré pattern can be used to show only differences between the reference object and some new object. In this way, moiré can be used to show only deviations from a good part. However, if the reference grating is a recording of how the grating looks on the part, then to achieve an accurate subtraction of the part geometry, the past must be repositioned where it was located when the reference grating was recorded. The tolerance on this repositioning is a function of the complexity of the part geometry.

Reid et al [2.24 - 2.27] described a phase measuring version of projected moiré topography which allows fully automatic on-line analysis of moiré fringe contour patterns. The technique described can be used for both absolute and comparative measurements of the surface form. Most authors describe apparatus that is similar to that shown schematically in the previous Figure 2.8.

A grating is projected onto the object while an image of the object is formed in the plane of a reference grating. The reference grating is a photograph of the grating projected onto a flat surface. Interference between the grating image and the reference grating causes a number of moiré fringes to appear superimposed upon the surface of the object.

It must be assumed that the camera and projector are geometrically similar (that is, they have the same ratio of grating pitch : lens grating separation) and have parallel optical axes. Further assumptions must be made with respect to the perspective centres of the camera and projector. Under these conditions, the fringes produced describe contours of equal height. The analysis of the fringe pattern by a phase measuring approach is then undertaken.

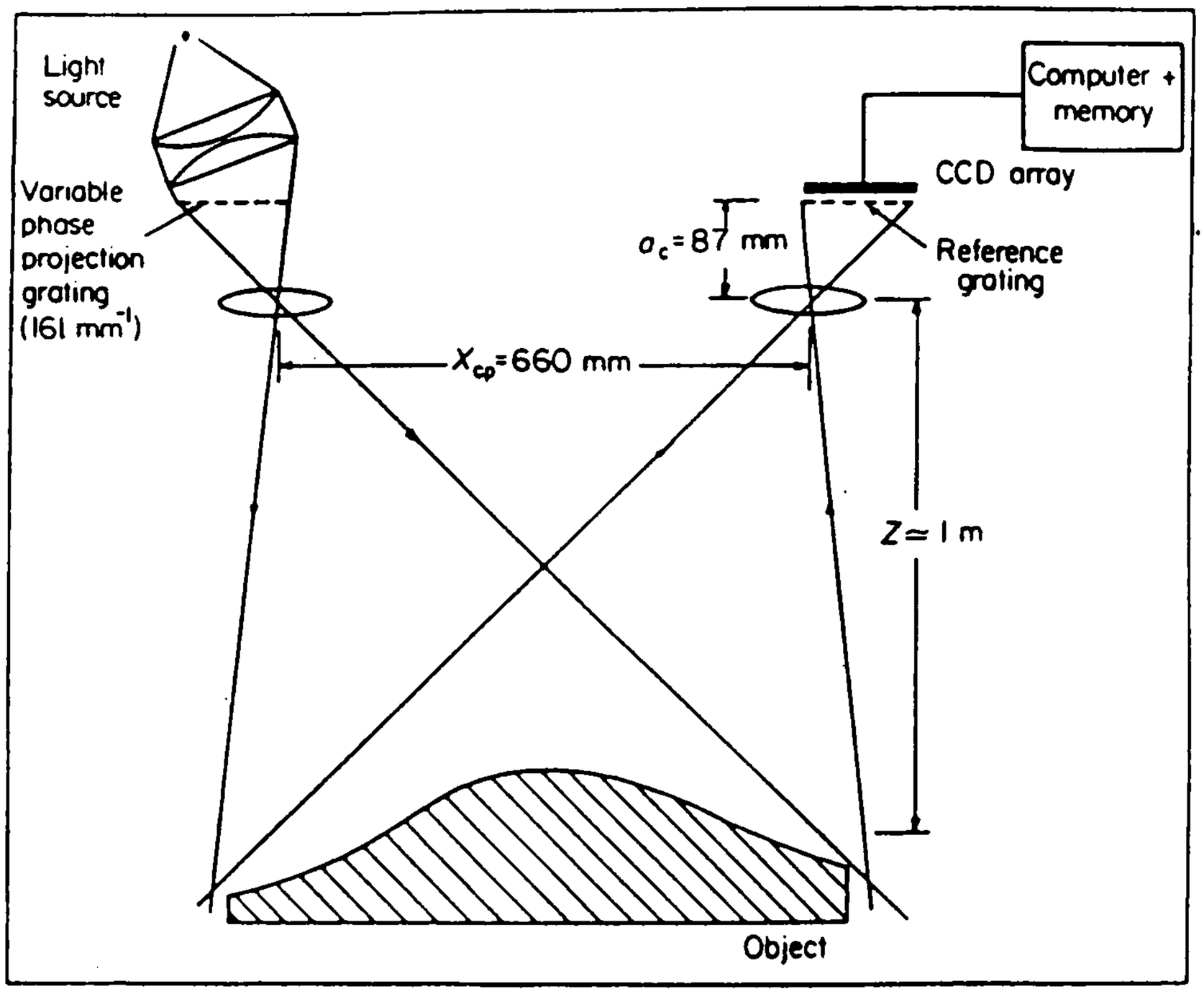

Figure 2.9 Phase-measuring moiré topography: Reid et al [2.24]

As shown in the figure 2.9, the basis of the system adopted by Reid et al, required the projection grating, of pitch Pp, to be moved through a distance Pp/K (that is, the phase of the projection grating is moved though 2π/K) and a second image is read into the computer though the CCD camera. This process is repeated until the projection grating is moved through (K-1) equal steps and a total of K images have been stored in the computer memory, in order for K intensity levels to have been stored at each pixel location.

To evaluate the phase of the moiré fringe pattern at each pixel co-ordinate, the Fourier series coefficients must be then evaluated. From which the height distribution may be determined.

The complexity of the optical setup and the computational intensity of the technique, are great disadvantages of this technique. Together with the fact that a comparative measurement would be a better solution, rather than an absolute measure, of which moiré is an example.

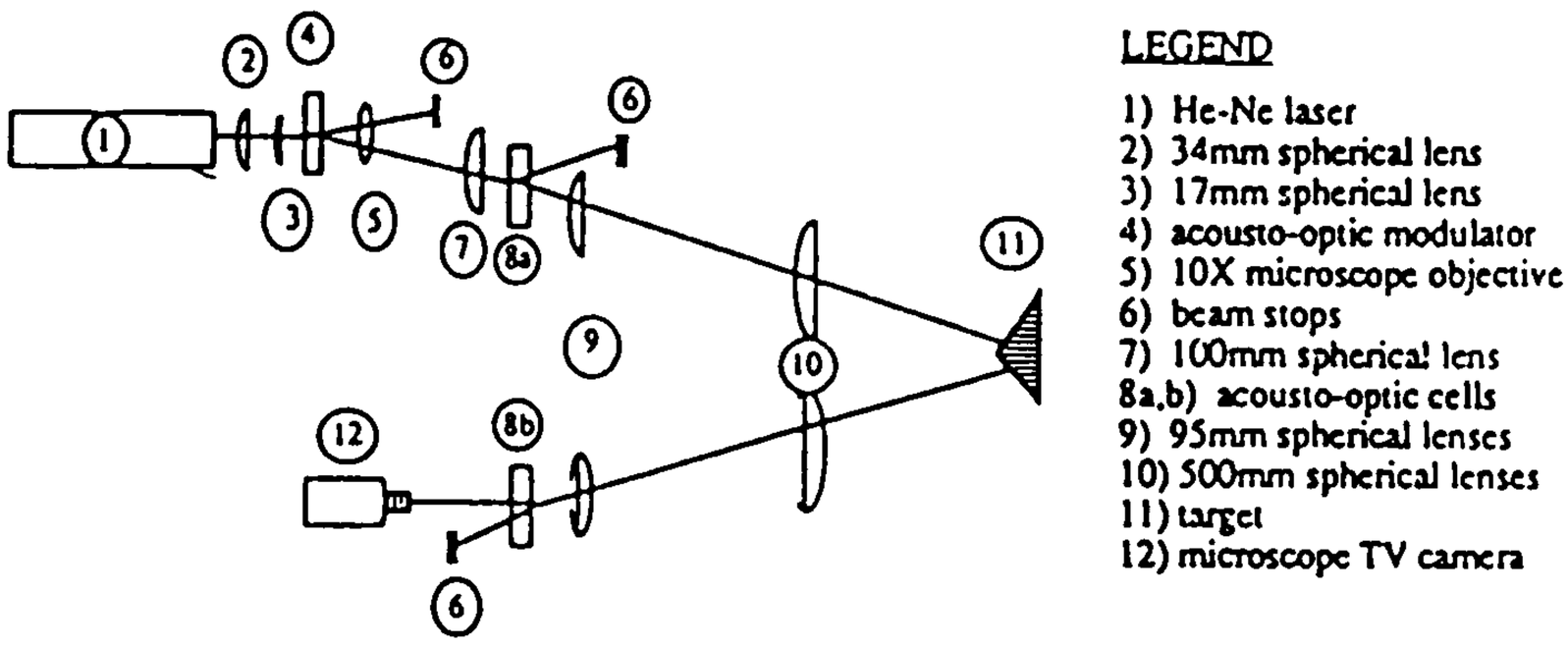

Figure 2.10 Acousto-optic moiré topology by Blatt et al [2.28]

An adapted projected moiré system developed by Blatt et al [2.28, 2.29], incorporated a method of generating and projecting contours of variable period magnitude. The main elements of the system are two acousto-optic cells (used because of its large refractive index, its low optical absorption and its resistance to optical damage). In general, similar in setup to projected moiré, the cells are placed in the same grating location, but with additional lenses (Figure 2.10). The modulated laser beam from one cell is projected upon the surface, with the output observed through the other cell. The space grating is generated electronically inside the acousto-optic cells by square wave modulation of the acoustic wave, with the spacing rapidly altered by changing the modulation frequency. The complexity necessary in producing a variable period grating is a major disadvantage, considering that a range of different period sized gratings is more than sufficient to achieve the same result.

An example of using shadow moiré topography was proposed by Jin and Tang [2.30], in which similar to Reid et al, the phase measuring approach is adopted. Although, optical much more simple, a major disadvantage is the requirement for the grating to be of the same size as the test object, severely restricting the free movement of the test object.

There are several more limitations to shadow moiré topography. First, the

surface to be measured cannot be too steeply sloped because the density of the fringes cannot exceed the resolution of the camera system. Second, the surface to be measured cannot be too flat because too flat a surface will produce either no moiré fringes or very coarse moiré fringes.

However, these limitations may be avoided by altering the sensitivity of the technique, simply by altering the angle, or period of the grating. The higher sensitivity, the more moiré fringes appear. Another limitation is that the area to be measured is limited because it depends on the collimating lens used to make all rays parallel.

Also, there are some sources of error in this method, in accurately determining the fringe grating period and angle. The grating period and the grating distance moved can be measured accurately if measured carefully, but the angle can hardly be obtained accurately if measured directly, with an inaccurate measurement resulting in a large error. A more accurate angle may be obtained from calibrating an object of known size.

There are two main reasons why basic moiré topography has been so successful. For one, the moiré fringes are formed by the grating and its shadow at the very first stage of the process. As a result, the spatial frequency which must be treated in the system is low. Secondly the picture noise is averaged by moving the grating. The spurious fringes are erased and the accuracy of the measurement is improved by the technique. Stimulated by the success of the basic type of moiré topography, new techniques have developed, but with the simplicity and accuracy of the basic method replaced sometimes by more elaborate, complicated and more expensive solutions. In fact, very powerful real-time data processing may be achieved by electronic moiré topography. But the complicated setup of instruments necessary, as well as high cost involved, may prevent the system being popular. The added problem is the requirement of the use of phase data (Reid [2.24-2.27]), although accurate, is computationally intensive since each point is analysed. Similar to any successful solution, the merits and disadvantages must be balanced against each other, and an

adequate compromise made between the two.

Other problems of processing moiré fringe patterns are, the ambiguous fringe pattern, i.e. the possible confusion between the primary and secondary fringes, the non-continuity of the fringes and the fact that an absolute as compared to a comparative measurement (a better solution) has been made.

2.3 Image Subtraction

Another interesting field of automated inspection where a significant amount of work has been achieved in the past, is in the field of printed circuit board (PCB) inspection. With this method a number of workers have developed comparative measurement techniques using image subtraction, as compared to the previous absolute measurement methods.

Image subtraction is the most simple approach to the visual inspection problem. With this approach the part to be inspected is scanned and its image compared to an ideal example. The subtracted image, showing differences, can be subsequently be displayed and analysed. Figure 2.11 shows the subtraction process.

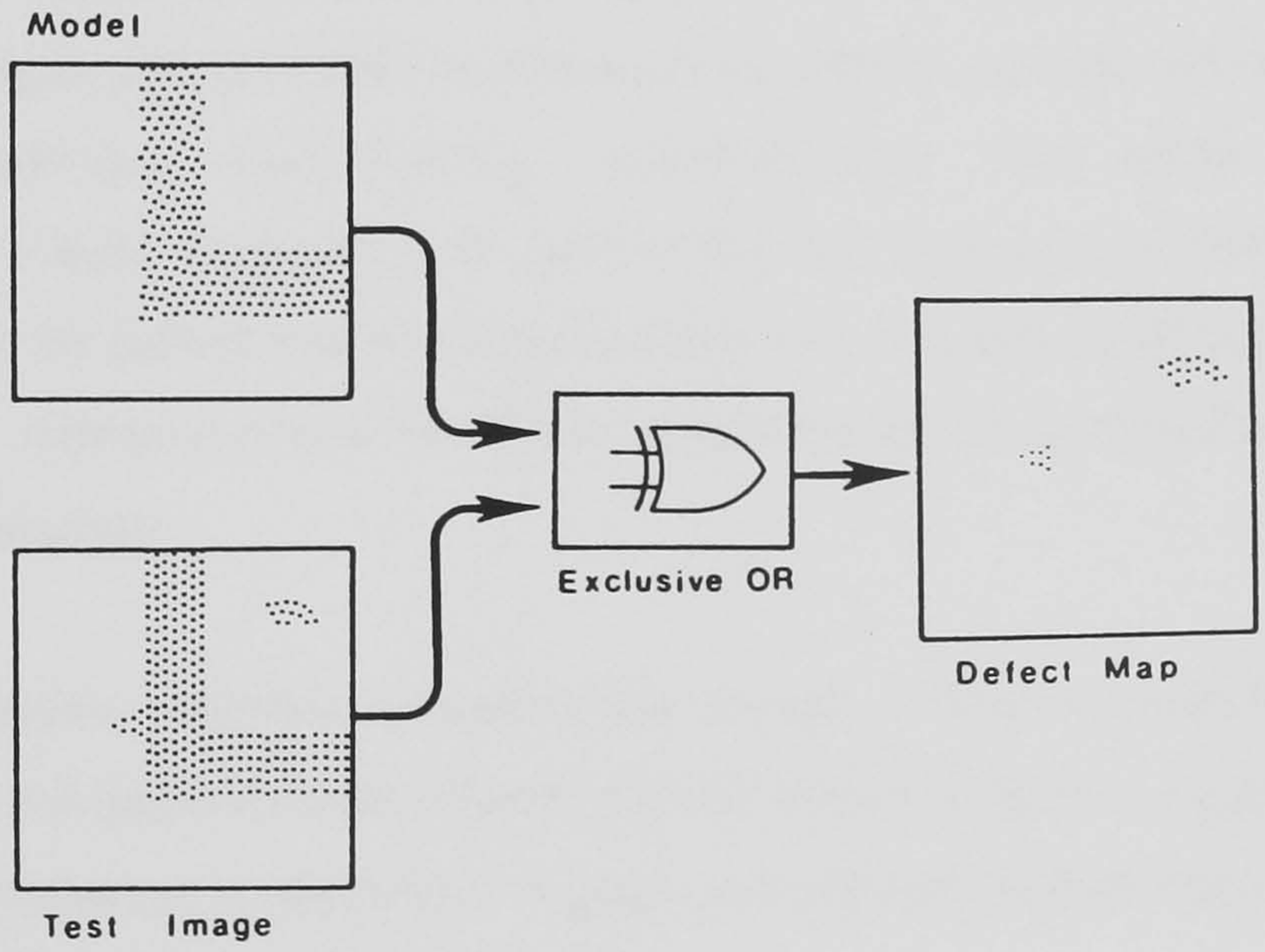

Figure 2.11 Image subtraction process [2.33]

The application of image subtraction together with fringe projection is an obvious and simple approach which may be adopted in the development of a surface inspection method. However, there are a certain number of assumptions that must be made in the application of subtraction.

By definition, the results of a subtraction is a difference. This difference may be due to a number of reasons. For instance, a surface defect or missing item, a relocation error or difference between the two images (no two items or scenes are identical). The difference may only be assumed to be a defect, providing the images align with on another perfectly (i.e. no relocation error) and there is no visual noise (which is impossible although visual noise may be minimised).

The following brief review has primarily been investigated in the context of inspection by image subtraction. The purpose of which is to illustrate the problems encountered in PCB subtraction methods. More comprehensive reviews of the different techniques involved in the inspection of PCB's have been described by a number of authors [2.31-2.35].

Printed circuit boards (PCB's), the heart of all electronic devices, are extensively inspected to isolate errors such as shorts, opens, missing holes, incorrect markings, over-etching, under-etching and other effects. Traditionally, visual inspection is performed by workers to detect large flaws, to align the board and to control tolerance. It is the small scale flaws, often tedious inspection and for these defects that an automated system would be invaluable.

All PCB inspection methods require some aspect of prior knowledge of the PCB, such as the geometric structure and dimensions as well as the various engineering tolerance standards. Image subtraction is the most obvious approach to the visual inspection of PCB.

A number of researchers have developed PCB inspection systems in the past, implementing this method in a video processor by comparing video frames with a perfect image stored on a video disc. Lee [2.36] has used an image subtraction method for inspection of printed thick film patterns on ceramic substrate. He also extended the method to include a searching scheme through the subtracted image for potential defects.

The method of image subtraction suffers from several problems such as the large reference data storage, precise alignment and sensitivity to illumination and scanner conditions. One other drawback of image subtraction is the fact that many and perhaps most acceptable PCB's do not match point to point identically, because of shrinkage and swelling of the board. In this situation the use of some method of compensation may result in systems which become impractical.

Feature matching is an extended approach of the image subtraction method. Typically, the PCB to be inspected is scanned while the required features are extracted. Then, instead of comparing the PCB and perfect pattern with each other directly, only the features extracted from the PCB and those in a perfect example are compared. If these correlate with one another, the PCB is satisfactory. This subsequent processing is referred to as local feature extraction and template matching. This method significantly reduces the image data necessary for storage, and the sensitivity of the input intensity data.

Chou [2.37] devised an inspection system for PCB's using a similar method. The method's important features comprises of vertically viewing the PCB and its resulting pattern from the direction of illumination. A fluorescent ring light or a number of fluorescent tubes are placed around the camera, surrounding the four sides of the PCB (Figure 2.12). With this configuration, the light is uniformly distributed with the incident angle of light ranging from 10° to 70°. The choice of lens is dependent on the different component whose size can range from 10 to 40mm.

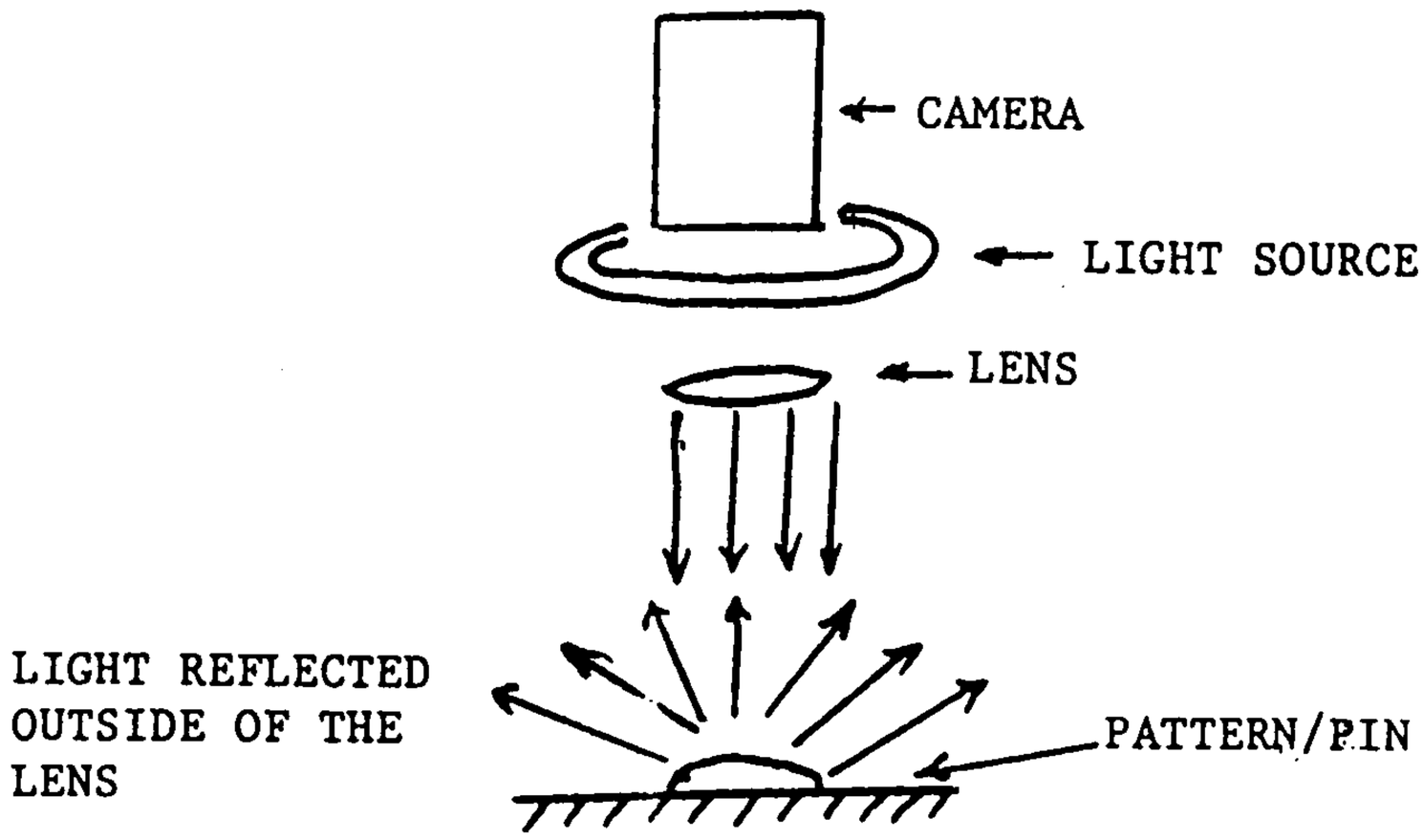

Figure 2.12 Detection of pattern vertically illuminated by Chou [2.37]

The actual final design comprised of two scanners, to enable both sides of a PCB placed on a two dimensional translation stage, to be examined.

Since all PCB inspection algorithms although diverse, utilise prior knowledge of a standard to be compared with, the method of image subtraction is the most obvious solution. But the problems suffered by this method of, large data storage, precise object alignment, and sensitivity to illumination and scanner conditions, resulted in incorporating feature matching in the subtraction. This involves creating a model of a set of chosen features which maximise the discrimination between each PCB specimen and master reference. A number of models comprising a variety of these features present, missing, orientated and misorientated are built up and stored in a database, to enable a semi-automatic training process to give the operator the opportunity to create best features to use during inspection.

However, there are problems with this method.
These include:

i) The complexity of the algorithm for matching each feature.

ii) The number of permutations of a misorientated feature. Thus, providing a large number of possible model sets.

iii) The slow speed of analysis for such a complex algorithm.

iv) The requirement for the XY table on which the PCB is placed, to move quickly (for real-time purposes) and accurately (for precise alignment).

Similarly, Mountjoy et al [2.38] developed a technique incorporating the most obvious approach of image subtraction. The basic technique consists of directly viewing the board to be inspected, placed upon an XY table, capable of positioning and rotating to any desired position. With the aid of a joystick, the operator selects the pertinent points from the image for storage, some components requiring more points than others. A training table is created containing, for each point, the location co-ordinated, digitised grey level value and associated component description. In this manner only a relatively few points from the image are stored, thereby increasing the inspection rate and decreasing the amount of storage required.

In the inspection phase, the data from the training table is accessed, to enable the correct features for those co-ordinates to be compared with. Thus, the decision is made to conclude whether a component is either present or missing.

However, as the data set of the image increases, the real-time inspection factor becomes critical. In order to have a fast inspection rate and minimal amount of storage, data reduction would be required. The abrupt changes in intensity along the edges separating the only two kinds of material of the board, metallic conductor and laminated plastic, give rise to simple approach to obtain a bilevel image.

Thresholding and edge detection techniques which were applicable to this problem were examined by Mountjoy et al. On implementation demonstrated that a Roberts [2.39] gradient edge operator and thresholding function, were quite appropriate in this application. With a reduction in the information retained by using only the edge location, a training table is created consisting of only information the line number, edge counts and location co-ordinates. During inspection, rather than performing subtraction on pixel by pixel between master and test images, edges on the test boards are compared with those on the stored table.

The advantages and disadvantages of this technique are identical to the previous method. However an additional advantage to this technique, with the inclusion of feature extraction and edge detection, is a significant reduction in data produced, increasing the speed analysis. This is countered by the disadvantage that with edge detection, information related to the difference in the images, thus missing components or defects, may be lost or confused with other data, due to the lack of detail in an edge extracted image.

Ejiri et al [2.40], developed a different and more interesting approach in inspecting PCB's. A method of detecting defects in complicated patterns is described. If the object to be tested has a plain or uniform surface, defects such as stains are easily detectable by thresholding the brightness of the surface reflection. However, when the object itself has a complex pattern such as that of a PCB, it is generally very difficult to discriminate the defective portions from the normal portions. According to the usual methods of pattern recognition, the defect pattern portions would be memorised and used as standard patterns for recognising similar defects. However, the patterns have an infinite number of shapes and sizes, and for this reason, it is virtually impossible to memorise all possible defect patterns.

The method dealt with in this technique does not require any predefined model of a perfect pattern. Instead it is composed of two-dimensional logical filtering operations based upon the nature of the object pattern.

These filtering operations introduce an irreversibility into the image processing.

This method is also equivalent to the generation of a pseudo-standard pattern, in which the defect portions are eliminated, from the input pattern. These are potential defect portions. To do this a process of expansion - contraction is developed on the binary image of the PCB to be inspected. Areas identified as conductors are first enlarged uniformly in all directions, and then contracted by the same amount. The enlargement eliminates all small scale features on the conductor. Here small scale features smaller than a certain size are considered to be defects and are eliminated from the input pattern. This enlarged pattern is then reduced by the same factor to eliminate small features within the substrate. The pattern derived from this expansion - contraction process is used as the model in an image subtraction process in which the input PCB pattern is compared with the derived model. Since this model is generated from the image pattern under inspection without using perfect patterns, the term pseudo-model is used. Figure 2.23 illustrates this pseudo-modelling and the subsequent image subtraction process.

The unique characteristic of this method is its generation of the pseudo-model. The feature is a set of small-scale objects (e.g. nicks and dots) found on the PCB. This feature is used only for the modelling process and not during the detection. The detection is an image subtraction process operating on two binary arrays. This eliminates the problems of positioning between the input and the model as well as the need to train the model manually before the inspection process begins. However, it only detects small defects.

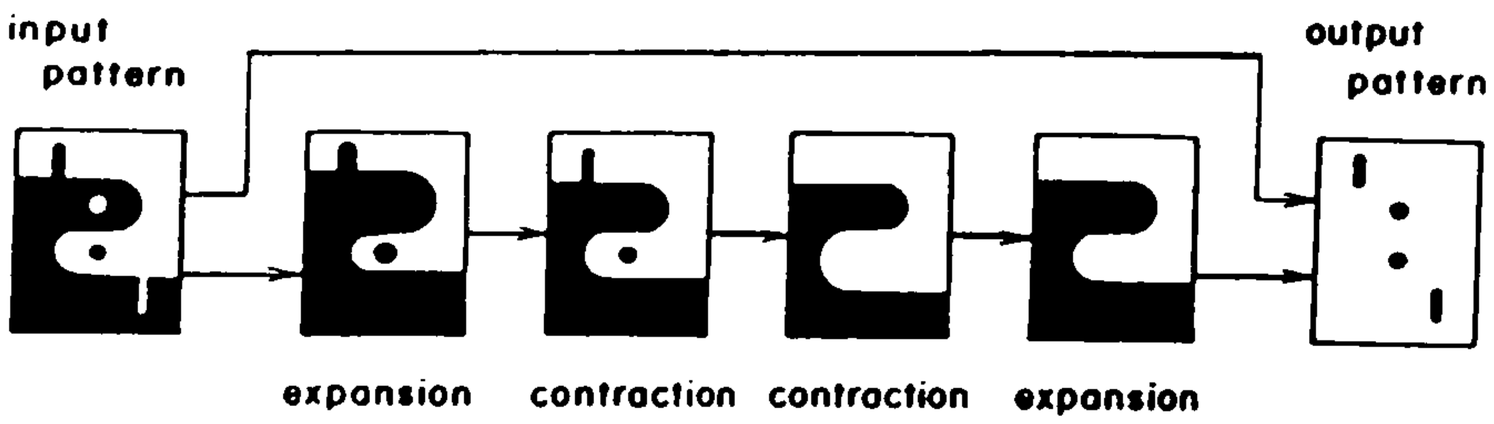

Figure 2.13 Principle of the expansion-contraction method for detecting small defects. Ejiri et al [2.40]

Chin et al [2.41] used an operator-interactive model building graph procedure to train the PCB inspection system. Operator interaction is necessary when features are extracted, noise reduced, model graph defined and model features modified. In this step, the operator uses a joystick and display, to select windows and to remove unwanted areas. In the later inspection phase, instead of searching for similar features through the PCB under examination, the inspection routine accesses the stored models for expected feature types and edge locations. Thus, directing the scanner to look for the expected features in the test image. If the feature is missing or measurably different, the graph model indicates an error. Unlike most of the other feature comparison methods, this procedure does not require scanning/processing the entire PCB image. However, it requires precise alignment, and isolated defects of a significant distance from the expected edge will be missed.

2.4 Surface Inspection by Subtraction

Subtraction has primarily been used in the field of PCB inspection but has also found uses in other areas.

Royer et al [2.42] devised a method of automatic measurement of a crater volume by means of light sheet projection. The method consists of projecting diverging fringes onto the object surface, viewed from a different direction to the direction of illumination. By translating the object and then scanning the surface again, the volume may be determined by the following relationship.

$$\text{Volume} = H.E.dx.\sum \frac{yi}{yo}$$

where
- H = Known depth.
- E = Fringe spacing.
- dx = Measurement step along fringe.
- yi = Distortion measured at given point.
- yo = Fringe distortion corresponding to the known depth H.

Therefore it can be seen that this system is in principle similar to phase stepping, but with the object moved and not the fringe projection system.

For complicated forms where some hollows may happen to be hidden by prominent parts, a diverging illumination and a double visualisation system (incorporating two symmetrical directions of observations) is used. (Figure 2.14)

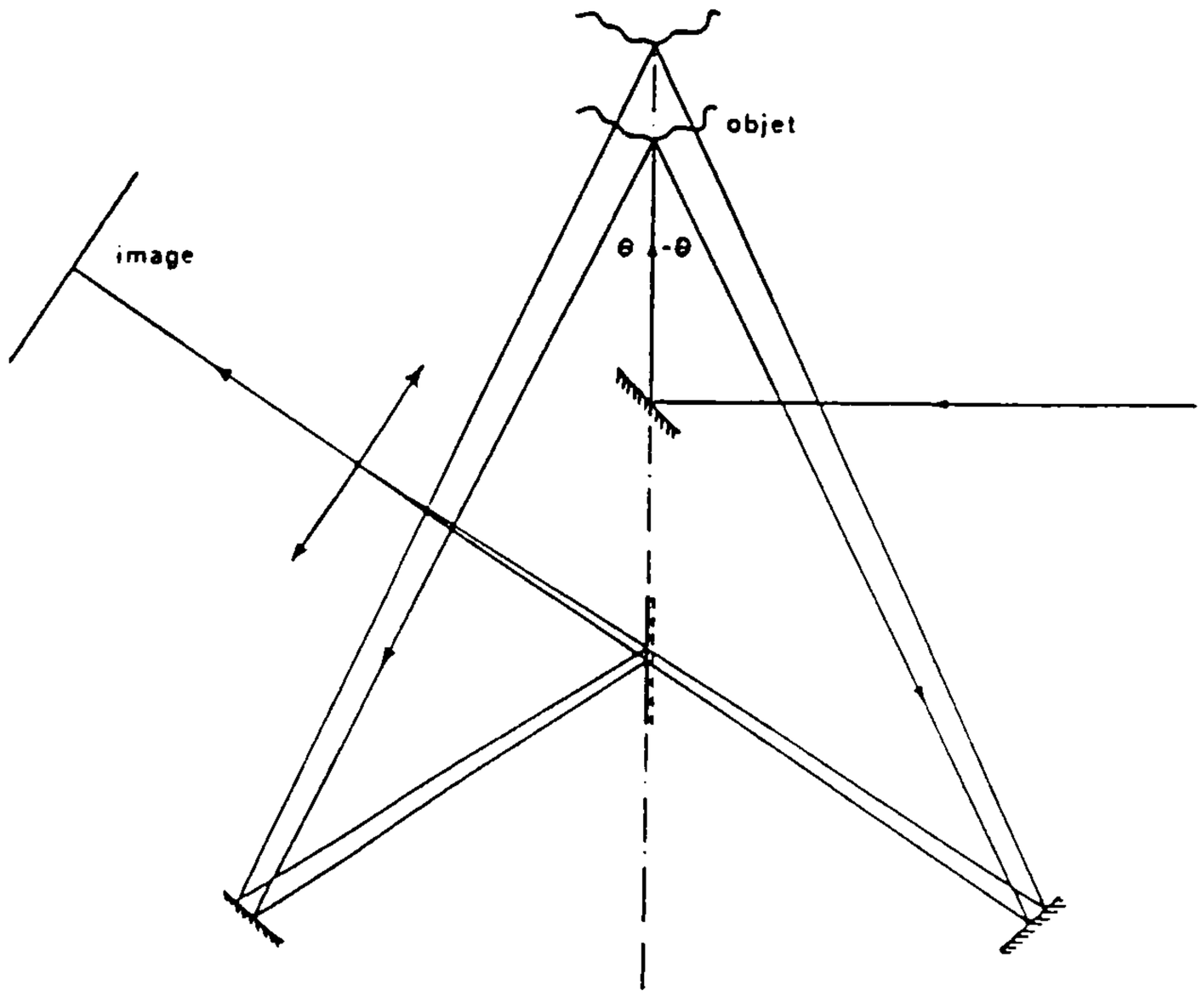

Figure 2.14 Royer and Schwab Crater volume measurement system [2.42]

The depth calibration is achieved with the help of an interferometer from which the fringes are observed in the same conditions as the object. The remaining automatic process includes five steps. (Figure 2.15)

i) Positioning the fringe on the object surface.

ii) Reduction of the fringe width to one pixel.

iii) Completion of the fringe discontinuities.

iv) Calibration of the magnification and compensation of its variation as a function of the measured depth.

v) Integration of the depth values.

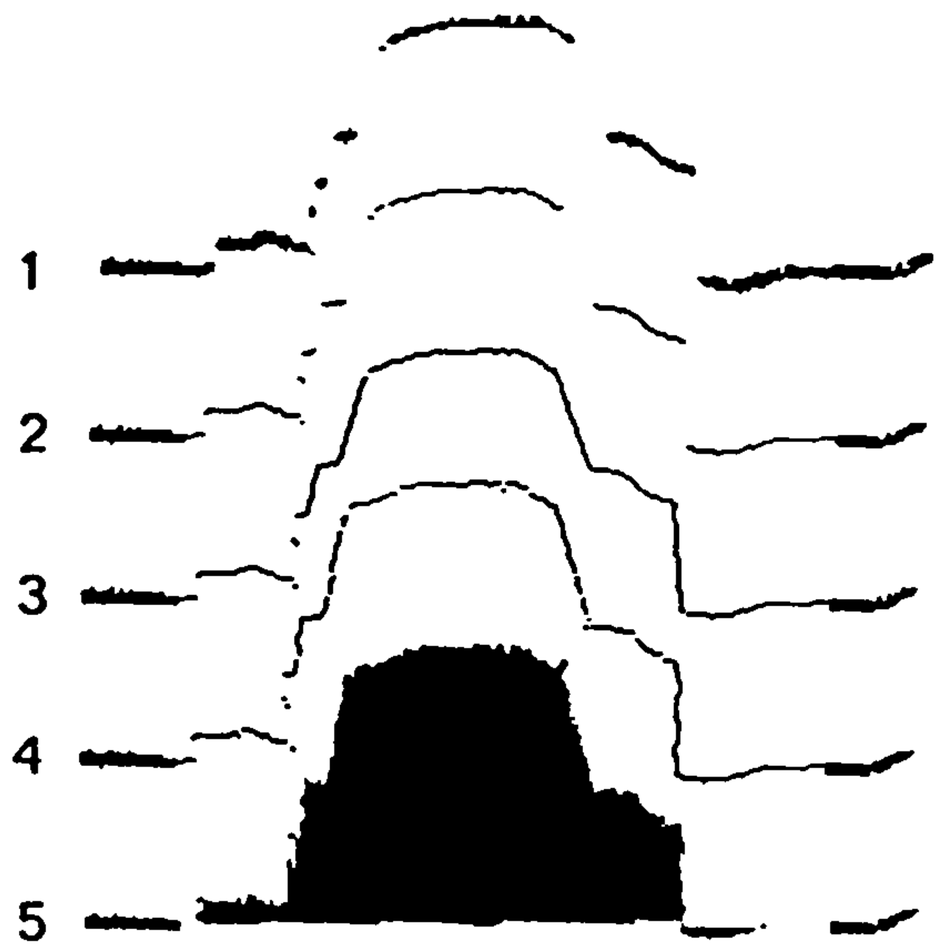

Figure 2.15 The Five steps of the automatic process by Royer et al [2.42]

A problem with this method is the accuracy required in determining a number of the parameters necessary in the volume expression. In addition, the assumptions that, the depth of the crater is the same throughout, and the fringe spacing is the same when the surface is translated towards the direction of the beam.

Decker [2.43, 2.44] proposed a method of inspecting the X-rays of cast parts used in the automobile industry, by automatically positioning and then subtracting the reference image from the image of the test part. A number of reference points are located on both sets of images, with the outer object contour used as a feature, to determine the necessary transformations required (i.e. rotation, translation, magnification). A feature is defined which exploits the contour of the object, detecting deviations from a line intersecting the contour.

The basis of image subtraction relies upon both reference and object images to be under identical conditions. For instance, the surfaces are of similar quality as well as the outer dimensions. This is however not the case for

the cast examples with which this technique has been applied. A number of unwelcome differences are encountered due to local geometric deformities of the used casting moulds and the casting flash lines, which provides additional and unwanted information not present in the reference data. In addition, the method of matching the two images to align with one another, results in the pixels shifting independently from its neighbours. The procedure is sensitive to statistical effects such as noise which causes false displacements. Therefore, the matching mechanism is only appropriate in the case of small displacements and little noise.

Gasvik [2.45] proposed a moiré fringe technique using a camera and image processing system, to enable real-time subtraction of a comparable surface to be possible. An image of the reference surface with projected fringes is stored, from which real-time subtraction is made.

Atkinson and Groves [2.46,2.47] proposed a number of methods in the analysis of the measurement of wear. Measurements were made by comparing suitable impressions of areas before and after a test. A number of methods interpreting the contour maps are described, including a computer technique, for the estimation of volume loss. The computer technique also produces "difference" contour maps of the wear scars.

Following the work of Konforti et al [2.48] and Tschudi [2.49], an idea suggested by Atkinson and developed by Koukash [2.50,2.51] developed a basic method of detecting surface defects on components such as cylinderical rollers. The basic system consists of an optical and digital system. The former sub-system consists of a laser, spatial filter, beam expander, amplitude square wave grating and a lens. A CCD camera provides the interface between the optical and digital sub-systems, with the latter digital sub-system consisting of an analogue-to-digital converter, frame buffer, digital-to-analogue converter, T.V. monitor and computer system. (Figure 2.16)

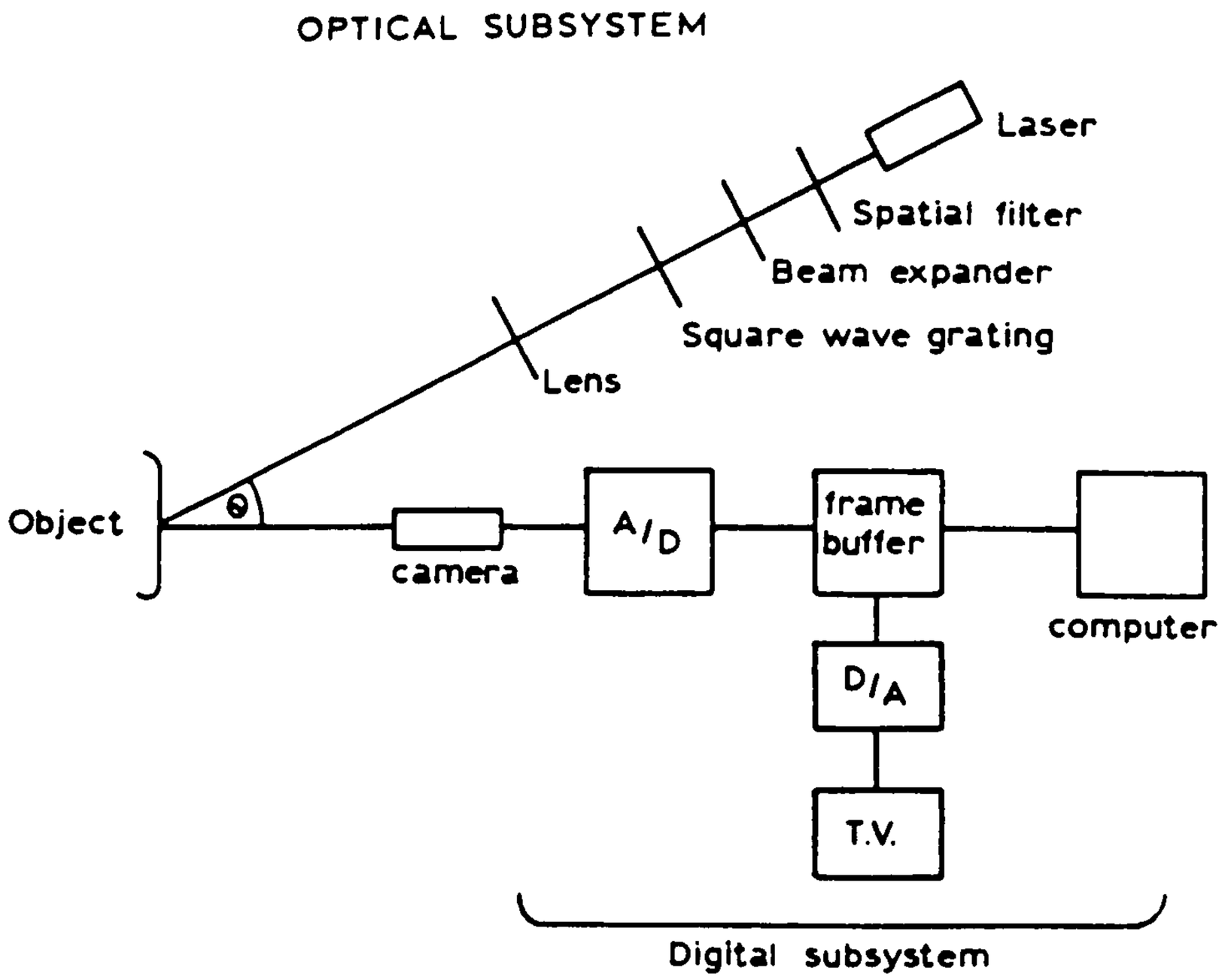

Figure 2.16 Detection of Surface Defects by Koukash[2.50]

However, the basic idea relied upon the precise relocation of components. Problems of misalignment for instance were not examined, with the test and model images aligning with one another precisely, in the most perfect experimental conditions possible.

Developed further from this, Chung [2.52] developed a simpler and more robust, low-cost technique using this "difference" method on larger engineering components on an IBM PC AT microcomputer and simpler optical set-up, an ordinary slide projector. The optical front end comprised of white light projected through a square wave Ronchi grating, onto surfaces such as a car door panel and a molybdenum tray.

There are several techniques available for image subtraction which are described in a review paper by Ebersole [2.53]. However, all are optical image subtraction methods, relying upon the optics to carry out the image subtraction. Although not in the image processing field of subtraction, some of the techniques described may be developed into real-time optical subtraction method, and so are of great interest in the development of an

automated measuring system.

2.5 Chapter Summary

This chapter has covered certain areas within the field of fringe contouring, in particular, fringe projection and moiré contouring. Various numerical techniques are also described to analyse these fringes to yield quantative results. Included also is a description of the PCB field, where the image subtraction technique is often utilised. The application of image subtraction together with fringe contouring techniques is an obvious development from which is the basis of the work described in this thesis.

2.6 References

2.1 G. T. REID, "**Automatic Fringe Pattern Analysis : A Review**", Optics and Lasers in Engineering, No. 7, p37-68, 1986/7.

2.2 J. T. ATKINSON, " **The Holographic Evaluation of Biomaterials**", Ph.d. Thesis 1979.

2.3 G. B. PORTER III, "**A Noncontact Visual Profilometer For Automatic Inspection**", SME VISION 85, Applying Automated Inspection, p66-71, 1985.

2.4 G. B. PORTER III, J. L. MUNDY, "**Visual Inspection of Metal Surfaces**", Proc IEEE IECON 82, p149-151, 1982.

2.5 T. YATAGAI, M. IDESAWA, Y. YAMAASHI, M. SUZUKI, "**Interactive Fringe Analysis System : Applications to Moiré Contourogram and Interferogram**", Opt. Eng, Vol 21, No. 5, p901-906, 1982.

2.6 H. STEINBICHLER, "**Holographic Non-destructive Testing With Automatic Evaluation**", SPIE Vol 654, p242-248, 1986.

2.7 R. ROTTENKOLBER, "**25 Years of Holography**", "**The Development of Holographic Testing**", SPIE Vol 863, p134-140, 1987.

2.8 G. INDEBETOUW, "**Profile Measurement Using Projection Of Running Fringes**", Applied Optics, vol 17, No. 18, p2930-2933, 1978.

2.9 F. BECKER, G.E.A. MEIER, H. WEGNER, "**Automatic Evaluation of Interferograms**", SPIE Vol 359, Applications of Digital Image Processing IV, p386-393, 1982.

2.10 D. W. ROBINSON, **"Automatic Fringe Analysis with a Computer Image Processing System"**, Applied Optics, Vol 22, No. 14, p2169-2176, 1983.

2.11 D. W. ROBINSON, **"Role For Automatic Fringe Analysis in Optical Metrology"**, Proc. SPIE Int Soc. Opt. Eng., Vol 376, p20-25, 1983.

2.12 M. TAKEDA, H. INA, S. KOBAYASHI, **"Fourier-transform Method of Fringe-pattern Analysis for Computer-based Topography and Interferometry"**, J. Opt. Soc. Am, Vol 72, No.1, p156-160, 1982.

2.13 M. TAKEDA, K. MUTOH, **"Fourier Transform Profilometry For The Automatic Measurement of 3-D Object Shapes"**, Applied Optics, Vol 22, No. 24, p3977-3982, 1983.

2.14 L. MERTZ, **"Real-time Fringe Pattern Analysis"**, Appl. Opt., 22, p1535-9, 1983.

2.15 W. W. MACY, **"Two Dimensional Fringe Pattern Analysis"**, Appl. Opt., 22, p3898-901, 1983.

2.16 G. R. HALSALL, D. R. BURTON, M. J. LALOR, C. A. HOBSON, **"A Novel Real-time Opto-electronic Profilometer using FFT Processing"**, IEEE ICASSP 1989, Vol 3, p1634-1637, 1989.

2.17 G. R. HALSALL, D. R. BURTON, M. J. LALOR, C. A. HOBSON, **"Surface Profile Determination by Real-time Signal Processing of Interferometric Contour Fringe Data"**, FASIG 90, Nottingham, p303-304, 1990.

2.18 A. A. MALCOLM, D. R. BURTON, M. J. LALOR, **"A Study of the Effects of Windowing on the Accuracy of Surface Measurements Obtained from the Fourier Analysis of Fringe Patterns"**, Fringe Analysis 89, FASIG 89, Loughborough, 1989.

2.19 D. R. BURTON, M. J. LALOR, **"The Precision Measurement of Engineering Form by Computer Analysis of Optically Generated Contours"**, Proc SPIE, Vol 1010, 1988.

2.20 D. R. BURTON, M. J. LALOR, **"Software Techniques for the Analysis of Contour Maps of Manufactured Components"**, Proc SPIE, Vol 952, 1987.

2.21 M. HALIOUA, H. LIU, **Optical Sensing Techniques for 3-D Machine Vision"**, SPIE Vol 665, p150-161, 1986.

2.22 K. G. HARDING, R. TAIT, **"Moiré Techniques Applied to Automated Inspection of Machined Parts"**, SME VISION 86, p2-1 to 2-16, 1986.

2.23 H. TAKASAKI, **"Moiré Topography From its Birth to Practical Application"**, Optics and Laser in Engineering, Vol 3, p3-14, 1982.

2.24 G. T. REID, R. C. RIXON, H. I. MESSER, **"Absolute and Comparative Measurements of Three Dimensional Shape by Phase Measuring Moiré Topography"**, Optics and Laser technology, Vol 16, No. 6, p315-319, 1984.

2.25 G. T. REID, R. C. RIXON, **Machine Vision Techniques For 3-D Surface Form Measurement"**, Proc. ISATA 85, ISATA 85025, p297-312, 1985.

2.26 G. T. REID, R. C. RIXON, S. J. MARSHALL, **"3-D Machine Vision for Automatic Measurements of Complex Shapes"**, Proc 7th Int. Conf. Automated Inspection and Product Control, p129-138, 1985.

2.27 G. T. REID, R. C. RIXON, **"Automatic Inspection of Quasicylindrical Objects by Phase Measuring Moiré Topography"**, SPIE Vol 665, p162-167, 1986.

2.28 J. H. BLATT, H. C. HO, E. H. YOUNG, "**Generation of Moiré Contours with Acousto-optic Cells**", Optical Engineering, Vol 28, No. 9, p996-998, 1989.

2.29 J. H. BLATT, J. A. HOOKER, R. V. BELFATTO, E. H. YOUNG, "**3-D Inspection of Large Objects by Moiré Profilometry**", L.I.A. Vol 70 ICALEO, p12-16, 1989.

2.30 G. JIN, S. TANG, "**Automated Moiré Contouring of Diffuse Surfaces**", Optical Engineering, Vol 28, No. 11, p1211-1215, 1989.

2.31 R. T. CHIN, "**Survey : Automated Visual Inspection : 1981 to 1987**", Computer Vision, Graphics and Image Processing, No. 41, p346-381, 1988.

2.32 R. T. CHIN, "**Automated Visual Inspection : A Survey**", TPAMI, Vol 4, p557-573, 1982.

2.33 R. T. CHIN, "**Algorithms and Techniques for Automated Visual Inspection**", HPRIP, P587-612, 1986.

2.34 K. S. FU, "**Pattern Recognition for Automated Visual Inspection**", Computer, Vol 15, Part 12, p34-40, 1982.

2.35 K. S. FU, "**Pictorial Pattern Recognition for Industrial Inspection**", Pictorial Data Analysis Procs, p335-348, 1983.

2.36 D. T. LEE, "**A Computerized Automatic Inspection System for Complex Printed Thick Film Patterns**", SPIE Vol 143, Applications of Electronic Imaging Systems, p172-177, 1978.

2.37 JEN-KOU CHOU, "**Automated Inspection of Printed Circuit Board.**", SME Vision 85, Applying Automated Inspection, p6.66-6.65.

2.38 D. MOUNTJOY ET AL, "**Automatic Visual Inspection of Printed Circuit Boards - Is the problem Too Difficult?**", Proceedings of the 7th Annual Automatic Imagery Pattern Recognition Symposium, p152-167, May 23-24, 1977.

2.39 L. G. ROBERTS, "**Machine Perception of Three Dimensional Solid**", Optical and Electro-optical Information Processing, p159-197, 1965.

2.40 M. EJIRI ET AL, "**A Process for Detecting Defects in Complicated Patterns**", Computer Graphics and Image Processing, 2, p326-339, 1973.

2.41 R. T. CHIN, C. A. HARLOW, S. J. DWYER III, "**Automatic Visual Inspection of Printed Circuit Boards**", Proc SPIE, Image Understanding Syst. and Industrial Applications, Vol 155, p199-213, 1978.

2.42 H. ROYER, J. SCHWAB, "**Automatic Measurement of a Crater Volume by Means of Light Sheet Projection**", SPIE Vol 863, p52-55, 1987.

2.43 H. DECKER, "**Automatic Positioning of Objects using Edges**", IEEE Proc, 6th Conf. PR., Munich, p850-852, 1982.

2.44 H. DECKER, "**A Difference Technique for Automatic Inspection of Casting Parts**", PRL2, p125-129, 1983.

2.45 K. J. GASVIK, "**Moiré Technique by Means of Digital Image Processing**", Applied Optics, Vol 22, No. 23, p3543-3548, 1983.

2.46 D. GROVES, M. J. LALOR, N. COHEN, J. ATKINSON, "**A holographic technique with computer aided analysis for the measurement of wear**", J. Phys. E: Sci. Instrum., Vol. 13, p. 741-746, 1980.

2.47 J. T. ATKINSON, D. G. GROVES, M. J. LALOR, **"The measurement of wear in dental restorations using laser dual-source contouring"**, Wear 76, p. 91-104, 1982.

2.48 N. KONFORTI, E. MAROM, **"Real time grid coding and interlacing for image subtraction"**, Applications of Holography and Optical Data Processing, Proc. Int Conf, p. 85-91, 1976.

2.49 T. TSCHUDI, H.P. WEBER, A. STADLER, **"Incoherent optical correlator using projected fringes patterns"**, Optical Engineering, Vol 18, No 4, p. 387-389, 1979.

2.50 M. KOUKASH, C. A. HOBSON, M. J. LALOR, J. T. ATKINSON, **"Detection and Measurement of surface defects by Automatic Fringe Analysis"**, Optics and Lasers in Engineering 7 (1986/87), p. 125-135.

2.51 M. KOUKASH, **"An automatic, Non-Contact, 3-D Measurement System For the Analysis of Change in Surface Form"**, PhD Thesis, Liverpool Polytechnic (1986).

2.52 R. Y. M CHUNG, **"Surface Flaw Detection"**, MSc Dissertation, Liverpool Polytechnic, 1988.

2.53 J. F. EBERSOLE, **"Optical Image Subtraction"**, Opt. Eng., Vol 14, p436-447, 1975.

CHAPTER THREE

THEORY OF FRINGE PROJECTION CONTOURING

3.1 Introduction

This chapter gives a brief account of the theory for modelling a fringe pattern for a previously known height distribution. This is essential for the purposes of developing a relationship for the intensity of any point on a plane surface, upon which a sinusoidal square wave grating is projected upon from an angle, the basis upon which the technique is based. The flat plane is used for the purposes of ease of explanation for theory derivation, although any shape is applicable.

3.2 The Modelling of the Fringes

The basic theory for the modelling of projected fringes is reviewed here from the point of view of generating fringe patterns for a prior known height distribution. It is important to remember that, in general this height distribution would be unknown, with the fringe pattern being the only indication of its form.

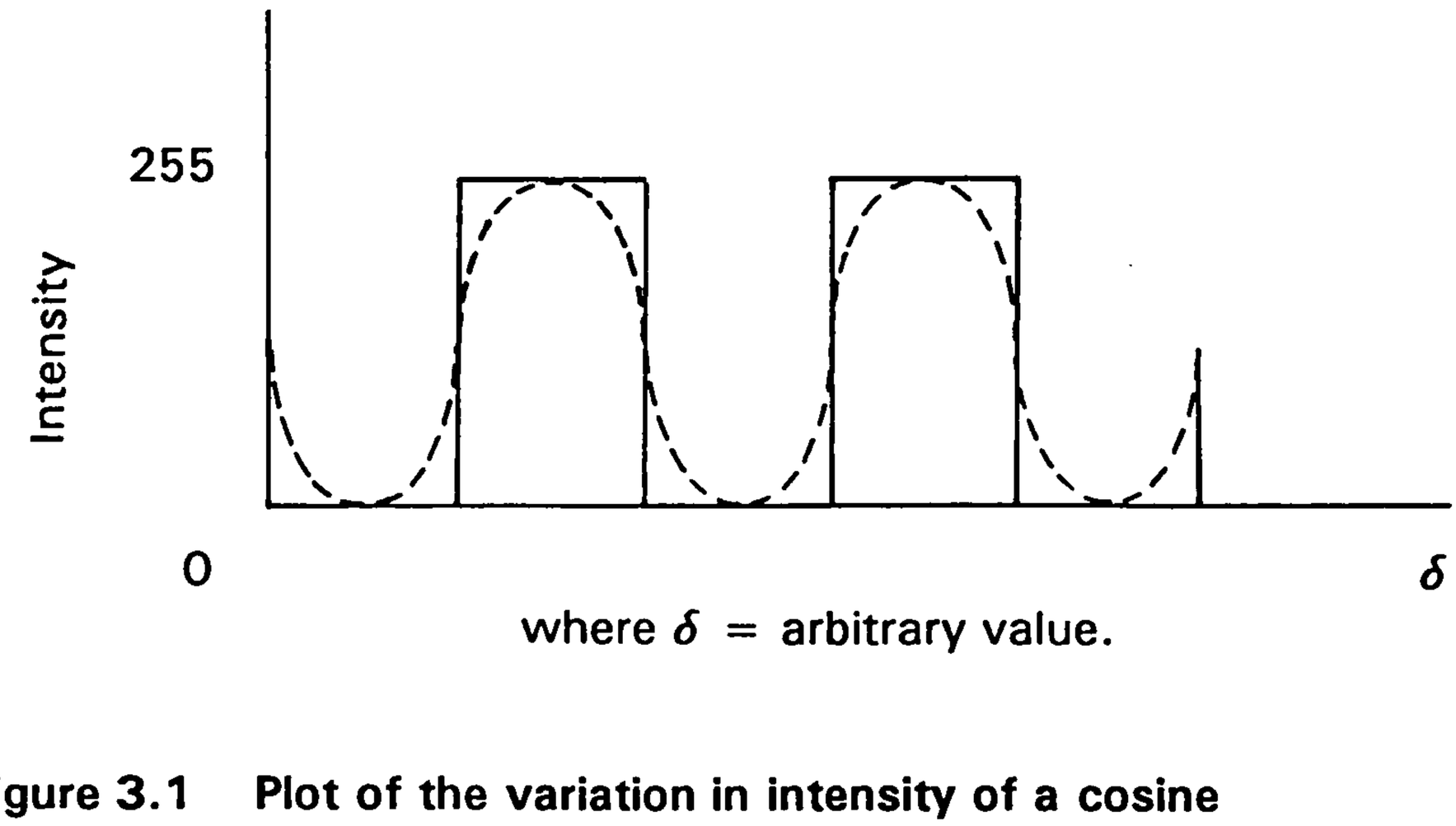

Figure 3.1 Plot of the variation in intensity of a cosine and square wave function.

To analytically represent a square wave is complex due to the function's discontinuous nature. However, we can simply represent a sinusoidal function, i.e. $\cos^2(\delta)$ and change this to a square wave by means of a straight forward test, as will be discussed later.

Figure 3.1 shows such a cosine squared function with a superimposed square wave. Note that the function is uniformly positioned with extreme values 0 and 255. This function while satisfying our sign requirements in being positive only is computationally inefficient.

With the use of trigometric identities the function $\cos^2(\delta)$ may be rewritten as follows:

$$\cos(2\delta) = \cos^2(\delta) - \sin^2(\delta)$$

$$= \quad \cos^2(\delta) - (1 - \cos^2(\delta))$$

$$= \quad 2\cos^2(\delta) - 1$$

Therefore, $\cos^2(\delta) = \dfrac{\cos(2\delta) + 1}{2}$

Within the frame buffer a video signal is represented in 256 grey levels, and so the function must now be scaled to this amplitude.

$$I = \frac{I_{max}}{2} (\cos(2\delta) + 1)$$

where I = Intensity and I_{max} = the Maximum intensity of 255

This expression is equivalent to the earlier $\cos^2$ function but it is more efficient for computational purposes. With the use of a programming conditional expressions "if" and "else", a square wave may be created simply by using

```
if ( I > 128)        { pixel = white }
else                 { pixel = black }
```

Given that (δ) is in fact an arbitrary parameter chosen to represent the overall length of the fringe i.e. the fringe spacing argument, a more useful representation is required in terms of pixel units.

Let $2\delta = \dfrac{2\pi j}{p}$

where j = distance in pixel units

and p = fringe period (black and white) in pixel units.

so $I = \dfrac{I_{max}}{2} (\cos \dfrac{(2\pi j)}{p} + 1)$

expanding this gives $I = \dfrac{I_{max}}{2} (\cos \dfrac{(2\pi j)}{p} + \dfrac{I_{max}}{2}$

Since p is the apparent spacing on the surface on a plane and not the actual projected fringe spacing, one must use

$$p = \frac{p_0}{\cos\theta} \qquad \text{(See Figure 3.2)}$$

where p = Period of observed square wave fringes viewed at an angle to that surface.

p_0 = Period of square wave fringes projected from the light source.

θ = Angle between the direction of illumination, and the direction of observation.

Therefore, $I = \frac{I_{max}}{2} \cos\left(\frac{2\pi j \cos\theta}{p_0}\right) + \frac{I_{max}}{2}$

letting $f = \frac{\cos\theta}{p_0}$ - the effective spatial frequency

Gives $$I = \frac{I_{max}}{2} \cos(2\pi f j) + \frac{I_{max}}{2} \qquad (3.1)$$

This equation allows a straight unmodulated sinusoidal fringe pattern to be calculated.Equation (3.1) would be true only if the fringes illuminated a plane orientated at an angle θ and viewed normal to that plane. (See Figure 3.2)

It should be noted that during this analysis the system has been assumed to have a pixel magnification of 1:1.

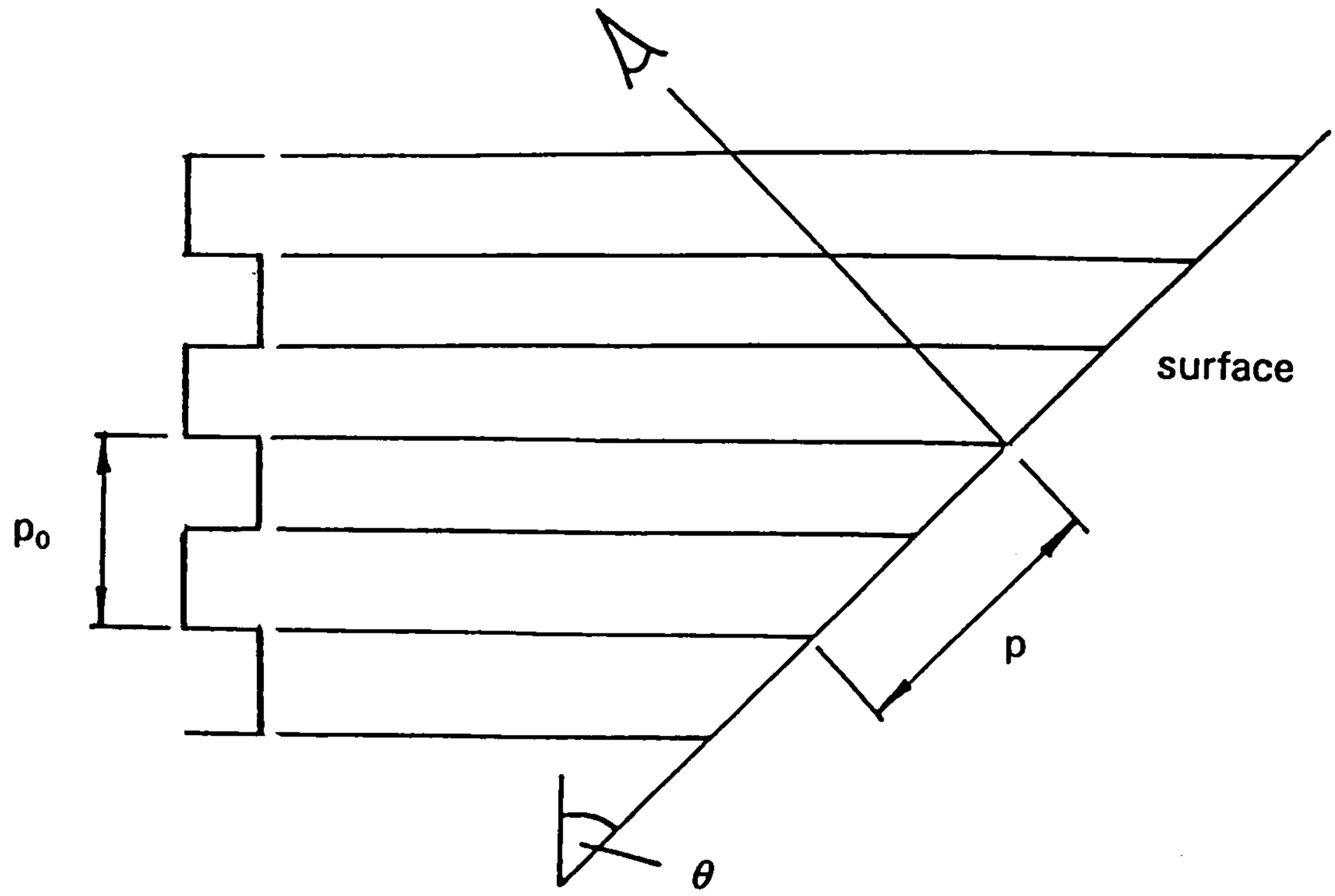

Figure 3.2

If the surface was not plane but had a defect, a hump for example, then the phase shift ϕ_s would result. Thus, the general form of equation (3.1) at any point position (i,j) should read:

$$I(i,j) = \frac{I_{max}}{2} \cos (2\pi fj + \phi_s (i,j)) + \frac{I_{max}}{2}$$

where $\phi_s(i,j)$ is the angular phase shift at a point (i,j) caused by a deviation in the illuminated plane equivalent to a height function h(i,j).

To write equation (3.2) in a form in which I(i,j) - the intensity at any point (i,j), is given in terms of h(i,j) - the height at any point, we must find a relationship between h(i,j) and $\phi_s(i,j)$.

Referring to figure 3.3 let us suppose that a light wave passed through the points A to B and is reflected off the surface B to position 1. If a height

deviation i.e. a defect is present, then this will be reflected off A to position 2 and an apparent phase shift will appear.

Figure 3.3

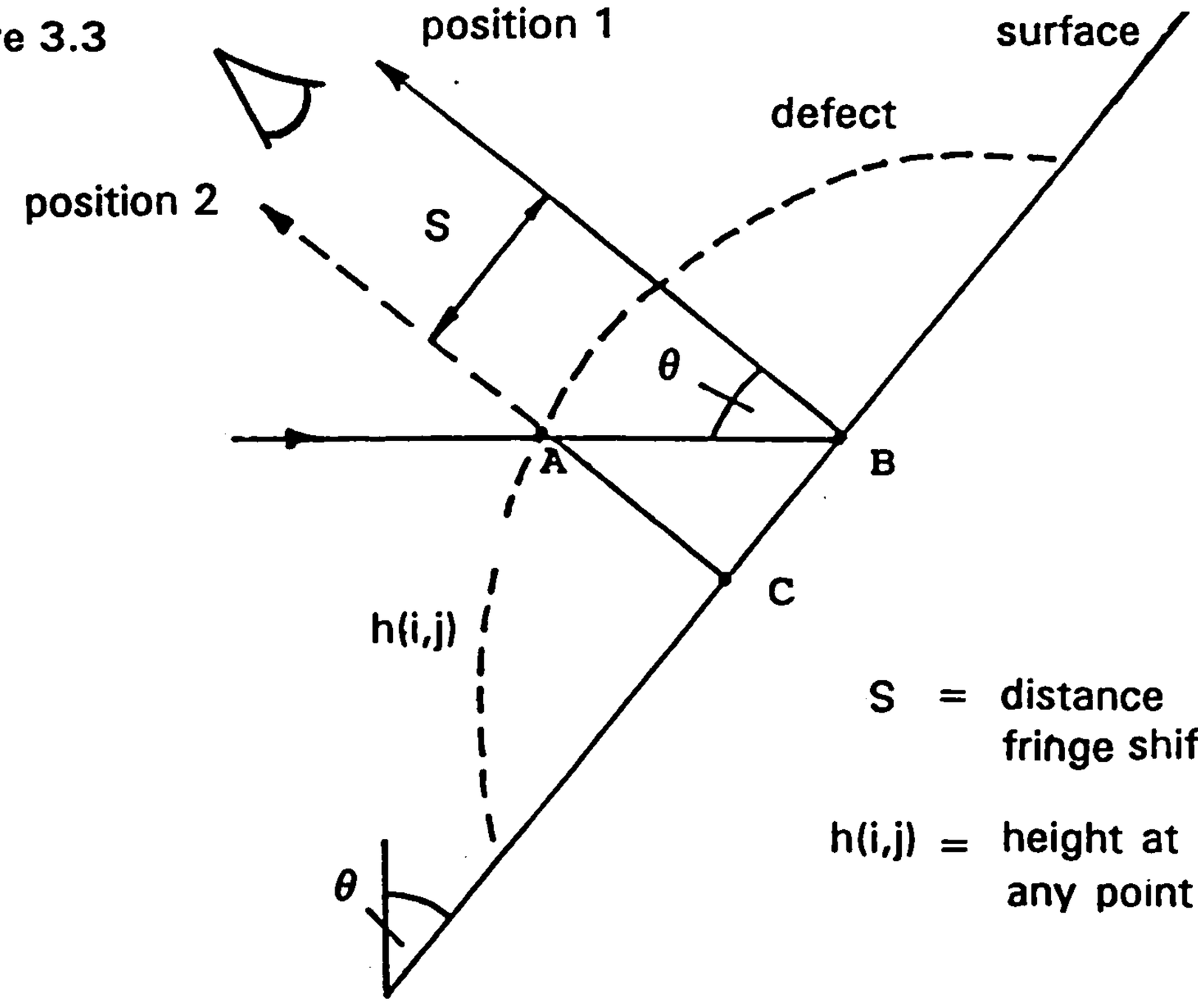

S = distance fringe shift

h(i,j) = height at any point (i,j)

Lifting out triangle ABC

Trigometrically $\quad \tan\theta = \dfrac{S}{h(i,j)}$

or rearranging $\quad S = h(i,j)\tan\theta \qquad (3.3)$

In angular terms, this fringe shift is $\quad \dfrac{2\pi S}{p} = \phi_s$

and also $\quad p = \dfrac{p_0}{\cos\theta}$

leading to $\quad \dfrac{2\pi S\cos\theta}{p_0} = \phi_s$

Thus $\quad S = \dfrac{p_0.\phi_s}{2\pi\cos\theta} \qquad (3.4)$

Hence we have a relationship between distance fringe shift and analogous angular phase shift.

Equating the relationships (3.3) and (3.4) we get

$$h(i,j)\ \tan\theta = \frac{p_0.\phi_s}{2\pi\cos\theta}$$

$$\text{Therefore } \phi_s = 2\pi\cos\theta\ \tan\theta\ h(i,j)\ \overline{p_0}$$

This may be simplified to give

$$\phi_s(i,j) = 2\pi\sin\theta\ h(i,j)\ \overline{p_0}$$

This is a very important expression since it shows the relationship between the phase shift ϕ_s and the height position h(i,j) at any particular point, the remaining parameters being constant.

We are now in a position with this, the desired relationship, to rewrite equation (3.2) in the form we require.

Substituting in expression (3.2) gives

$$I(i,j) = \frac{I_{max}}{2}\cos\left(2\pi fj + 2\pi.\ \frac{\sin\theta}{p_0}\ h(i,j)\right) + \frac{I_{max}}{2}$$

and also substituting for f, we get

$$I(i,j) = \frac{I_{max}}{2}\cos\left(2\pi\frac{\cos\theta}{p_0}\ j + 2\pi.\ \frac{\sin\theta}{p_0}\ h(i,j)\right) + \frac{I_{max}}{2}$$

Giving,

$$I(i,j) = \frac{I_{max}}{2}\cos\left(\frac{2\pi}{p_0}\ (j\cos\theta + h(i,j)\sin\theta)\right) + \frac{I_{max}}{2} \qquad (3.5)$$

This is correct for a modulated $\cos^2$ pattern. To obtain a modulated square wave we apply the conditional expressions

```
if      (I(i,j) > 128)
        {pixel = white}

else
        {pixel = black}
```

Knowing equation (3.5), we are now in a position such that if we specify h(i,j), i.e. some mathematically defined height function, we can calculate the exact appearance of the resulting fringe pattern, when viewed at an angle θ and illuminated with a set of projected fringes of primary period p_0.

3.3 Chapter Summary

This chapter briefly describes the theory behind the modelling of fringe patterns for a previously defined height. When viewed at an angle θ and illuminated with a set of fringes of primary period p_0, a set of fringe patterns can be created with this intensity expression (equation 3.5), when it is used in conjunction with some mathematically defined height function. An example of which is used in the following chapter to validate the basic idea behind this technique.

CHAPTER FOUR

TECHNIQUE PRINCIPLE

4.1 Introduction

Figure 4.1 is a schematic diagram of the complete system. It consists of two sub-systems, one optical and the other digital. The optical sub-system consists of a white light projector, from which light of uniform intensity is projected through a square wave amplitude grating.

Its purpose is to project fringes onto the surface of the object. A camera provides the interface between the optical and digital sub-systems, with the digital sub-system consisting of an analogue-to-digital converter, frame buffer, digital-to-analogue converter, T. V. monitor and computer system.

Figure 4.1 Complete System.

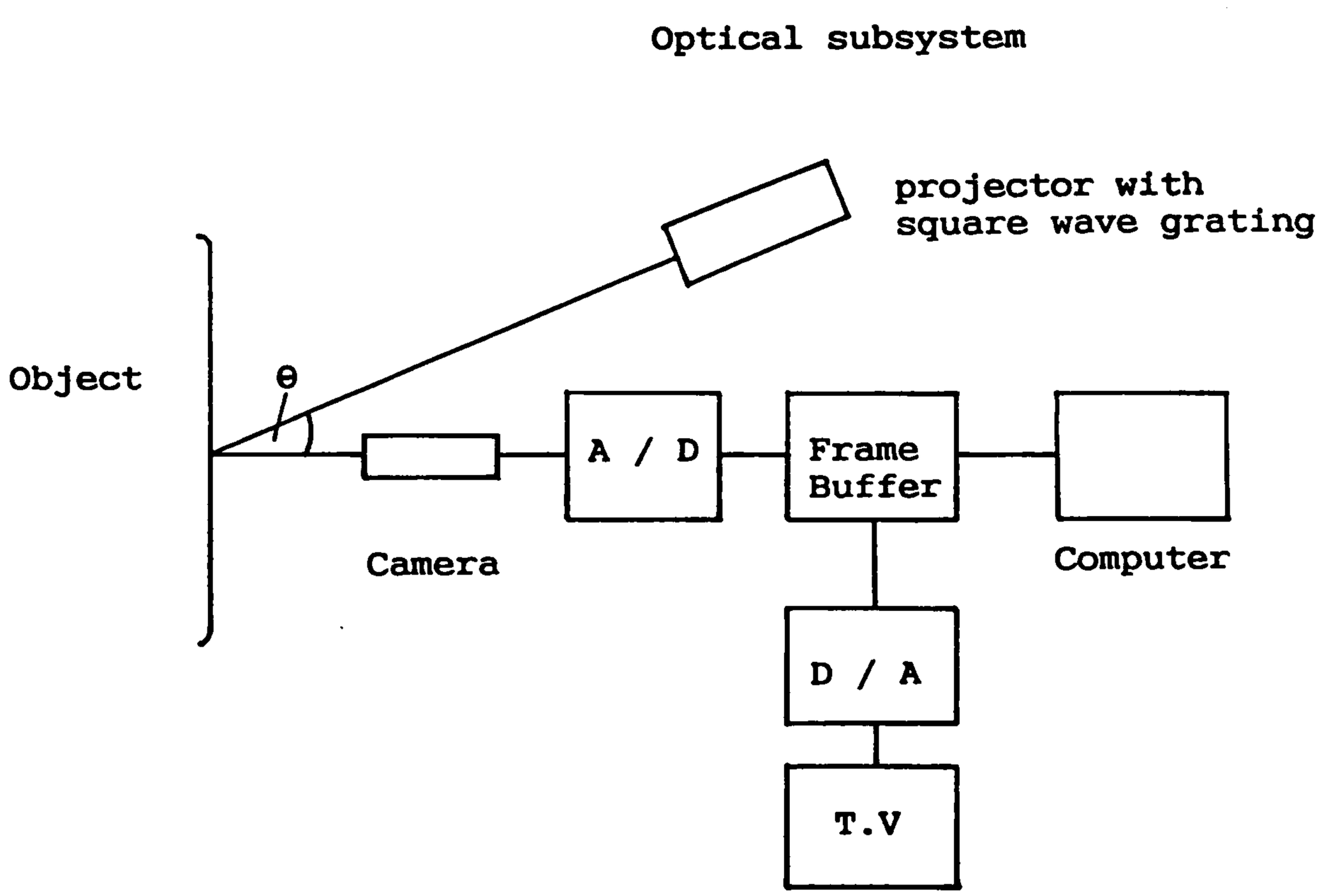

A fringe pattern is formed by passing a beam of light through a square amplitude grating in a projector. The lens in the projector focuses this pattern onto the surface of the object, the resulting image of the pattern produced is then captured by the camera and then digitised using an analogue-to-digital converter. The digitised image is then thresholded, to either black or white pixel values by using look-up tables (LUT) memory, before being sent to the display screen. (See Figure 4.2)

Figure 4.2 Application of a Pixel Scale Transformation Using a Look-up Table.

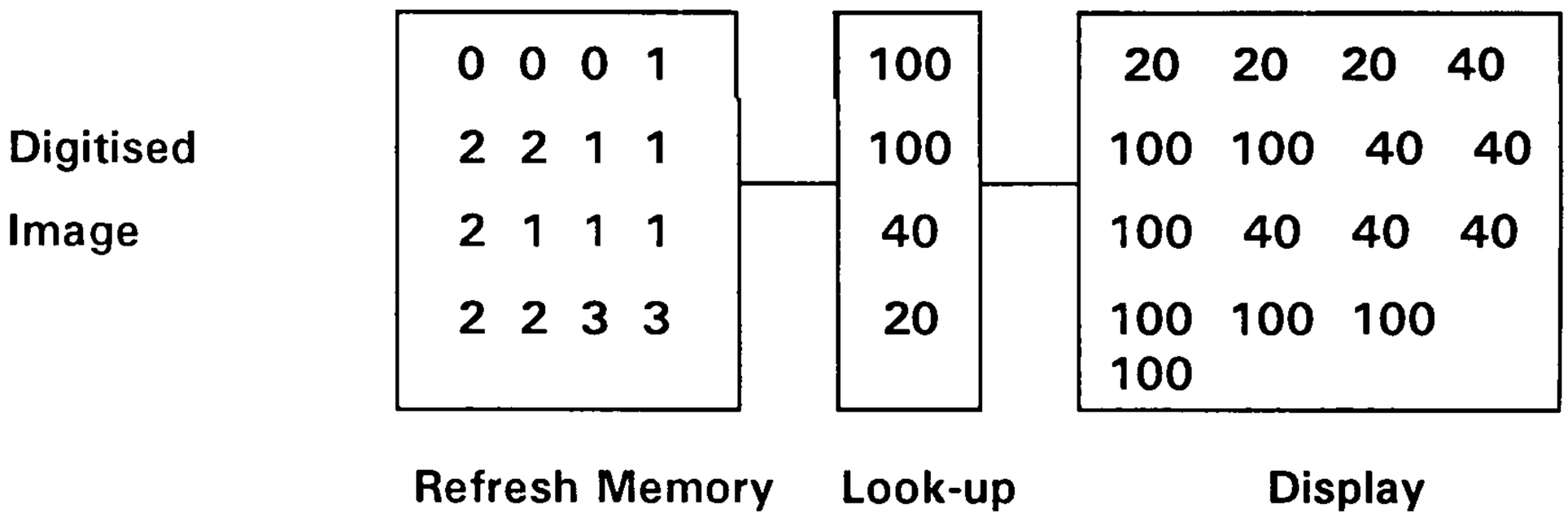

A normal unprocessed image consists of pixel data varying from the range black, grey to white (values 0 to 255). With the use of image subtraction to detect the differences between two images, one with a surface defect and the other without (i.e. Perfect), difficulty may be encountered in distinguishing the difference. The surface defect may have a value which is indistinguishable from its surrounding neighbours in the difference image. The solution would be to use a method of generating an image which consists of only two distinct values, one black 0 and the other white 255. Thus, when two images, one with a surface defect as before and the other perfect, are processed in this manner, the difference would be quite visible. This is achieved by using the thresholding facility.

The purpose of thresholding is to divide the image into contrasting areas of light and dark. Grey areas must be interpreted as being either black or white, depending upon their relative brightness. This is done by selecting

a threshold brightness level and assigning each picture element (pixel) to one of the two states, depending on whether the brightness is greater or less than the threshold value.

The function used from the itex library, creates a look-up table (LUT) that can binarise an image. The image is digitised before it is put through the temporary memory LUT where it is thresholded, before being displayed on the monitor. The selected look up table is changed, so that the pixel values that are above a lower bound value and below a higher bound of the threshold, are displayed as value 255 (white) and the rest as 0 (black).

It should be noted that a number of types of LUT's are similar within an image processor. A look up table (LUT) is simply a small block of fast memory that transforms pixel values. The use of a LUT is an efficient means of applying transformations because in order to change the display characteristics, the contrast or brightness for example, only a new table must be loaded, and not the entire image. A table only requires one entry for each possible input pixel value, for example, 256 for an 8 bit data, whereas the image may be over one million pixels.

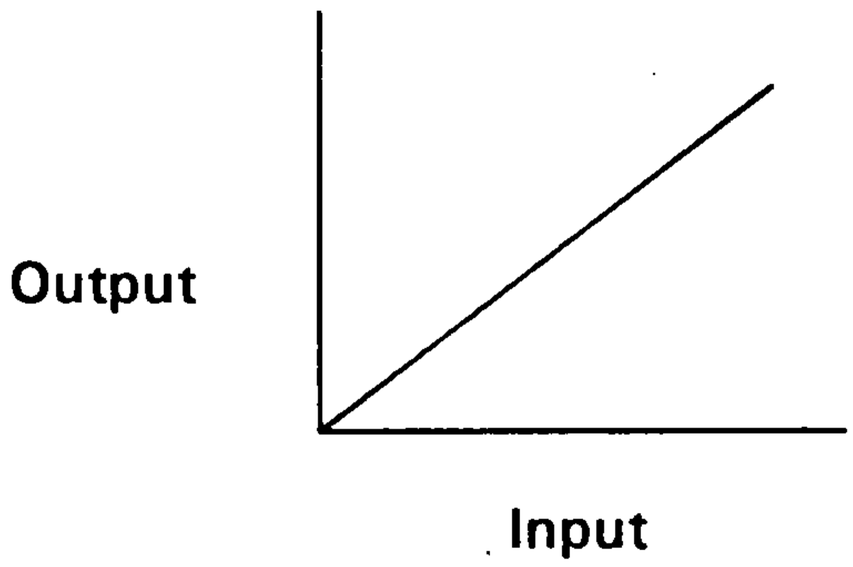

Figure 4.3 Grey Image.

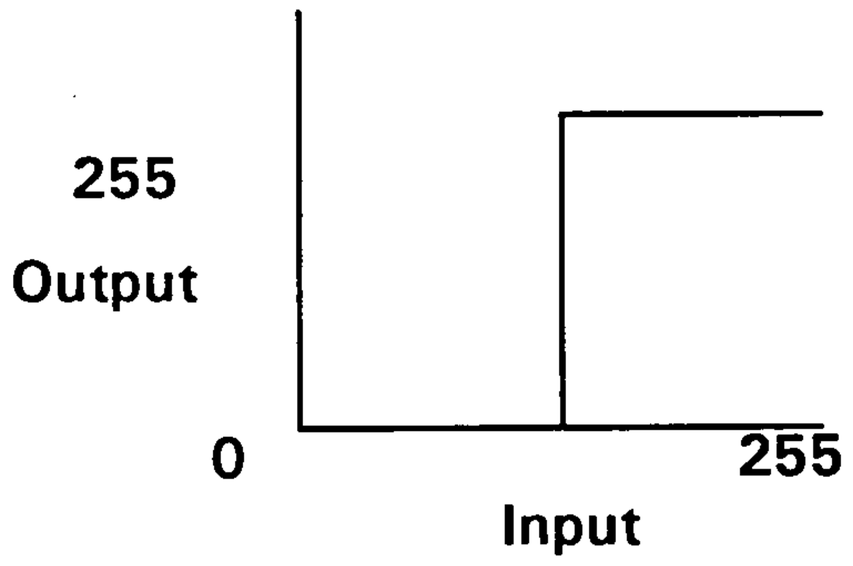

Figure 4.4 Thresholded Image.

It may be observed in Figure 4.3 of the camera input plotted against display output, a typical distribution of a grey image (with pixel data ranging from 0 to 255), as compared to the resulting threshold result for our application using a LUT. (Figure 4.4). Here, the pixel data is defined as nothing other than 0 or 255, the two extremes of the range, as compared to a grey image

(Figure 4.3) where data varies between the two.

A choice of LUT's are available within the image processor. An input LUT or three output LUT's used together. The input LUT transforms the input from the camera outputting the transformed data into the frame memory, where it can be analysed and manipulated further. This is then displayed on a monitor (Figure 4.5 below).

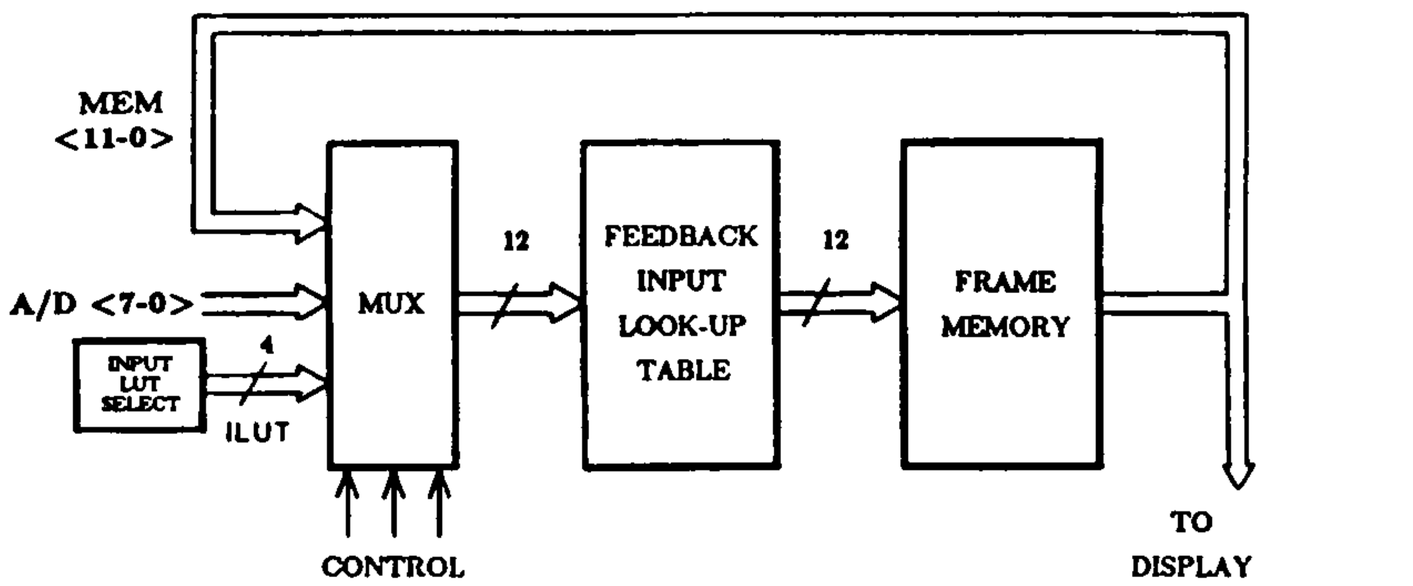

Figure 4.5 Input LUT

This compares to the output LUT's (Figure 4.6) which uses data stored in the frame memory, transforming this data before outputting onto a monitor. The data in the frame memory when using output LUT's remaining unaltered but with the impression, through the monitor, of being transformed.

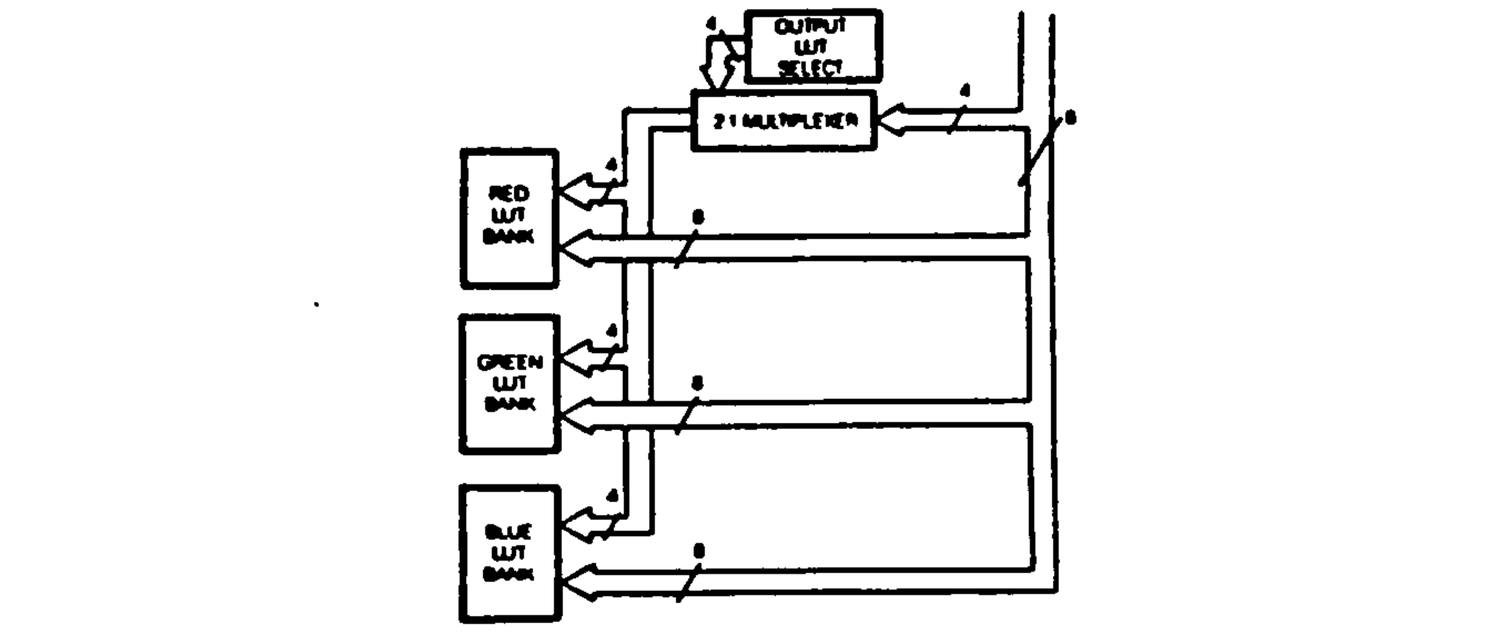

Figure 4.6 Output LUT's

For this reason, for the initial system for this technique the input LUT is preferred.

4.2 Technique Principle

The following section describes the theory behind this technique and is developed with a flat plane as its example. The flat plane is a special case for ease of theory explanation and derivation, but this comparative technique may be applied to any shape. The main principle used in this technique involves illuminating the surface to be measured with light which has been passed through a square wave amplitude grating, observing the resulting effect produced on this surface from an angle. Any flaw on the surface will be highlighted, by the fringes shifting in their lateral position (which is dependent upon the size of the flaw, see Figure 4.7)

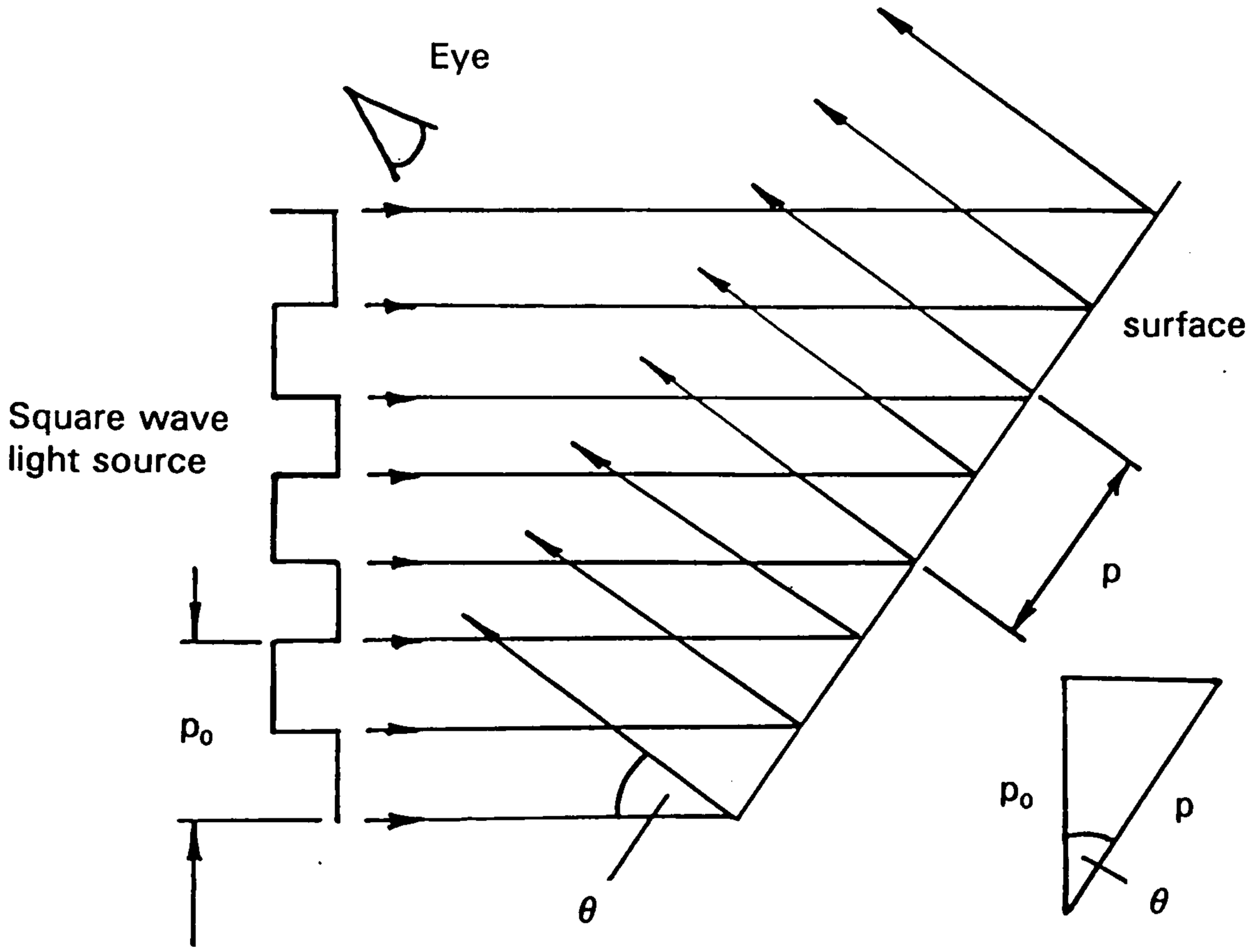

Figure 4.7 Projection of fringes onto surface viewed at an angle to that surface.

where p_o = Period of the square wave fringes projected from the light source.

p = Period of observed square wave fringes viewed at an angle to that surface.

θ = Angle between the direction of illumination and the direction of observation.

As may be observed in Figure 4.7,
the observed fringe period $p = \frac{p_0}{\cos\theta}$ (4.1)

Proving that as the angle θ between the direction of illumination and the direction of observation increases, the greater in magnitude the observed period appears. Thus, any fringes projected onto a surface flaw will be amplified in magnitude as the angle θ is increased. Therefore, for any surface flaw to be detected, the surface must be viewed at an angle to that surface.

With the use of image subtraction to compare any surface flaw with a perfect surface, it is possible to measure the actual volume of the surface area of the flaw. However, care must be taken to ensure that the angle and fringe period are such that, the resulting fringe shift within the subtracted image, is not greater than the fringe width (half fringe period). If this were the case, the result produced within the difference image would be of the wrong magnitude (in relation to the surface flaw). Data due as a result of the fringe shift would be lost, in overlapping with the incorrect corresponding fringe within the reference image. Thus, a comparison of any surface shape may be made, providing the fringe shift is no greater than the fringe width.

Volume Determination

The basic theory in determining the defect volume may first be more easily explained in the three dimensional view of a deformed surface with fringes projected upon it. (See Figure 4.8)

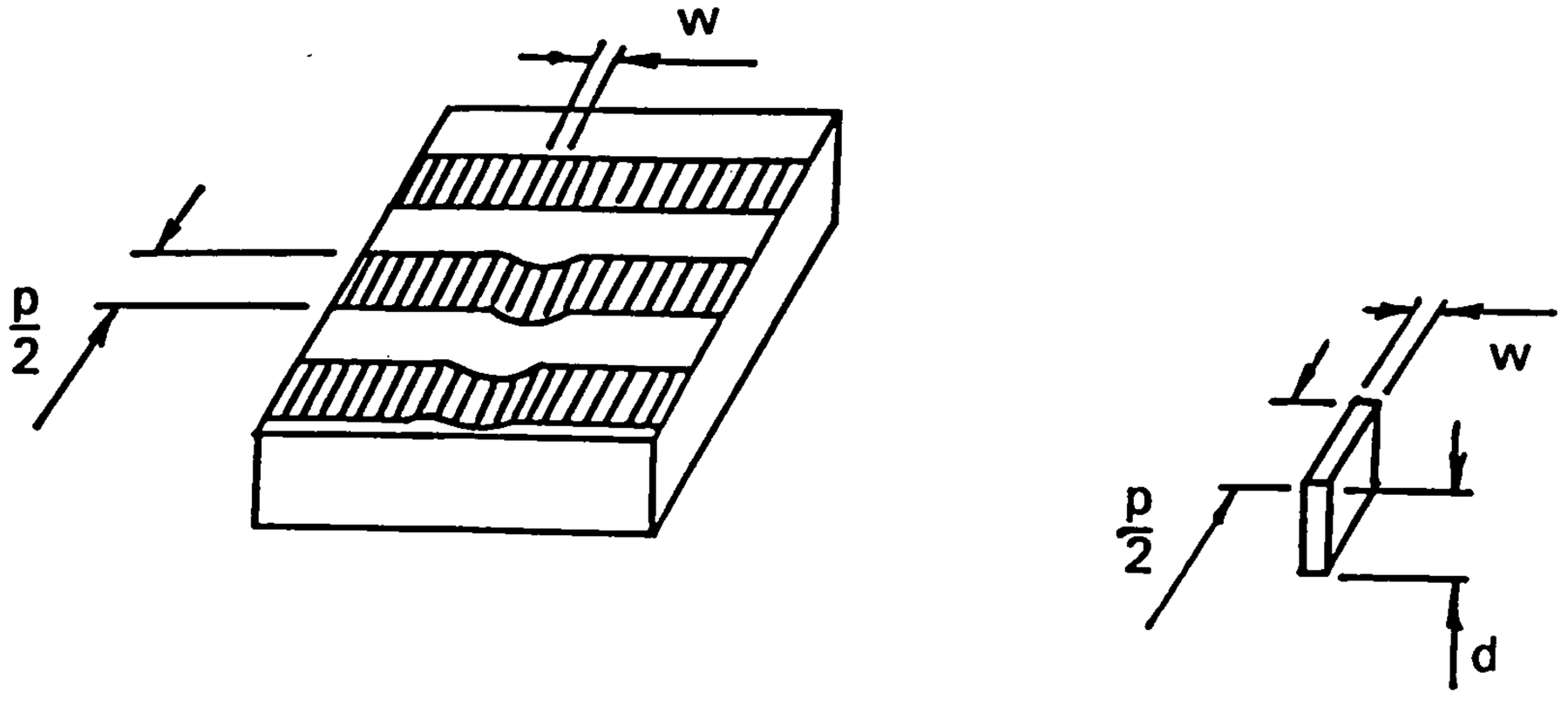

Figure 4.8 Three dimensional view of a defective surface with fringes projected upon it.

where $\frac{p}{2}$ = half observed fringe spacing.

w = width of single scan line on the image.
(effectively the width of a pixel line)

d = depth of the defect at the position under consideration.

Assuming that the depth of the defect is constant within one fringe along a scan line, the defect volume between two fringes (see Figure 4.8) may therefore be given by :

$$\text{Volume of element} = \frac{p}{2}.w.d \qquad (4.2)$$

Depth Determination

Consider a surface with a defect. The surface is illuminated at an angle θ between the direction of illumination and the direction of observation. As a result of the defect of depth d, the observed position on the surface moves by S. The depth of change (d) in this case, is defined as the change in surface position along the direction of viewing.

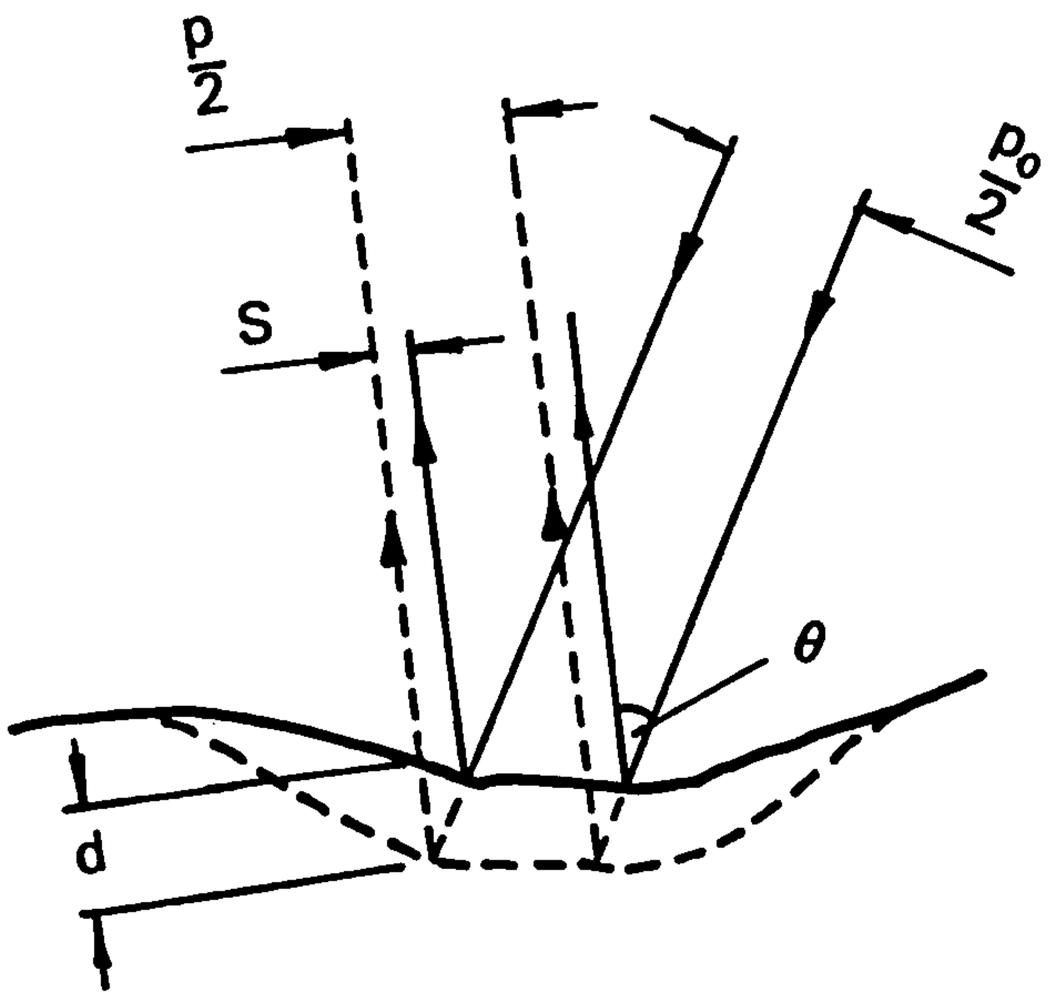

Figure 4.9 Depth Determination

From Figure 4.9, it may be observed that

Trigometrically $$d = \frac{S}{\tan \theta} \qquad (4.3)$$

Substituting for d from (4.3) into (4.2) gives

$$\text{Volume of element} = \frac{p.w.S}{2.\tan \theta} \qquad (4.4)$$

Therefore, summing over all the scan line

$$\text{Total Volume} = \frac{p.\Sigma w.S}{2.\tan \theta} \qquad (4.5)$$

But $\Sigma w.S$ = Total white area A

So,

$$\text{Total Volume} = \frac{p.A}{2.\tan\theta} \qquad (4.6)$$

But, expression (4.1) $p = \frac{p_0}{\cos\theta}$

$$\text{Total Defect Volume} = \frac{p_0.A}{2\sin\theta} \qquad (4.7)$$

This is the final expression for the defect volume, in terms of the period of the grating from the light source, the total area of the bright regions in the difference image and the angle θ between the direction of illumination to the direction of observation.

For simulation only, equation 4.7 is adequate, since the answer required is in terms of cubic pixels. However, for real measurements this needs to include a conversion factor to cubic millimetres.

In the simulation, equation 4.7 is sufficient since it is obviously easier to input data in pixel terms. For example

Period p_0 = [pixel] units.

Total Area A = count of [$pixel^2$] units

$$\text{Giving, Total Defect Volume} = \frac{\text{Period [pixel]} \times \sum \text{Count [pixel}^2\text{]}}{2\ .\ \sin\theta}$$

In Unit terms Volume = [$pixel^3$].

For practical purposes, some method of incorporating the pixel size (for the set measurement conditions), in terms of millimetres must be used. For example

Period p_0 = [mm] units.

Total Area A = count of [$pixel^2$] x Area of pixel [mm^2]

Giving, the Total Volume of Defect.

$$= \frac{\text{Period [pixel]}\left[\frac{mm}{pixel}\right] \text{ x Count [pixel}^2\text{] x [Sx . Sy]}}{2 \cdot \sin\theta}$$

where Sx = size of pixel in x direction = $\frac{mm}{pixel}$

Sy = Size of pixel in y direction = $\frac{mm}{pixel}$

$$\text{Volume} = \frac{\text{Period [pixel]}\left[\frac{mm}{pixel}\right] \text{ x Count [pixel}^2\text{]}}{2 \cdot X \cdot Y \sin\theta}$$

where $X = \frac{1}{Sx}$ = Scaling Factor X = $\frac{pixel}{mm}$

$Y = \frac{1}{Sy}$ = Scaling Factor Y = $\frac{pixel}{mm}$

Thus,

$$\text{Volume} = \frac{\text{Period [pixel]}\left[\frac{\text{mm}}{\text{pixel}}\right] \text{ x Count [pixel}^2\text{]}}{2.\left[\frac{\text{pixel}}{\text{mm}}\right].\left[\frac{\text{pixel}}{\text{mm}}\right}. \sin\theta}$$

In terms of only units.

$$\text{Volume} = \frac{[\text{ mm }] . [\text{ pixel}^2\text{ }]}{\left[\frac{\text{pixel}^2}{\text{mm}^2}\right]} = \text{mm}^3$$

Verifying this for the previous simulation estimation in terms of cubic pixels, assuming X and Y = 1

i.e. Square pixel.

$$\text{Pixel Volume} = \frac{\text{Period [pixel] . [1] x Count . [pixel}^2\text{]}}{2[1][1] . \sin\theta}$$

In terms of only units.

$$\text{Volume} = \text{pixel} . \text{pixel}^2 = \text{pixel}^3$$

The final expression for the defect volume may therefore be.

$$\text{Total Actual Volume of Defect} = \frac{p_0 . \sum \text{Count}}{2 . X. Y. \sin\theta} \qquad (4.8)$$

where p_o = Fringe Period mms.

$\sum$ Count = Total Number of white pixels.

X = Scaling Factor. Number of pixels per mm in x direction.

Y = Scaling Factor. Number of pixels per mm in y direction.

θ = Angle between the projector and camera.

4.3 Simulated Demonstration

To ultimately calculate the volume of a defect on a surface, the system must first be validated, to ensure that the system is performing correctly. To achieve this, the system may be validated on a simulated defect of known volume, generated mathematically within the system. In this example, a sphere protruding partially from a plane (see Figure 4.10) has been simulated, with an assumed magnification of 1:1.

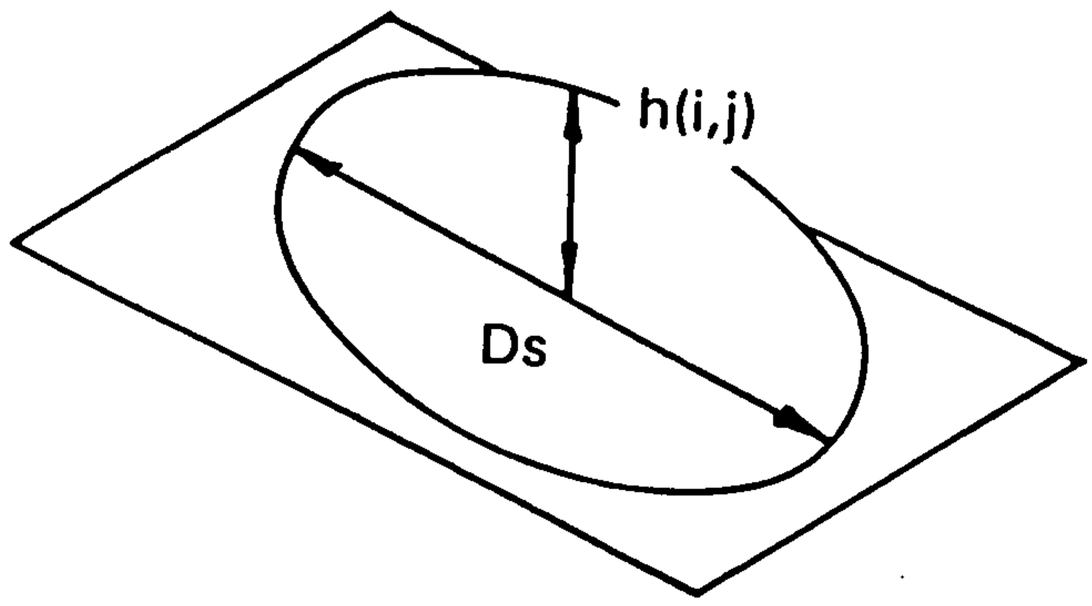

Figure 4.10

Having derived the expansion for Intensity at any point (i,j)

$$I(i,j) = \frac{I_{max}}{2} \cos\left(\frac{2\pi}{p_0}\left(j\cos\theta + h(,i,j)\sin\theta\right)\right) + \frac{I_{max}}{2} \qquad (3.5)$$

in chapter 3, a suitable function h(i,j), to model this geometry is necessary.

Let h(i,j) equal the height at any point on the surface of the sphere.

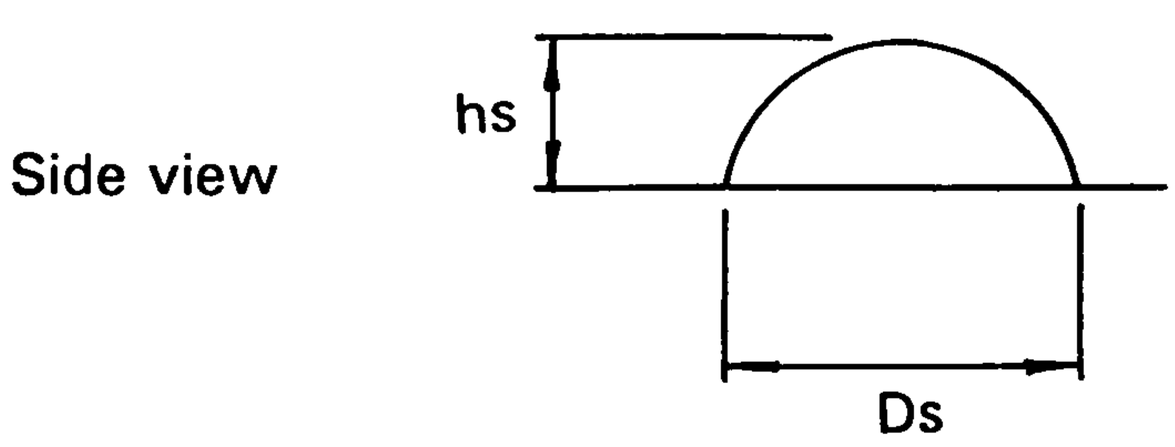

Also for the user defined maximum height to be equal to hs and the fixed diameter of the sphere protruding form the plane to equal Ds.

Now suppose we have a circle with parameters a, b, c,d, and D.

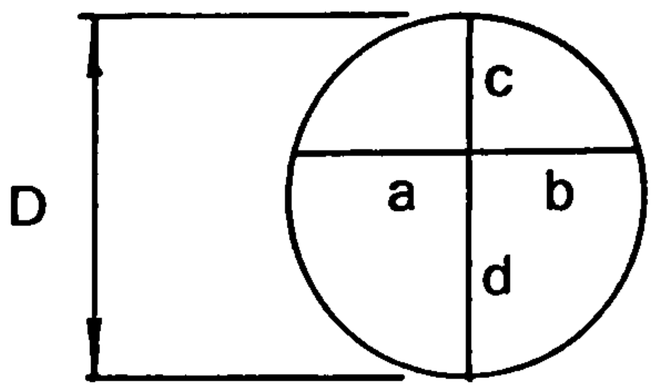

Newton's Intersecting Chord theorem

gives $a.b = c.d$ (4.9)

But $d = D\text{-}c$ and $a = b$

Substituting into equation (4.9) gives,

$$a^2 = (D\text{-}c).c \qquad (4.10)$$

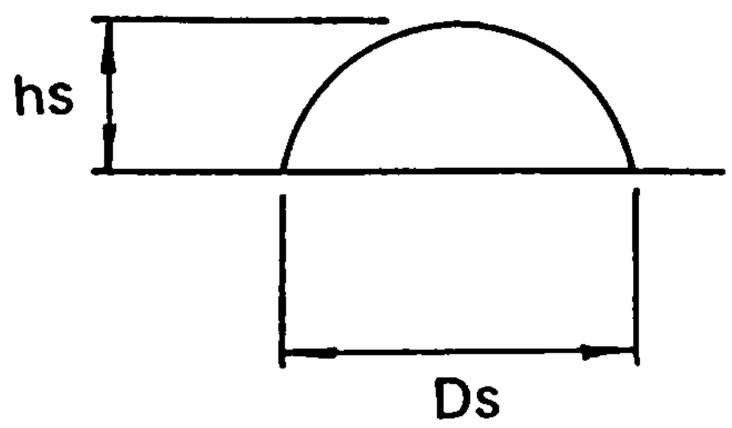

In this case, $a = \frac{Ds}{2}$ and $c = hs$

Substituting into equation (4.10) gives,

$$\frac{Ds^2}{4} = (D\text{-}hs).hs$$

Since diameter D = twice the radius i.e 2R

This would give,

$$R = \frac{1}{2}\left(\frac{Ds^2}{4hs} + hs\right) \qquad (4.11)$$ Radius of Sphere

Since the volume of this "lump" is given by

$$V = \pi hs^2 \left(R\text{-}\frac{hs}{3}\right)$$

Substituting for R from equation (4.11)

$$\text{Volume} = \pi hs^2 \left(\frac{Ds^2}{8hs} + \frac{hs}{6}\right) \qquad (4.12)$$

Therefore, given a maximum height of impingement hs and fixed diameter of impingement, the volume of this protrusion may be obtained from equation (4.12)

To obtain the height at any point in this sphere, from Pythagoras Theorem, it may be observed that $(x-x_c)^2 + (y-y_c)^2 + (z-z_c)^2 = R^2$

For ease, x_c and y_c are the centres of the current frame buffer of size 512. In which case $x_c = 256$ and $y_c = 256$. The value of z being the height at any point on the surface h(i,j), the centre z_c equalling the radius of the sphere, minus the maximum protrusion through the plane. i.e. $z_c = (R-hs)$

Giving,

$$(i-256)^2 + (j-256)^2 + \left[h(i,j) - (R-hs)\right]^2 = R^2$$

where x is equivalent to i and y to j, for the purpose of consistency in the notation and pixel distance units employed.

Manipulating gives

$$h(i,j) - (R-hs) = (R^2 - (i-256)^2 - (j-256)^2)^{1/2}$$

Hence, in terms of the height at any point

$$h(i,j) = (R^2 - (i-256)^2 - (j-256)^2)^{1/2} + (R-hs) \qquad (4.13)$$

Given the Radius of the Sphere R, obtained previously

$$R = \frac{1}{2}\left(\frac{Ds^2}{4hs} + hs\right)$$

Substituting into equation (4.13) gives,

The Height at any point h(i,j),

in terms of defect area in the (i,j) plane is given by,

$$h(i,j) = \left(\left(\frac{1}{2}\left(\frac{Ds^2}{4hs} + hs\right)\right)^2 - (i - 256)^2 - (j - 256)^2\right)^{\frac{1}{2}} + \left(\frac{1}{2}\left(\frac{Ds^2}{4hs} + hs\right) - hs\right) \quad (4.14)$$

Thus, if the maximum defect height hs and impingement diameter Ds are given, the height at any point on this protrusion may be obtained.

This may now be employed in equation (3.5) to calculate the resulting fringe pattern, with the added condition that ALL height values outside Ds are equal to zero.

4.3.1 Writing to the Frame Buffer.

Once the intensity and height at any point is known, it is necessary to write this to the frame memory of the image processor. This is essential to eventually generate a simulation program. To do this, a little must be known about the image processor.

Since the protrusion will not fill the whole of the frame buffer, the height of any point around this protrusion will equal zero. (See Figure 4.11)

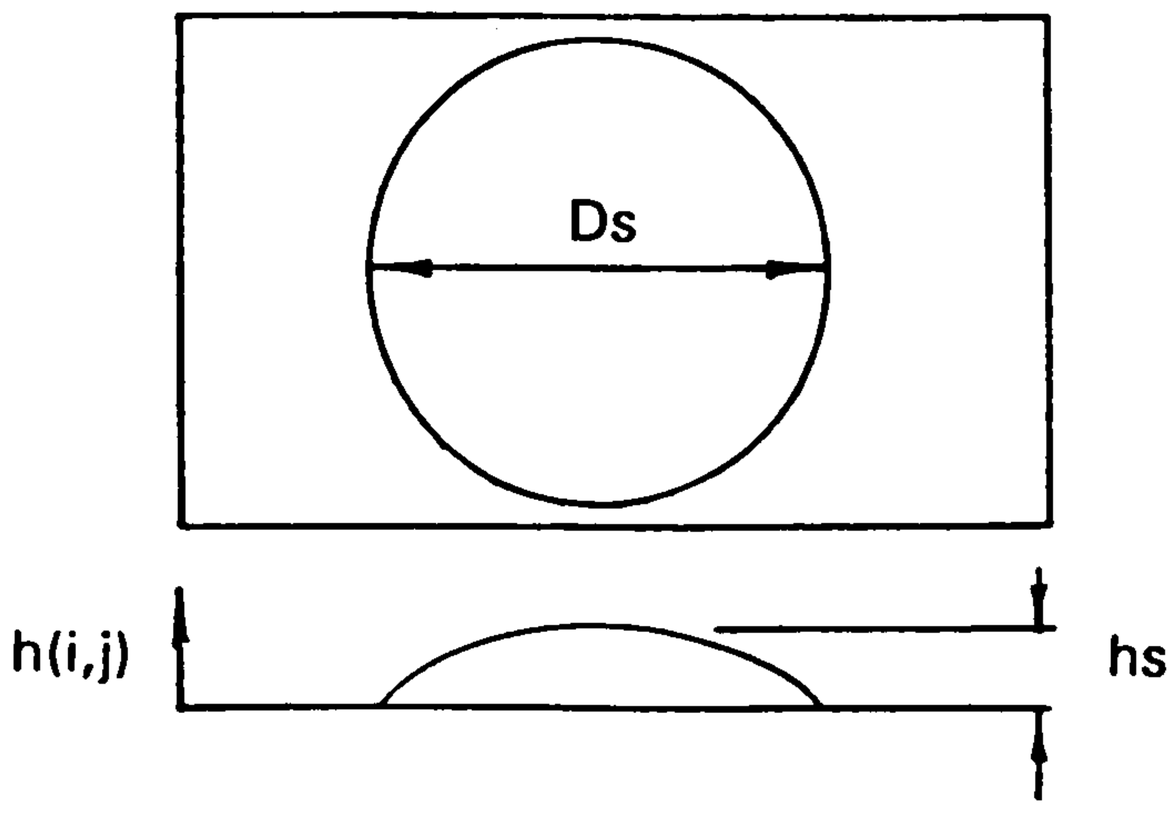

Figure 4.11

where Ds is equal to the diameter of the protrusion above the plane. h(i,j) is equal to the height at any point (i,j). hs is equal to the maximum height defect.

To realise this effect within the frame buffer, it is essential to test the position of this point, whether inside or outside the vicinity of this protrusion. Presuming the centre of this protrusion is again at the centre of the frame buffer, it may be possible to test whether this point is inside or outside of this protrusion by using the following expression.

$$Rtest = ((i - 256)^2 + (j - 256)^2)^{1/2}$$

obtained as in equation 4.13 from Pythagoras Theorem.
where Rtest is equal to the Radius of the tested point.
and i and j are equivalent to x and y in the Frame Buffer.

Applying the conditional expressions if and else, the height outside the area of this protrusion may be said to be zero, while inside it is of a height dependent upon the position and the actual maximum height plus the width of the protrusion above the plane, as given by the user.

For example;

If (Rtest $< \frac{Ds}{2}$)

{

$$h(i,j) = [(\frac{1}{2}(\frac{Ds^2}{4hs} + hs)) + (i - 256)^2 - (j - 256)^2] - [\frac{1}{2}(\frac{Ds^2}{4hs} + hs) + hs]$$

}

else

{

h(i,j) = 0.0

}

where h(i,j) = Height of surface in frame buffer.
(As derived in the sub-section of this chapter).

Ds = Width of protrusion above plane.

hs = Maximum height of protrusion.

If Rtest is less than the width of the protrusion, the height of that point h(i,j) will be within the spherical surface domain and hence equal the expression derived previously (equation 4.14) else, if it is large, equal a value of zero.

The frame buffer of size 512 by 512 pixels is now complete with the simulated fringes of a defect.

4.4 Subtraction Test

To exactly simulate a defect, it is necessary to create a set of straight black and white fringes, (Figure 4.12) (where the surface is said to be perfect and flat), and a set of black and white fringes, shifted in their lateral position (Figure 4.13) (due to a change in surface curvature, i.e. defect).

Copies of both images are ultimately stored in different parts of the frame memory and subtracted from one another, producing a white region indicating the difference between the simulated fringes with both positive and negative pixel values outputted (Figure 4.14).

Thus, the volume may be estimated from the number of pixels remaining, given that the fringe spacing and angle of inclination is known.

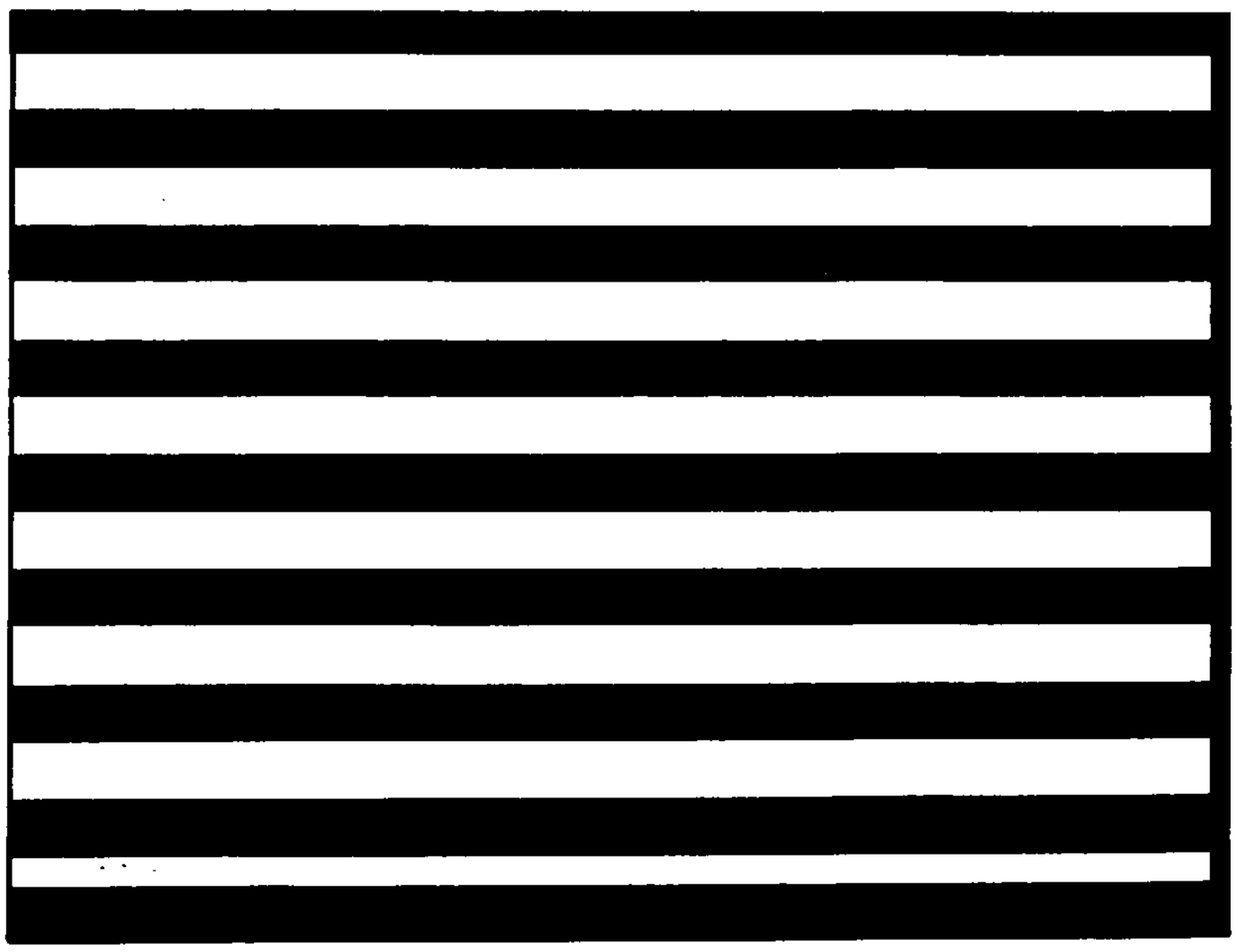

Figure 4.12 Simulated Surface with Straight Fringes.

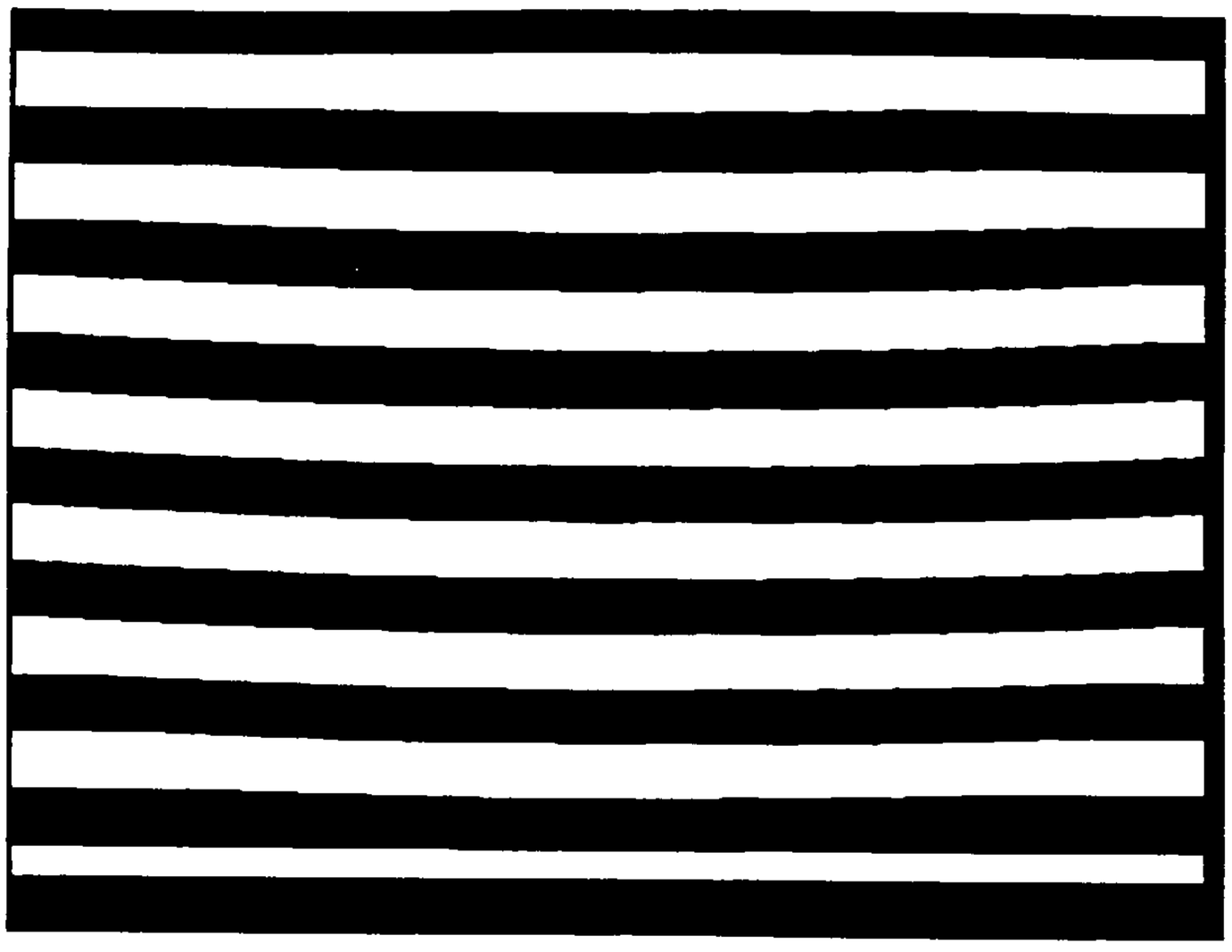

Figure 4.13 Simulated Surface with Shifted Fringes.

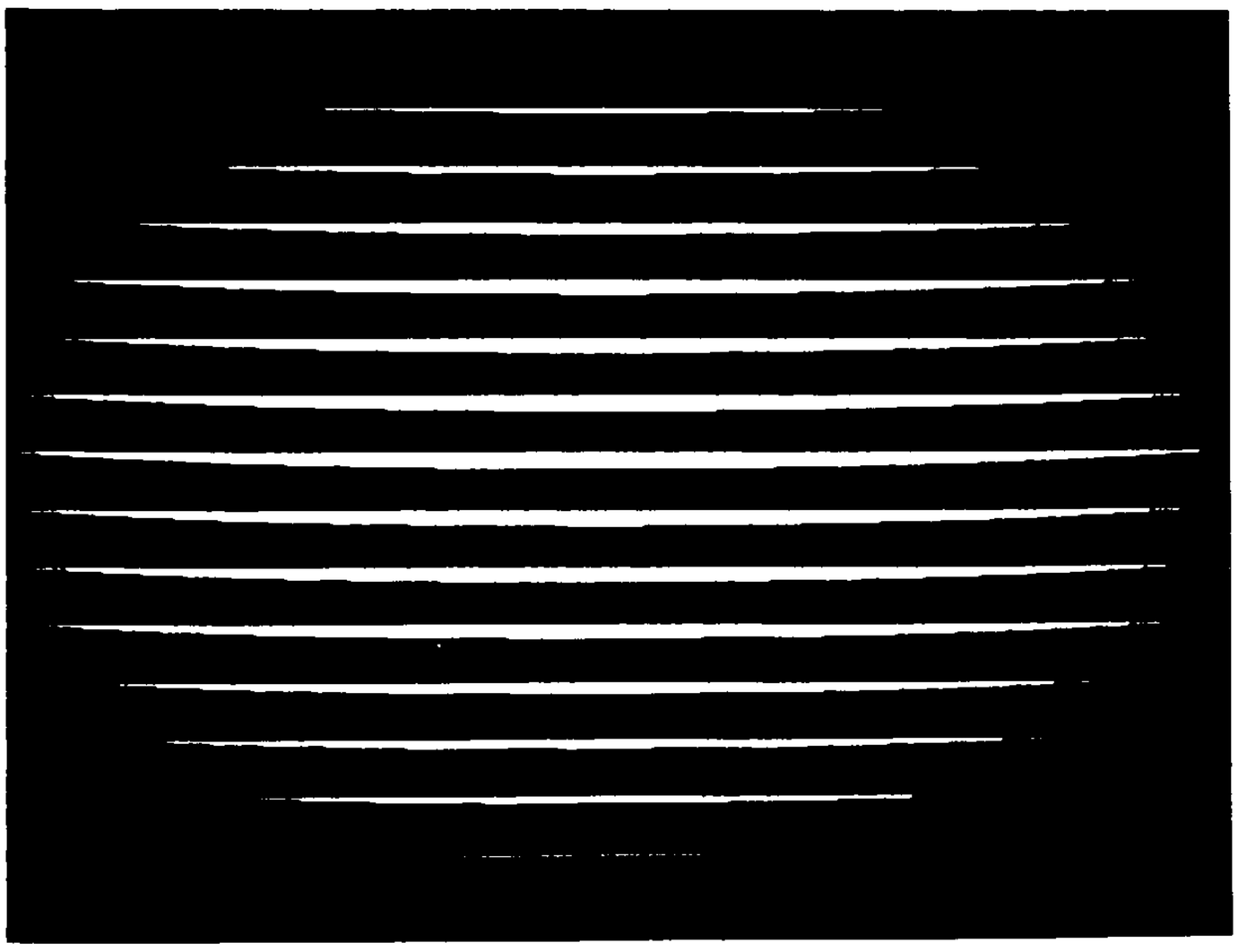

Figure 4.14 Simulated Resultant Difference Image.

4.4.1 Validating Theory.

To verify that the theory for volume estimation is correct, the volume estimated must be compared to the theoretical value. For a user defined size of defect. The following results were produced, showing the percentage error involved in comparing the estimated volume against the theoretical volume. Three examples for various defect sizes are provided.

It should be noted that for each example,

fringe period p_0 = 50

Angle θ = 45°

hs = maximum defect height of protrusion.

and ds = maximum impingement diameter of protrusion.

$$\text{Volume (estimated)} = \frac{p_0 \cdot \sum \text{pixels}}{2 \sin \theta}$$

where $\sum$ pixels = Total number of white pixels in the resulting difference of final subtraction.

$$\text{Volume (Theoretical)} = \pi hs^2 \left[R - \frac{hs}{3} \right]$$

$$\text{where Radius } R = \frac{1}{2} \left[\frac{Ds^2}{4hs} + hs \right]$$

Comparison of simulated results

	Estimated Volume	Theoretical Volume	Percentage % Error
Example 1			
hs = 10	**1026700**	**1021900**	**0.4%**
ds = 510			
Example 2			
hs = 20	**2047700**	**2047000**	**0.03%**
ds = 510			
Example 3			
hs = 50	**1243500**	**1714700**	**27 %**
ds = 300			

The above results from the subtraction of the simulated fringes indicate that the system and method of measurement is working correctly. The first two examples indicate this, with both the estimated and theoretical volumes approximately equal to one another.

However the reason for the large error estimated in example 3, is due to the fringes shifting in their lateral position more than the fringe width. Hence, when a subtracted image is created, the number of white pixels (a result of the protrusion) is significantly smaller than in actual fact. The basic theory for the estimation of the volume of a surface flaw, is dependent on the resulting fringes not shifting more than a fringe width. Any deviation from this would give results as in example 3.

Further simulation tests were also performed to observe the effect of altering the angle (with the same fringe period), on the estimated volume of

the same simulated defect. The process as before, involved the analysis of a subtracted image, created from subtracting the simulated images of, a flat plane and a flat plane with a surface defect (or hollow) both with the same desired fringe period and angle. This process is repeated for a variety of angles and the results displayed graphically in Figure 4.15.

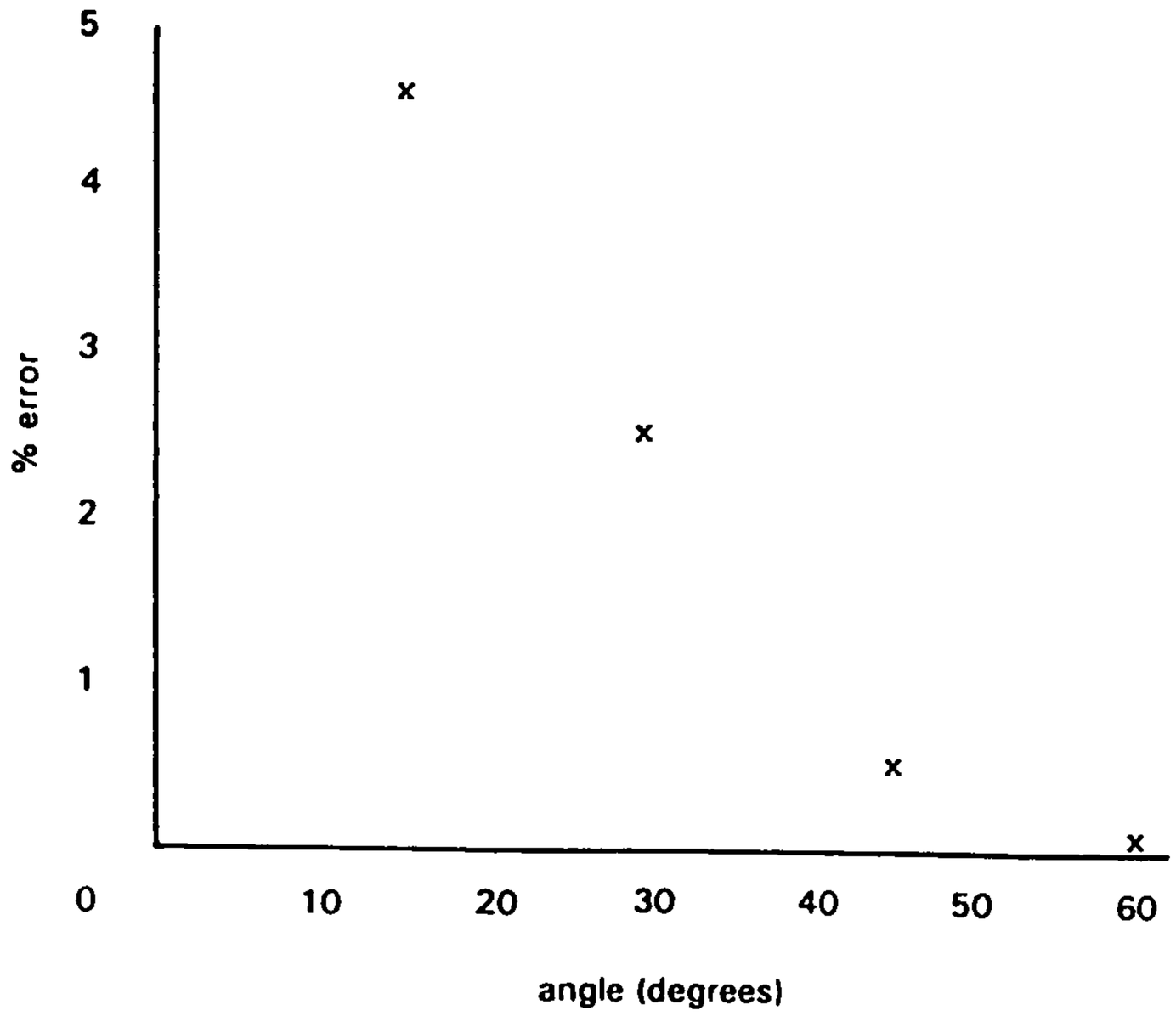

Figure 4.15 Effect of the variation of the angle on the percentage error

As may be observed in the Figure 4.15, as the angle of inclination between the camera and projector is increased, the percentage error of the estimated volume, as a proportion of the theoretical volume, decreases. Thus, giving the conclusion that the greater the angle, the greater the accuracy.

Similarly, the procedure was repeated to observe the different effect of altering the fringe period (with the same angle). The results may be observed in Figure 4.16.

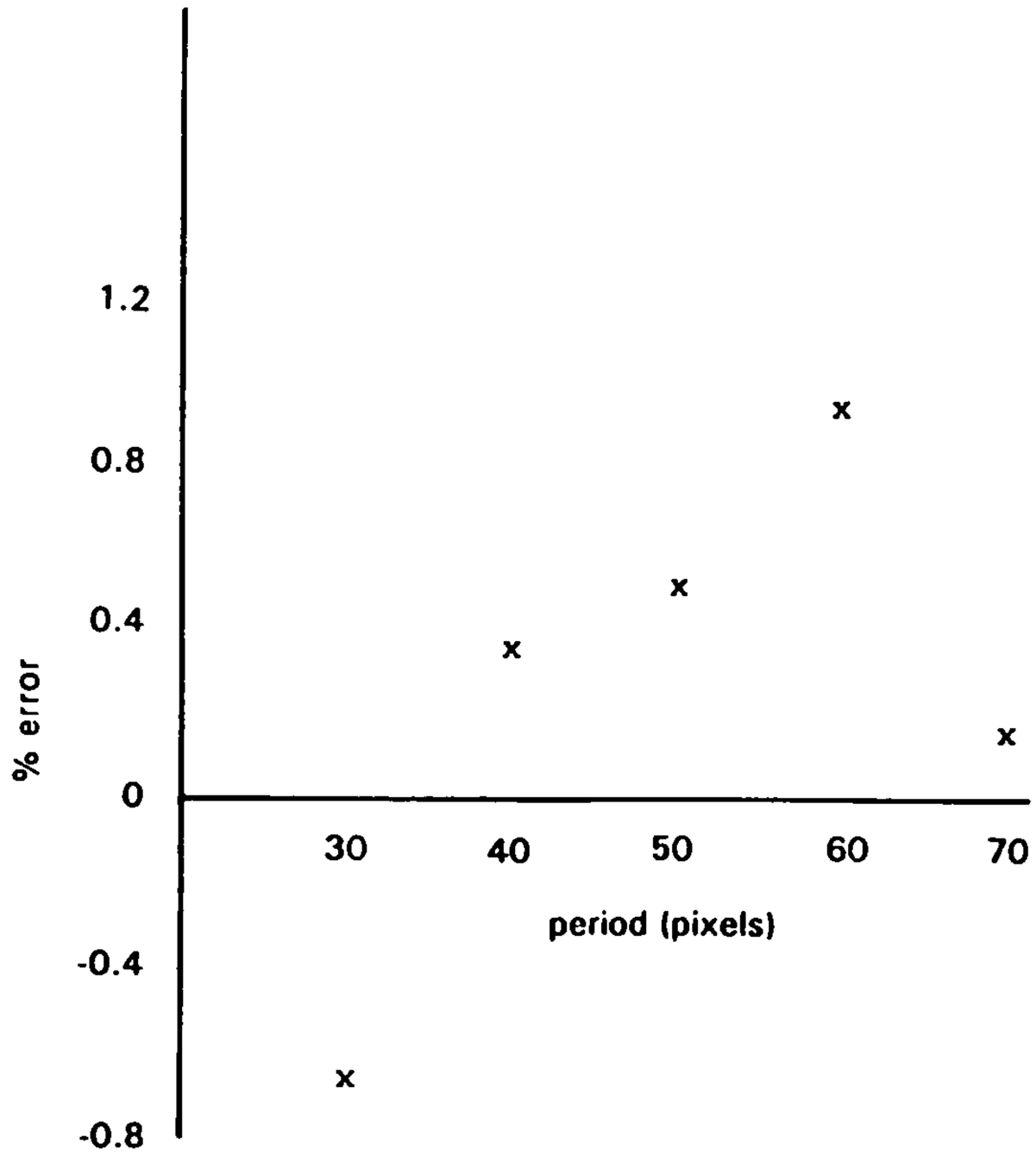

Figure 4.16 Effect of the variation of the fringe period on the percentage error

As may be observed from Figure 4.16 the effect of decreasing the size of the fringes is a smaller error, until a point is reached where the fringes shift is too great. It must be remembered that a prerequisite of this technique is that the fringe shift should not be greater than the fringe width. For this reason, a large underestimate in the volume would occur, thus explaining the negative error when the fringe period is reduced to a size too small. A similar error is produced on the other portion of the graph, due to the fringe period being too large in magnitude. With a large fringe period, the shift in the fringe and number of white pixels will not be significant enough to produce the desired effect. Too large a fringe period for a given defect, will cause the fringe shift to be not as great, producing a lower estimate for the volume defect (negative error).

Therefore in summary, for the most suitable set-up, the greater the angle of inclination between the camera and projector, the more accurate the result. However, this is provided that the magnitude in the fringe shift is not greater than the width of a fringe. The optimum angle would seem to be 45° from the results. Care must be taken in choosing the size of the fringe period, since too small a size may cause too great a shift, or too large a size too small a shift. The fringe period size must be dependent on the surface defect detectable (thus fringe shift), and so is dependent on the application that the system is to be applied.

4.5 Chapter Summary

The principle used in this technique relies upon viewing a surface with black and white fringes projected upon it. For ease of the explanation and derivation, the theory is developed using a flat plane as its example. It should be noted though that this comparative technique is applicable to any shape. For example, with a perfectly flat surface, the fringes will remain straight, as compared to a surface with a defect, where the fringes will shift in their lateral position in proportion to the defect depth or height.

With added use of thresholding, to create a distinct black and white image, instead of an image varying between black and white with grey, the area due only to the defect may be distinguished more easily. This is achieved with the use of subtraction of one thresholded image of a "Flawless" surface from another with a "Flaw", similarly processed and illuminated.

It is important that when the theory for volume estimation has been developed, the system must first be validated. It is essential that the volume of a defect calculated by the system is correct. One way in which this is possible, is if the volume to be calculated is known beforehand. Testing on simulated fringes where the theoretical volume may be known is an obvious solution.

The results from the subtraction of simulated fringes indicate that the system and method of measurement is working correctly. Also from the results a large error may be observed proving a prequisite of this technique is dependent on the resulting fringes not shifting more than a fringe width. Any deviation from this would give great errors as in the final example.

CHAPTER FIVE

PRACTICAL TECHNIQUE

5.1 Introduction

This chapter describes the problems encountered with this technique together with solutions to these problems.

A number of problems arise in the application of this basic technique, in enabling an accurate estimate for the volume to be made. These include.

(1) Exact Relocation - The surface to be gauged must be relocated in the same position as the master surface with which it is to be compared. Relocation removes any ambiguity.

(2) Same Surface Reflectivity - Both surfaces must have the same reflectivity. If not the subtracted image will have areas which will be confused with reflectivity differences and not purely due to a defect.

(3) Shift in fringe not greater than fringe spacing - If the shift in the fringe's lateral movement is greater than the projected fringe spacing, the subtracted image produced will be significantly smaller. The number of white pixels will be significantly smaller than should actual be. Thus a prerequisite is that the fringe spacing must be such that the deepest protrusion likely to be encountered must not lead to a fringe shift greater than the projected spacing.

(4) Visual Noise - Fluctuations due to the lighting conditions, cannot be totally eliminated but may be filtered out.

The following chapter investigates some of these problems, giving various solutions to try and provide a more robust system of measurement, eliminating some of these problems.

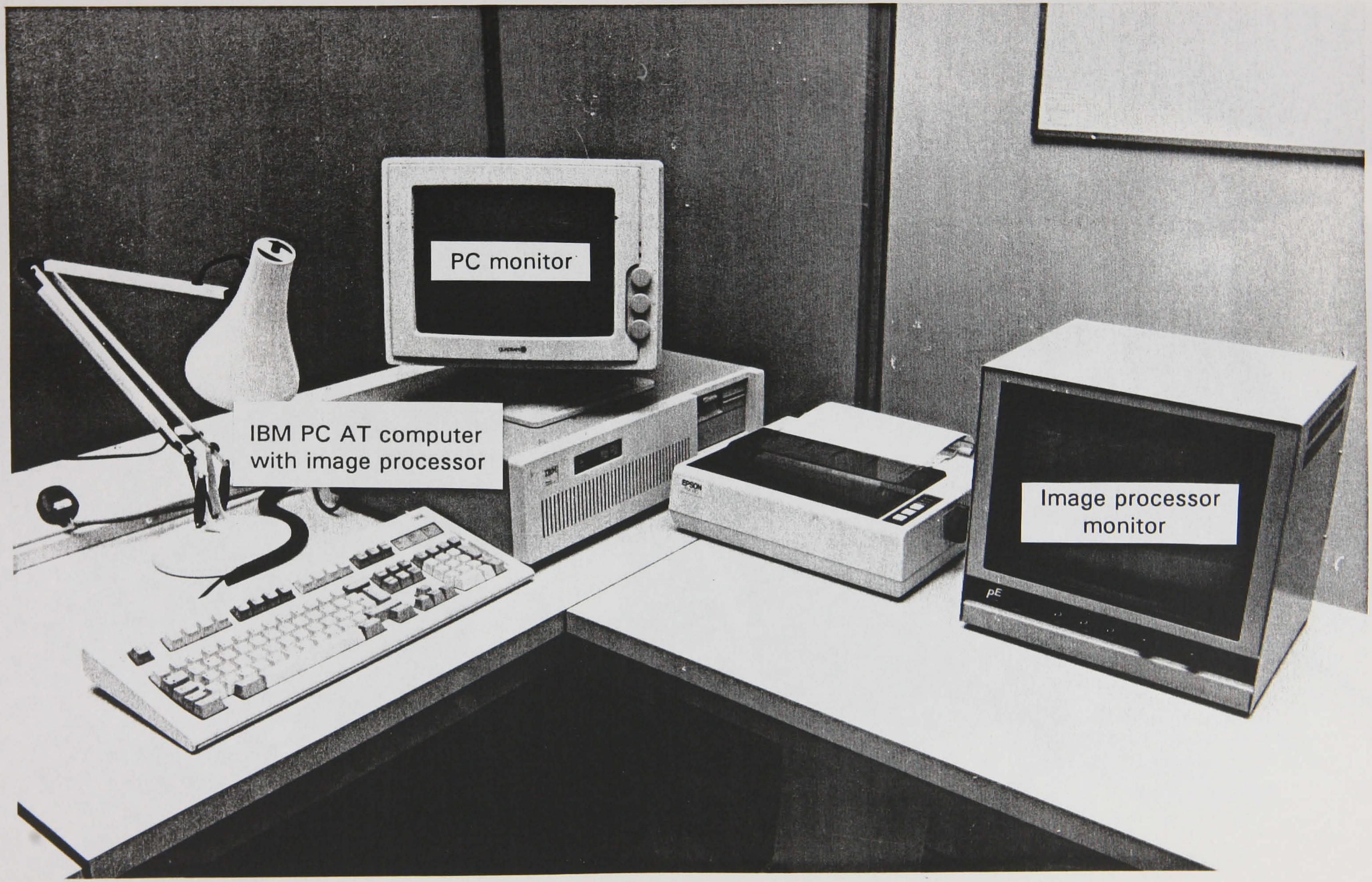

Figure 5.1(a) **Photograph of the Digital set-up**

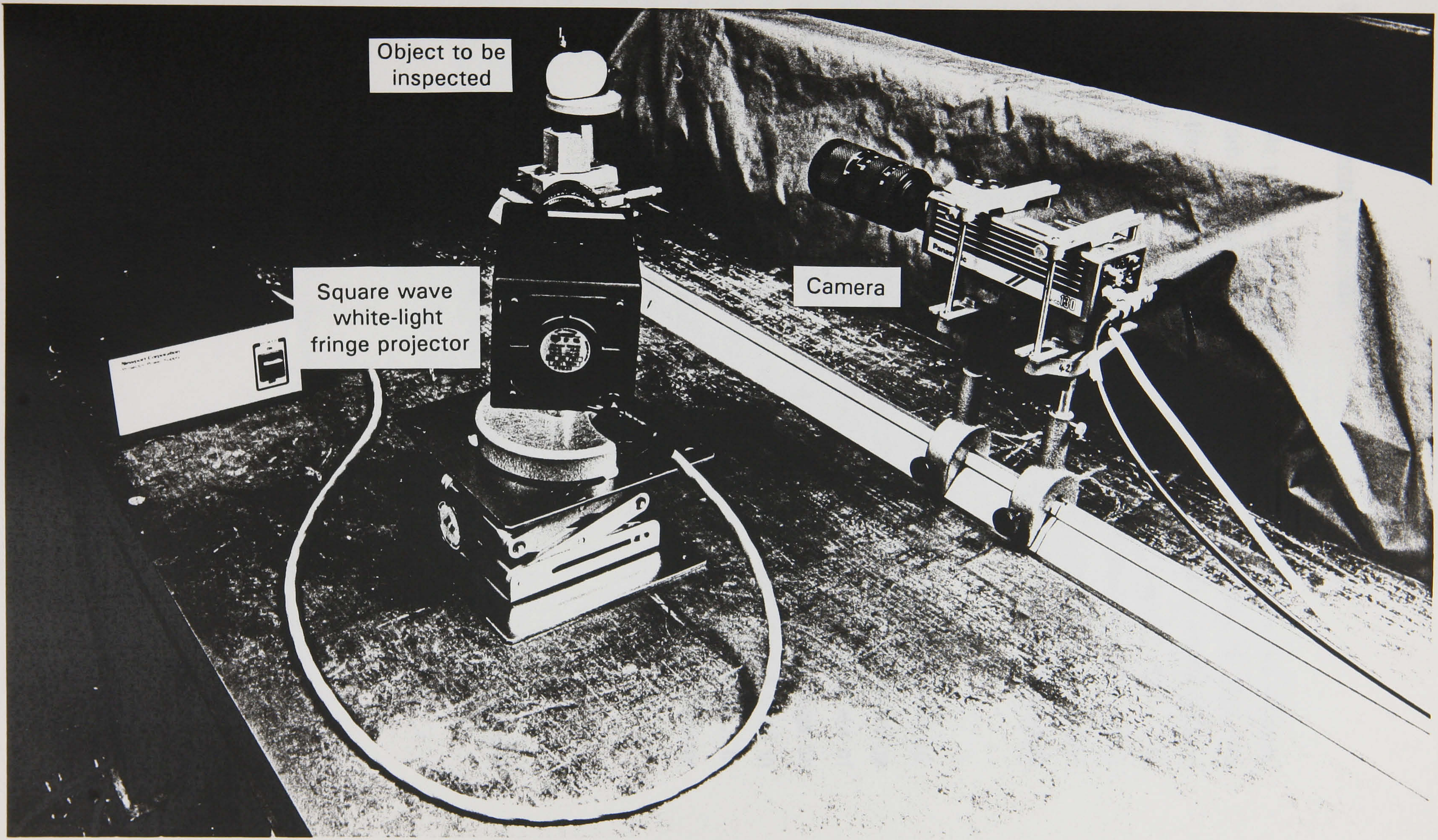

Figure 5.1(b) Photograph of the optical set-up

5.2 Experimental Validation

With the basic theory of this technique for the estimation of the volume, validated from the simulation tests, it still is necessary to test this experimentally. To achieve this, the fringes are projected onto the surface at an angle and viewed from a camera as shown in figure 5.1(b). The fringes are produced by projecting light through a small grating, placed within the projector. The projector itself produces light of uniform distribution across the entire grating, thus the fringes on the surface to be measured are of constant amplitude.

For the determination of the volume other parameters are required such as, the angle between the camera and projector, and also the observed fringe period on the surface, as viewed through the CCD camera. These are of great importance in respect to the magnification and aperture settings on both fringe projector and camera, when capturing the two images used in this comparison. These obviously must be the same for both images. In addition, the aspect ratio is required and is described later in this chapter in the rotation theory section.

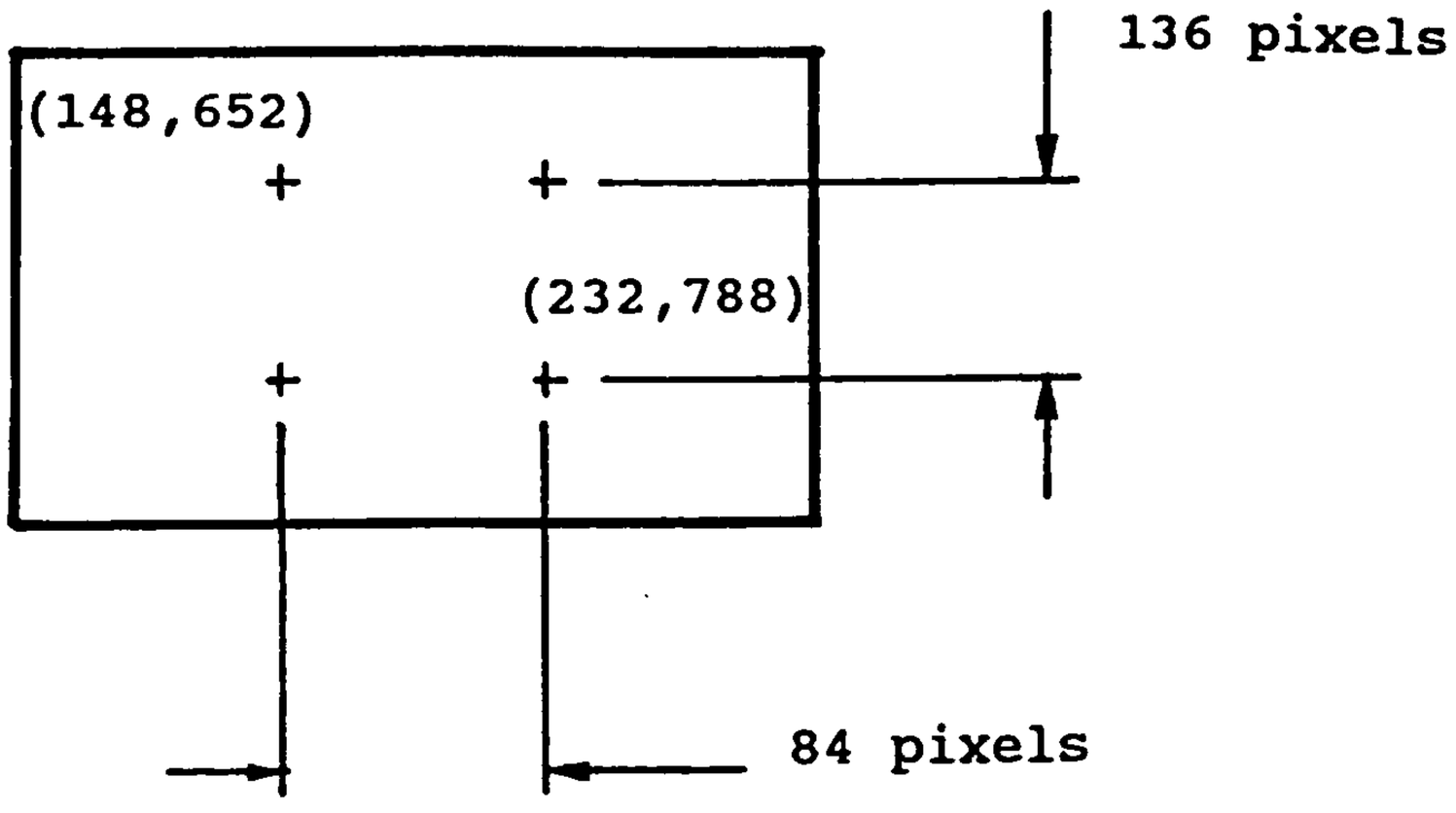

Figure 5.2 **Slip gauge with marks of known distances apart in millimetres and eventually in pixel terms.**

5.2.1 Fringe Period and Aspect Ratio Parameters

The fringe period and aspect ratio are obtained by analysing the fringe pattern as it appears on a flat surface painted white, to aid the contrast in the projected fringes. For this experiment a slip gauge face was used. Marked on the face of one side of the slip gauge, are the corner points of a square, of known dimensions, which is then viewed through the camera. (Figure 5.2)

With the use of a cursor function within the software, the fringe period distance is calculated by dividing the total width of a number of fringes, by the total number of fringes. Using this average fringe period, the effect of the fringes increase in size by a fraction in width across the image, would be eliminated. Also by using the cursor function, the marked points may be selected, giving the pixel co-ordinates and hence number of intermediate pixels over a distance of known dimensions in mm. Thus, the fringe period, scale factors and aspect ratio are determined. This calibration is performed a number of times to give an average value for each parameter.

5.2.3 Angle Parameter

The angle between the camera and projector was initially determined by using a variety of methods. A protractor and then a projector placed upon a turntable with vernier angle scales were initially used with varying degrees of success, but the most successful involved the following set-up. (Figure 5.3).

The angle is determined by obtaining the angle readings on the turntable, for reflecting the beam of light source back to its source, and by rotating the mirror, reflecting the beam to the camera.

The required angle between the light source and camera being the equivalent to double the difference between these two readings. Care must be taken to ensure that the mirror is placed upon the centre of rotation of the

turntable and aligned correctly with both the projector and camera, where the object would be placed. This is achieved by a combination of trial and error, until the beam reflected on the mirror (or in this case a highly polished metal surface) is not shifted when rotating the mirror.

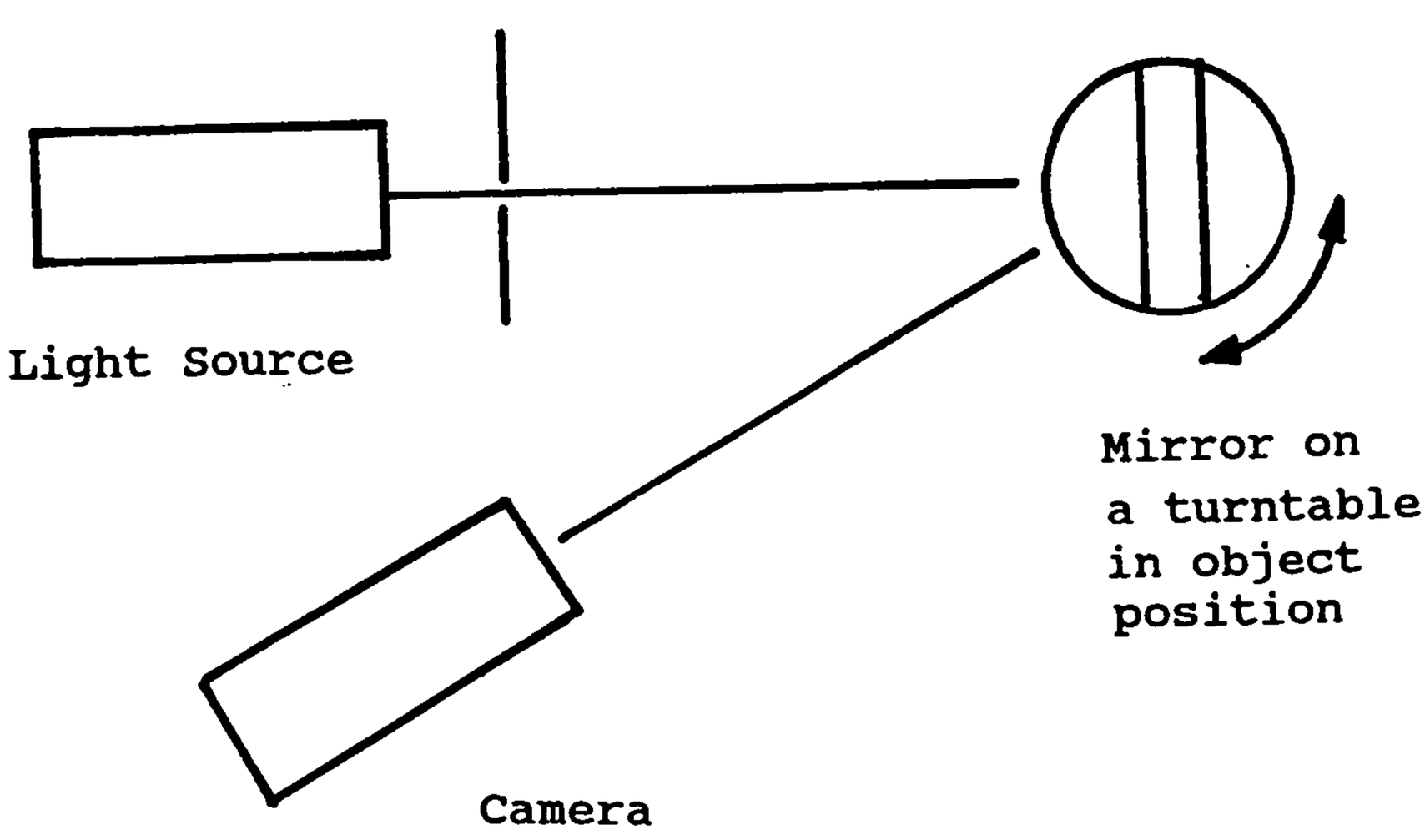

Figure 5.3 Angle Determination using rotating mirror.

5.2.4 Calibration for Linear Relationship

Practical measurements of a slip gauge, placed upon a three dimensional translation stage, were made with the fringe period and angle known. However problems were encountered in the accuracy of the volume estimation compared to the theoretical value (determined from a known translation).

As a result of the sensitivity of the technique to these parameters that are essential in determining the volume, an alternative solution was investigated. This involved determining a linear relationship between the number of white pixels in a subtracted image and its related volume, as shown in Figure 5.4. Thus eliminating the requirement to input the fringe period and angle parameters.

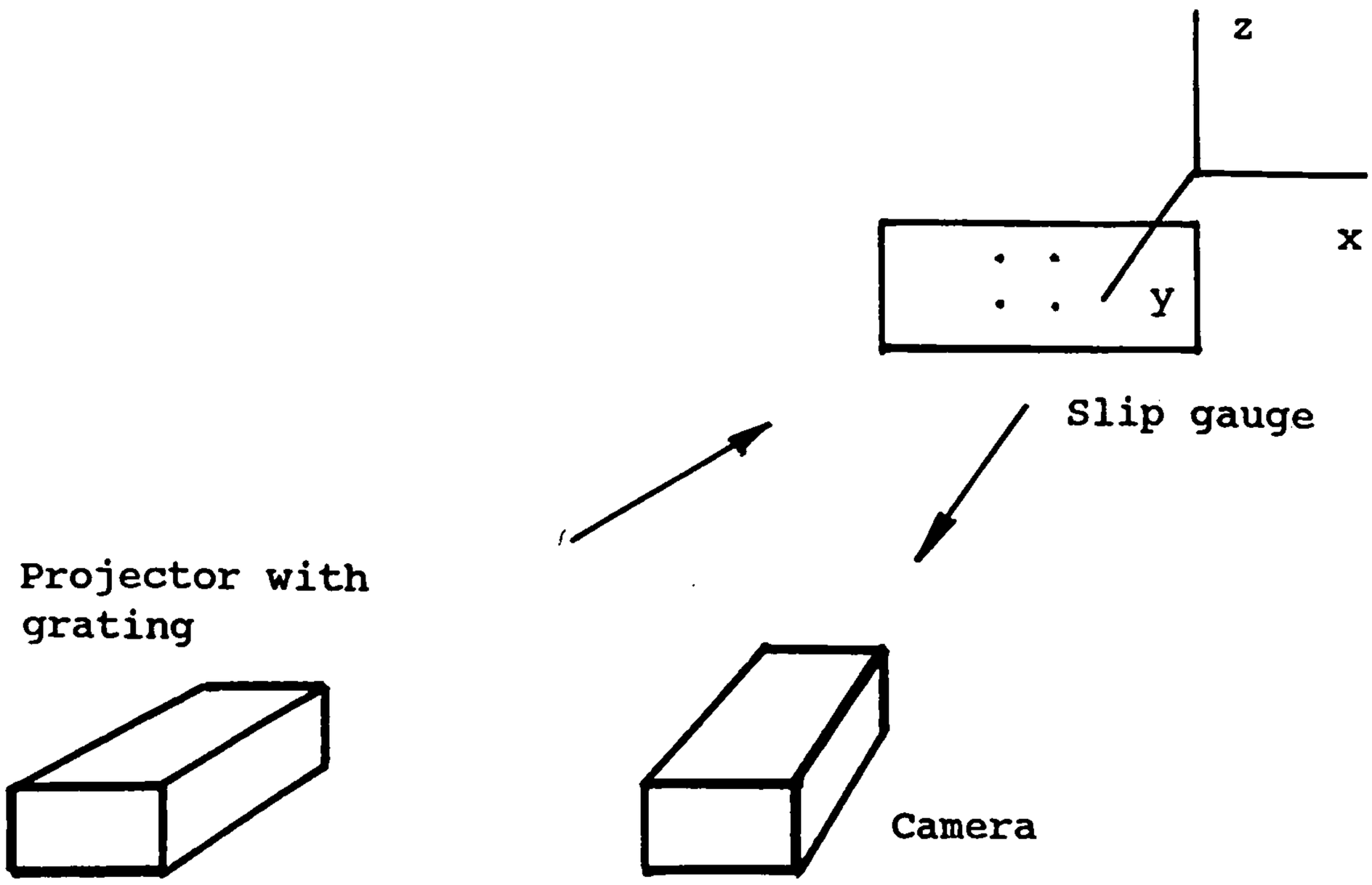

Figure 5.4 Set-up with slip gauge of 3D translation stage.

A slip gauge is placed upon a 3D translation stage, a rig able to shift in any three directions using micrometer screw threads. One face of the slip gauge is painted white, with four points of the corners of a square marked upon it, with these points visible through camera.

These points were then accurately measured using a SIP - a 3 co-ordinate measuring machine, to enable the exact area between these points to be calculated. The purpose for which is for the volume to be determined, when analysing a subtracted image, produced from shifting the slip gauge a known amount towards the camera. From using a cursor function, the exact area for determining the column may be chosen, in this case a diagonal pair of these points. (Figure 5.5)

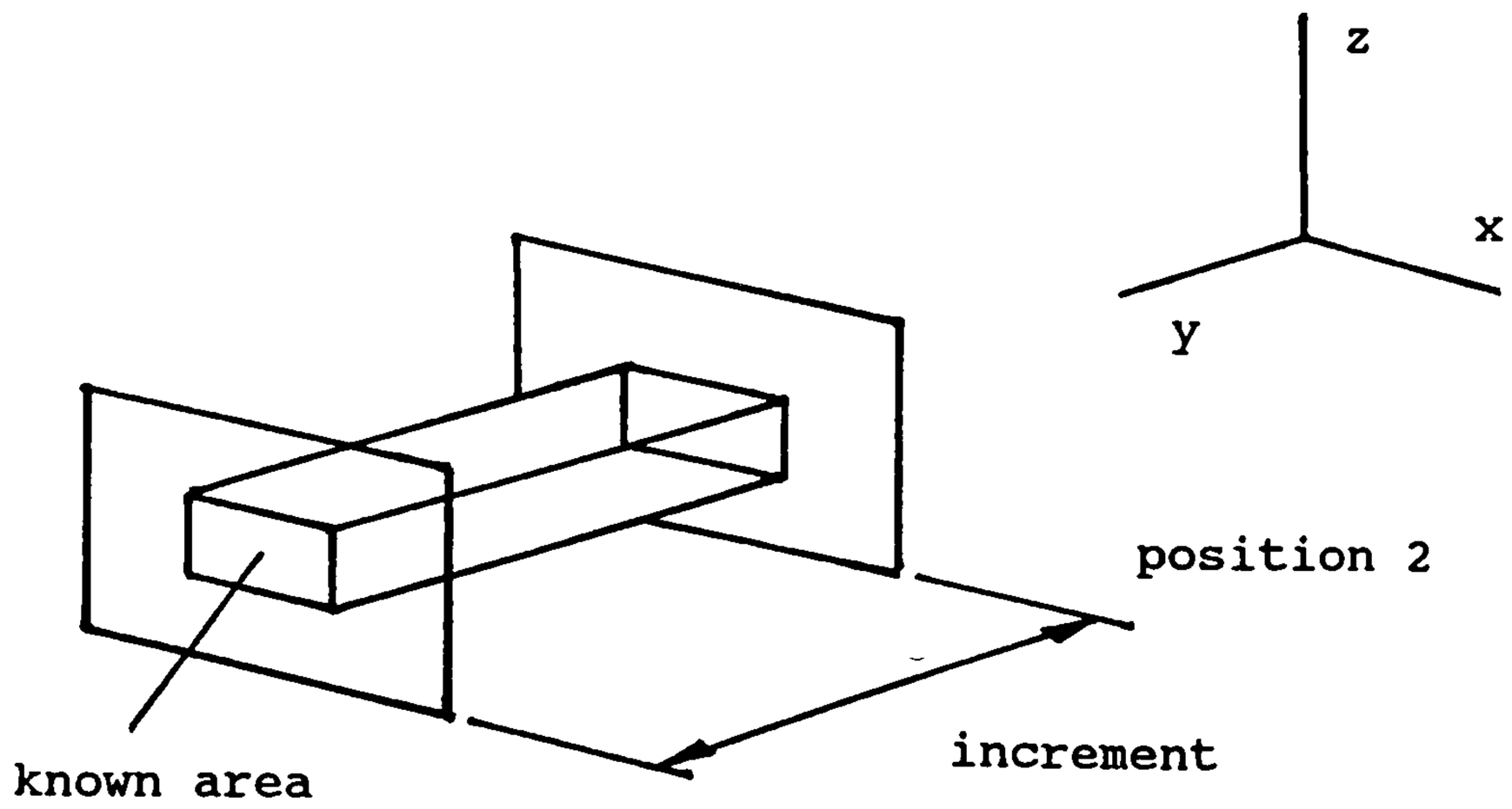

volume = area x increment

Figure 5.5 Volume Swept From Known Area.

This procedure is repeated a number of times, with the screw thread incremented known amounts, in the same direction to avoid any backlash, to provide a number of images. These images are compared with an initial image which is taken to be the datum, to provide a number of subtracted images, where the number of pixels and its related theoretical volume (from its area and distance incremented from the datum), may be produced. An example is demonstrated below.

Example.

Increment From Datum. (mm)	Number of Pixels	Theoretical Volume (Area x increment) mm^3
0	528	0
0.127	1003	52.2
0.254	1803	104.4
0.381	2532	156.6
0.508	3325	208.8
0.635	3931	261.1
0.762	4972	313.5
0.889	5539	365.5
1.016	6383	417.7
1.143	7039	469.9
1.270	7710	522.1
.	.	.
.	.	.

Note: The increment values have been converted from thousandths of an inch into millimetres.

A relationship between the latter two columns, of the number of pixels and its related theoretical volume, using the least squares theorem, may then be derived.

i.e. $A = \frac{\sum y - B.\sum x}{n}$ $B = \frac{n\sum xy - \sum x.\sum y}{n\sum x^2 - (\sum x)^2}$

where A = Constant Term. B = Regression Coefficient.

With a relationship of the form: $y = Ax + B$

In this case, $y = 0.070625x - 25.0888$

i.e. See Figure 5.6 for plot of example.

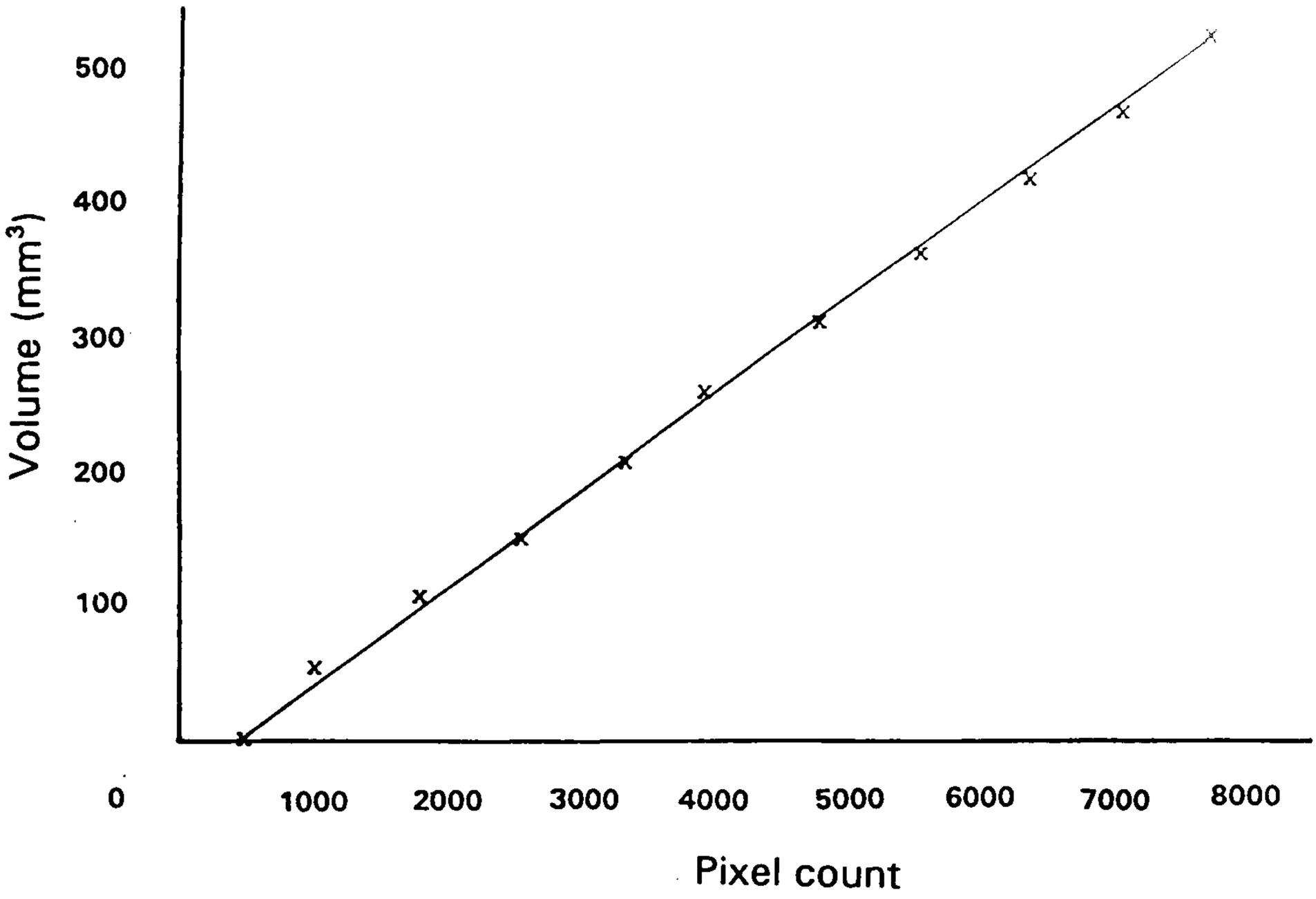

Figure 5.6 Graph of Pixel count against Volume.

Thus, eliminating the requirement to input any other parameters, once the system has been calibrated, to determine the volume.

5.2.4 Experimental Tests

At this point it is necessary to carry out some validating experiments. This was done under controlled conditions in which volumetric difference would be independently known.

These tests were performed with three objectives in mind.

(1) To validate the technique experimentally, comparing the theoretical against derived volume, using user inputted fringe period and angle.

(2) To show the effect of varying the angle of projection.

(3) To show the accuracy of the linear calibration method.

From the results a variety of graphs are produced Figures 5.7 to 5.12. Comparisons may be made between the known volume (calculated from the displacements) and the estimated volume (from the technique, using the fringe period and angle data). Displacements of 0.127 mms have been detected, for a variety of angles between the camera and projector.

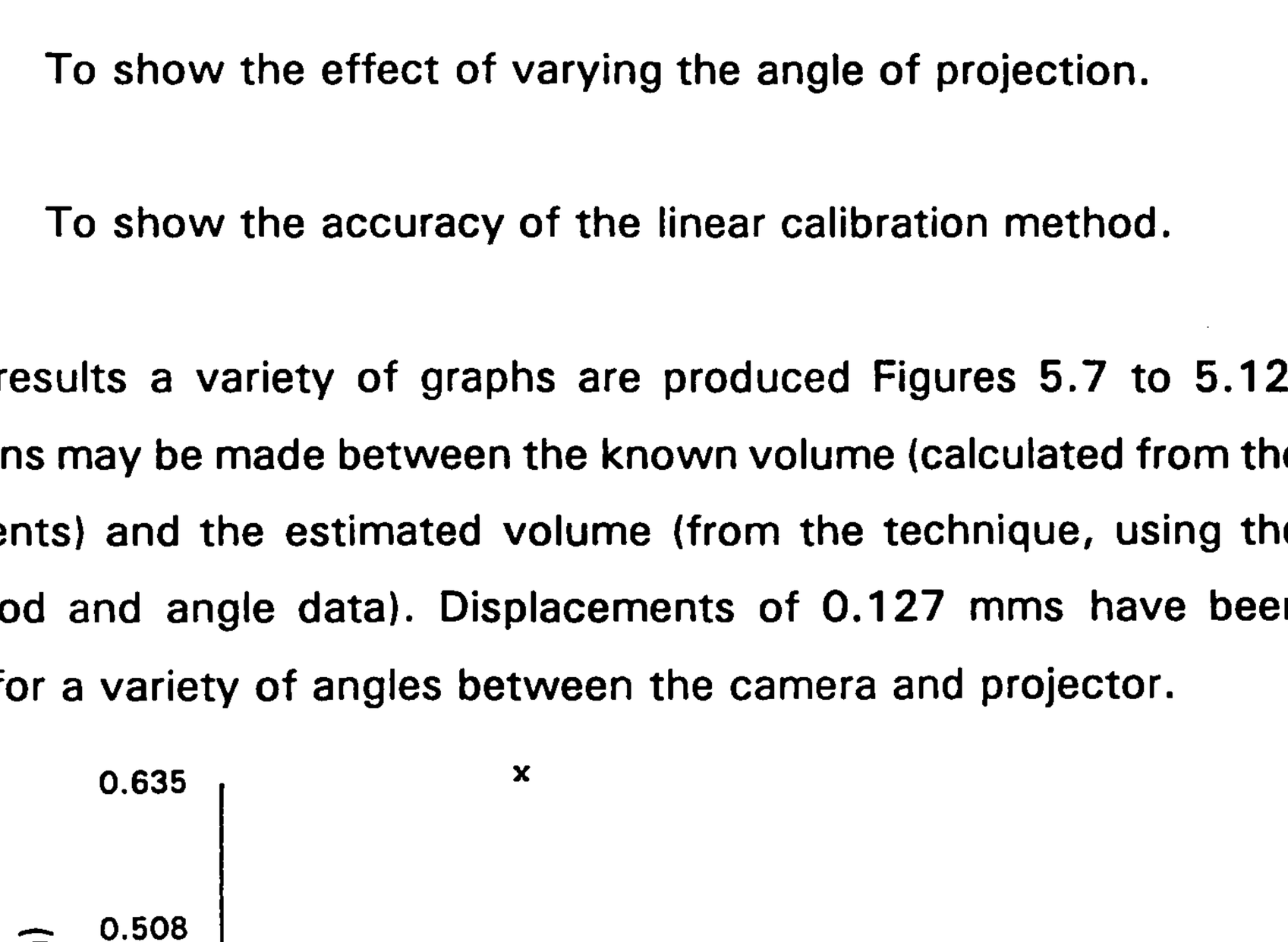

Figure 5.7 Smallest Detectable Displacement vs Angle

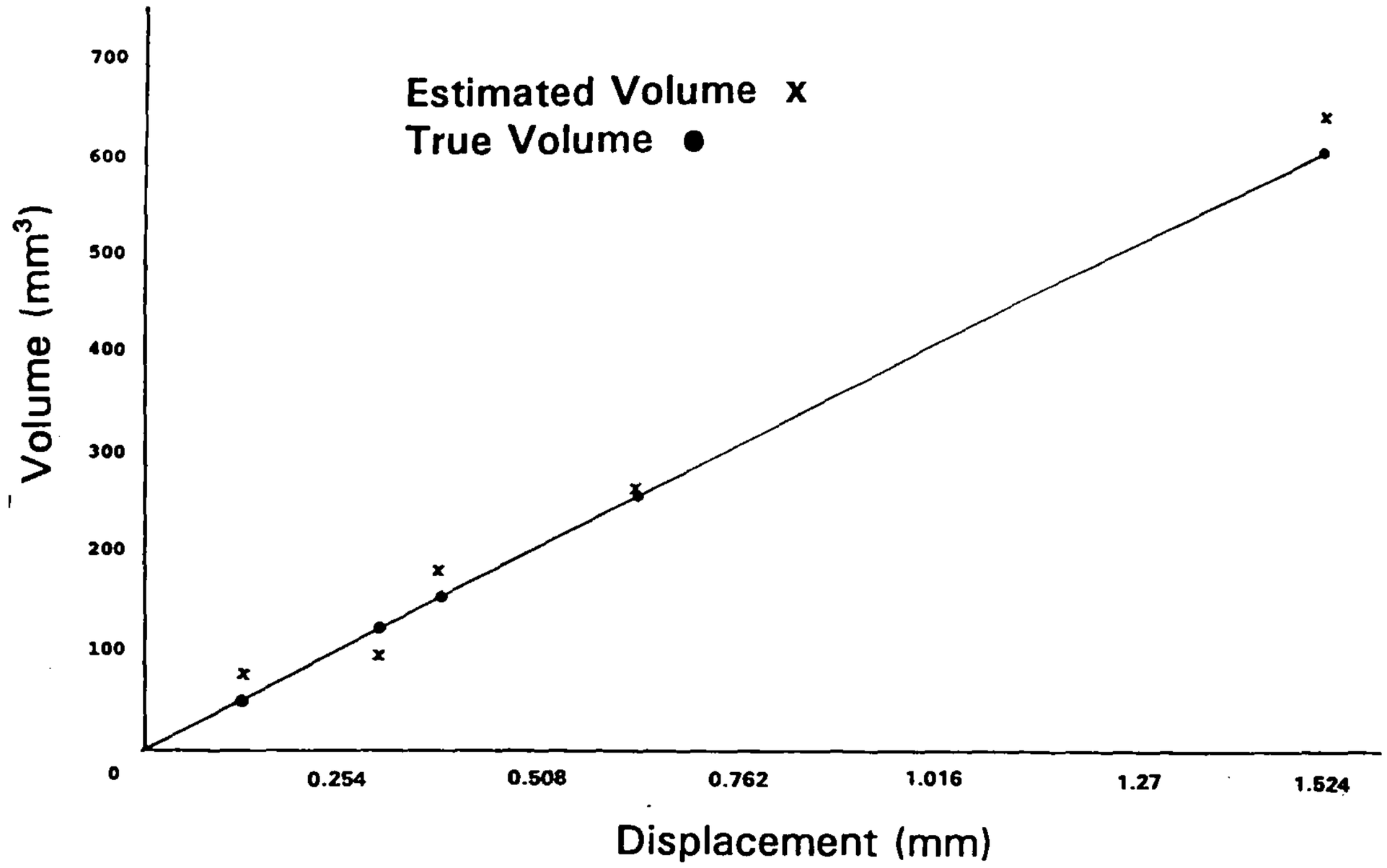

Figure 5.8 Slip gauge - Angle 10 degrees Displacement vs Volume

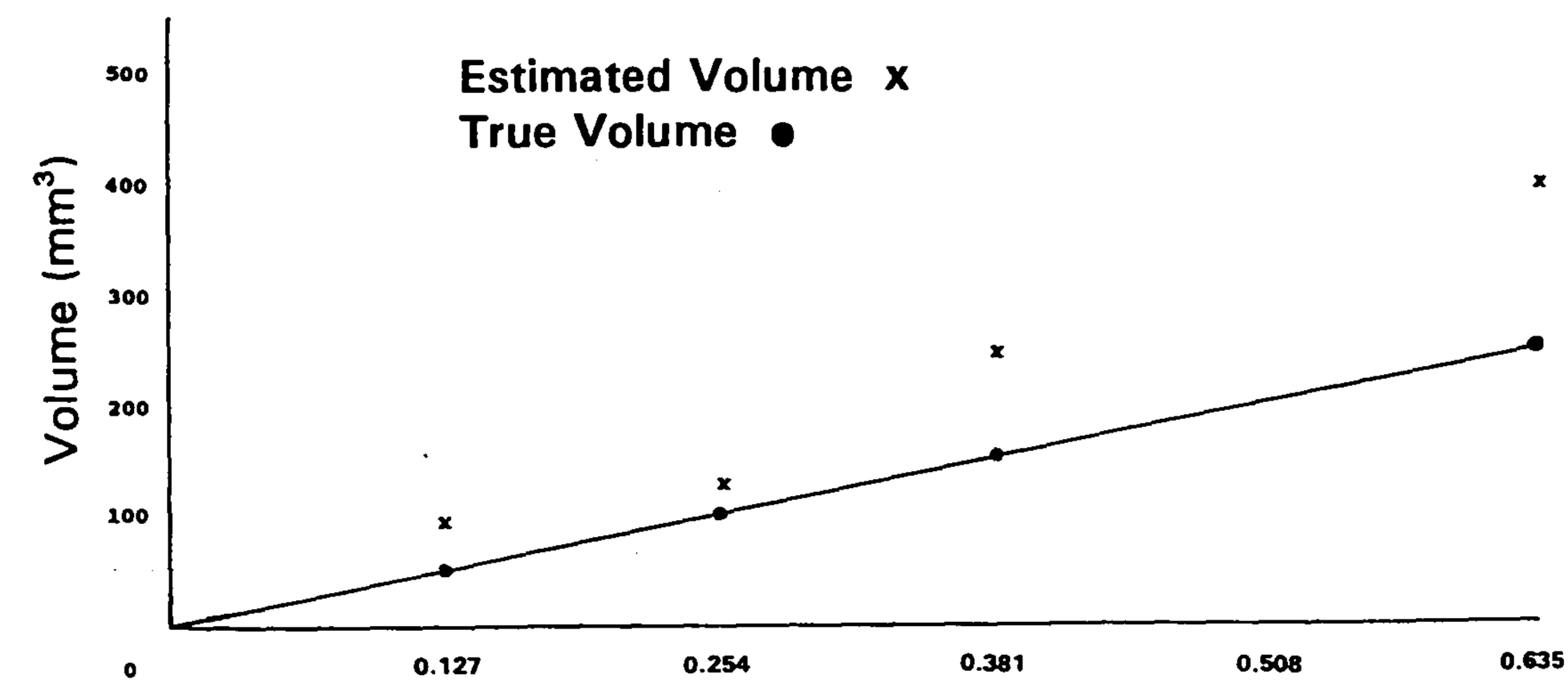

Figure 5.9 Slip gauge - Angle 20 degrees Displacement vs Volume

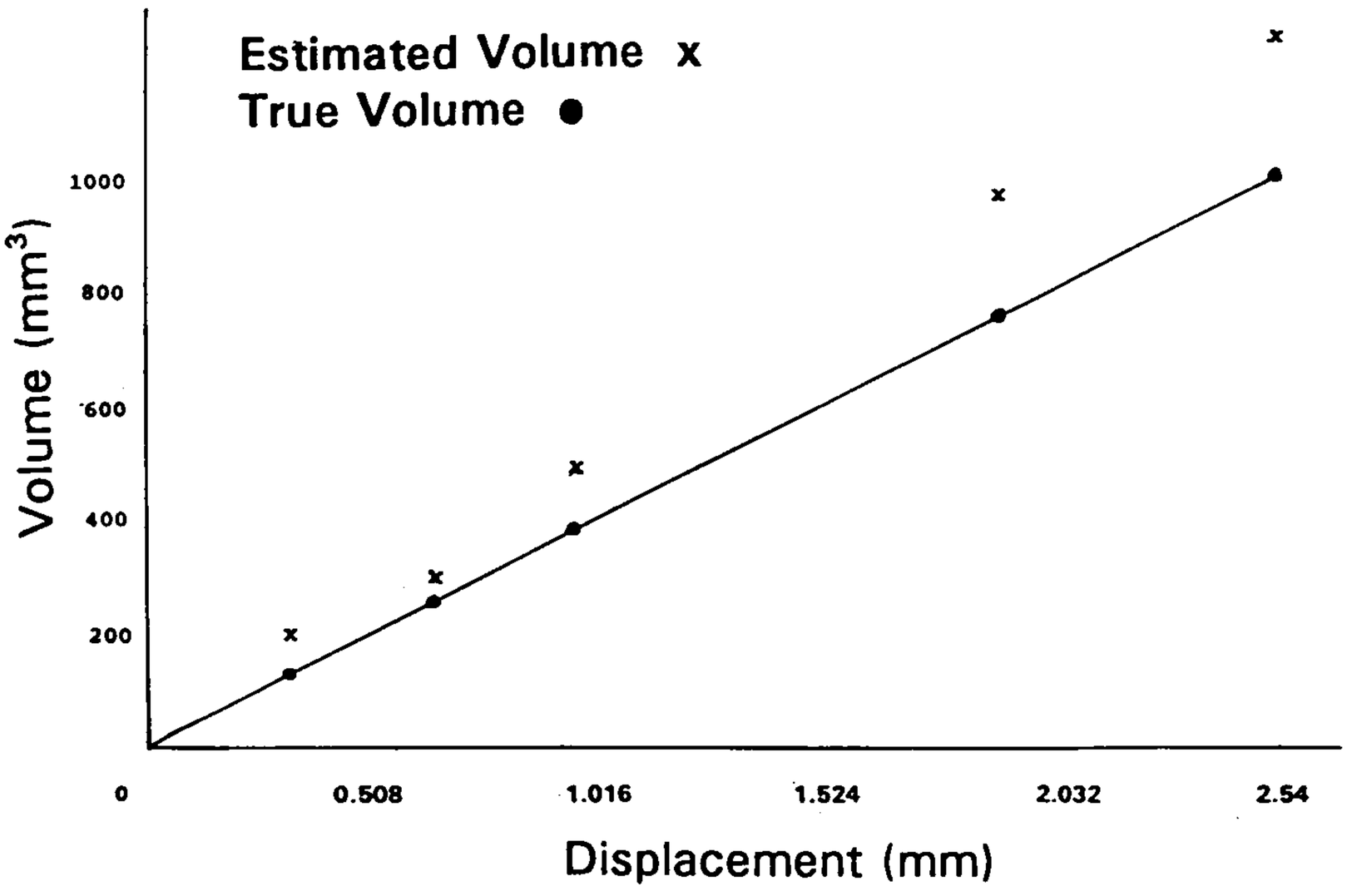

Figure 5.10 Slip gauge - Angle 30 degrees Displacement vs Volume

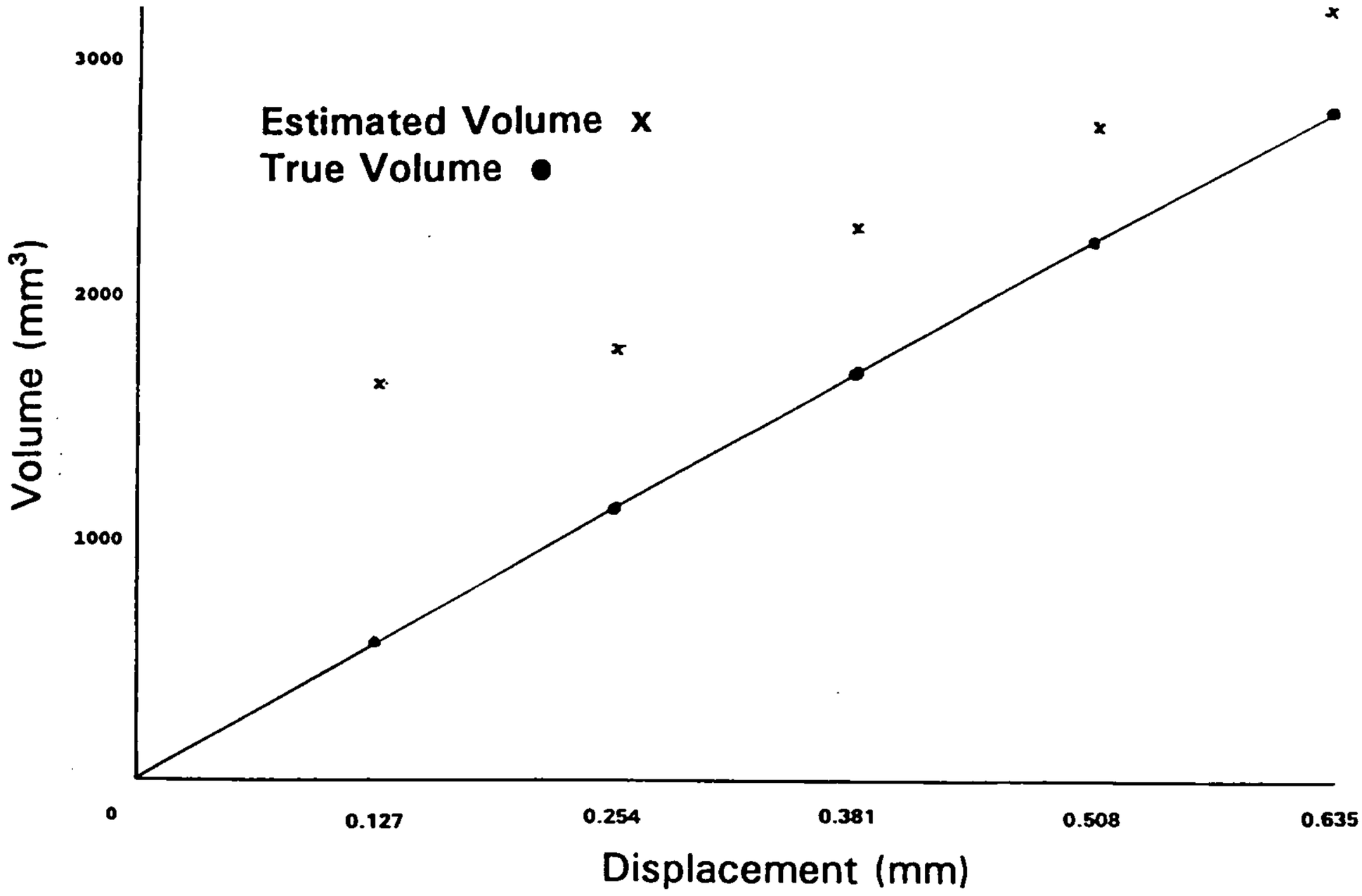

Figure 5.11 Soap bar - Angle 10 degrees Displacement vs Volume

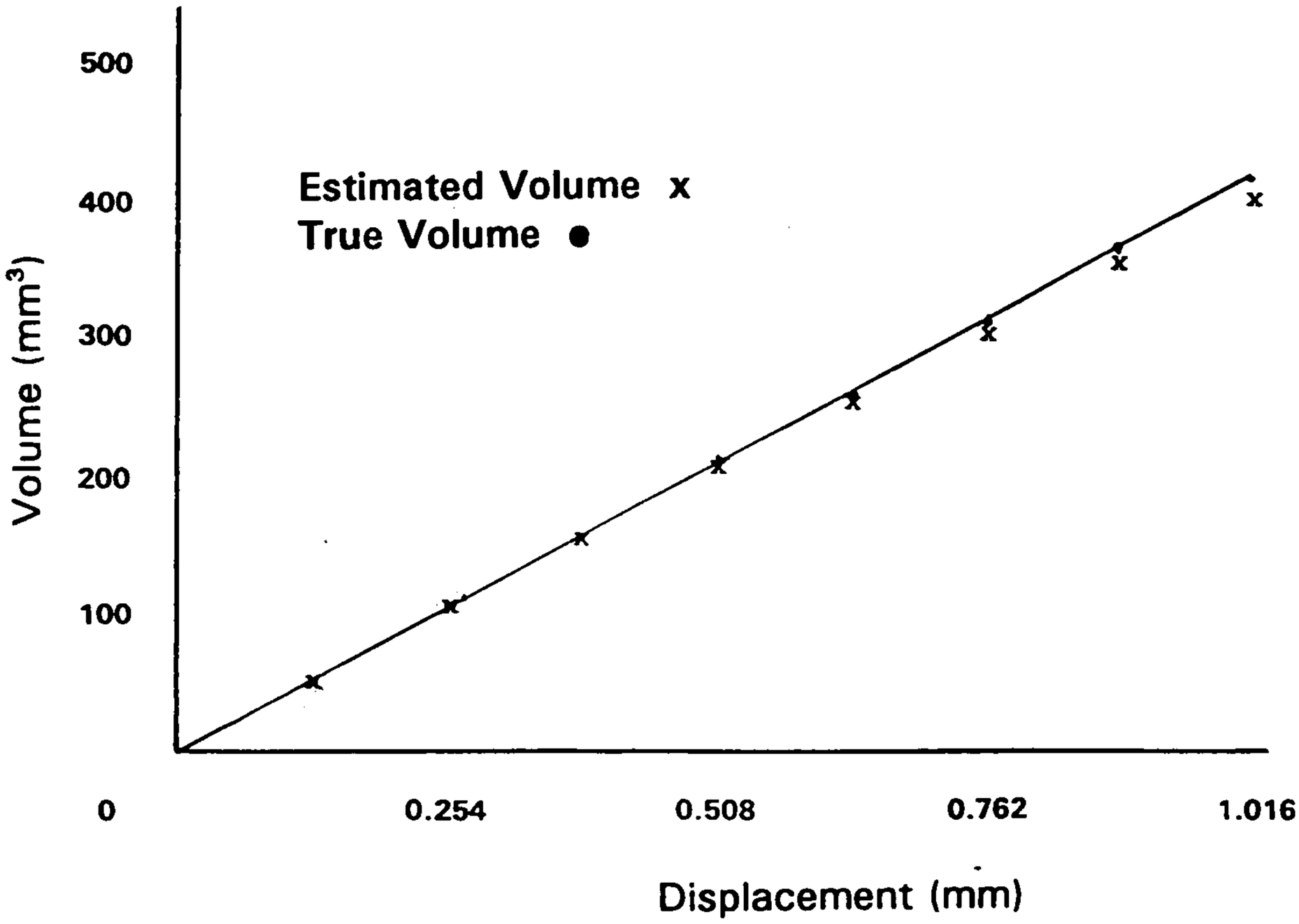

Figure 5.12 Soap bar - Angle 34 degrees Displacement vs Volume

Figure 5.7, a plot of the most detectable displacement plotted against its angle, gives an indication of the effect of the angle to the sensitivity of the technique of fringe projection. For the best accuracy of this technique, the greater the angle, the greater the sensitivity. This is dependent on the prerequisites previously mentioned in this chapter. That is, the fringe spacing must be such that the deepest protrusion likely to be encountered must not lead to a fringe shift greater than the projected spacing. In other words, the system must be initially set up at a suitable angle to enable the fringes to shift as near to the maximum spacing for the deepest protrusion possible. Thus providing the greatest sensitivity.

Various graphs for different angle settings (Figures 5.8 to 5.11) have been provided. Figures 5.8 to 5.10 are of the displacement of a slip gauge and Figures 5.11 and 5.12 of a soap bar. It may be observed from the first of these (Figure 5.8) that the figures for the estimated volume are in good agreement with the theoretical values, indicating the technique's accuracy. As previously described increasing the angle will increase the sensitivity of the technique.

In the case of Figure 5.9, now at an angle of 20 degrees, the estimated values exceed the theoretical, and increase in their divergence as the displacement increases. This is due to the fact that the projected fringes diverge as they leave the projector. Thus, the fringe period will grow, as the distance from the projector increases. For this reason the resultant estimated volume will be greater in magnitude than the true value.

In addition the problem in accurately determining the angle and fringe period may have affected the result. Other than for these reasons, Figures 5.9 and 5.10 (for 20 and 30 degrees (approximately) would have produced similar results to Figure 5.8 (For 10 degrees). The sensitivity of the technique at a greater angle, would magnify any error in either of the problems discussed and produces results demonstrated for 20 and 30 degrees.

In the latter case of a bar of soap (Figure 5.11), it may be observed that

both slopes are of the same gradient (indicating good correlation) but with the experimental values exceeding the theoretical by a constant amount. This is partly due to the problems discussed earlier, particularly the accuracy of determining and inputting the angle and fringe period, but also due to the problem of misalignment. This problem will produce a significant increase in white pixels produced in a subtracted image and therefore experimental values. This is discussed and analysed further, later in this chapter.

Enabling these problems to be solved will enable significant improvements in the results for experimental values as displayed in Figure 5.12. The experimental and theoretical volumetric values show an improved correlation, diverging slightly due to displacement errors towards the camera. However this error is insignificant.

The application of this technique in producing results as in Figure 5.12, with a bar of soap as the practical example, is used partly to give a suitable example where this technique could be applied in industry, but also due to the interesting phenomenon of different coloured soaps exhibiting different light absorption properties. With tests on a white painted slip gauge, ideal conditions are encountered. The application of this technique on a more difficult and practical example, even with its resulting problems, show the success of this technique. Providing a bar of soap is compared to a similarly coloured bar of soap, this problem will not be encountered. But as was mentioned in this chapter, for a comparison to be made, surfaces of similar reflectivity should be compared.

Tests in verifying the accuracy of the linear calibration method were also performed, to provide an alternative to the necessity of inputting the set-up data. With the system calibrated and a linear relationship established, results produced from separate tests were within 1 to 2.5% of the true volumes, indicating the success of this method. However, due to the sensitivity of this technique in relying upon images to align exactly with one another, the results give a misleading impression of their quality. Later results in the accuracy of this technique produced were not of the same magnitude.

Inaccuracies produced as a result of backlash, resulted in the misalignment of the image to be gauged, with the datum image with which it is to be compared. This backlash was the result of the screw thread used to displace the slip gauge. Thus, this linear calibration alternative is not a viable solution until the misalignment problem is solved. This exemplifies one of the prerequisites of this technique, for both images and fringes to align with one another. The problem of fringe alignment is discussed later in this chapter.

5.3 Noise

Images of the same stationary scene will never be identical to one another, due to the visual noise ever present. One of the main reasons for this is the fluctuations in the lighting conditions in this technique. This background noise cannot be totally eliminated and so must be minimised as far as possible, since these areas may be confused with the defect on the surface.

To achieve this a number of methods were investigated, two of which are described in the following section.

5.3.1 Erosion

This method eliminates the unwanted noise in the subtracted image of two thresholded images. Every pixel within the image is compared with a number of neighbouring pixels and a logical AND performed of neighbouring pixels using a threshold value. If the AND is true, the intensity value of the centre pixel is set to the lowest value from the surrounding pixels. Since the elements of the thresholded image are either black or white, the effect is thinning of the number of white elements in the image.

The method of erosion is performed as many times as required until the majority of this background noise has disappeared. However, problems may arise if white pixels (corresponding to the areas of a defect) are eroded away, thus reducing the apparent magnitude of the defect. This technique was found to be unsuitable since it irreversibly altered the subtracted image. A more suitable solution is the use of averaging of a number of images.

5.3.2 Averaging Function

The purpose of averaging as described earlier is to minimise the visual noise that is always present. This function is used to minimise these variations, by averaging a number of snaps of the same stationary scene, and subsequently storing the resultant averaged image into the frame memory.

This is performed for each inputted image of perfect and gauged samples.

The mechanism for the method of averaging is achieved by the capture of a number of 6 bit images which are then summed into 11 bits using a two-pass algorithm. The first pass sums the most significant bits of the input image with the least significant six bits of the image currently in the frame memory, producing a 6 bit sum and a carry bit. The second pass then adds the carry bit to the top 5 bits of the accumulated image. With proper scaling, this 11-bit sum can be converted to an average. The most significant 5 bits of the averaged image are displayed during acquisition to allow the averaging process to be monitored.

Averaging of Multiple Images

Consider a noisy image [5.1] g(x,y) which is formed by the addition of noise n(x,y) to an original image f(x,y); that is

$$g(x,y) = f(x,y) + n(x,y)$$

where it is assumed that every pair of co-ordinates (x,y) the noise is random and has zero average value. Given a set of noisy images $\bar{g}_i(x,y)$ it is possible to obtain a smoothed result formed for an image $\bar{g}(x,y)$ by averaging M differerent noisy images from the relationship,

$$\bar{g}(x,y) = \frac{1}{M} \sum_{i=1}^{m} g_i(x,y)$$

it follows that $E\{\bar{g}(x,y)\} = f(x,y)$

$$\text{and} \quad \sigma^2_{\bar{g}(x,y)} = \frac{1}{M} \sigma_n{}^2_{(x,y)}$$

where $E\{\bar{g}(x,y)\}$ is the expected value of $\bar{g}$,

and $\sigma^2_{\bar{g}(x,y)}$ and $\sigma^2_{n(x,y)}$ are the variances of $\bar{g}$ and n all at co-ordinates (x,y).

The standard deviation at any point in the average image is given by

$$\sigma_{\bar{g}(x,y)} = \frac{1}{\sqrt{M}} \sigma_{n(x,y)}$$

This indicates that as M increases, the variation of the pixel values decrease. Since E $\{ \bar{g}(x,y)\} = f(x,y)$, this would indicate that $\bar{g}(x,y)$ will approach f(x,y) as the number of noisy images used in the averaging process increases. However, the main problem with this technique is the ability to register the images, in order for these corresponding pixels to line up correctly. In addition, the amount of time necessary to achieve this is long.

A problem encountered in the execution of this function is the fact that it will only function in one particular part of the frame memory. Therefore, if more than one averaged image is required (as in this case, one "Perfect" and another with a "Defect"), it is necessary to copy the first averaged image into another part of the frame memory, before obtaining the second. However, in addition to this, another problem is encountered in that, any images stored in the frame memory, will be shifted in position. As a result of the wrap around nature of the frame memory, an image on the right will, when shifted, re-appear on the left of the frame memory. When investigated, it was found that when the second averaged image was captured, the first stored image shifted in a proportion related to the number of averages taken in total for both images.

Providing, the number of averages for each scene is known, and therefore the total for the two, the total shift can be determined and hence the exact location of the first image is the frame memory. The subtraction function may then be applied.

With the use of this averaging function (essential in minimising the visual noise), the thresholding function was found to be inoperative when used in conjunction with the averaging function. However, an alternative method of thresholding was found and discussed later in this chapter.

5.4 Image Alignment

A problem with this technique of image subtraction is the necessity for both images to align with one another. This is impossible to guarantee but can be solved by shifting and rotating one of the images to align with the other. Picking identical reference points on each of the two images would not only give the amount necessary to shift one image to align with the other, but also a suitable reference point for producing the subtracted image.

Rotating the image would be more of a problem. The library of image processing functions provided, to be used with the image processor, included a rotation function. This however, was found to be unsuitable since the resultant rotated image was distorted in shape. The rotating routine did not take the aspect ratio into account. For this reason, a new rotating function had to be derived, taking the aspect ratio into account.

5.4.1 Aspect Ratio

It is essential when analysing an image, to be able to correlate a relationship or ratio between the absolute dimensions of an item and the image of that item viewed by a camera, with its magnification and aperture settings. This was discussed earlier in obtaining the parameters essential for this technique.

The aspect ratio is also required, since the image is comprised of a large number of picture elements (pixels), which are not square in shape but rectangular. With the use of image manipulation such as rotation, the aspect ratio is required to ensure the image does not distort in appearance. A ratio between the vertical and horizontal component in pixel terms is required and is known as the aspect ratio.

5.4.2 Rotation Theory

Consider a real world co-ordinate set xw, yw and an image thereof;

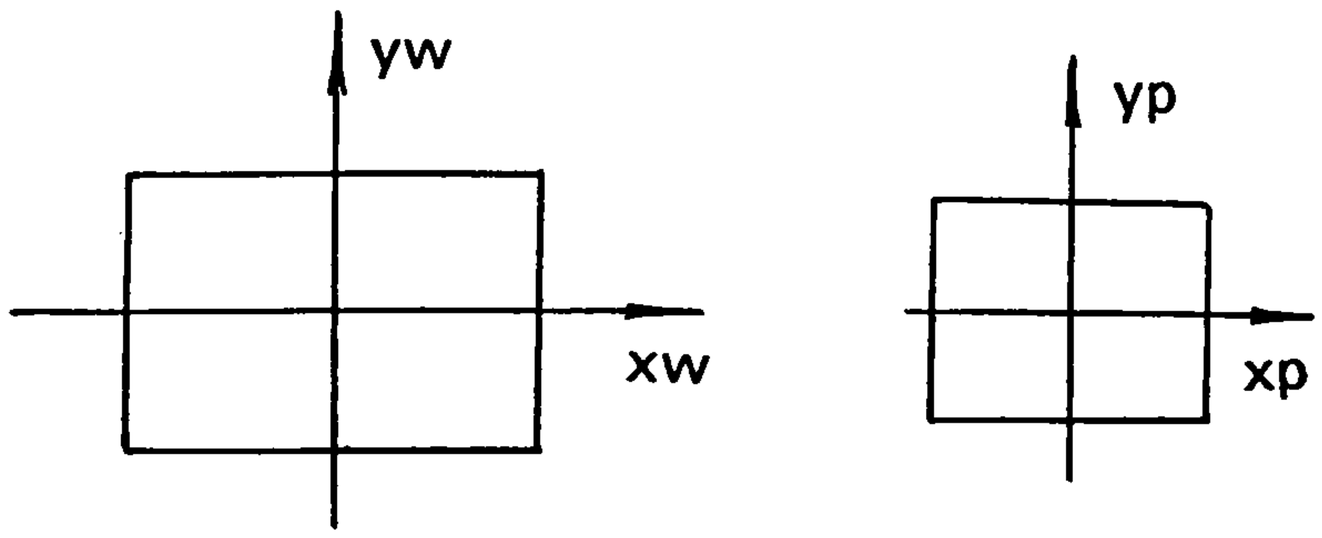

The relationship is;

$$yp = sy.yw \text{ and } \quad xp = sx.xw \tag{5.1}$$

where sy and sx are the x and y scaling factors

and $\frac{sy}{sx}$ = camera aspect ration α

Rotating the world set by θ then;

$$\begin{aligned} y'w &= yw \,.\, \cos\theta - xw \,.\, \sin\theta \\ x'w &= yw \,.\, \sin\theta + xw \,.\, \cos\theta \end{aligned} \tag{5.2}$$

Where (x'w,y'w) are the co-ordinates in the post-rotated world set.

From equations (5.1)

$$y'w = \frac{y'p}{sy} \quad \text{and} \quad x'w = \frac{x'p}{sx}$$

Where (x'p,y'p) are the point co-ordinates in the post-rotated set.

Therefore,

$$\frac{y'p}{sy} = yw \cdot \cos\theta - xw \cdot \sin\theta \qquad (5.3)$$

$$\frac{x'p}{sx} = yw \cdot \sin\theta + xw \cdot \cos\theta$$

so,

$$\frac{y'p}{sy} = \frac{y'p}{sy} \cdot \cos\theta - \frac{xp}{sx} \cdot \sin\theta \qquad (5.4)$$

$$\frac{x'p}{sx} = \frac{y'p}{sy} \cdot \sin\theta + \frac{xp}{sx} \cdot \cos\theta$$

Which may be simplified to;

$$y'p = yp \cdot \cos\theta - \frac{sy}{sx} \cdot xp \cdot \sin\theta \qquad (5.5)$$

$$x'p = yp \cdot \frac{sx}{sy} \cdot \sin\theta + xp \cdot \cos\theta$$

Simplified further, letting $\alpha = \frac{sy}{sx}$

The relationship for the local co-ordinate system taking the aspect ratio into account is;

$$y'p = yp \cdot \cos\theta - \alpha \cdot xp \cdot \sin\theta \qquad (5.6)$$

$$x'p = \frac{yp}{\alpha} \cdot \sin\theta + xp \cdot \cos\theta$$

With the expressions (5.6) for the local co-ordinate system derived, it may

now be possible to produce a correctly rotated image, taking the aspect ratio into account. With the aid of a cursor routine, the operator can decide whether or not the image to be analysed is required to be rotated. If this is the case, the cursor function is used again, to indicate the area of the image to be rotated. The diagonal corners of a window are chosen before the new co-ordinates are calculated in the rotation function.

Basic Rotation Algorithm.

Rotation ()
{
Calculate from old co-ordinates (x1,y1), the new co-ordinates (x2,y2) of a new rotated image taking the aspect ration into account.

Copy the pixel value of the old co-ordinate (x1,y1) into the new co-ordinates (x2,y2) in a different part of the frame memory.

Repeat process for next pixel in the window
}

However, an additional problem is encountered, due to the rounding off errors caused in converting double precision floating point values into integers. The resulting effect of this, is an image with pixels at various intervals with no data. An example of which is demonstrated in Figure 5.13 and 5.14.

Various alternative solutions were investigated, one of which included averaging the pixel values around a central pixel, another the most common pixel value, but the most suitable was found to be interpolate the new pixel values. The theory of which is explained in the following section.

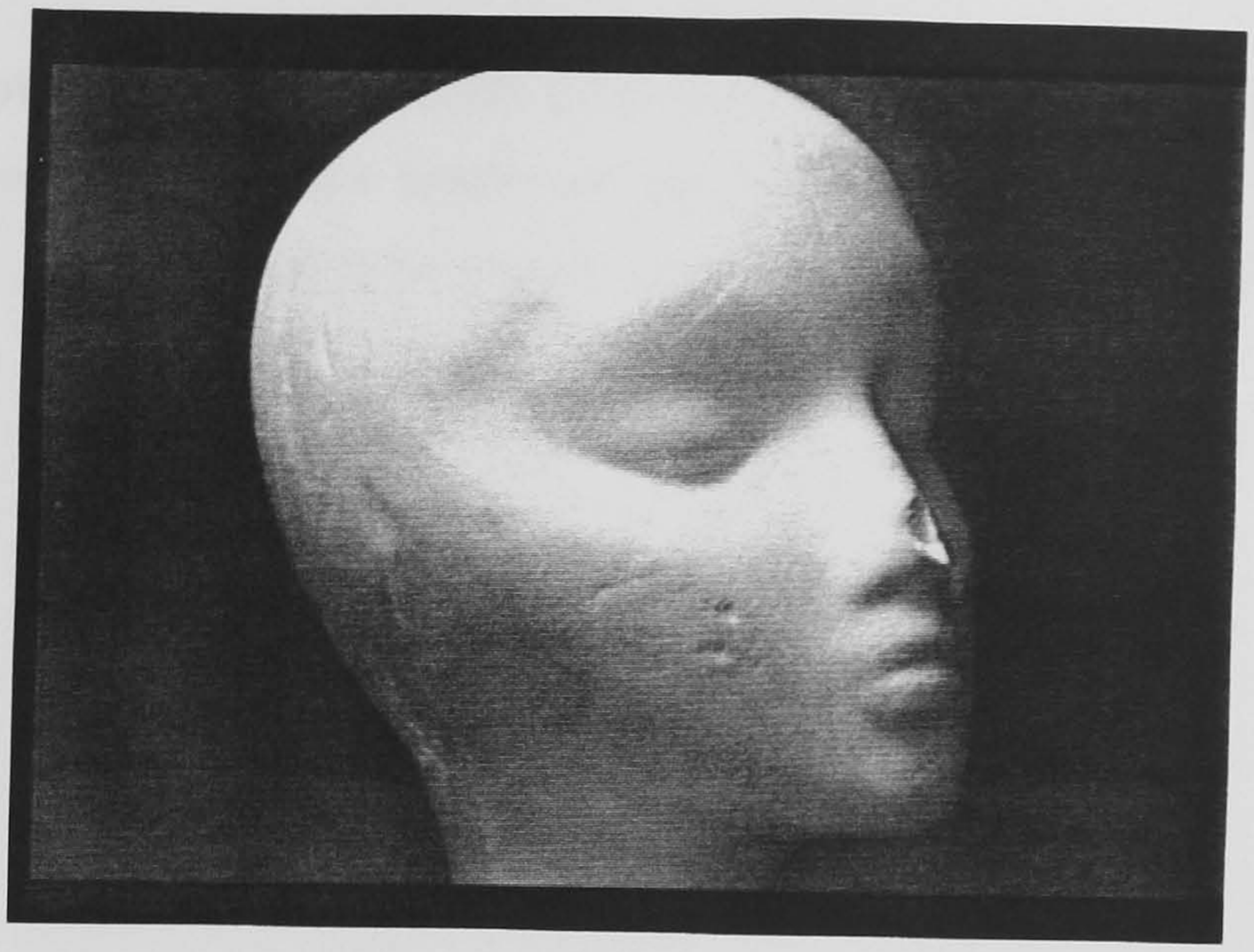

Figure 5.13 Image to be rotated

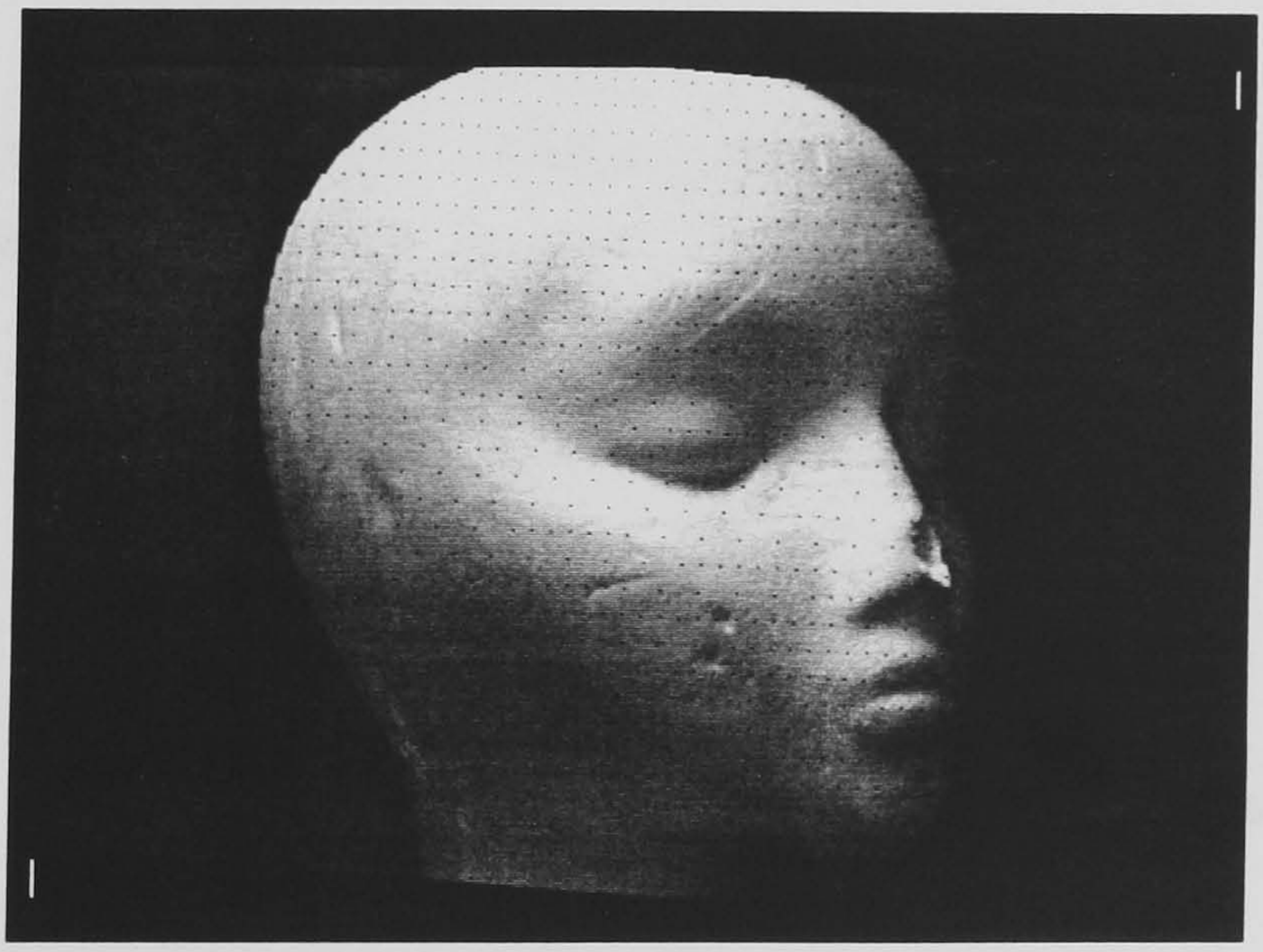

Figure 5.14 Image rotated with missing data

5.4.3 Linear Interpolation

Consider a pixel P(i,j) of unknown pixel value but known location, centred in any region between four neighbouring pixels, the centres of which are indicated by A, B, C, and D of known pixel values and co-ordinates.

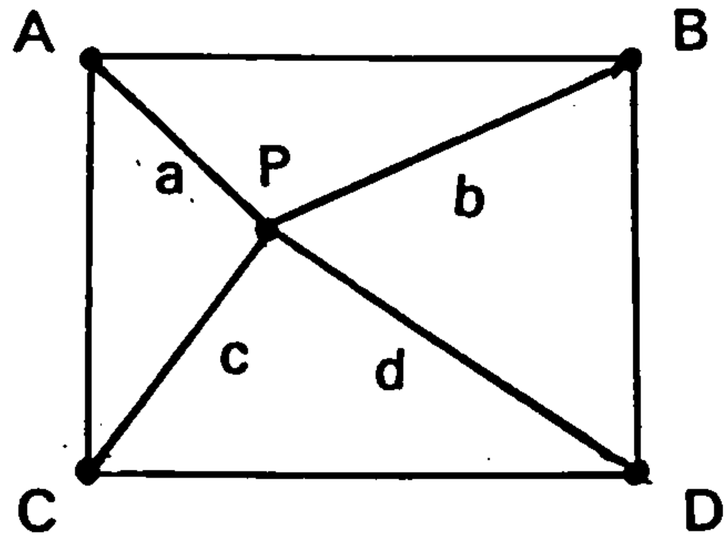

The nearer the point P is to A, B, C, and D, the nearer the unknown pixel of P(i,j) is to A, B, C, or D, and also the smaller the distance from point P to either point A, B, C or D. It is for this reason, that an expression may be derived, to take this effect into consideration, by multiplying the pixel value at A, B, C, or D, to its corresponding distance a, b, c, or d but as an inverted percentage of its inverted sum.

i.e. Pixel Value at P. = PvA.a + PvB.b + PvC.c + PvD.d
(i.e Pv (i,j))

where Pv = Pixel Value at A, B, C or D.

and a, b, c, or d = Weighted inverted value of distance from point P to either A, B, C or D.
- the greater the distance away, the less the effect.

i.e. Weighted value (for a, b, c, or d) $= \frac{1/n}{\sum 1/n}$

where n = a, b, c, or d and $\sum 1/n$ = sum of a, b, c + d.

Similar to the previous rotation section, once the operator has indicted the area to be rotated (with the aid of a cursor routine), a new rotation function is executed, comprising a different algorithm and briefly described below.

Rotation with linear interpolation algorithm.
{

Calculate from old co-ordinates (x1,y1), the new co-ordinates (x2,y2) of a new rotated image taking the aspect ratio into account.

From the new co-ordinates (x2,y2) of a new rotated image, recalculate exact old co-ordinates (x3,y3) in double rather than integer.

Interpolate pixel from pixels around old co-ordinates (x3,y3), to be placed in new co-ordinates (x2,y2) in different part of frame memory.

Repeat process for next pixel in window

}

Figure 5.15(a) illustrates the new rotation with interpolation function, and figure 5.15(b) the difference between the two rotation functions (with missing data) .

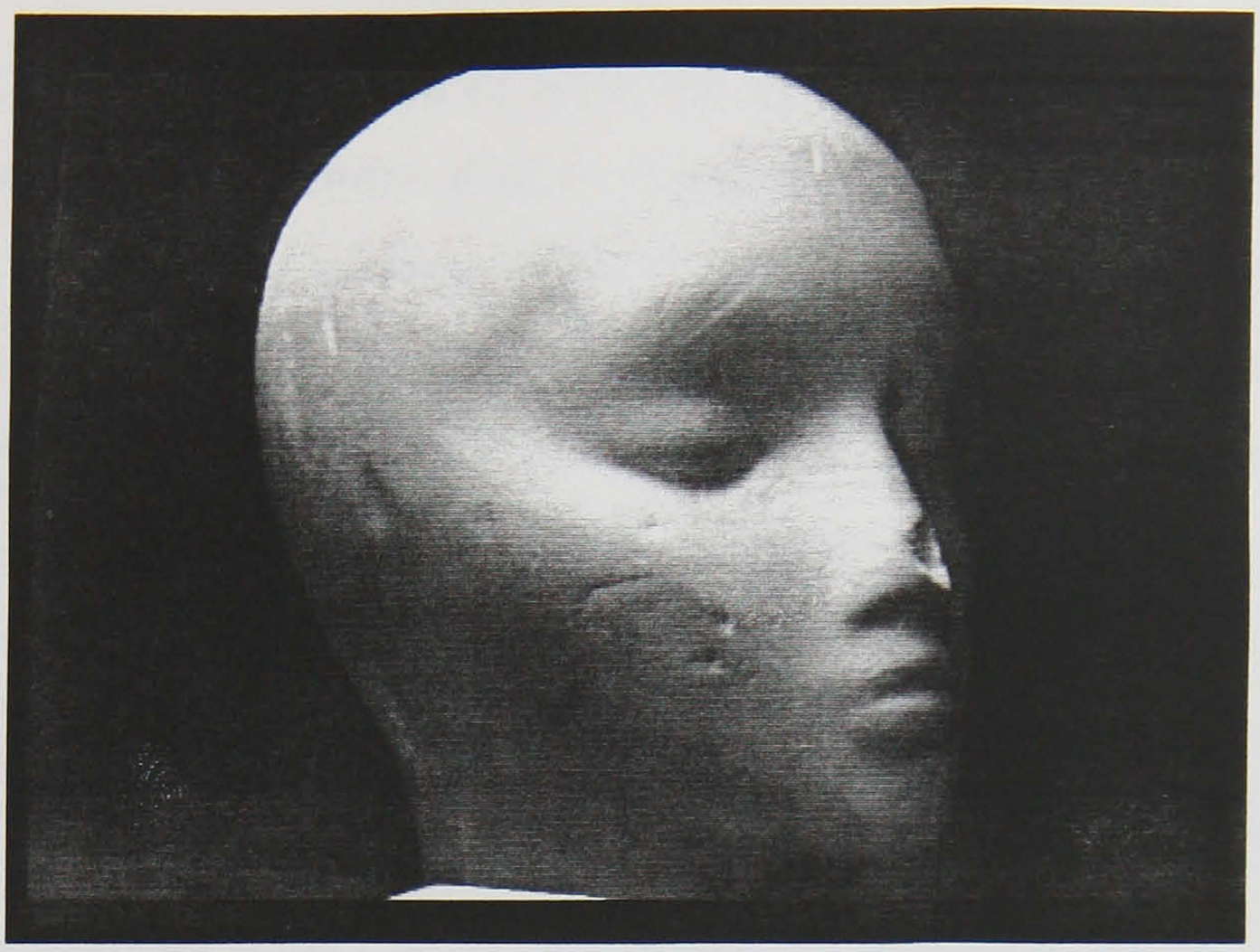

Figure 5.15(a) Rotation with interpolation

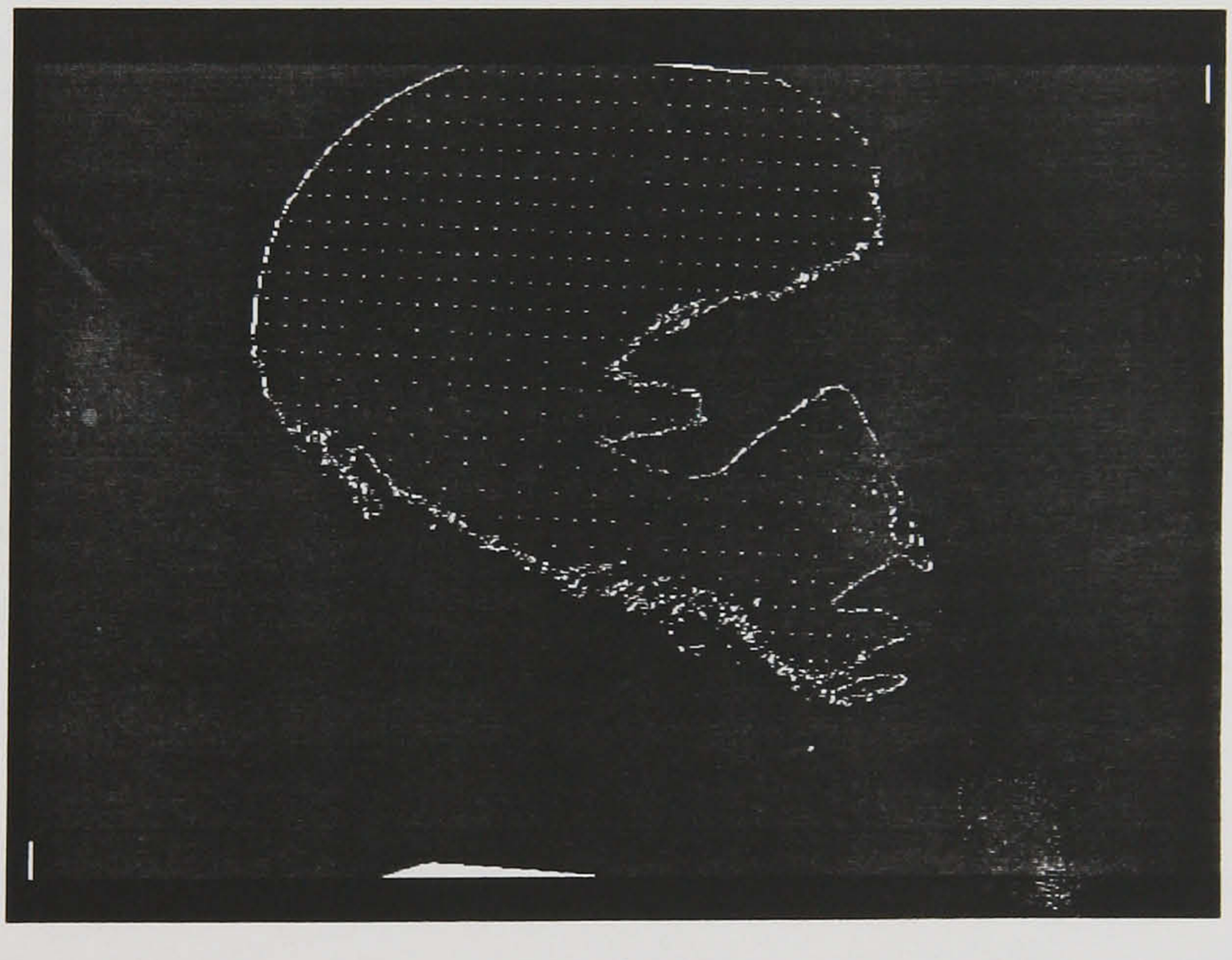

Figure 5.15(b)

Difference between the outputs of two rotation functions (indicating the locations of missing data)

5.5 Thresholding

It is essential for this technique to produce thresholded images to highlight the differences between them and to ultimately produce a final difference image. As stated in the previous chapter, a number of types of look-up tables (LUT) are available within an image processor, the use of which is an efficient means of applying transformations. This is due to the fact that altering the transformation characteristics, would only entail a new table to be loaded, and not the entire image. The employment of the use of an input LUT, to transform incoming data (ranging from 0 to 255) to threshold data (0 or 255), is the most efficient means of applying the thresholding function.

However, with the use of a new rotation function incorporating the interpolation of pixel data, it is important that the data stored in the frame memory is not thresholded (either 0 - black or 255 - white) but instead grey, ranging from 0 to 255.

The use of the thresholding function of an input LUT would therefore be unsuitable as described in the initial system for this technique, since the data stored in the frame memory is 0 and 255. Alternatively, the use of the three output LUT's would solve this problem, since the data in the frame memory is directly inputted from the camera (i.e. grey 0 - 255), and the outputted data displayed on the monitor is thresholded. However, this gives a false impression of the data stored. For these reasons the thresholding function is unsuitable.

As a result of calling the averaging function (to minimise the visual noise) the thresholding function became inoperative. Therefore in any case, the thresholding function is redundant.

Instead another method is required to achieve this. Since the grey data for both images is stored in the frame memory, the obvious solution is to read each individual pixel and then alter this accordingly to black or white once a suitable threshold level is found.

The functions used were:

a =	rpixel (i,j)	-	where the grey level of a pixel is determined at a specific i,j, co-ordinate and equal to parameter a.
b =	wpixel (i,j,c)	-	where the value in parameter c is written into a specific i,j co-ordinate location.

Although slower than the thresholding function, it is the most suitable solution available considering the problems encountered.

5.6 Real-time Image Subtraction

The basic method of image subtraction is to find the difference between one image and another and requires both images to be relocated in exactly the same position. This may not always be possible but is essential if comparisons are to be made of one item with another. For this reason, but also for the purposes of practical experimental repeatability, the use of real-time image subtraction was investigated. The use for which is not only for off-line measurement, ensuring that the item that is to be measured is as near as possible relocated in the same position as the stored perfect specimen, but also possibly on-line.

The routine loads the input and output look-up tables to subtract a 6-bit image acquired from a previously static image. The entire input LUT is modified to subtract a 6-bit image being acquired, from a 6-bit image previously stored in the top 6-bits of the frame memory and then take the absolute value of this result. The feedback multiplexer is set to subtract the two 6-bit images and the output LUT is modified to shift the resulting 6-bit image (to the left) two bits for display.

To perform this operation the top 6-bits of the frame memory are loaded with an image (the "standard" or "template" image) before this routine is called to set up the LUTs. The specified bank for display is selected by using the static_luts and setlut functions. Subsequent images for comparison are then acquired by the use of the grab function. The swap6 function is designed to swap the top 6-bits of the frame memory, with the bottom 6-bits of the frame memory, in one frame time. This is useful when using the frame memory as two 6-bit images and the images for display or processing need to interchanged, i.e. and the images for display or processing need to interchanged.

The images ultimately produced by this operation are bright where the two images are different, and dark where they are not.

Pseudocode Real-Time Subtraction.

```
Subtraction of 6-bit images real-time continuously from a stored image.
{
        Initialise and clear the hardware.
        Set board into static mode.
        Set input multiplexer to allow 6-bit input image
        to interact with 6-bit stored image.

        Input 6-bit stored image.

        Move this 6-bit image to the top 6-bits of the frame memory.

        Setup LUT with rtsubtract.

        Continuously grab 6-bit input image to show
        difference between it and stored image.

        Quit when required.
}
```

5.7 Histogram

The technique's requirement for both images to align with one another, as described earlier in the real-time subtraction section, led to the investigation of the use of this function in generating a histogram. The purpose for the call of this function is combination with real-time subtraction, is to give a graphical representation, i.e. A histogram plot of the difference between the continuous 6-bit input from the camera and the stored images, to give an indication of as near relocation as possible.

The procedure generates a histogram by sampling the points within the indicated area. Executed together with text and graphical functions, the histogram sample function generates a histogram of the number of pixels plotted against the intensity values (ranging from 0 to 255), an example of which is demonstrated in Figure 5.16.

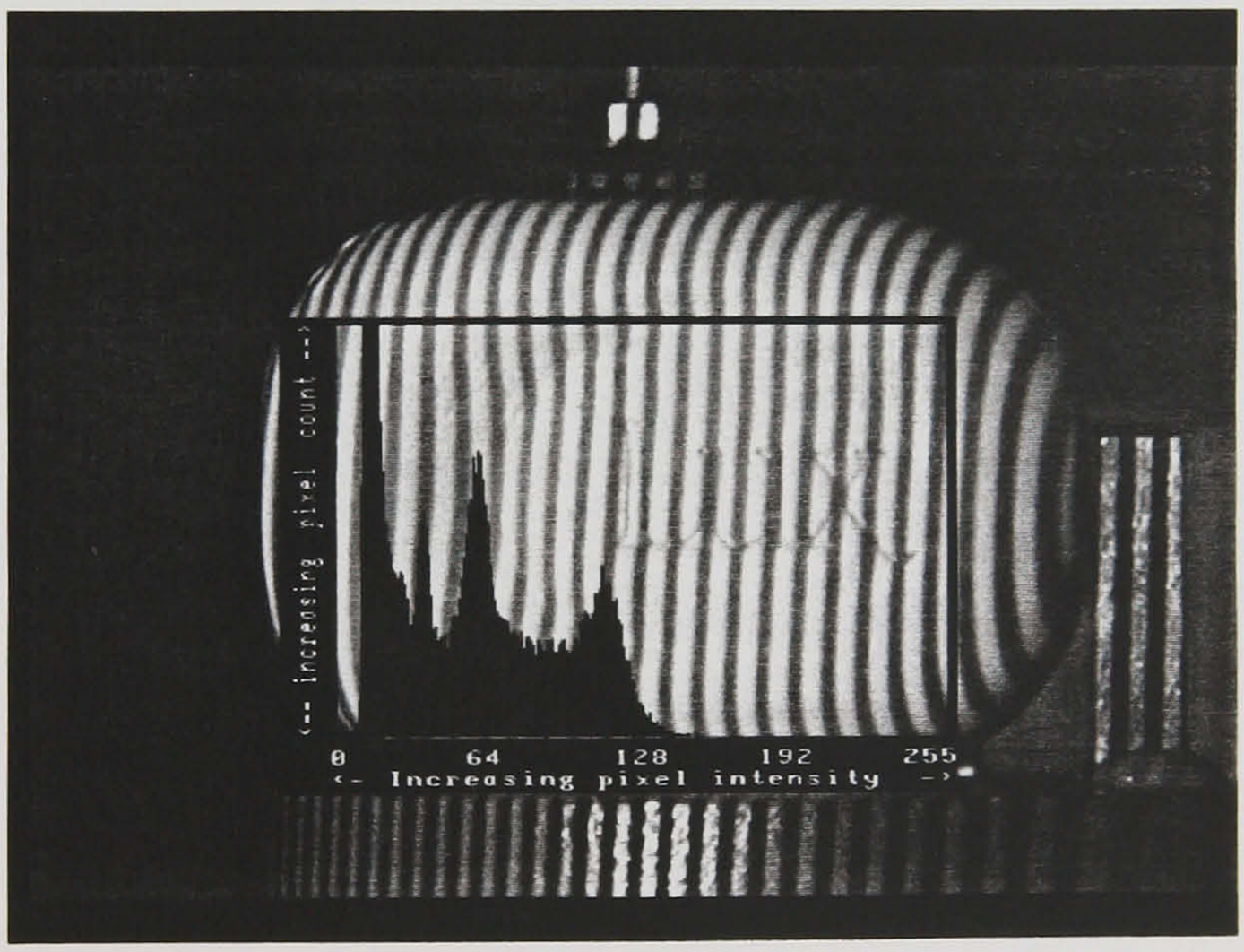

Figure 5.16 Histogram example

5.8 Fringe Alignment

Although the two images used in this comparison may be easily aligned with one another (with the use of a common reference point), the problem still exists in aligning the fringes on the image with one another. This is impossible to achieve. It may however be possible to analyse the subtracted image and intelligently distinguish data due to fringe non-alignment from data due to surface imperfections. Distinguishing the differences in these areas is difficult. As a result of the non-alignment of fringes, the resulting image will be striped in nature. As a consequence there will be a greater number of white pixels, uniformly distributed across the image, of the same width. (i.e. Figure 5.20(a) later in this chapter).

Due to the nature of the technique in detecting a height difference between the two surfaces used in the comparison (resulting in a fringe difference), it is essential that the fringes approximately align with one another. A large mis-alignment will result in too great a difference. As a consequence of which, useful data is lost in the mis-alignment data. Approximate relocation is sufficient on the condition that the fringes do not approach anti-phase with one another. At this most point, a completely white subtracted difference image of a surface would result. This would be unacceptable.

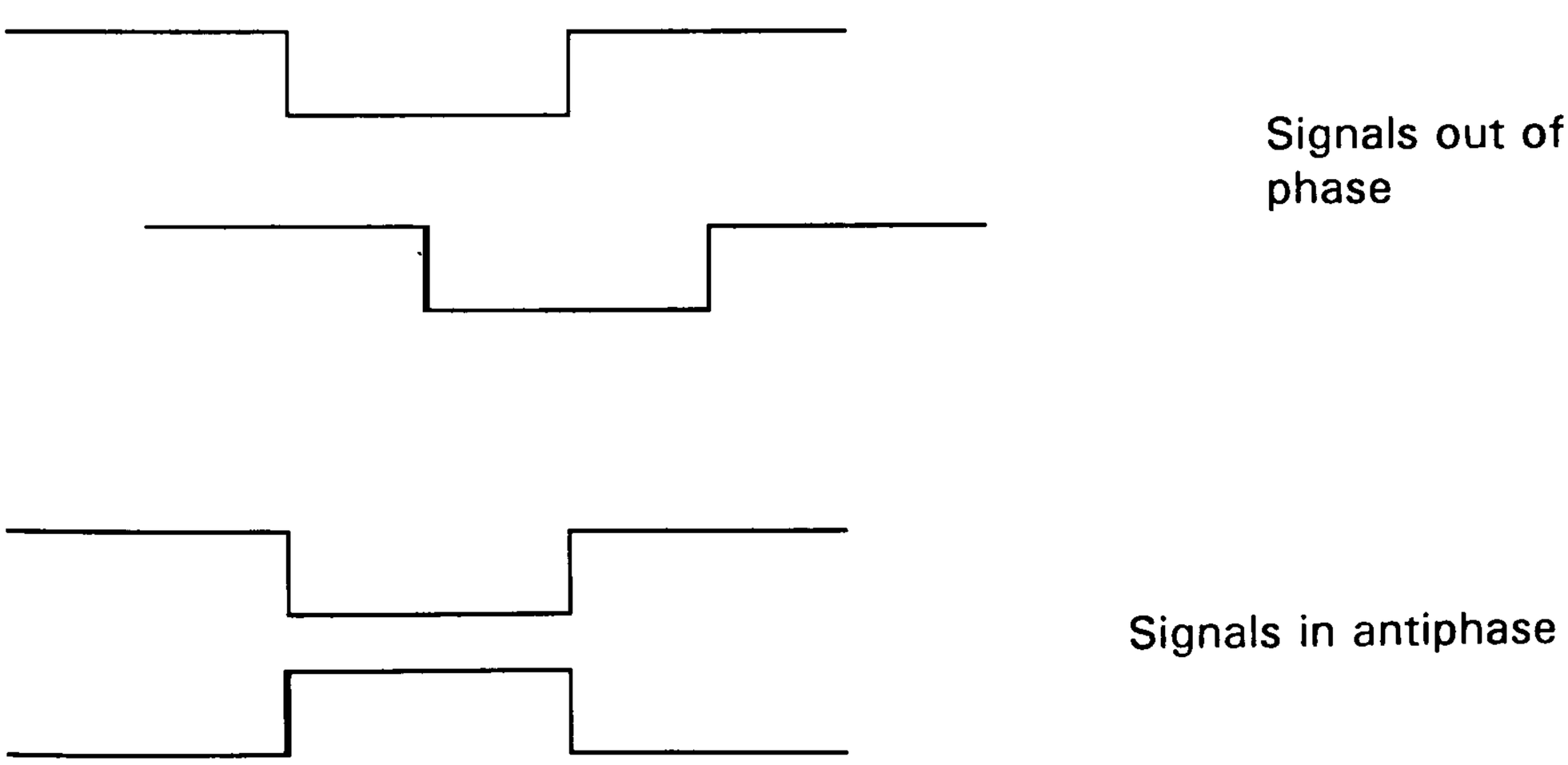

Figure 5.17 Sketch of Phase examples.

A variety of methods were investigated, with the most successful described in the following sections.

5.8.1 Sobel with Colour Edges

A solution investigated for this problem, involves the application of the Sobel edge operation in conjunction with the colour edges function. The purpose for which is to highlight the difference in the fringe data due to misalignment and that due to surface flaws. It was hoped that misalignment data would have a predominant direction and hence colour. Enabling a distinction to be made (see below).

The Sobel edge or orientated edge operation results in an encoded pixel representing the edge of orientation and strength. The Sobel uses the following pair of 3 x 3 kernels to enhance edges of objects within the selected area.

Kernels.	-1	0	1	1	2	1
	-2	0	2	0	0	0
	-1	0	1	-1	-2	-1

After processing each pixel through these kernels, this function applies additional non-linear algorithms to complete the strength and direction of each edge. The strength and direction information is stored in a pixel value as follows:

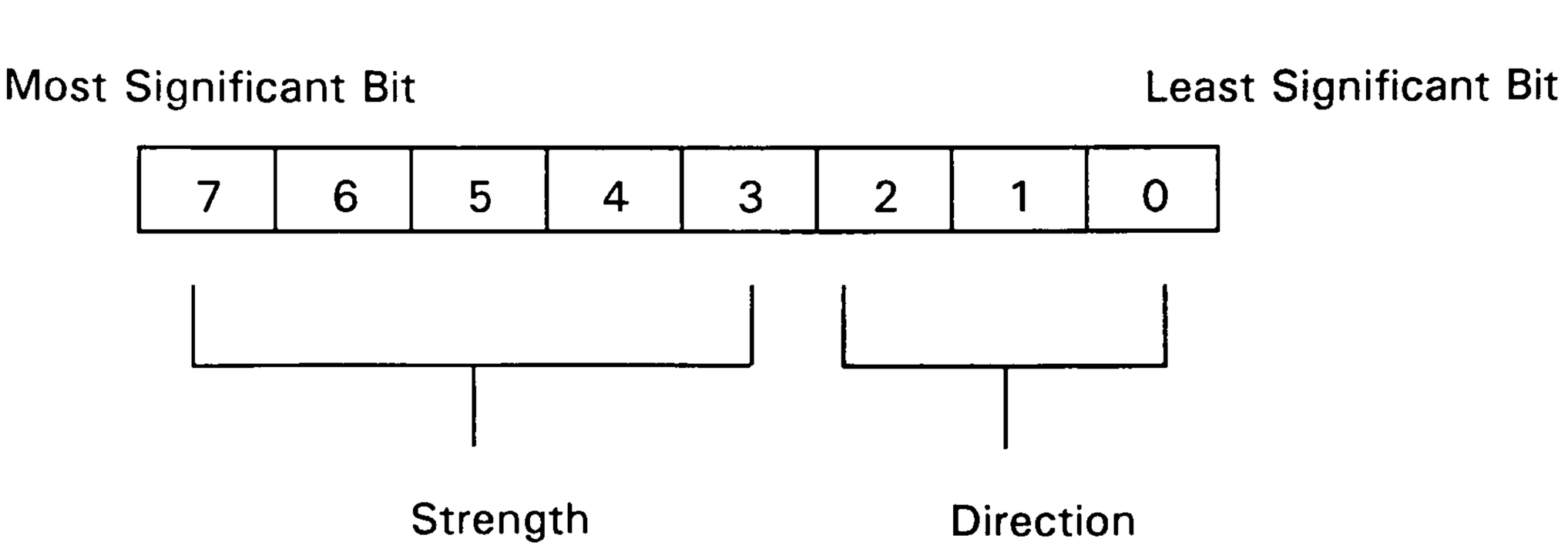

The operation can produce strength values between 0 and 2047, but only five bits (32 steps) are allowed for storage of this information. For this reason, the strength of the edge must be scaled before being stored in the pixel. The output edge strength is scaled by dividing the results by a factor. For example, if this factor is 16, then this output edge strength is divided by 16. The scaled edge strength is truncated to five bits. The direction is encoded in bits 0 to 2. This provides eight possible directions. Using the colouredges () function to illuminate the edges of the image enhanced by the Sobel operation.

The Sobel operator enhances edges in eight directions, similar to the points of a compass:

NW	N	NE
W		E
SW	S	SE

The colour edges procedure applies a distinct colour to each edge detected, as follows:

Yellow-Green	Yellow	Orange
Green		Red
Blue-Green	Blue	Violet

The edges found with the Sobel operator are colour-coded according to their orientation and intensity-coded ascending to the intensity (sharpness) of the edge. To do this, the selected bank of output LUT is modified. This modifies all areas of the screen, even if the Sobel is only applied to a part of the screen.

Applied to the resultant subtracted image, this technique did not enable it to be possible to distinguish data due to misalignment, and data due to a defect, as was first thought. Data in the least significant bits of the Sobel edge, were of the same direction and when shown with the aid of the colouredge function, were clearly the same colour. The only visible

difference indicated by the length of the edge. For this reason another method had to be investigated.

5.8.2 Window Method Filter

This method of analysis, involves comparing a fixed size of a window of pixels, throughout an image, analysing data from one window and then the next. The number of pixels that are white are counted, with the inclusion of a suitable inequality statement, for instance less than a certain number of pixels are white, then alter the central pixel to a value equivalent to black. This has the effect of thinning areas of very few white pixels, leaving areas of significant white pixels alone.

Pseudocode Window Method.

```
Main ( )
{
    Analyse subtracted image.

    Shift from one pixel to next down.

    Analyse window of pixels around this central pixel.

    Count the number of pixels with values equal to 255 . (White)

    If this number if less than a value 4 for instance,
    change middle value to black.

    Continue to next central pixel.
}
```

5.8.3 Row and Column Method Filter

With this technique, the basic principle involves a line of pixels being analysed and counted vertically. If a certain proportion are white, indicating data due to fringe shift (misalignment) or a defect, another line across is analysed. Again, if a certain proportion is white, the probability is that it would be due to a defect and not a misalignment. The relevant pixel is then copied to a different part of the frame memory and the process continued for the next pixel. On completion of this process a second image is produced, containing only data thought to have a high probability of being due to a defect.

Further additional adaptions may be made to enhance the speed. This involved analysing a line of white pixels continuously vertically until black value data is encountered. Again, additional horizontal data is analysed if certain inequalities are met. Altering these inequalities and the relevant conditional values would result in either data for fringe or defect data to be copied into a different area of the memory.

Although the idea of distinguishing data due to misalignment from defect data appears difficult, this simple method apparently efficiently achieves this objective successfully. As may be shown in the following results over a range of images with different fringe misalignment displacements and defects.

Pseudocode Row and Column Method.

Main ( )

{

Analyse subtracted image.

Shift from one pixel to next down.

Analyse line of pixels down, counting
the number of white pixels

If this value is less than a value of 4,
then analyse line across, keeping count of white pixel data

If this value is less than a value of 4,
the copy relevant pixel to different point of frame memory.

Continue to next central pixel.

}

5.8.4 Comparison of Filter Method

Tests were performed to observe the effects of the different filtering techniques on various subtracted images, with different degrees of misalignments. These are demonstrated in Figure 5.18, of a defective soap bar with slight misalignment, Figure 5.19, of a soap bar shifted a more significant amount, and finally Figure 5.20, a large shift.

As may be observed in the photographs produced in Figures 5.18(b) to 5.18(c), the filtered images from the different methods, successfully distinguish small fringe mis-alignments from the defect areas. The latter (Figure 5.18(c)) being more successful in distinguishing the defect area.

In the case of a larger misalignment of a defect free soap bar, as shown in figures 5.19(a) to (c), it may be observed that the window filter failed to totally eliminate data due to misalignment, figure 5.19(b). However. the row and column sucessfully achieved the task, figure 5.19(c).

The last two photographs, figures 5.20(b) and 5.20(c), show an even larger shift, which is not very successfully filtered out by either technique.

This may not be so important, since the magnitude of the misalignment has lost a significant amount of height data, essential if comparisons are to be made. Retesting the item to be measured would be a better option, ensuring the fringes are not misaligned as much.

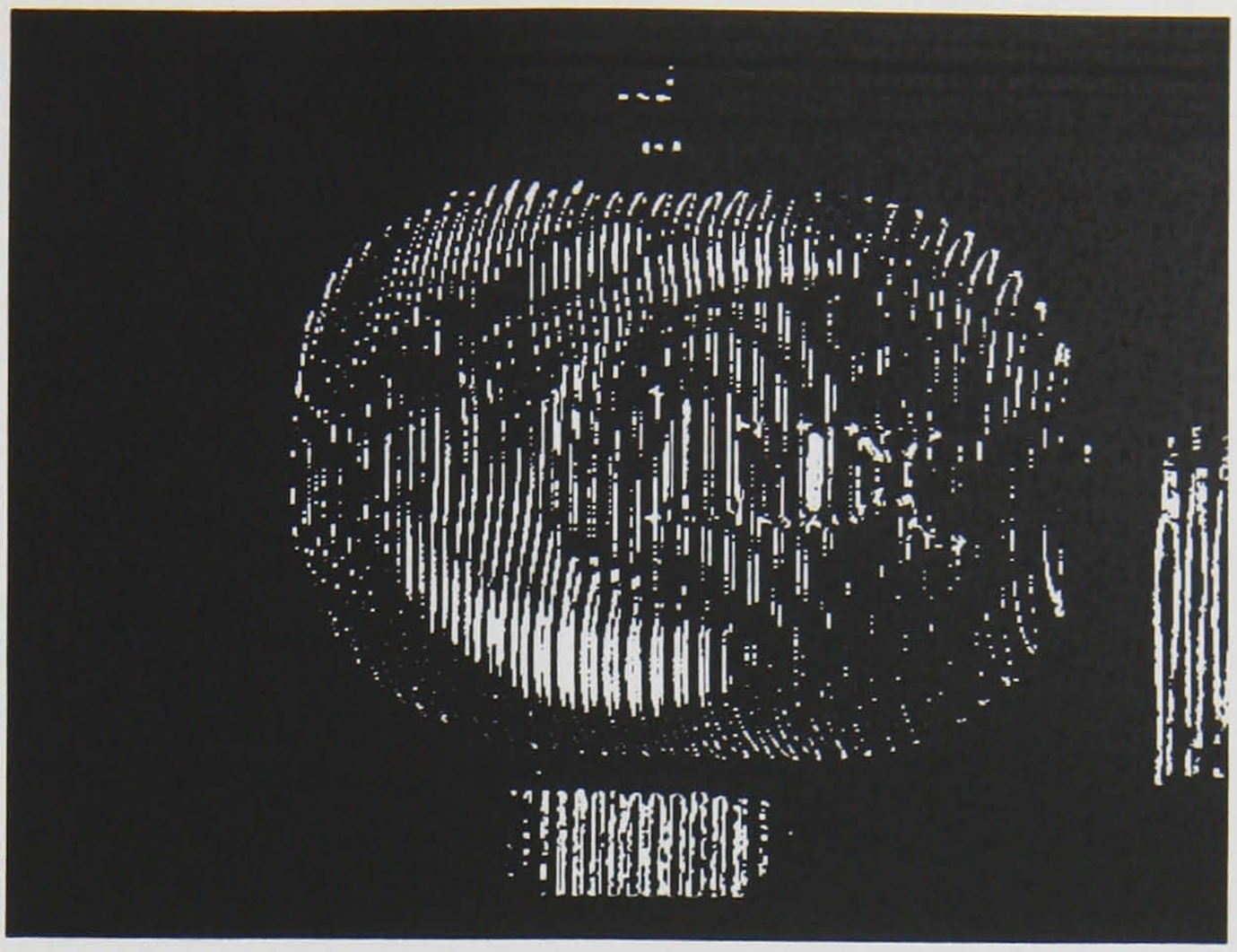

Figure 5.18(a) Defect and small misalignment

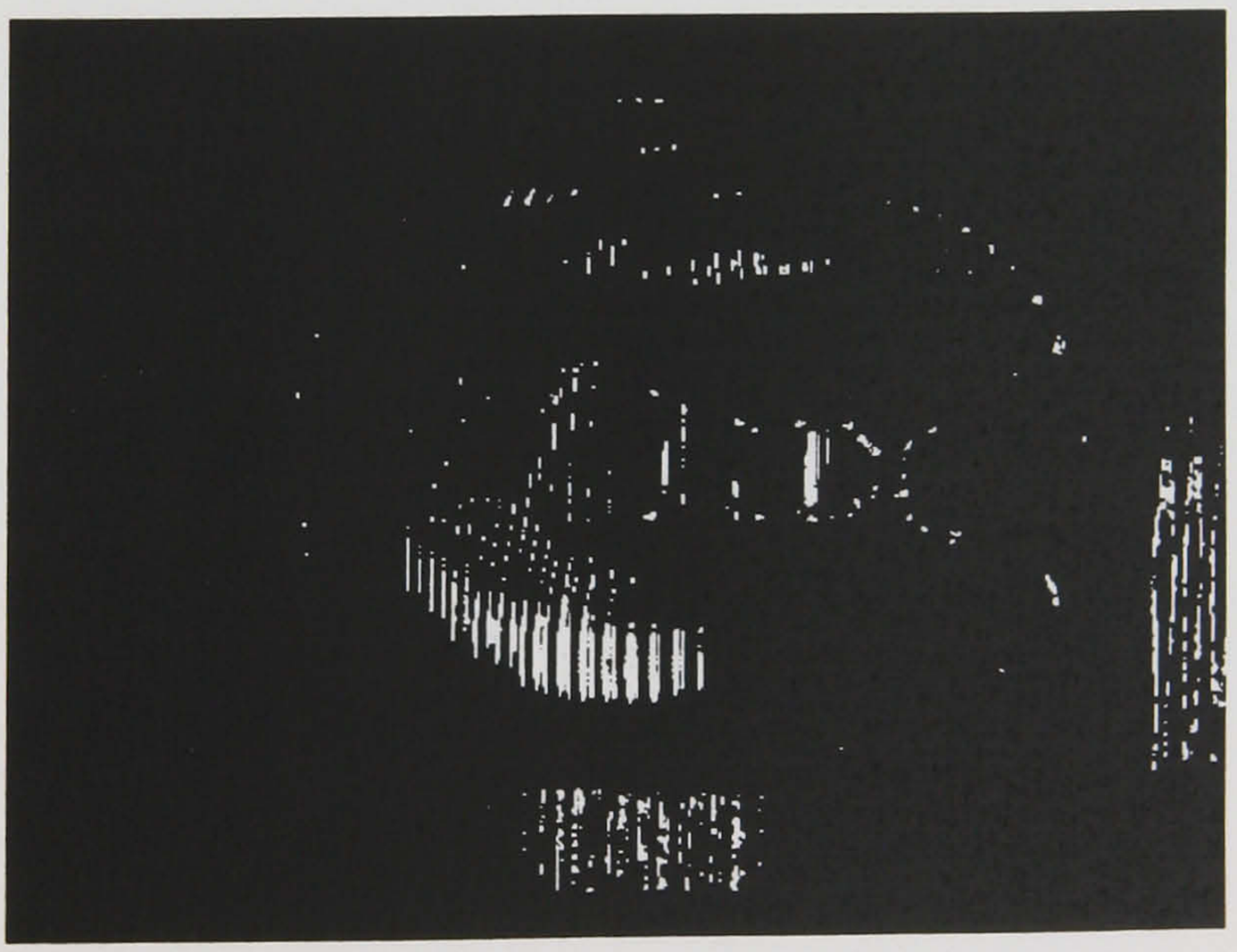

Figure 5.18(b) Analysed window filter method

Figure 5.18(c) Analysed row and column filter method

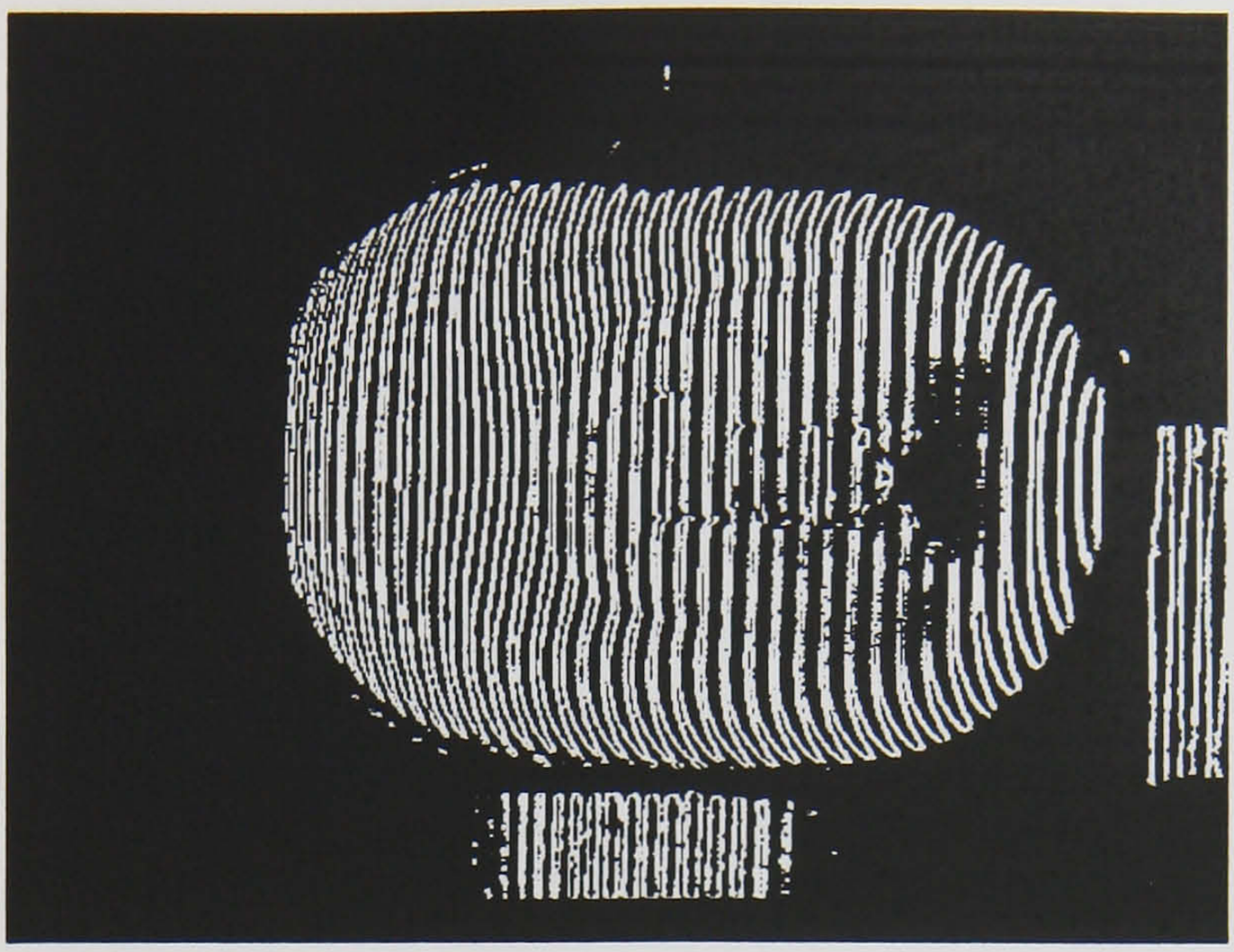

Figure 5.19(a) Defect and medium misalignment

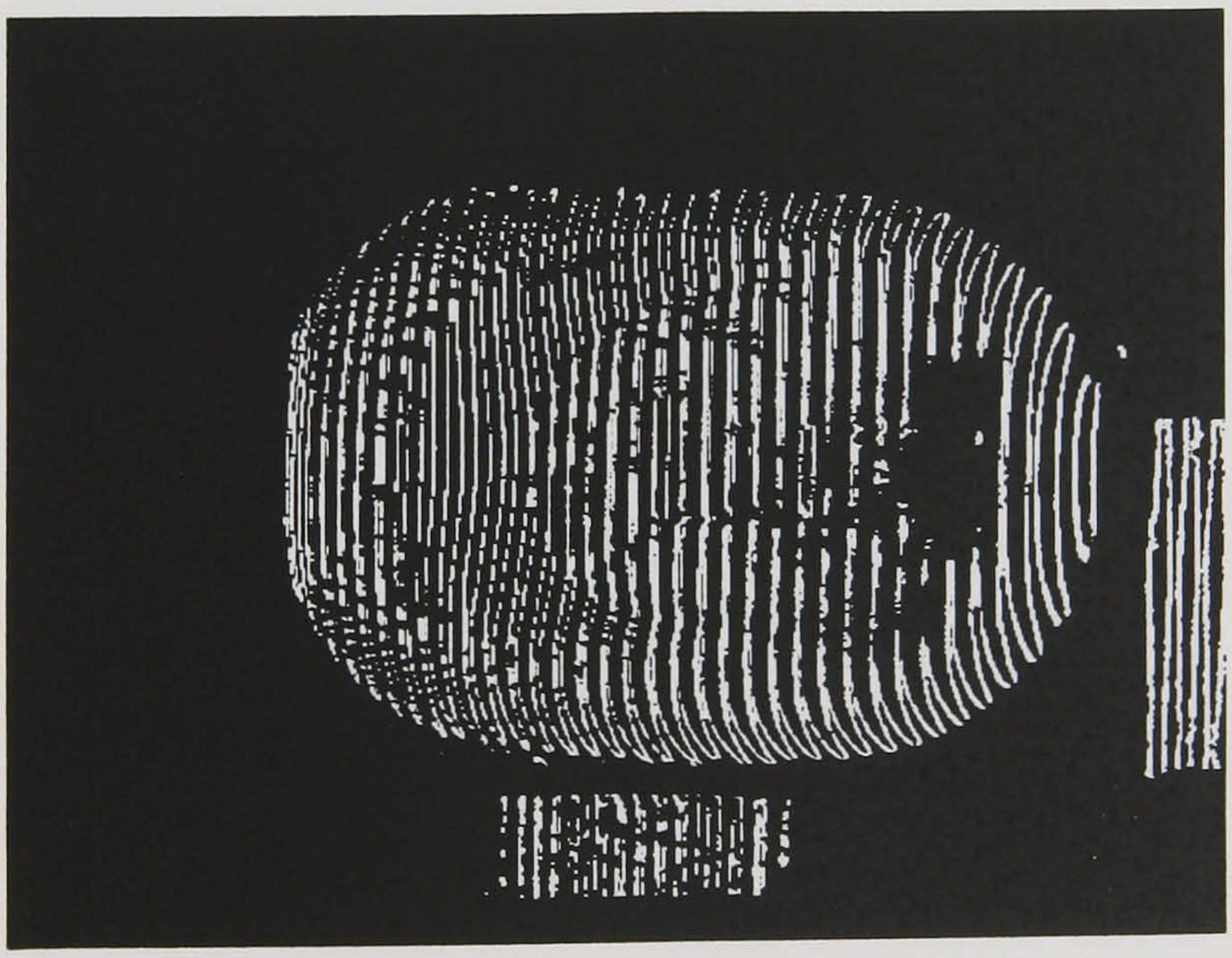

Figure 5.19(b) Analysed window filter method

Figure 5.19(c) **Analysed row and column filter method**

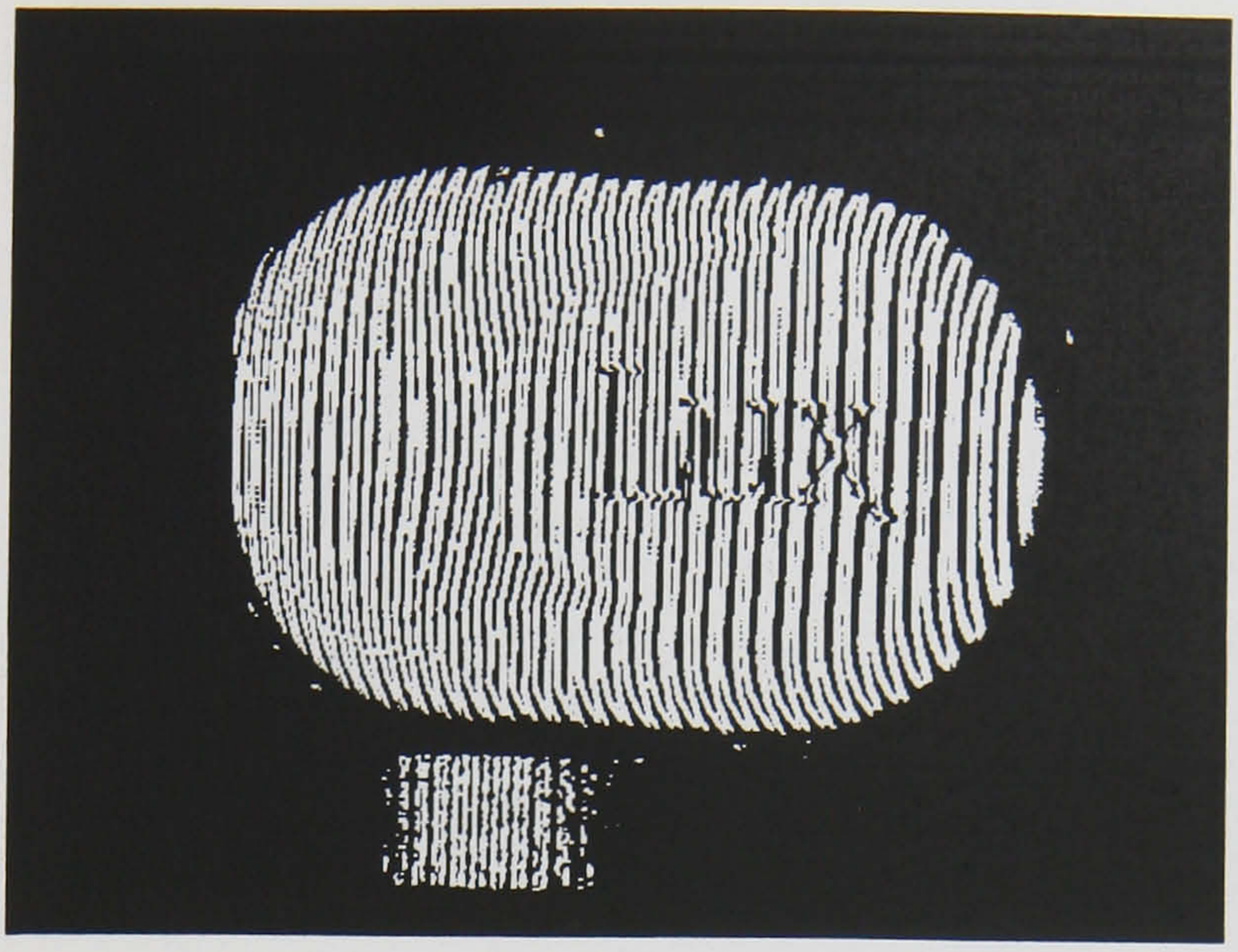

Figure 5.20(a) Defect and large misalignment

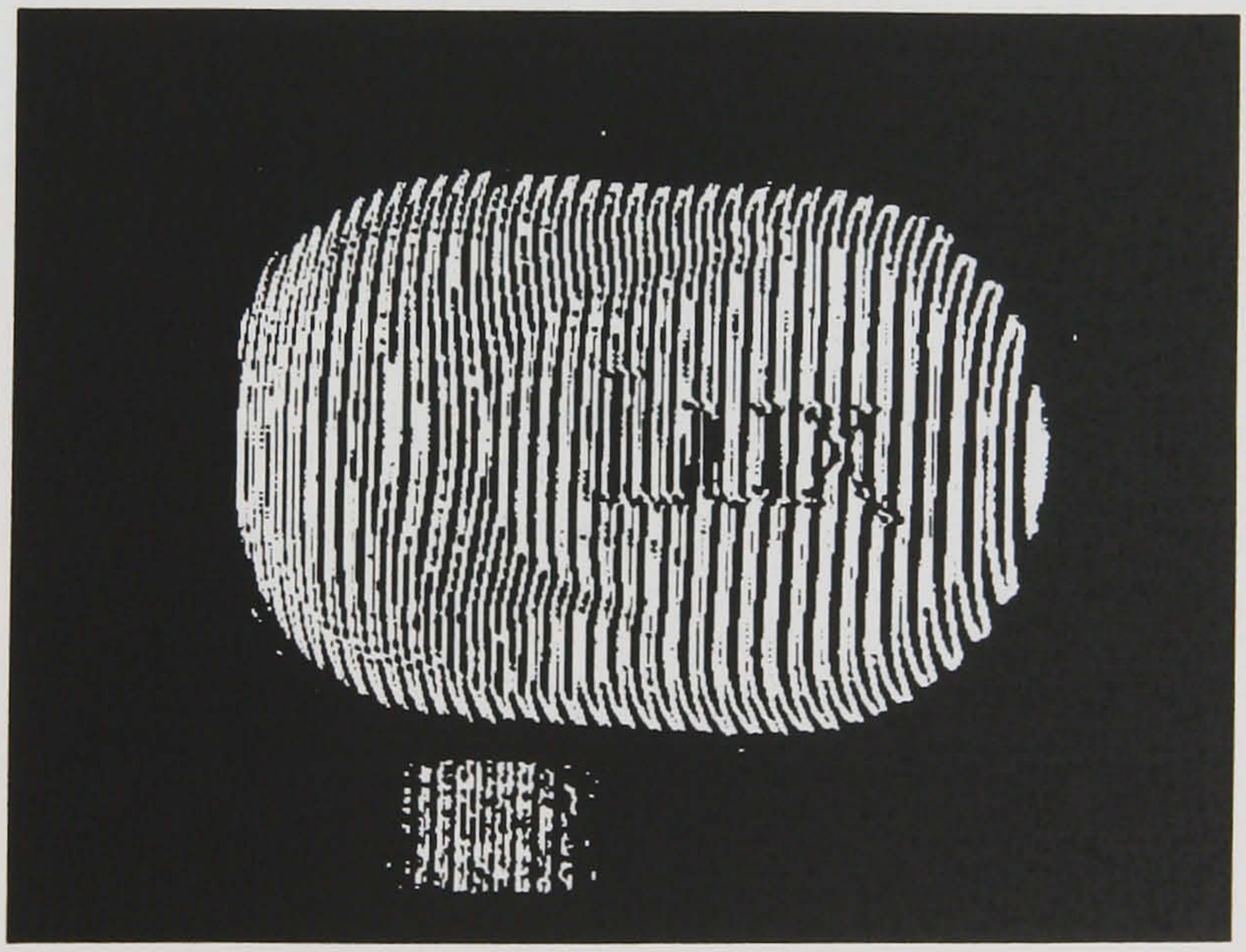

Figure 5.20(b) Analysed window filter method

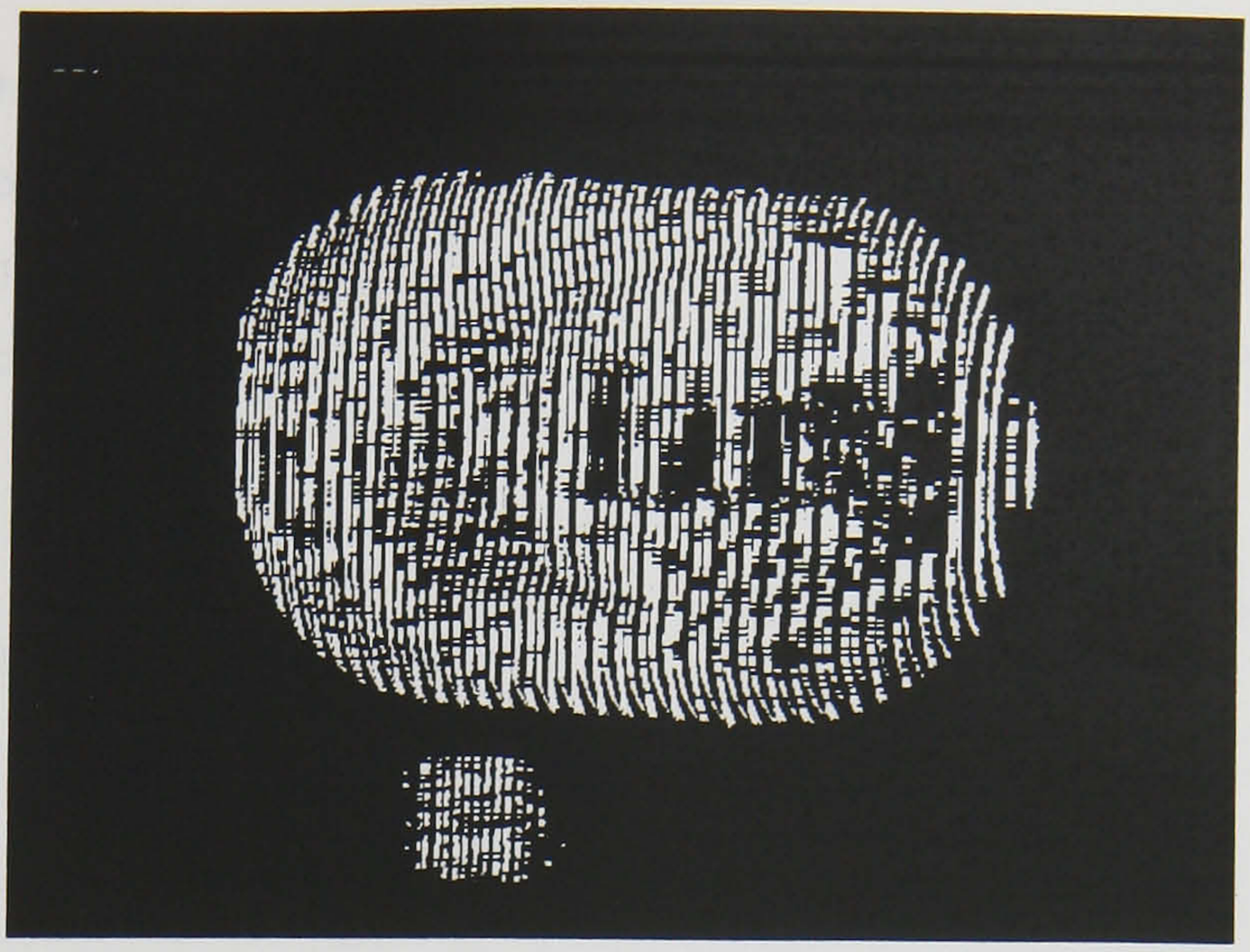

Figure 5.20(c) **Analysed row and column filter method**

5.9 Adapted Method

A solution to the problem of fringe alignment is instead of the projection of black and white fringes onto the surface and viewing from an angle, is to view a black and white fringe grating placed directly against the surface (see Figure 5.21). In terms of optical arrangement this is a shadow moiré system.

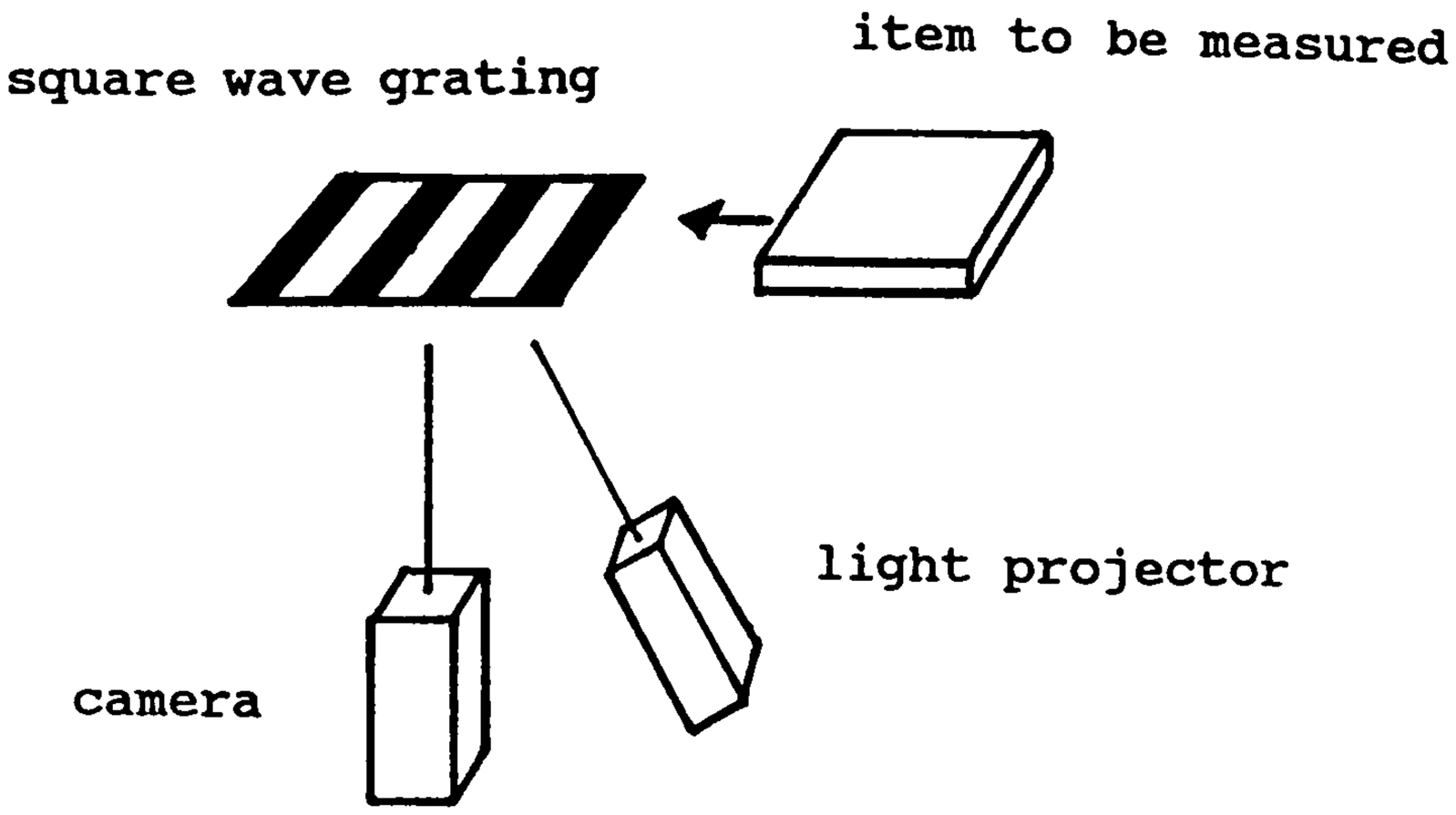

Figure 5.21 Adapted fringe grating setup

The effect would be similar to the fringe projection system, with light projected at an angle through the grating placed against the surface to be measured causing a shadow. The subtraction of a master image, consisting of the grating on a flat plane, from the image of the grating and the surface to be measured, will give an estimate of the volume between the surface and grating. The additional refinements for this technique as discussed previously would be unnecessary.

The purpose of the master image in this case is to aid in the elimination of the fringe pattern from the second image. With this adapted method no data due to fringe misalignment will result, since the same fringe grating appears in both images, and one of the surfaces consists of a flat plane. In particular, the necessity of orientating the item to be measured, with that with which it is to be compared, is removed. Similarly, the filtering scheme

developed to distinguish useful data from misalignment data becomes redundant. Therefore, although optically the same as shadow moiré, the subsequent analysis is different.

Figure 5.22 shows a photograph of the alternative to the fringe alignment problem. The item to be measured is placed against the grating, to give a suitable reference, from which all subsequent measurements are made. This is a similar setup as the shadow moiré technique described in Chapter 2, but with the subtraction theory described in Chapter 4.

However, there are disadvantages to this method. These include the fact that this is no longer a non-contact method. It may prove impossible in the soap bar application, since damage may be caused to both the grating and the soap bar. Smearing onto the grating of the hot plastic soap may occur.

Similarly, an absolute measurement of the volume (between the grating and surface) is produced by this method, as compared to the original comparative method. The subtracted image produced from the original comparative method enabled only a surface defect to be clearly visible, as compared to the adapted method, where a difference is ever present. Difficulty may be encountered in the analysis of the result, since both defective and perfect samples will produce absolute volumetric values.

Another problem relates to the size of the grating required for a large item, which may be a hurdle too difficult to overcome.

This adapted technique may prove to be successful depending upon the type of application the system is applied to, where the grating is not large and contact is unimportant. Despite its problems and limitations, this adapted method is a success in eliminating the misalignment problem, enabling a real-time inspection system to be possible.

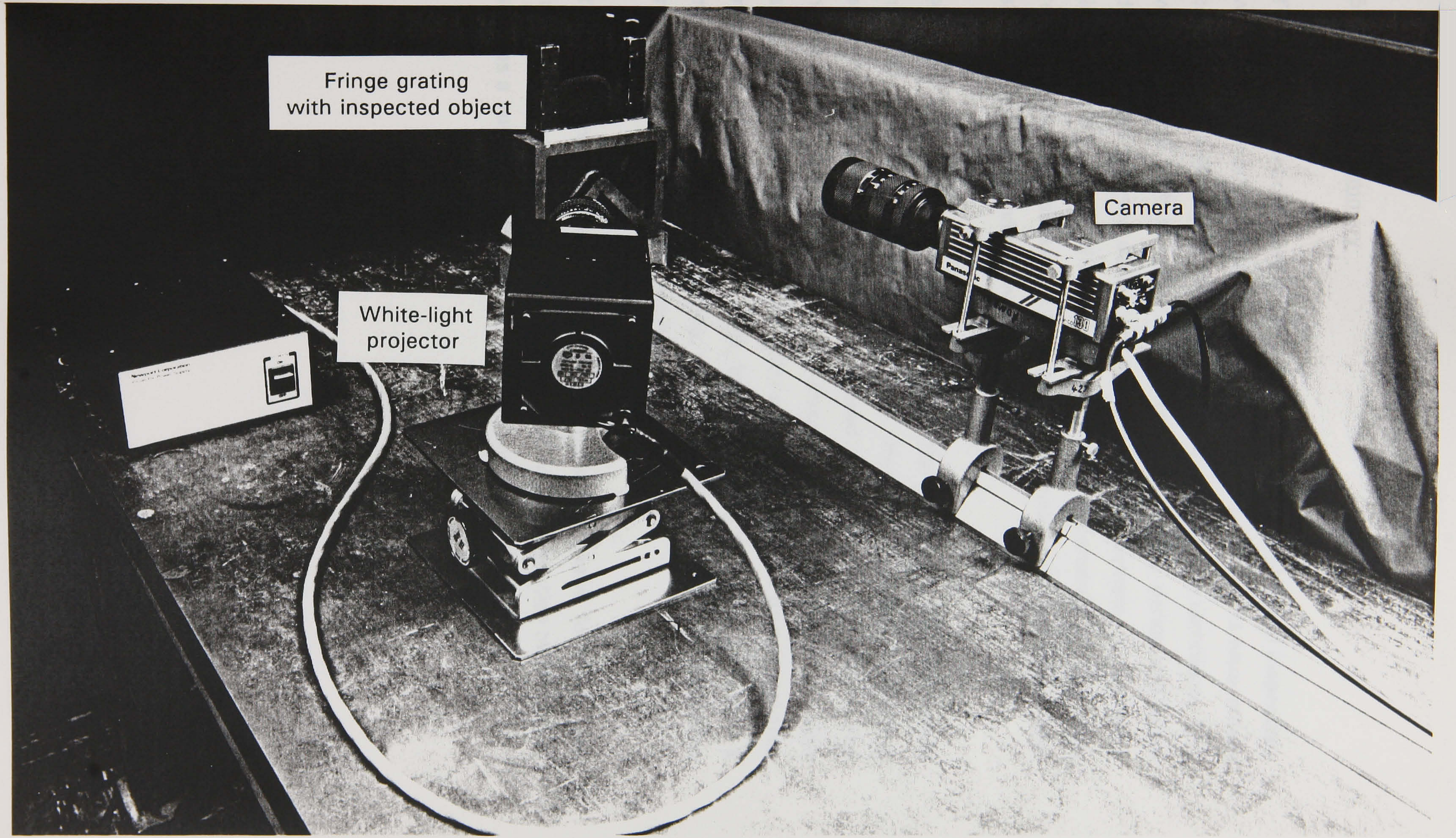

Figure 5.22 Photograph of set-up of adapted method

5.10 Chapter Summary

The problems encountered in developing a practical method of inspection, were numerous but hopefully successfully remedied. Problems were initially encountered in obtaining the required data essential to this technique. This was overcome with more accurate methods of fringe period and angle determination, and the alternative of calibrating the system, to develop a linear relationship which would make the requirements of this data redundant and un-necessary. Validating the basic theory experimentally, showed that the technique worked.

Problems with visual noise and image alignment, required alternative methods to produce a thresholded image. However, the greatest problem encountered for this technique, is caused by the fringe alignment. The necessity of both fringes in the images to be compared, to align approximately or ideally exactly with one another. The use of real-time image subtraction of a 6-bit image, together with a histogram plot, gave a means of partially remedying this, with the final filtering of the subtracted image, producing a suitable solution.

The interesting adapted alternative to eliminate the need for image and fringe alignment, and a variation of the basic fringe projection technique, is perhaps a better solution, particularly for real-time measurement.

5.11 References

5.1 GONZALEZ, WINTZ, Digital Image Processing, Addison-Welsey Publishing, 1977.

CHAPTER SIX

ILLUSTRATIONS OF THE SYSTEM IN ACTION

6.1 Introduction

The purpose of this chapter is to illustrate a number of results that the technique is capable of producing. Only a selection of particular results are presented to illustrate certain features of the technique. The range of results also provides an indication of the limitations and problems associated with this technique, and their solutions.

The measurement of the bar of soap is to demonstrate the feasibility of using this technique on one possible example, with many more other applications possible.

In addition, sample results of an alternative technique are presented, to demonstrate the feasibility of this adaption of the previous method, in the development of a simpler inspection system.

6.2 System Calibration

To enable the volume to be estimated by the technique, it is essential before any measurement is made, for the system to be calibrated. Certain parameters essential for volume estimation by the technique are required to be accurately determined. This is achieved by the methods described in the previous chapter in section 5.2, where techniques to determine the angle and fringe period (and associated scaling factors) are described. Once achieved the following expression derived in chapter 4 may be used:

$$\text{Total Volume} = \frac{p_0 . \sum \text{Count}}{2.X.Y.\sin\theta} \qquad (6.1)$$

where p_0 = Fringe Period

$\sum$ Count = Total number of white pixels

X = Scaling Factor in x direction

Y = Scaling Factor in y direction

θ = Angle between the projector and camera

The only variable once the system is setup, will therefore be the total number of white pixels produced from the subtracted image.

6.2.1 Sample Calibration Results

1) Determining the fringe period, p_0

The fringe period may be obtained from the relationship (explained in chapter 4).

$$p_0 = p.\cos\theta$$

where p_0 = the fringe period in the direction of illumination.

p = the observed fringe period, as observed from the direction of observation.

θ = the angle between the direction of illumination and the direction of observation.

The observed fringe period p is initially determined by illuminating, with black and white fringes a slip gauge painted white which is placed such that its surface normal is towards the camera. With the use of a cursor routine within the software, the equivalent number of pixels per fringe may then be determined.

e.g. 10 fringes = 143 pixels.

Observed fringe period = 14.3 pixels.

since the scaling factor = 4.26 pixels/mm
(derived in example 3 later)

Observed fringe period = $\frac{14.7}{4.26}$ = 3.36mm
(in terms of mm)

fringe period p_0 = 3.36 cos 43.3

= 2.45 mm

2) Determining the aspect ratio, α and the scaling factors X,Y.

The aspect ratio (used in the rotation theory) and the scaling factors in the x and y directions may be determined by using the same slip gauge. On the surface of which are markings of known separation, where the distances between which are accurately measured on a 3-axis co-ordinate measuring machine. With these points within the field of view of the camera, the number of pixels for the equivalent distance in millimetres may be calculated.

e.g. Vertical separated distance (y) = 20.58 mm

Equivalent number of pixels = 129 pixels

Horizontal separated distance (x) = 19.97 mm

Equivalent number of pixels = 85 pixels

Aspect ratio α (Chapter 5.4.1) $= \frac{129}{85} = 1.51$

From Chapter 4.2

Scaling Factor X $= \frac{85}{19.97} = 4.256$ pixels/mm

Scaling Factor Y $= \frac{129}{20.58} = 6.268$ pixels/mm

3) Determining the angle θ

As described in detail in chapter 5 (figure 5.3), the angle θ maybe obtained by reading the angles from a rotating turntable with an angular vernier scale. By taking a reading when the beam of light is reflected into the camera, and then another when the beam is reflected into the laser, the required angle between the two is equivalent to double the difference between the two readings.

e.g. Reading 1 222° 30′

Reading 2 200° 50′

Angle θ = (220° 30′ - 200° 50′) x 2 = 43.3°

It should be noted that the calibration results obtained above are different for each individual setup. The results produced are only examples to demonstrate how they are determined. For each setup the same calibration procedure must be repeated.

6.3 Measurement Procedure

Measurements are performed on bars of soap to demonstrate an industrial application where the technique may be applied. Many other examples may be used, other than the one presented. The problems and subsequent solutions associated with this specific example, demonstrate the success and flexibility of the technique in overcoming these problems in this specific example. Additional problems may arise in other applications of this technique. The problem that different coloured bars of soap exhibit different light absorption properties, lead to the requirement that the surfaces, to be compared with one another, must be of the same reflectivity (as mentioned at the beginning of the previous chapter).

In addition, another problem associated with this example, is the fact that each bar of soap is unique in weight and outer dimension. This is due to the plastic and malleable nature of the soap, in expanding in size once produced from the moulds used in the manufacture. For this reason, conventional contact measurement is impossible. To limit as many variables that might affect the technique and to accommodate the fact that each bar of soap is unique is size and weight, the procedure for determining the volume of a surface defect, involves comparing the same bar of soap, before and then after a surface defect is purposely introduced upon it. By weighing the soap bar before and after the defect is introduced, the volume removed may be easily determined with the density known.

The value for the density was first determined by using the standard volume displaced by known mass method, and subsequently verified by the soap manufacturers. The method involved weighing a bar of soap to find the mass, and then immersing the soap within a measuring vessel containing water. With the volume of water displaced and mass of the bar of soap known, the density may then be evaluated.

Similarly, by analysing images of the bar of soap, with fringes projected upon the surface before and after the defect is introduced, a system determined volume may be found. By comparing this figure, with the known volume removed, the error for each comparative measurement may be calculated.

6.4 Sample Results

The following results in Table 6.1 illustrate the comparative measurements of a number of bars of soap with surface defects of varying magnitude. The fringes are projected onto the surface at an angle of 22° to enable the relatively deep surface defects to be more easily measured. The bars of soap are also relocated in the same position as the reference image (with the use of the real-time subtraction described in section 5.6), to enable an accurate volumetric measurement by the technique to be possible.

Table 6.1 Results of the system determined volume and error, when relocated accurately (angle at 22°)

Percentage Mass removed (%)	Removed Mass (kg x 10^{-3})	Removed Volume (mm^3)	System Volume (mm^3)	Percentage error (%)
1	1.1371	1083	1161	7
0.22	0.2647	252	276	9
0.15	0.1851	176	242	37

By comparing the volumetric results determined by the system, with the known volumes (determined from the mass removed), illustrated in Table 6.1, reasonable estimates for the system volume are given. The results obtained give an indication of the range of different sizes of defects detectable by the technique. The percentage error produced for the first two examples are comparatively small, considering the range of mass removed (1% - 0.22). However, the large error in the last example for a small removed mass of only 0.15%, illustrate that at this angle of 22°, the system is not of sufficient accuracy and sensitivity to detect a difference of this magnitude. The system is set at a relatively shallow angle of 22°, to enable relatively deep defects to be measured. As mentioned previously in

the description of the technique, the greater the angle between the direction of illumination and the direction of observation, the more sensitive and accurate the technique to smaller differences.

As a consequence, further examples of some measurements at a greater angle of 43° are performed and illustrated in Table 6.2

Table 6.2 Results of the system determined volume and error, when relocated accurately (angle at 43°)

Percentage Mass Removed (%)	Removed Mass (kg x 10^{-3})	Removed Volume (mm^3)	System Volume (mm^3)	Percentage Error (%)
0.30	0.3562	339.0	326	3
0.09	0.1111	105.8	124	17
0.06	0.0701	66.7	63.2	5
0.05	0.0668	63.6	73.4	15

The results produced in Table 6.2, collectively indicate that at this greater angle, smaller defects of less significant depth, may be accurately measured. The range of measurements are of significantly smaller defects (0.3% - 0.055% mass removed) compared to previous results (1% - 0.22%) illustrated in Table 6.1. The small error for such small differences clearly indicate that at this greater angle, the small defect may accurately be estimated.

The repeatability of the technique was assessed over 10 measurement cycles. The deviation was found to be less than 18.5 mm^3, for a defect of size 264 mm^3, with a setup angle of 30.8° and an observed fringe period of 5.8 mms.

The results so far illustrate the effect of altering the angle to suit the

magnitude in size and depth of a defect. Care must be taken in setting the system up, in order that the shift in the fringe's lateral movement on the surface is not greater than the projected fringe spacing. If this were to occur, the number of white pixels produced in the subtracted image would result in significantly smaller system volume.

Therefore a pre-requisite for this technique (previously described at the beginning of Chapter 5) requires the angle and fringe spacing to be such that the deepest protrusion likely to be encountered, must not lead to a fringe shift within the subtracted image, greater than the projected fringe spacing.

The fringe shift in each of the two images to be compared with one another, may shift any amount providing the fringe shift between the two is no greater than a fringe spacing. Thus, any surface shape may be measured provided each image is alike. For this reason, large deep defects (which cause a greater shift in the fringes) may be detected at one angle, with smaller defects requiring greater accuracy at a greater angle.

However, the additional problem of fringe misalignment, as described in the previous chapter, must also be examined. With this in mind, an additional set of results of a range of surface defects, displaced different amounts are presented in Table 6.3, to illustrate the effect of filtering on the accuracy of the technique. The same row and column filter is used on all of the results for consistency. Figures 6.1 to 6.5 illustrate an example of this feature.

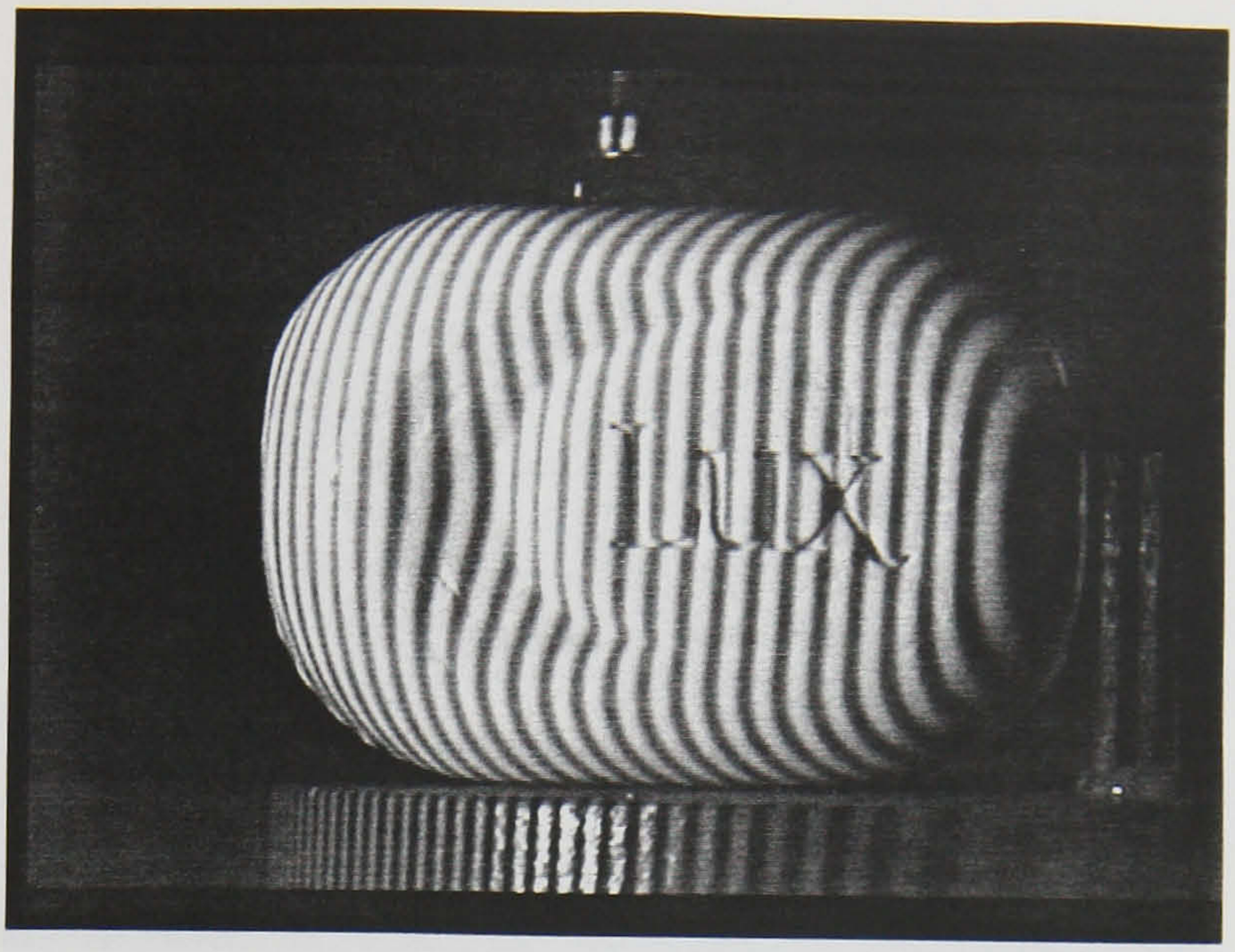

Figure 6.1 Image of reference bar of soap

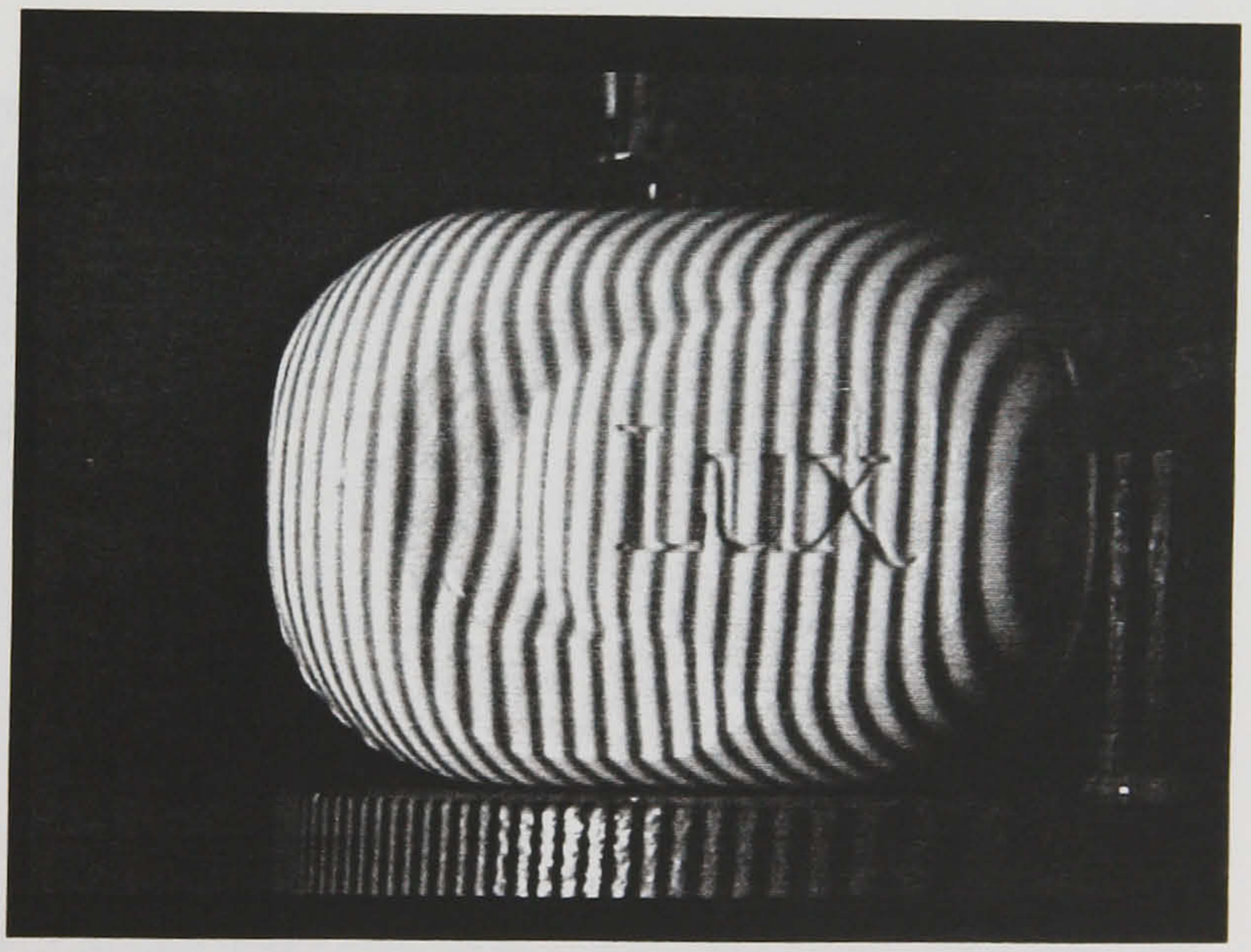

Figure 6.2 Image of bar of soap with surface defect

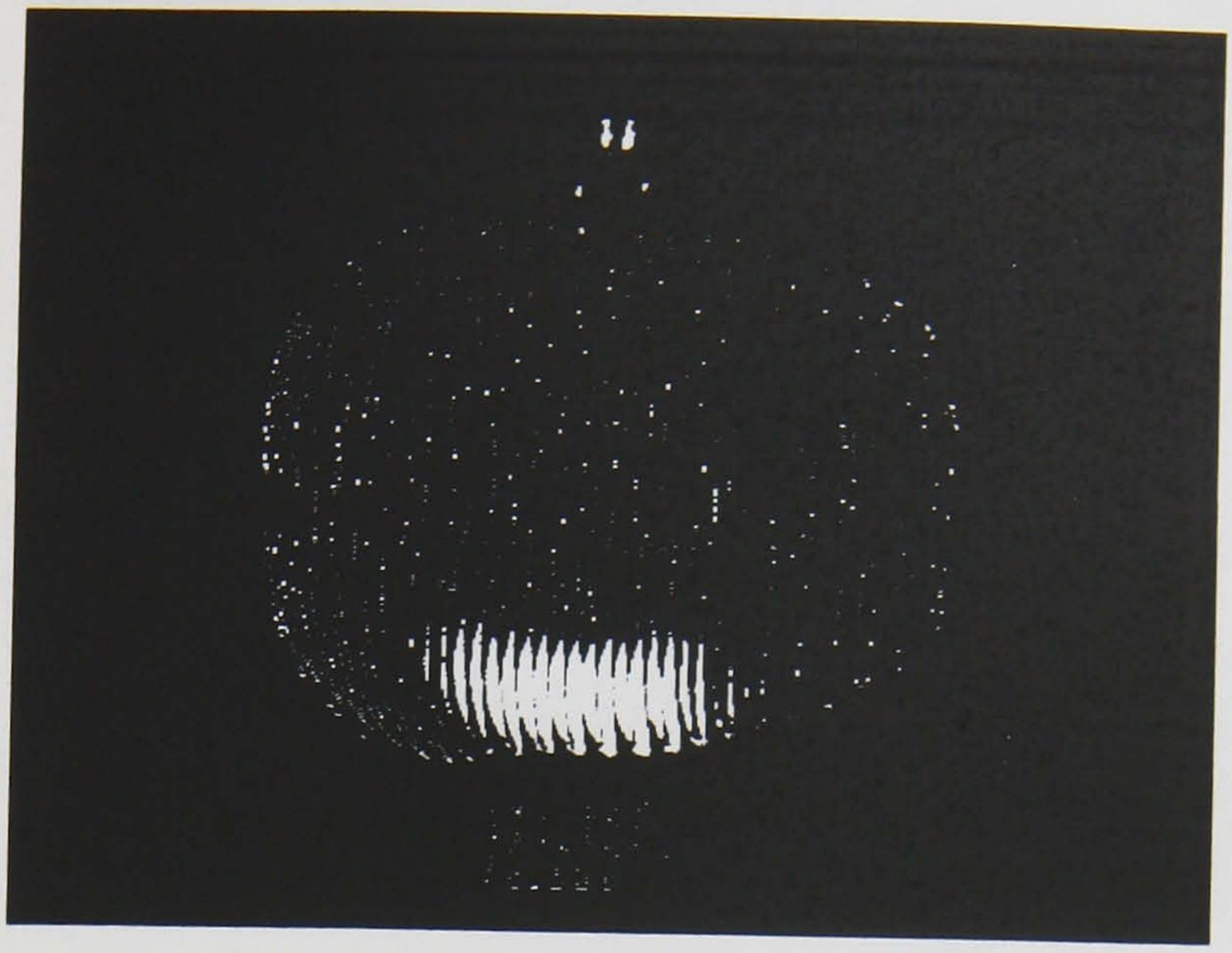

Figure 6.3 Difference of thresholded images relocated accurately

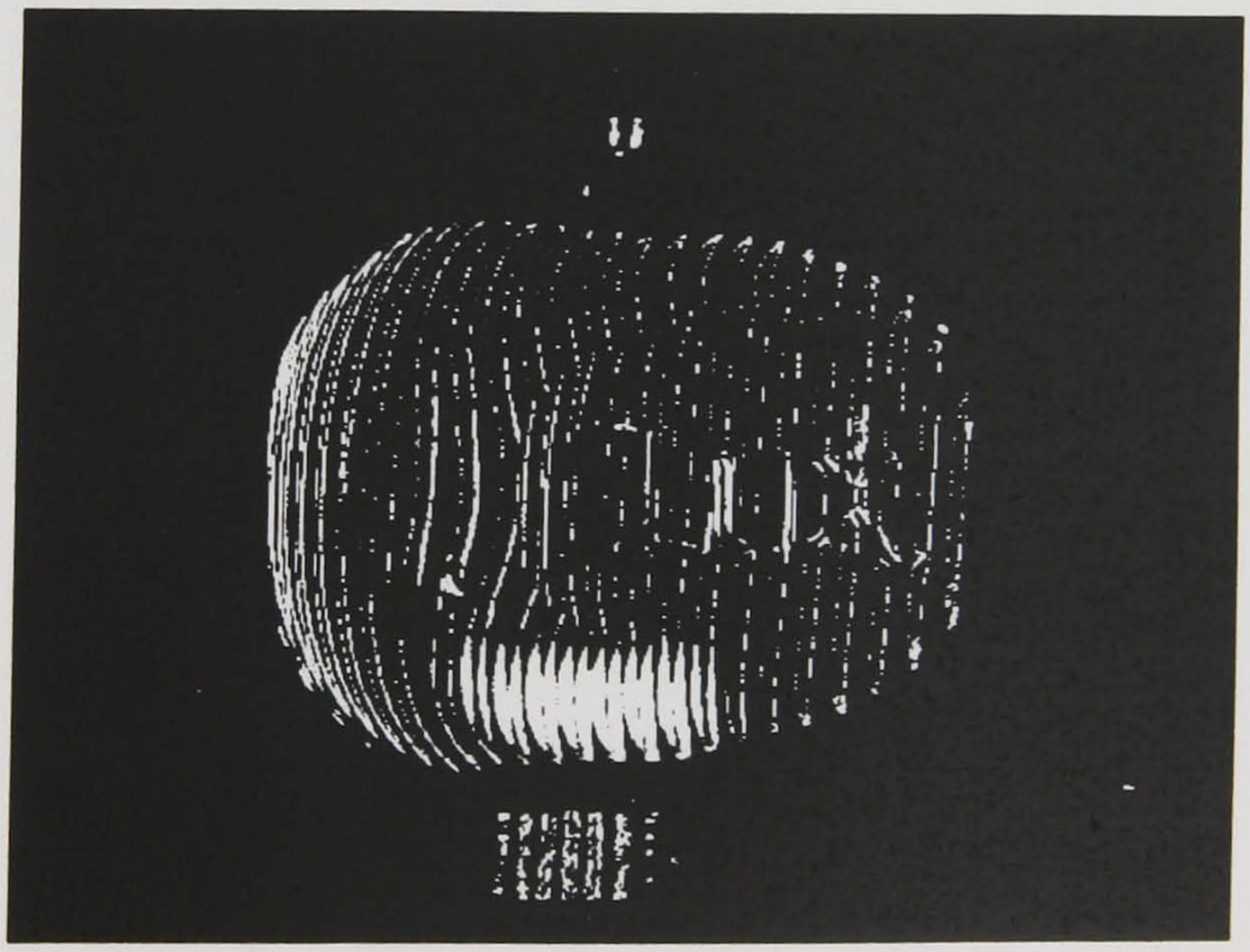

Figure 6.4 Difference of thresholded images with fringes misaligned

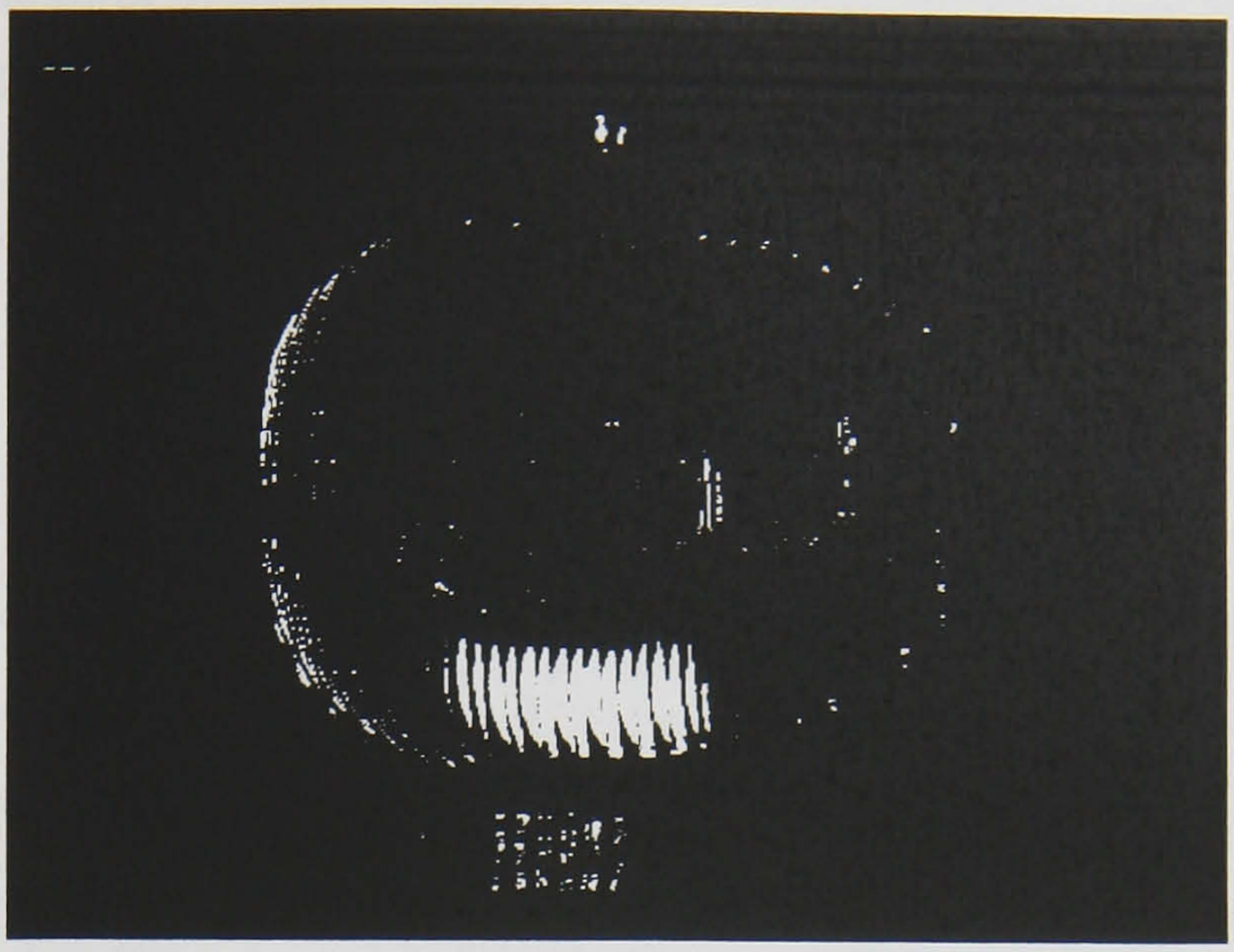

Figure 6.5 Filtered misaligned subtracted image

Table 6.3 Results of system determined volume and error (Angle 43°) on filtered data using row and column filter.

Percentage Mass Measured (%)	Displacement (mm)	True Volume (mm^3)	System Volume (mm^3)	Percentage Error %
0.30	1.12	339.2	304	10
0.30	0.51	339.2	282	16
0.30	0.25	339.2	279	17
0.09	1.09	105.8	*	*
0.09	0.43	105.8	79	25
0.06	0.86	66.76	*	*
0.05	0.33	63.61	57	9

* Denotes the difficulty for the row and column filter in distinguishing data due to a defect from data due to misalignment.

The results illustrated above in Table 6.3, indicate for the greater defect (i.e. 0.3%), significant displacements of the sample, up to more than a millimetre, give a reasonable and relatively unaffected system volume, once the image is filtered. However, for the smaller differences, displacements of the same magnitude, provide unacceptable large errors after filtering. The confusion lies in the difficulty in distinguishing data due to a misalignment, from data due to the small defect. As a consequence of which, the results will be produced in Table 6.3, highlighted with the additional asterisk *, indicating the difficulty in distinguishing defect data from misalignment data. Although smaller displacements of small defects provide reasonable results, with only small errors, as demonstrated in this example as shown in Table 6.3.

The results produced after filtering are acceptable, for the examples of large defects and significant displacement. However, this is not the case for the

small defects with displacements of a similar magnitude. For this to be explained, the basis of the technique must first be described.

Due to the nature of the technique involving image subtraction and fringe contouring, the height of the surface, highlighted by the modulation of the fringes, is of significant importance. With a defect introduced on part of the surface, the fringes situated in the area of the defect will shift in their lateral position as we have seen. In producing a subtracted image by comparing this image with some perfect reference, the difference in the fringes, as a consequence of the height difference caused by the defect, is what enables the volume to be found.

In producing a small shallow defect, a small height difference will result and as a consequence a small lateral shift in the fringes. When occurring in conjunction with a large displacement (resulting in a significant shift in the fringes themselves), difficulty will occur in distinguishing data due to misalignment from data due to this defect. Due to the sensitivity of the technique to the height of the surface, small shallow defects can only be measured when only misaligned or displaced a fraction. For larger defects of greater depth, a significant misalignment is acceptable, as indicated by some of the results (i.e. 0.300% Mass displaced 1.117mm).

Additional results in the case of rotating an image to align with another have not been presented, since great errors are produced. In rotating a fringe illuminated item, the image would rotate as would the fringes on its surface, making fringe alignment impossible.

6.5 Adapted Method Results

This adapted solution described in section 5.9, would reduce the alignment problem. Rather than projecting fringes onto the surface of the object, the object is placed against a large grating. Similar results would be produced on the surface, by the modulation of the shadows from the fringes. With the use of image subtraction, the grating fringes would be eliminated, enabling a suitable surface comparison to be made.

Similar to the procedure described earlier in this chapter in section 6.3, the procedure undertaken in the verification of this adapted technique, involves the comparison of the known volume of a sample, with a system determined figure. To illustrate the viability of this technique, the test objects used are machined concave samples of which the maximum depth and concave radius are measured, with the use of a 3-axis co-ordinate measuring machine and a Rank-Taylor Hobson Form Talysurf. Each object is different and produced on a CNC machine tool.

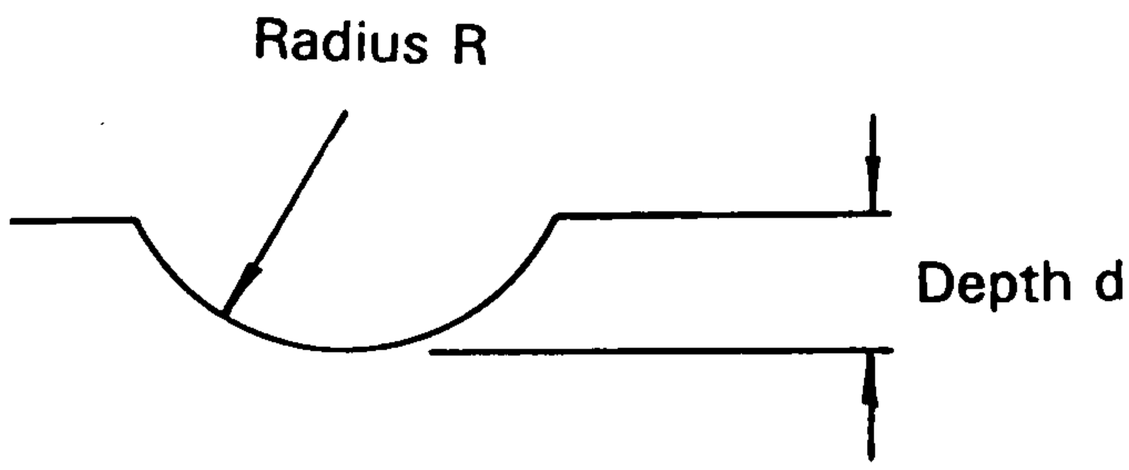

From these parameters, the actual volume of each hollow may be determined with the following relationship (6.2) (as previously mentioned in Chapter 4.3), and listed in Table 6.4

$$\text{Volume} = \pi d^2 \left(R - \frac{d}{3}\right) \qquad (6.2)$$

Table 6.4 Test objects for the adapted technique

Radius R (mm)	Depth d (mm)	Actual Volume (mm^3)
57.69	3.10	1712
78.61	3.17	2442
100.29	3.12	3037

The expression for the system volume (6.1), as used earlier in this chapter, must be altered to accommodate for this adapted technique. The original expression took the resulting effect of the modulation of both black and white fringes within the subtracted image, to enable a result to be produced. With the application of this adapted technique, only the modulation of the black fringes (i.e. shadow created by the grating) will occur, resulting in only half the effect within the subtracted image. By multiplying the expression by a factor of two, a suitable expression may then be applied, to enable the investigation of this adapted method.

i.e. Adapted Volume Expression:

$$\text{Volume} = \frac{p_0 . \sum \text{count}}{X . Y . \sin\theta} \qquad (6.3)$$

where p_0 = Fringe Period

$\sum$count = Total number of white pixels

X = Scaling Factor in x direction

Y = Scaling Factor in y direction

θ = Angle between the camera and projector.

Similar to the previous technique, once the system is setup, the only variable will be the total number of white pixels. A flat plane is used as the reference image to produce the final results as presented in Table 6.5.

Table 6.5 Results of the adapted system volume and error (angle at 21.5°)

Actual Volume (mm^3)	Adapted System Volume (mm^3)	Percentage error (%)
1712	1604	6
2442	2062	15
3037	2525	16

Table 6.6 Results of the original system volume and error when relocated accurately (angle at 22°)

Actual Volume (mm^3)	Original System Volume (mm^3)	Percentage Error (%)
1712	1820	6
2442	2270	7
3037	2717	10

The volumetric results produced by the adapted technique (Table 6.5), provide reasonable estimates for the volume. When these figures are compared with those achieved by the original method (Table 6.6) described earlier in this chapter, the adapted technique's results in the worst case is only 5% different. If one considers the fact that the sample has not been relocated to a high degree of precision, the relatively small resulting error compared to the original technique is encouraging.

The development of this alternative, an adaption of the original projection method, is a more suitable solution in enabling a real-time automated inspection system to be possible. The following figures (6.6 to 6.10) illustrate adapted technique in action.

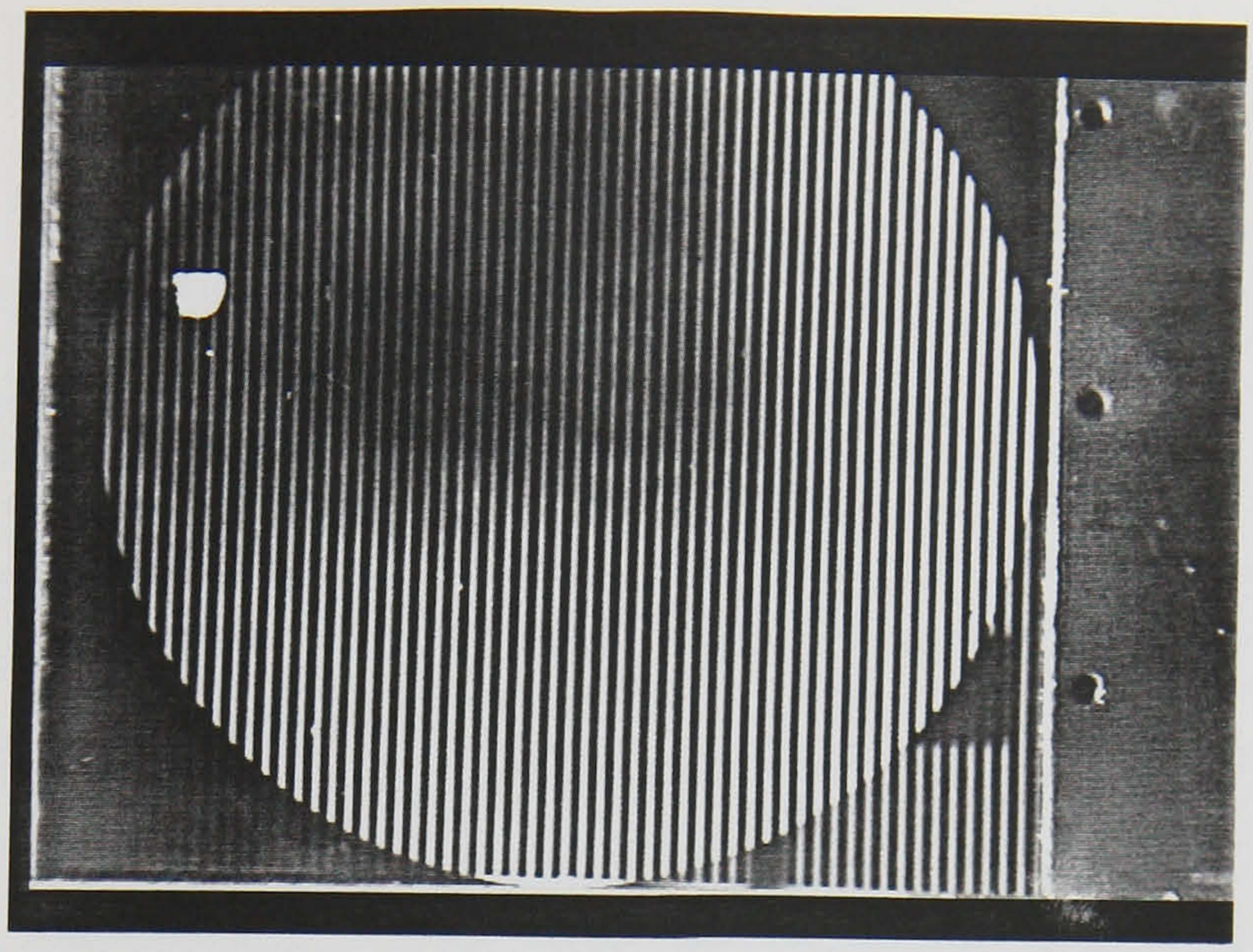

Figure 6.6 Image of grating with flat reference

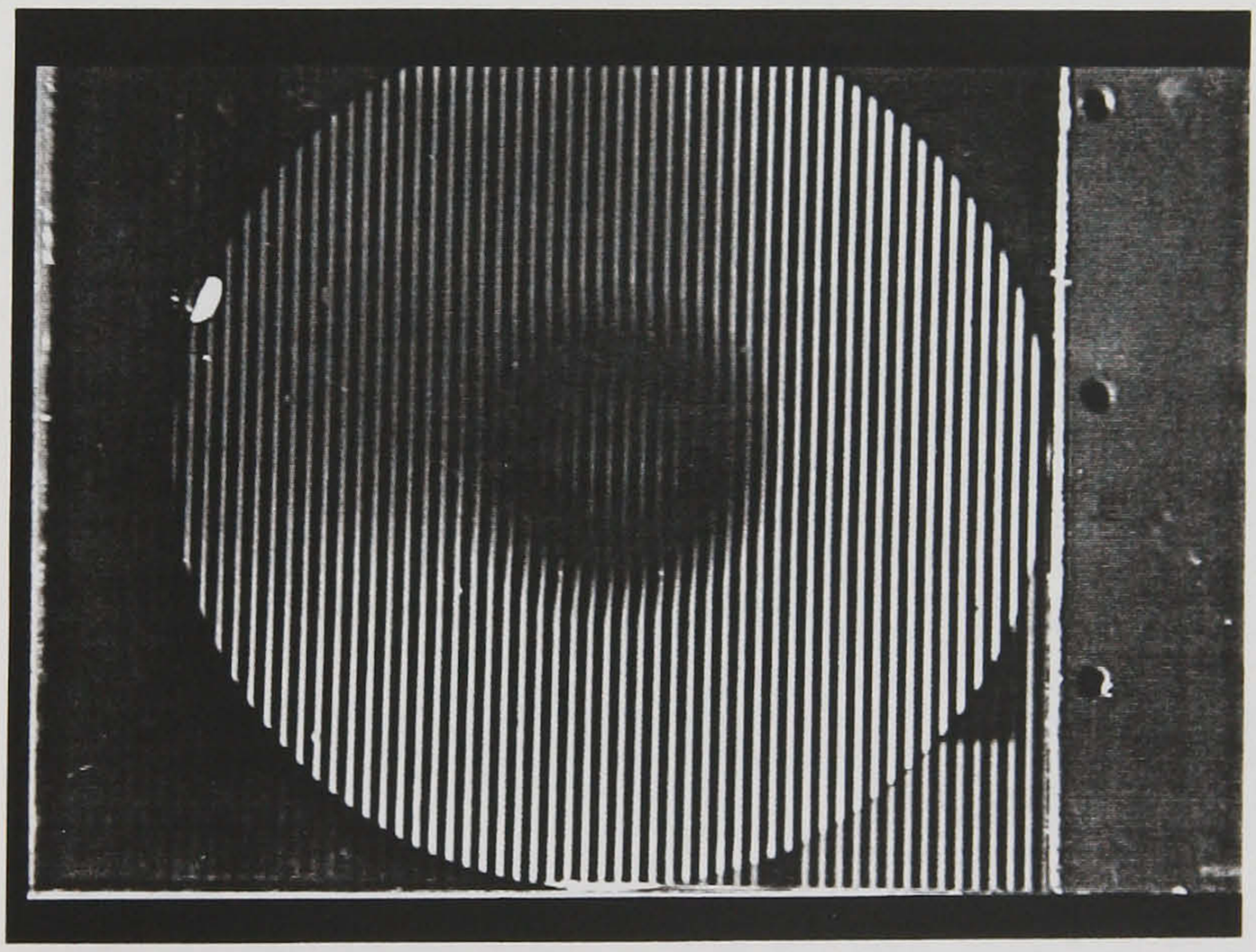

Figure 6.7 Image of grating with concave sample

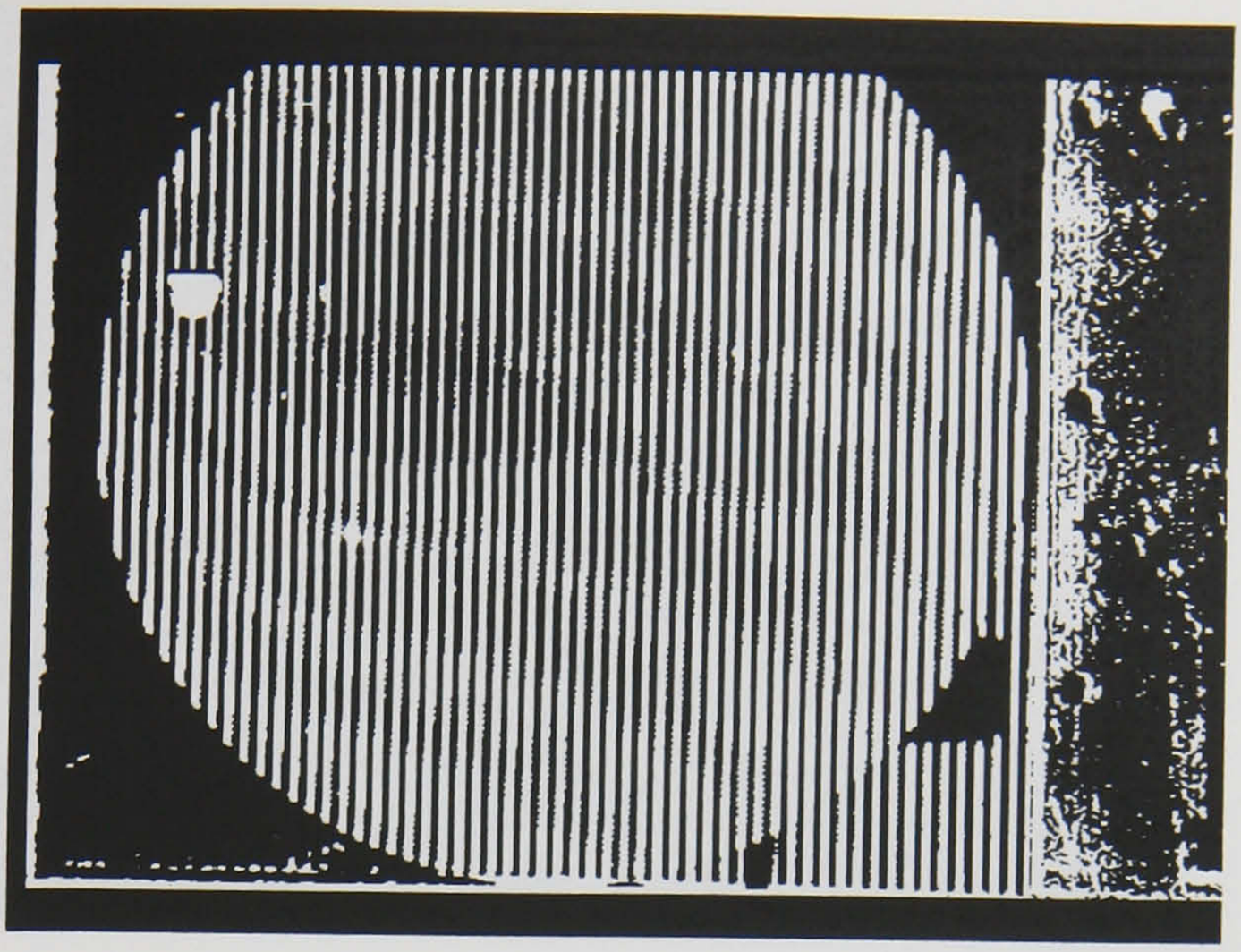

Figure 6.8 Thresholded image of grating with flat reference

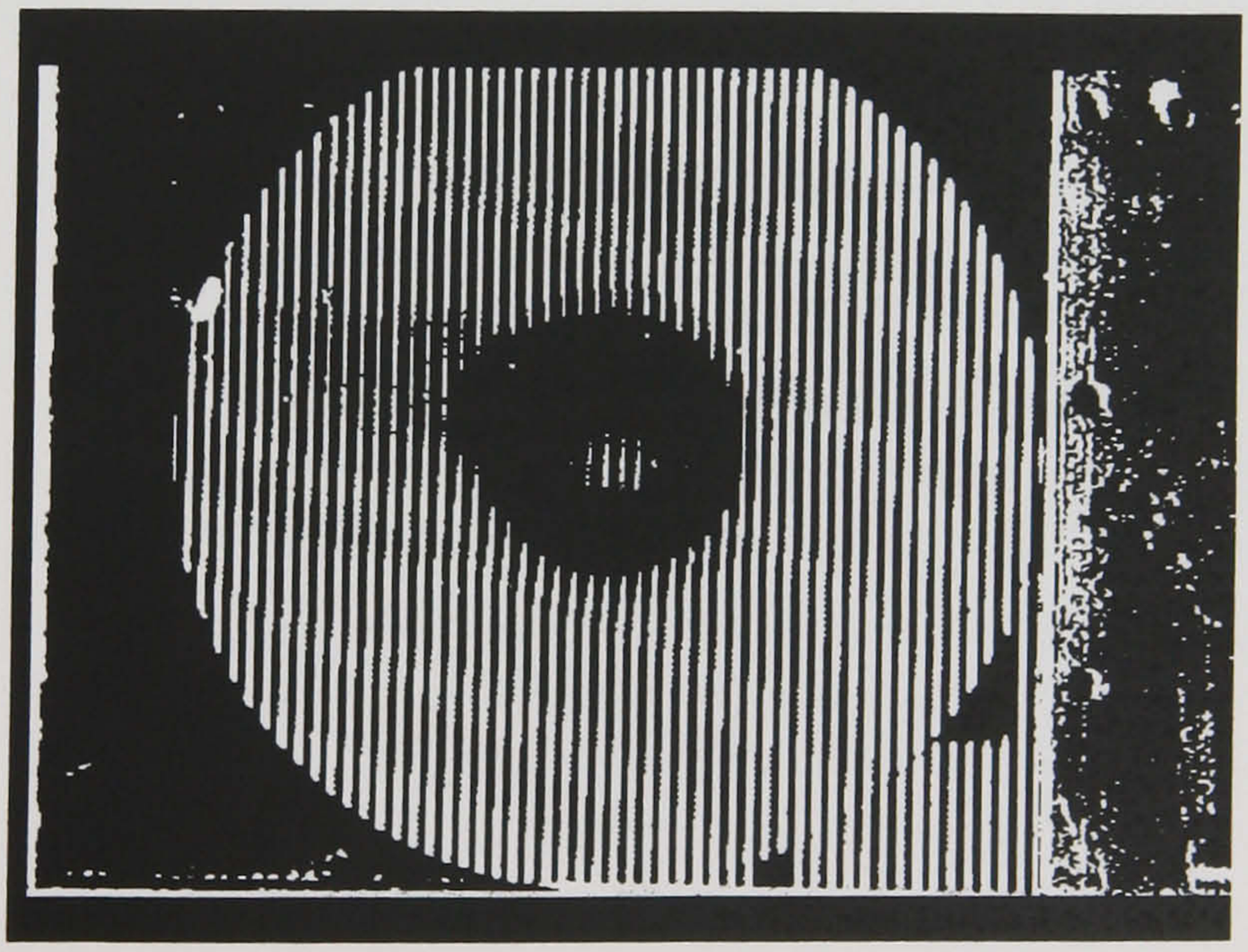

Figure 6.9 Thresholded image of grating with concave sample

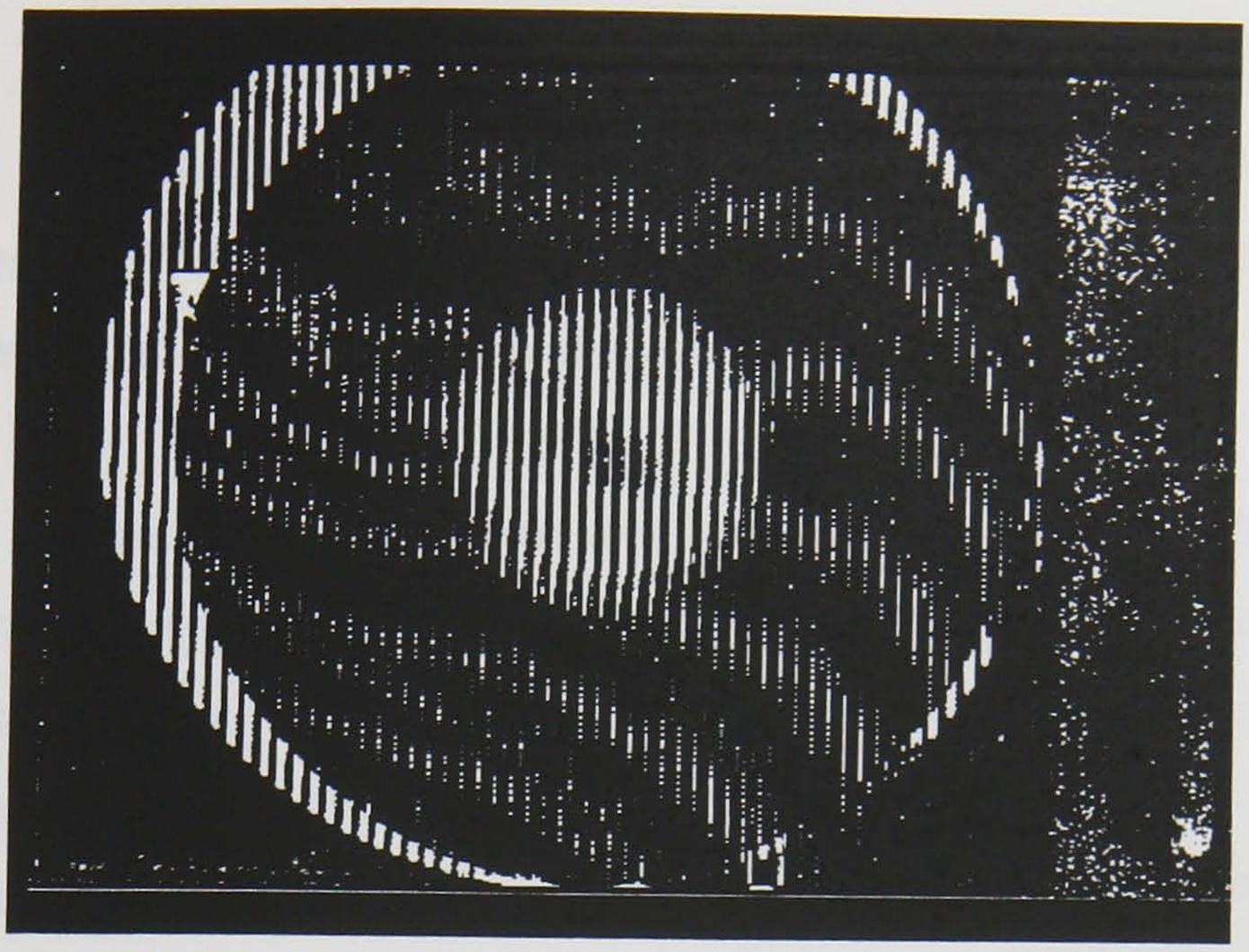

Figure 6.10 Difference image of adapted technique (6.8 - 6.9)

6.6 Chapter Summary

To provide a quantitative means of assessing the technique's performance, experiments have been devised in which defects of known volume have been introduced. The accuracy with which the system determines these known volumes can then be analysed.

However, it should be noted that the objective of this work is not to accurately measure volumetric difference but to gauge the acceptability of a component. The volume difference is merely part of a decision criteria, where if the difference exceeds a certain threshold, then the component under inspection is deemed to have failed. Therefore the absolute accuracy in volume measurement is not critical. The device is a comparator and not a measuring instrument.

All components will exhibit some difference, with the most important features to be taken into consideration including, the magnitude (with respect to some threshold), and the distribution of this difference over the object surface. The latter point is particularly important. For example, a difference of 50mm^3 in volume is not significant over an area of 3000mm^2, but it is over an area of 50mm^2.

To enable a range of defects, of varying size and depth, to be measured by this technique, a number of camera and fringe projectors set at different angles would be ideal. Defects of significant depth could be accurately measured at a shallow angle, and small defects at a greater angle. Care must be taken to ensure that the fringe shift is not greater than the fringe spacing, otherwise a large error in the system volume would occur.

The development of the alternative solution (an adaption of the previous method) of using a large fringe grating, against which the sample to be measured is placed against, is the more suitable method for development in a real-time inspection system. The necessity to relocate approximately is eliminated as is the problem of fringe misalignment.

CHAPTER SEVEN

UNCERTAINTY ANALYSIS

7.1 Introduction

The purpose of this section is to briefly outline the sources of error which could affect the final results. These potential causes of error include:

i) Incorrect pixel count

ii) Calibration Errors

7.2 Operational Errors and Uncertainties

i) Incorrect pixel count

The inherent use of thresholding in this technique may affect the number of pixels related to a surface defect. The purpose of thresholding is to divide the image into contrasting areas of light and dark, in particular the fringes produced on the surfaces to be compared with. Thus, when two images are processed in this manner, the difference between these two images (i.e. a defect) will be quite visible and easy to quantify. Depending upon the thresholding value chosen, the number of pixels may be above or below the true number related to the surface defect. The additional fact that the image is divided into pixels, make the representation of the exact path of a surface defect boundary difficult. This quantising error is similar to an analogue to digital converter, where the incoming data of variable magnitude is converted to distinct integer values, thus rounding off and truncating this data. Figure 7.1 illustrates the thresholding limiting value and truncating effect.

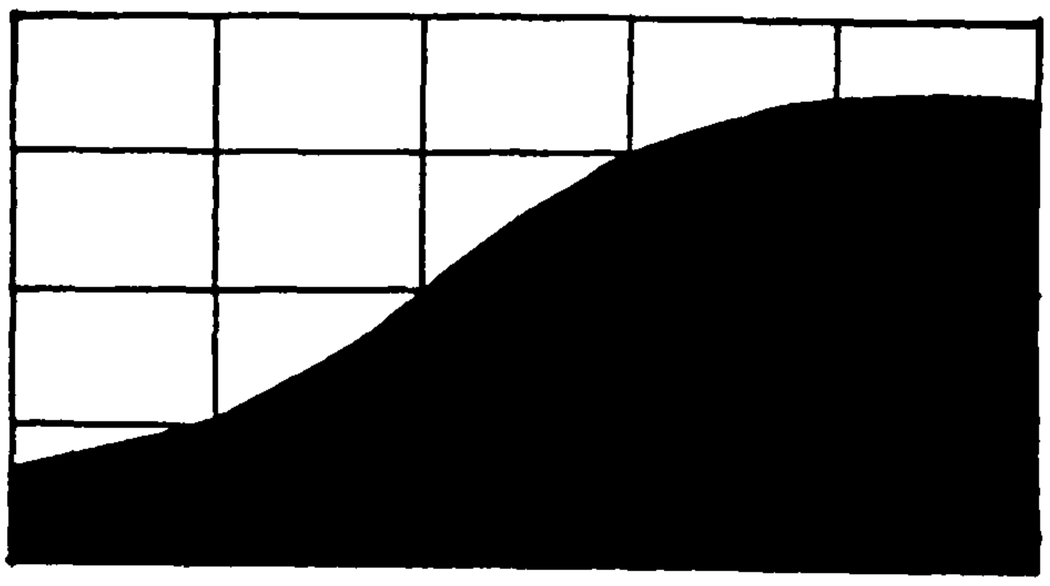

a)

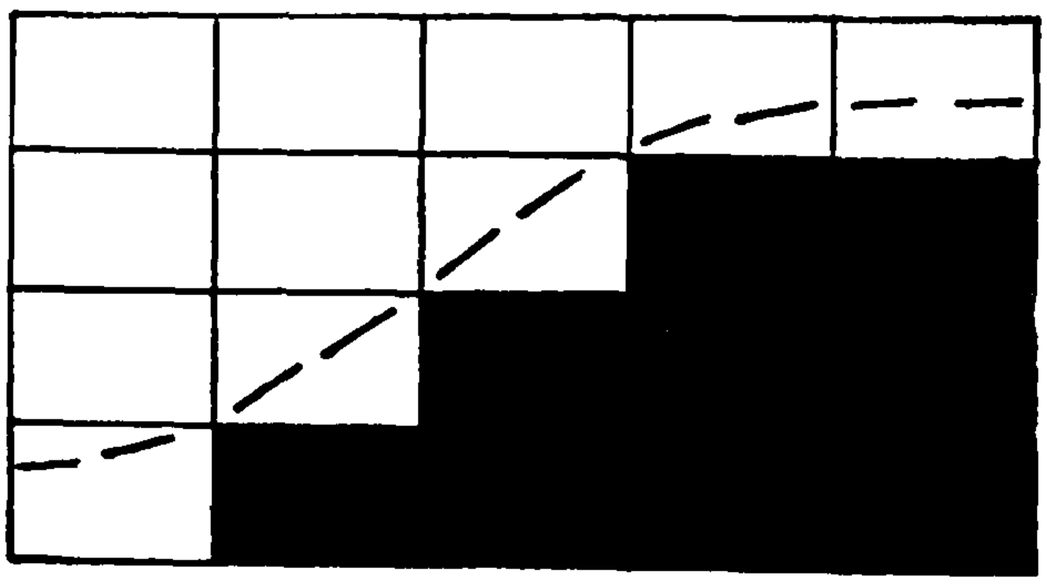

b)

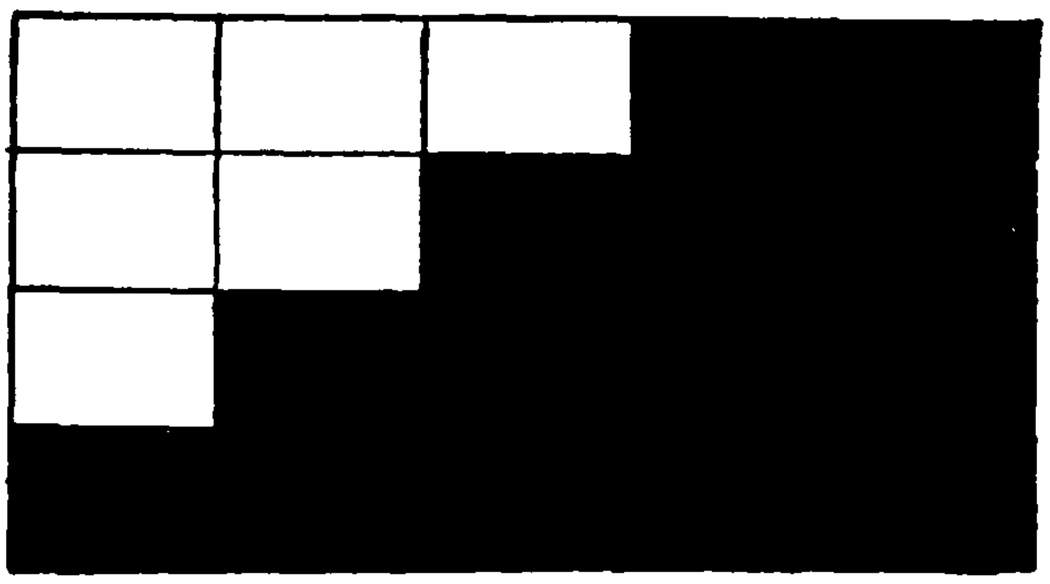

c)

Figure 7.1 a) Sample true boundary

b) Overestimate of boundary

c) Underestimate of boundary

The choice of threshold limiting value is important, with the effect on the final volumetric result demonstrated in Table 7.1 below.

Table 7.1 An Example of the effect of the variation of threshold lower limiting value on the system volume.

Threshold Value (lower limit)	System Volume (mm^3)	Actual Volume (mm^3)	Percentage Error (%)
65	240	339	-29
70	275	339	-18
75	293	339	-11
80	312	339	-7
85	329	339	-3
90	331	339	-2
95	323	339	-4 *
100	294	339	-13 *

*** Denotes point at which the modulation in the fringe has exceeded the fringe period.**

In the particular example demonstrated in Table 7.1, it may be observed that the effect of lowering the threshold value, is an increase in the system error. The actual value applied experimentally in this case was a thresholding value of 90. At this value a good contrast in the appearance of the fringes upon the surfaces inspected was possible. Below this value, the contrast in these fringes was poor, with each individual thresholded image (before subtraction) considerably brighter (more white pixels) than before. The resulting error for a thresholding value of 95 (denoted with asterisk *) is the result of the modulation of the fringes, exceeding the fringe period. Care must be taken to ensure that this will not occur. In order to produce accurate results, a good contrast in the appearance in the fringes on the surface is necessary. This is achieved by the choice of threshold limiting value chosen. Thus, this value is of great importance.. Further investigation

of this problem is undoubtedly required to enable an automatic system to be possible.

Similarly, the added problem of visual noise which is ever present, will also effect the pixel count. However, this effect has been minimised by not totally eliminated with the use of image averaging (and previously described in Chapter 5).

ii) Calibration Errors

The accurate determination of the optical set-up constants p, X, Y and θ is crucial for a precision measurement to be achieved, since this method requires these parameters in determining the volume of a surface defect (see expression 7.1).

$$V = \frac{p.\cos\theta.\sum c}{2.X.Y.\sin\theta} \qquad (7.1)$$

where,

V = Volume of difference.

p = Observed fringe period.

θ = Angle between direction of illumination and direction of observation.

$\sum c$ = Total number of white pixels.

X = Scaling Factor in X direction.

Y = Scaling Factor in Y direction.

By using the uncertainty theory [7.1], it was possible to derive expressions which show how uncertainties in one constant may affect the final volumetric result. The uncertainty theory states that the uncertainty in the volume for a particular constant is related to the partial derivative of the volume (with respect to that constant), multiplied by the uncertainty of that constant.

Thus, the following uncertainty expressions were derived.

$$\delta V = \frac{\partial V}{\partial p} . \delta p = \frac{\sum c}{2.X.Y.\tan\theta} .\delta p \qquad (7.2)$$

$$\delta V = \frac{\partial V}{\partial X} . \delta X = \frac{-p.\sum c}{2.X^2.Y.\tan\theta} .\delta X \qquad (7.3)$$

$$\delta V = \frac{\partial V}{\partial Y} . \delta Y = \frac{-p.\sum c}{2.X.Y^2.\tan\theta} .\delta Y \qquad (7.4)$$

$$\delta V = \frac{\partial V}{\partial \theta} . \delta \theta = \frac{-p.\sum c .1}{2.X.Y \sin^2\theta} .\delta \theta \qquad (7.5)$$

where δV = Uncertainty in the volume V.

$\frac{\partial V}{\partial p}$ = Partial derivative w.r.t the fringe period p.

$\frac{\partial V}{\partial X}$ = Partial derivative w.r.t the scaling factor X.

$\frac{\partial V}{\partial Y}$ = Partial derivative w.r.t the scaling factor Y.

$\frac{\partial V}{\partial \theta}$ = Partial derivative w.r.t the angle θ.

δp = Uncertainty in the fringe period p.

δX = Uncertainty in the scaling factor X.

δY = Uncertainty in the scaling factor Y.

$\delta \theta$ = Uncertainty in the angle θ.

and the other symbols have been previously defined in expression 7.1.

These relationships have been individually investigated in the following sections. Equations 7.2 - 7.5 are plotted in figures 7.2 - 7.5.

7.2.1 The System Uncertainties (δp, δX, δY and $\delta\theta$)

By using the set-up constants demonstrated in the calibration exercise, as described δp, δX, δY and $\delta\theta$ of the system may be determined.

i) System Uncertainty in the Observed fringe period, p.

10 fringes = 143 pixels

Lowest p = 14.25 pixels

Highest p = 14.35 pixels

$\therefore$ Uncertainty δp = 0.1 pixels = 0.0235 mm

ii) System Uncertainty in Scaling Factor, X.

Scaling Factor X direction

Line separation = 19.97 mm

Number of pixels = 85

Lowest X = 4.231

Highest X = 4.281

$\therefore$ Uncertainty δX = 0.050 pixels/mm

iii) System Uncertainty in Scaling Factor, Y.

Scaling Factor Y direction

Line separation = 20.58 mm

Number of pixels = 129

Lowest Y = 6.244

Highest Y = 6.292

$\therefore$ Uncertainty δY = 0.048 pixels/mm

iv) <u>System Uncertainty in the Angle, θ.</u>

Readability of the vernier = $\pm$ 1/12°

<u>$\therefore$ Uncertainty $\delta\theta$ = 1/24°</u>

7.2.2 Illustrations of the System Uncertainties

These set-up constants, as described in the previous section and calibration chapter, are employed together with the derived uncertainty equations to produced a series of graphs.

i) For an Uncertainty in p.

The System $\delta p = 0.0235$ mm

Figure 7.2(a) illustrates the linear relationship between the uncertainties of the volume and fringe period, i.e. the uncertainty in the volume V is directly proportional to the uncertainty in the fringe period p, examples of which both are included in the following table.

Uncertainty in p (% of p)	(mm)	Uncertainty in V (mm^3)
10	0.3359	32.696
5	0.1679	16.348
0	0	0

Examination of Figure 7.2(b) and equation (7.2) indicate that the uncertainty in V is inversely proportional to the tangent of the viewing angle. Figure 7.2(b) uses the worst case value for δp (= 0.0235 mm) and indicates for a small viewing angle, a large error in V results, as compared to that for a larger angle where the result is a smaller error.

By using the uncertainty in p of 0.0235 mm and a viewing angle of 43.3°, and error in the volume V indicated in Figure 7.2(b) is 2.286 mm^3, a comparatively small error. System results produced in Chapter 6, are of a similar magnitude with only 1% difference.

Figure 7.2(a) Uncertainty Plot for equation (7.2)

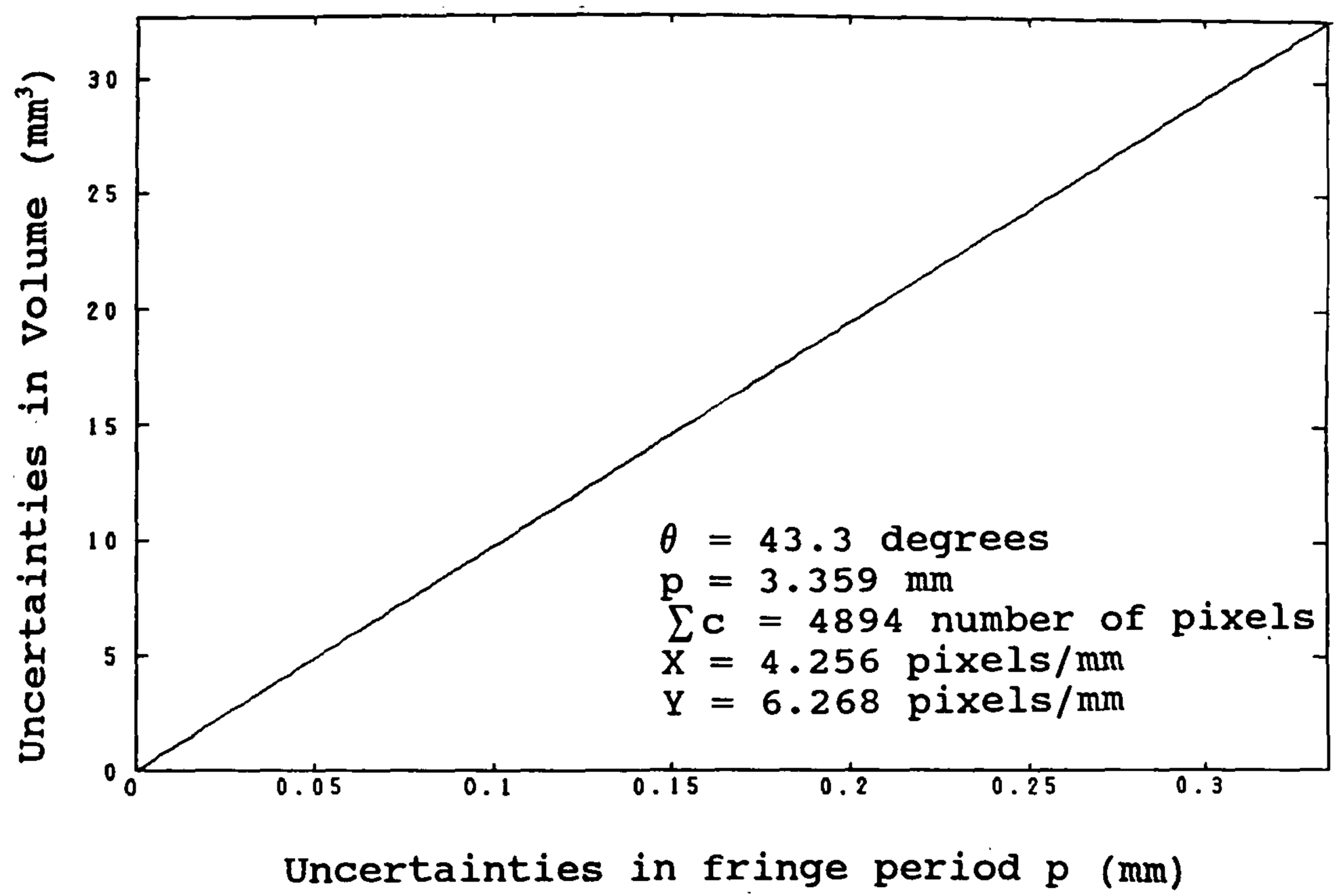

Figure 7.2(b) Plot of Uncertainties in the Volume against θ

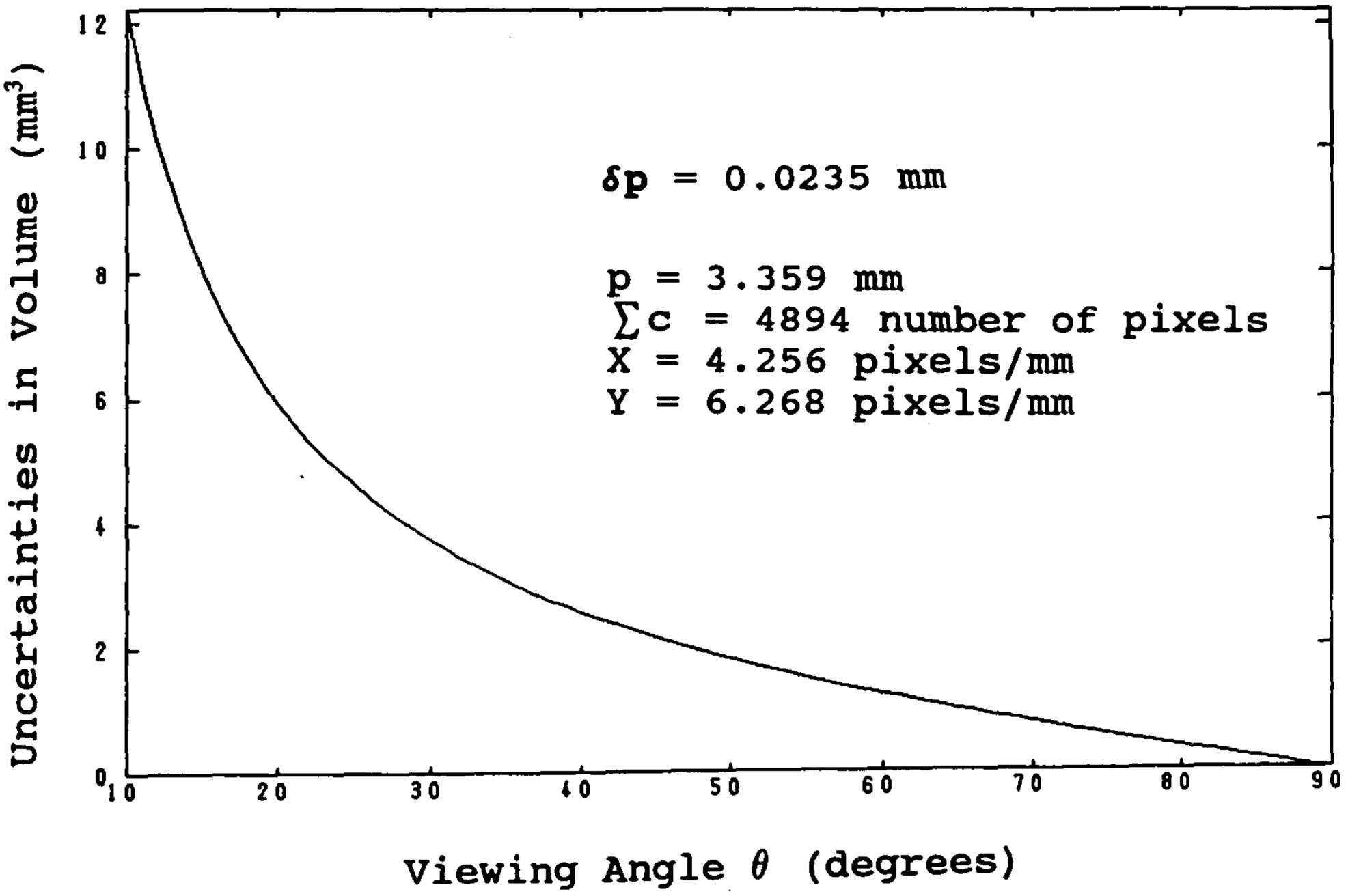

ii) For an Uncertainty in X

The System $\delta X = 0.05$ pixels/mm

Figure 7.3(a) shows that the uncertainty in the volume V is directly proportional to the uncertainty in the scaling factor X, and a negative constant. Examples of which are shown in the following table. As a consequence of this, a small error in over-estimating the scaling factor X will result in an under-estimate in the system volume. Similarly, under-estimating the scaling factor X will result in an over-estimate in the system volume.

Uncertainty in X (% of X)	(pixels/mm)	Uncertainty in V (mm^3)
10	0.4256	-32.696
5	0.2128	-16.348
0	0	0

Examination of Figure 7.3(b) and equation (7.3) indicate that the uncertainty in the volume V is inversely proportional to the tangent of the viewing angle. By using the system worst possible uncertainty value for X of 0.05 pixels/mm and a system viewing angle of 4.43°, Figures 7.3(b) reveals an error in the system volume V of 3.841 mm^3. However, the results achieved by the technique as displayed in Chapter 6, were more accurate than the figure indicated here.

Figure 7.3(a) Uncertainty Plot for equation (7.3)

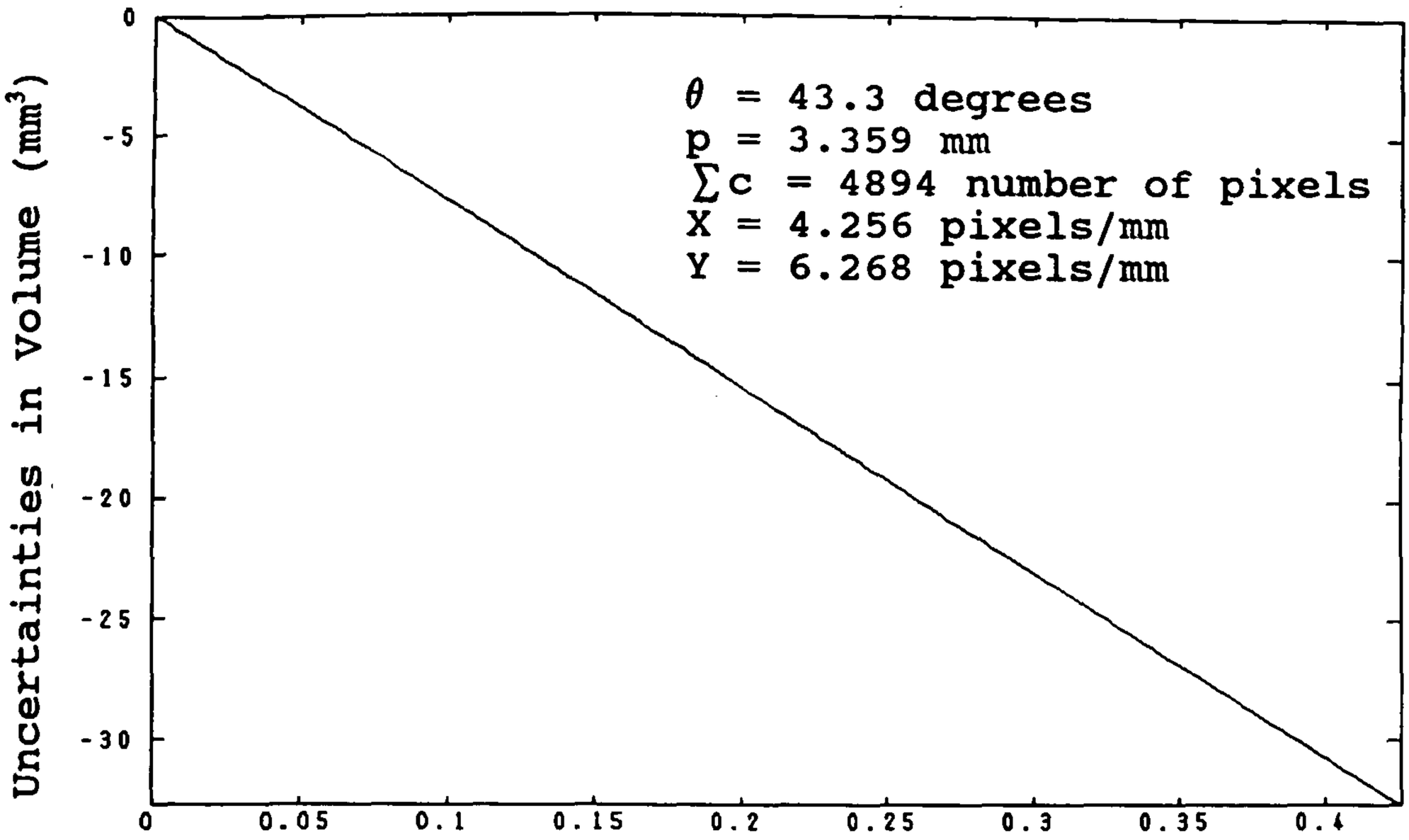

Figure 7.3(b) Plot of Uncertainties in the Volume against θ

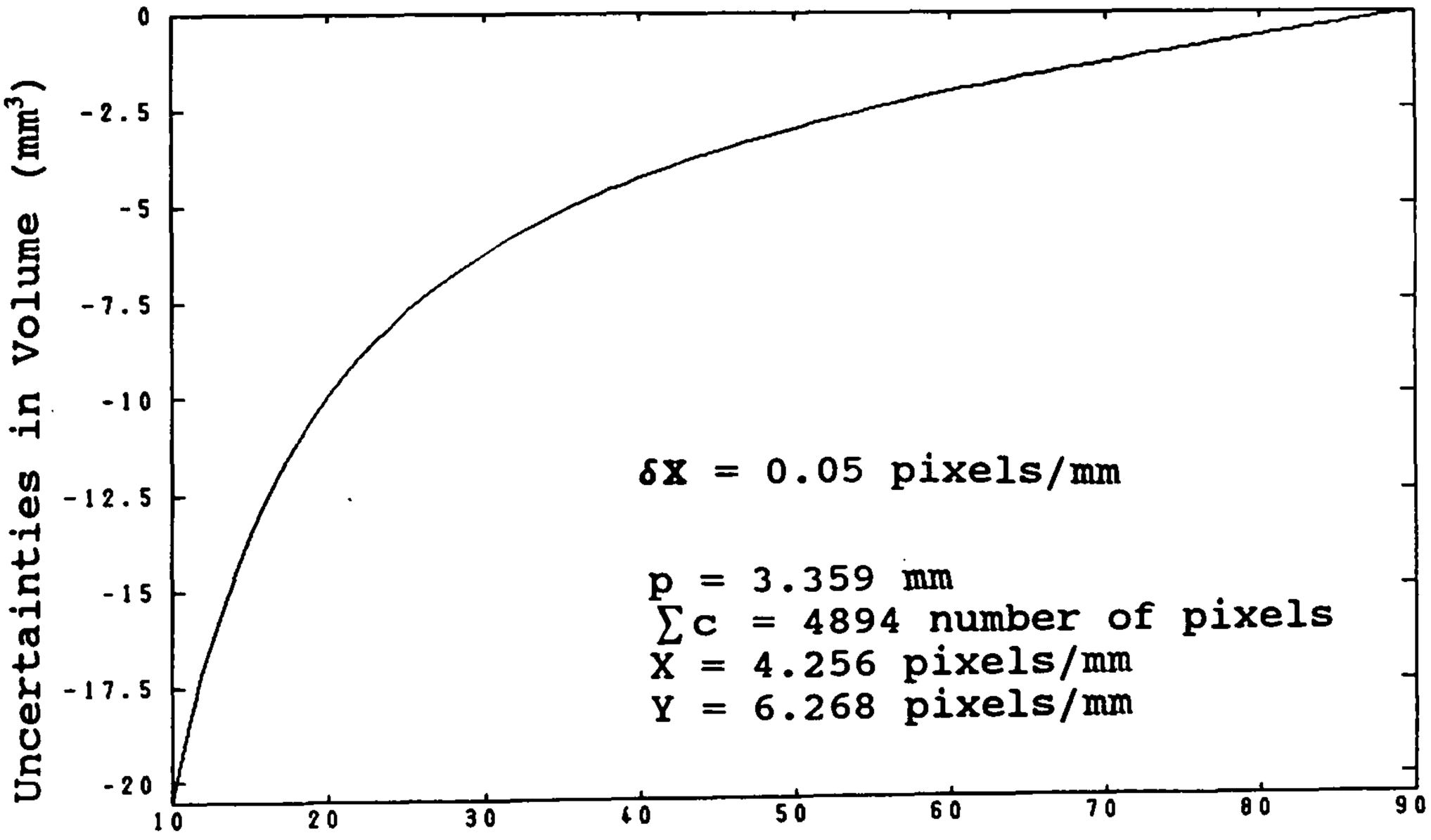

iii) For an Uncertainty in Y

The System $\delta Y = 0.048$ pixels/mm

Figure 7.4(a) shows that the uncertainty in the volume V is directly proportional to the uncertainty in the scaling factor Y, and a negative constant. Examples of which are shown in the following table. As a consequence of this, an error in over-estimating the scaling factor Y will result in an under-estimate in the system volume. Similarly, under-estimating the scaling factor Y will result in an over-estimate in the system volume.

Uncertainty in Y (% of Y)	(pixels/mm)	Uncertainty in V (mm^3)
10	0.6268	-32.696
5	0.3134	-16.348
0	0	0

Examination of Figure 7.4(b) and equation (7.4) indicate that the uncertainty in the volume V is inversely proportional to the target of the viewing angle. By using the system worst possible uncertainty value for Y of 0.048 pixels/mm and a system viewing angle of 43.3°, Figure 7.4(b) reveals an error in the system volume of 2.503 mm^3. Results achieved by the system (as displayed in Chapter 6), are of a similar magnitude and with only 1% in difference.

Figure 7.4(a) Uncertainty Plot for equation (7.4)

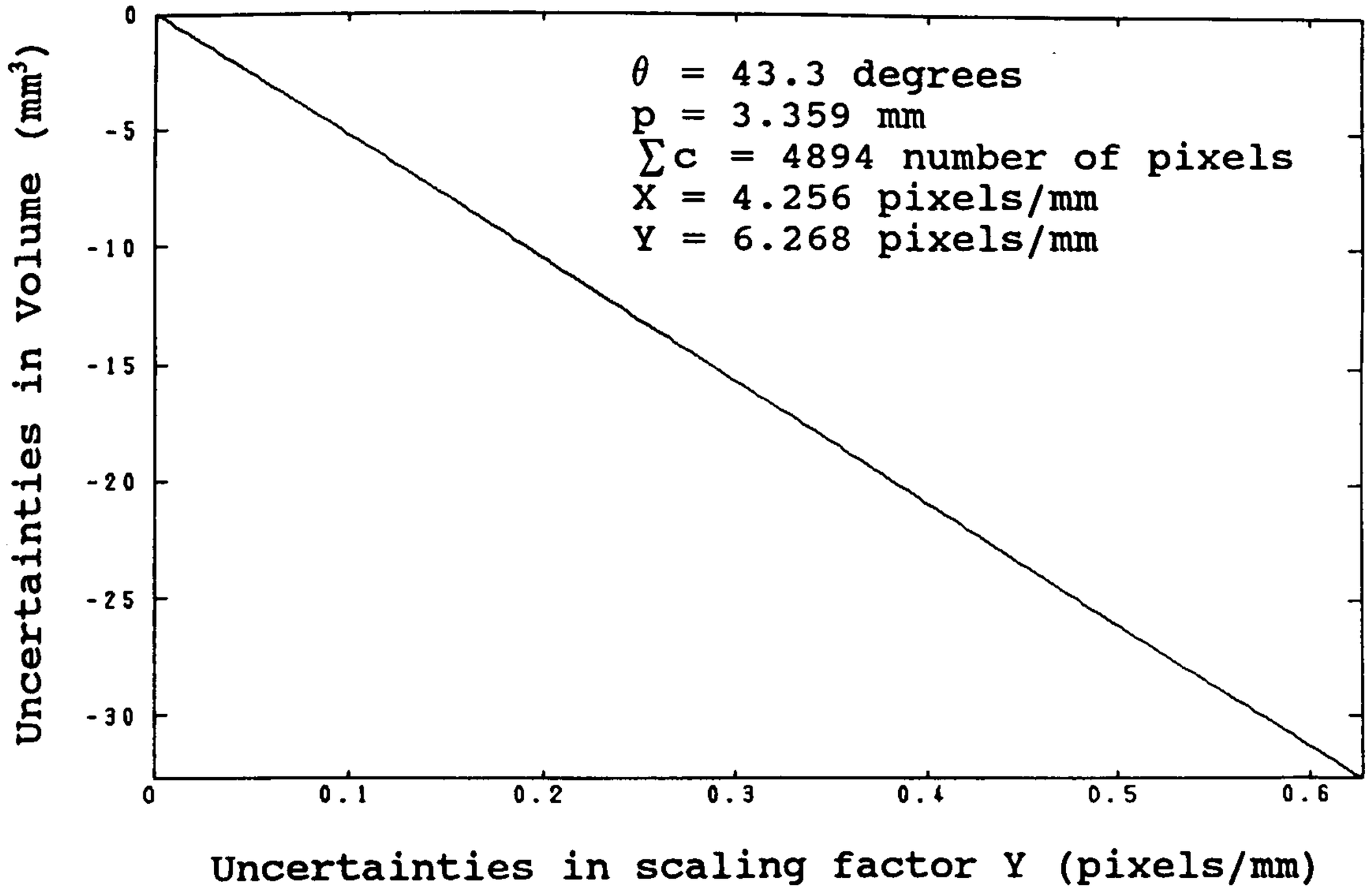

Figure 7.4(b) Plot of Uncertainties in the Volume against θ

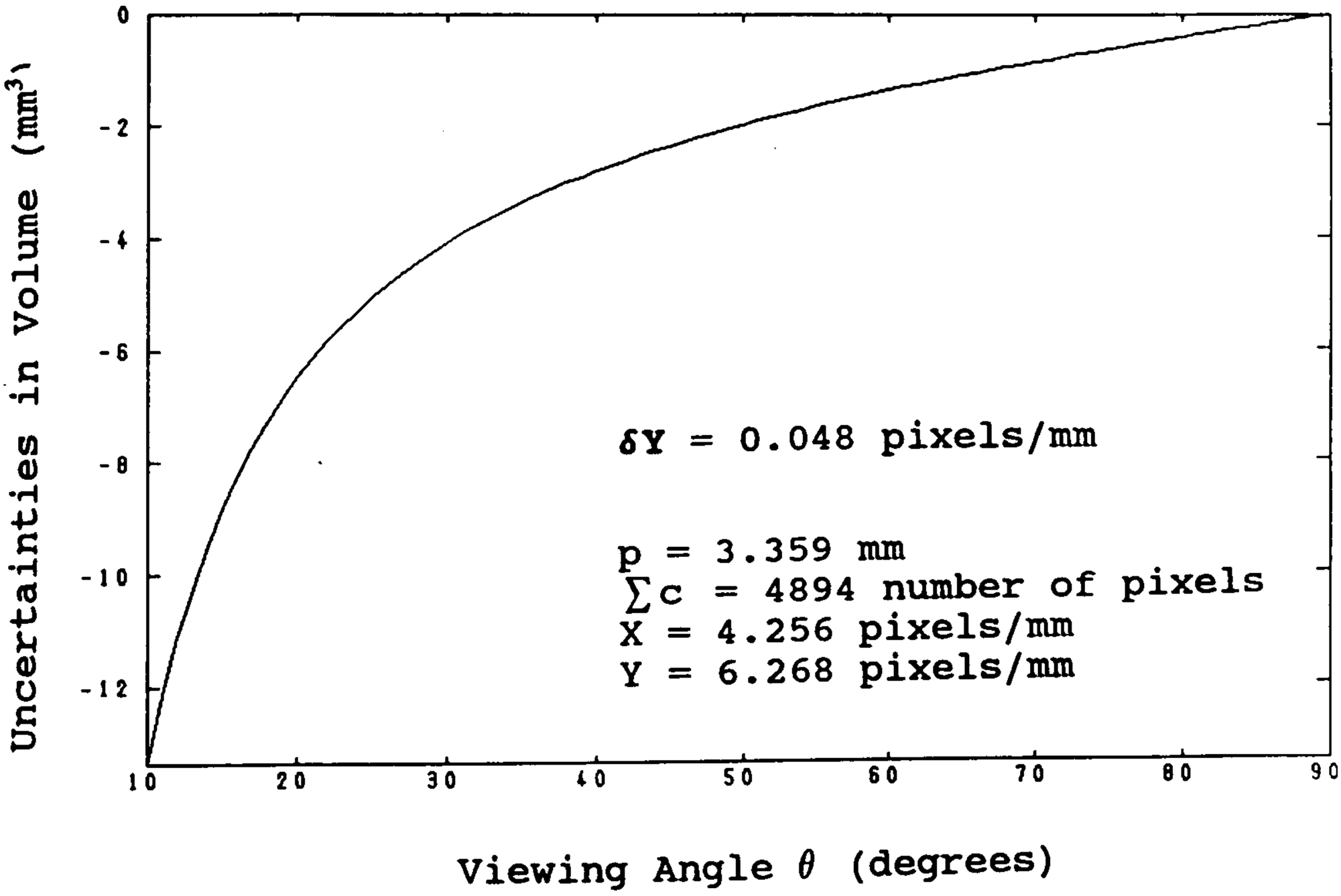

iv) For an Uncertainty in θ

The System $\delta\theta = 0.04167°$

Figure 7.5(a) illustrates the uncertainty in the volume V to be directly proportional to the uncertainty in the angle θ and a negative constant. Examples of which are shown in the following table. As a consequence of this and identical to the scaling factors X and Y, an error in over-estimating the angle θ (more than likely) will result in an under-estimate in the system volume. Similarly, under-estimating the angle θ will result in an over-estimate in the system volume.

Uncertainty in θ (% of θ) (degrees)	Uncertainty in V (mm^3)
10 4.337	-2836
5 2.215	-1418
0 0	0

From the examination of Figure 7.5(a) and equation (7.5), it may be observed that the uncertainty in the volume is inversely proportional to the sine squared of the viewing angle. The magnitude of the uncertainty in the volume from -425.75 to -12.83, not reaching 0 as compared to the previous uncertainty plots against the angle, indicate the sensitivity of the technique to the viewing angle. The importance of maintaining a large viewing angle, is essential in reducing any uncertainty in the volume.

Interestingly, using the system worst uncertainty in θ (= 0.04167°) and the system's viewing angle of 43.3°, Figure 7.5(b) shows an error in the volume of 27.29 mm^3. This figure however, does not correspond with the results produced in Chapter 6, where the results for this angle were far more accurate.

Figure 7.5(a) Uncertainty Plot for equation (7.5)

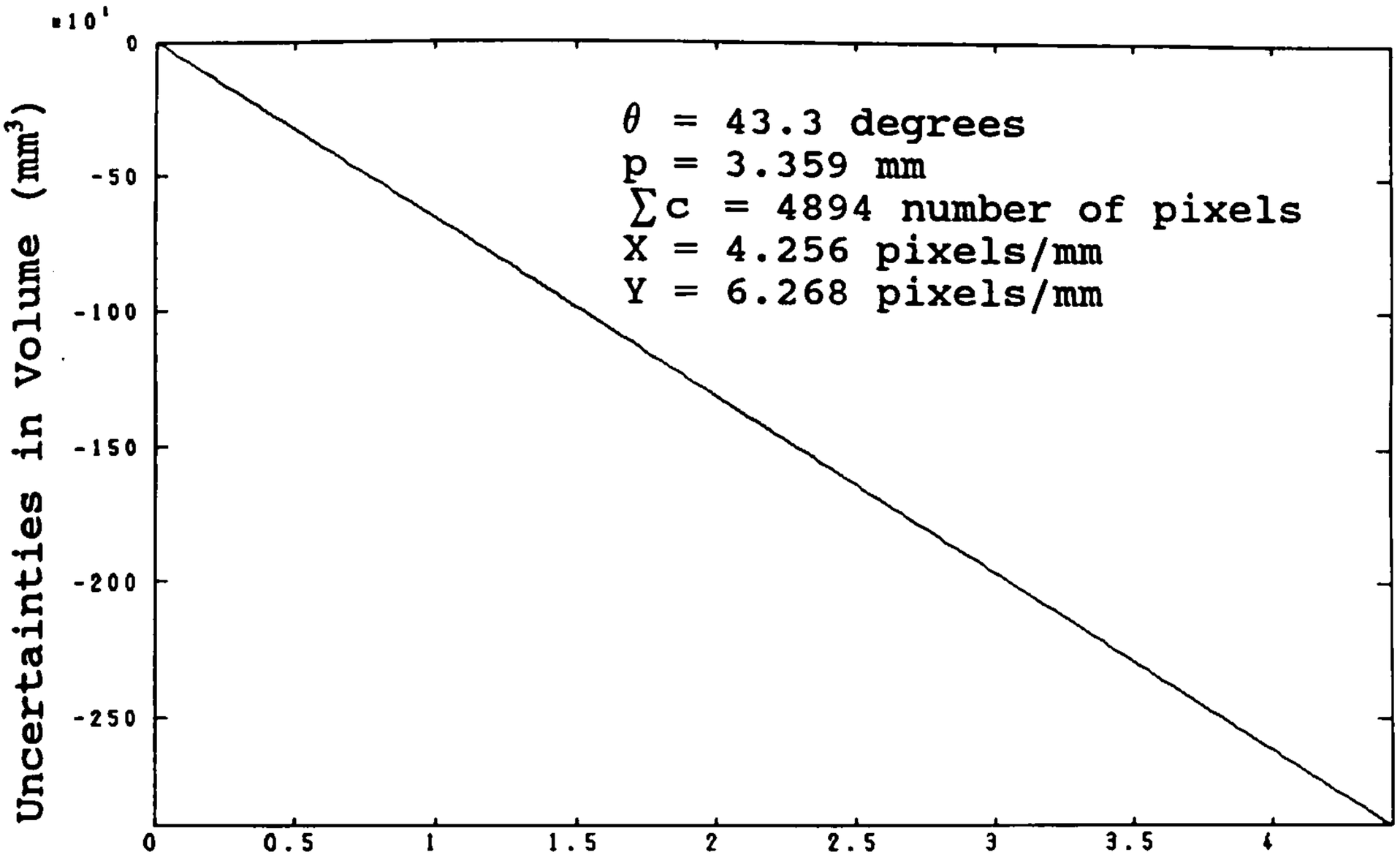

Figure 7.5(b) Plot of Uncertainties in the Volume against θ

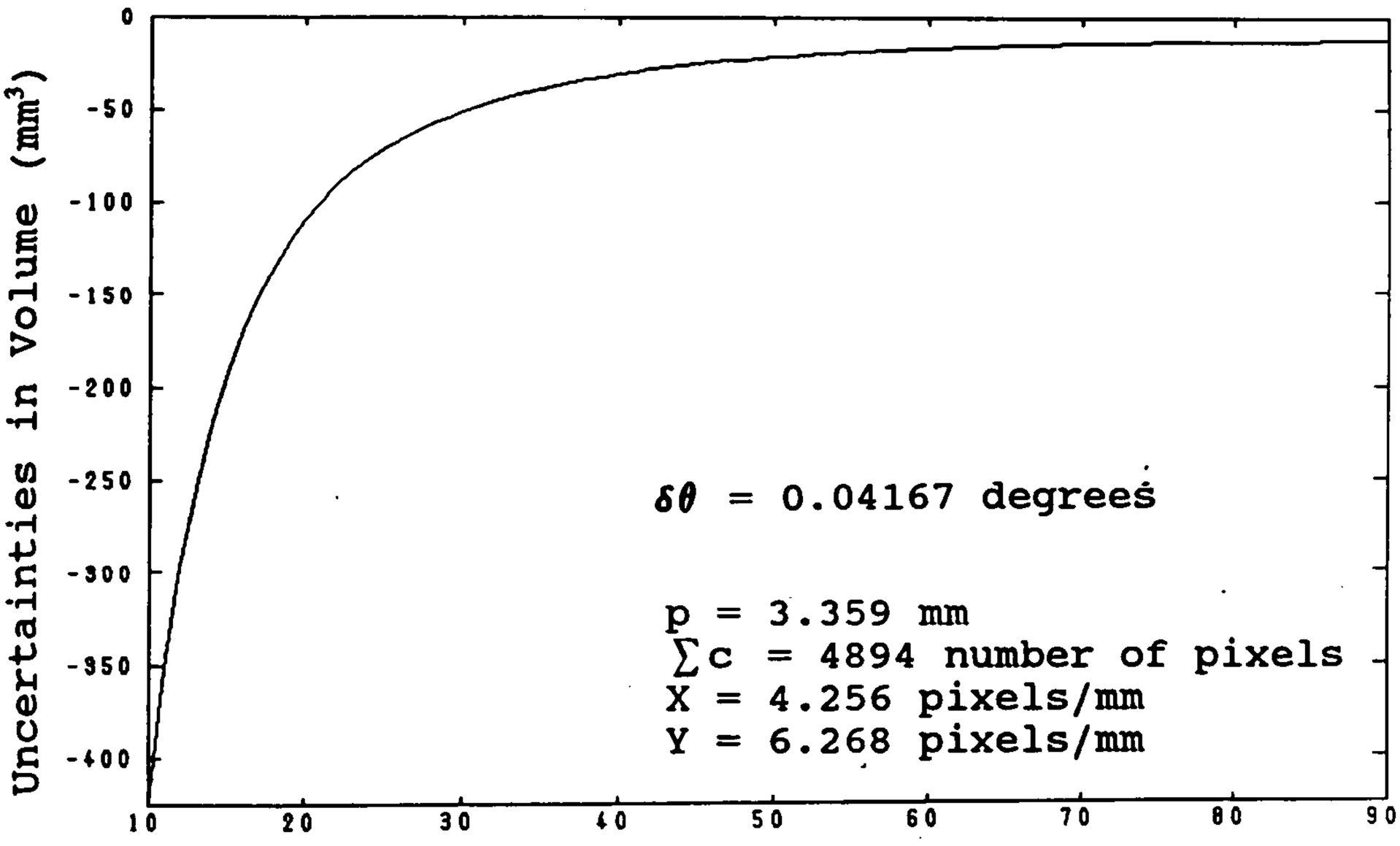

7.2.3 The Overall System Uncertainty

The overall uncertainty for the volume is given by the sum of all the individual uncertainties [7.1]. i.e.

$$\delta V = \frac{\partial V}{\partial p} . \delta p + \frac{\partial V}{\partial X} . \delta X + \frac{\partial V}{\partial Y} . \delta Y + \frac{\partial V}{\partial \theta} . \delta \theta$$

Which may be expanded from the individual uncertainty expressions 7.2 - 7.5 in section 7.2 to,

$$\delta V = \frac{\sum c.\delta p}{2.X.Y.\tan\theta} - \frac{p.\sum c.\delta X}{2.X^2.Y.\tan} - \frac{p.\sum c.\delta Y}{2.X.Y^2.\tan\theta} - \frac{p.\sum c.1.\delta\theta}{2.X.Y \sin^2\theta}$$

Where the symbols have been previously defined.

For an operating setup of

$p = 3.359mm \quad \theta = 43.3° \quad X = 4.256$ pixels/mm $\quad Y = 6.268$ pixels/mm

$$\delta V = \sum c \, [\, 0.02\delta p - 0.134\delta\theta - 0.016\delta X - 0.011\delta Y \,]$$

Since the individual uncertainties as described in section 7.2.1 are

$\delta p = 0.0235mm \quad \delta\theta = 1/24° \quad \delta X = 0.050$ pixels/mm

$\delta Y = 0.048$ pixels/mm

$$\delta V = \sum c \, [\, 0.00047 - 0.0056 - 0.0008 - 0.00053 \,]$$

$$\delta V = \sum c \, [\, 6.46 \times 10^{-3} \,]$$

In this case, the number of pixels $\sum c = 4894$. Therefore, the uncertainty

for the volume δV is 31 mm^3, for a defect of nominally 327 mm^3, in the region of 10% of the correct figure.

7.3 Chapter Summary

The results produced from the uncertainty analysis cannot be taken too literally, since the "worst case" values for δp, δX, δY and $\delta\theta$ have been used. However, the trends in the effects of these errors in the final result are useful.

The graphs produced of the uncertainties of the volume plotted against each set-up constant, indicate that the viewing angle has the most effect on the final result. This is reinforced by the values in the second graph for each case, e.g. 7.2(b), 7.3(b), 7.4(b) and 7.5(b).

In addition, an error is produced in the system at whichever angle setting is chosen, as displayed in Figure 7.5(b), when the worst uncertainty in θ is applied. Even at an angle of 90°, an error of -12.83 mm^3 is obtained. Similar plots illustrated earlier (Figures 7.2(b) to 7.4(b)), set at each respective worst uncertainty value, produced no error at an angle of 90°. However, an error is produced in Figure 7.5(b) since the angle may not be 90° due to the uncertainty.

An overall uncertainty for the volume δV is 31 mm^3, for a defect of nominally 327 mm^3, about 10% of this figure.

The analysis showed in order of importance, the following:

i) The Viewing angle - crucial for a successful inspection to be possible.

ii) The fringe period p - important and related to the angle.

iii) The scaling factors X and Y - influence on the Final result not as great compared to the first two.

7.4 References

7.1 J. R. TAYLOR, "**An Introduction to Error Analysis : The Study of Uncertainties in Physical Measurements**", University Science Books, 1982.

CHAPTER EIGHT

DISCUSSIONS, CONCLUSIONS AND FURTHER WORK

8.1 Introduction

The previous chapters have discussed a number of features that have arisen during the development of this simple and relatively low cost, comparative measuring system. These discussions included:

i) The development and implementation of the method for volume determination on an image processing system.

ii) The use of simulation and validation tests in verifying the theory of the technique, and the effects of altering certain parameters such as the angle and fringe period.

iii) The accuracy of the technique is analysing real data and their associated problems.

iv) The effect of fringe misalignment and its associated solutions.

The chapter then continues with a summary of the conclusions drawn from the results of the research work and ends with a discussion of possible future work.

8.2 System Operational Timings

The purpose of this research work was to develop a comparative non-contact inspection system, capable of producing a quantitive measurement for any surface imperfection. With this objective realised, it is necessary to summarise the key features of the amount of time necessary to complete the system's operation. Table 8.1 describes the steps necessary to produce a successful inspection, with the amount of time necessary if each step is chosen also listed.

Table 8.1 System Percentage Timings for the various technique steps.

Step	Description	Timings as a percentage of the overall total
1	Input averaged reference image 1, indicating a suitable reference point (for alignment purposes) with the cursor function in the software.	0.064
2	Input averaged gauged image 2, indicating with the cursor function, whether rotation is necessary.	0.085
3	If necessary, indicate the area within image 2 to be rotated with cursor before Rotation with interpolation.	61.3
4	Indicate reference point on image 2.	0.021
5	If necessary, shift image 1 to align with image 2.	0.004
6	Threshold images 1 and 2.	0.1
7	Subtract images from one another.	0.05
8	If necessary, filter subtracted image.	38.3
9	Indicate area of interest for volume estimation with cursor.	0.085

The amount of time undertaken for each step (if required by the user) is only approximate and dependent upon the reference points chosen, together with the size of areas rotated or filtered. However these figures give an

indication of the possible areas in the technique where improvement may be necessary.

The results illustrated in Table 8.1, indicate that steps 3 and 8 are the most time consuming tasks. Step 3 involving the rotation of an image, is time consuming, since a forward and reverse rotation transformation (see Chapter 5) is necessary. The experimental results of the technique in the comparison of a rotated image with its reference image, give errors of significant magnitude. In rotating a fringe illuminated item, the image would rotate in addition to the fringes on its surface, making fringe alignment with the reference image impossible. For this reason this step is redundant.

Step 8 involving the filtering of the subtracted image, to distinguish data due to a surface defect from data due to misalignment, is an obvious area where improvement may be possible. Adapting the filtering technique is an obvious solution.

It should be noted that the hardware used in this research work consists of a 286 based IBM PC with a slot-in image processing board. No co-processor was used, which undoubtedly would have improved the performance, as would also the transfer of the software to alternative hardware. Figure 8.1 illustrates the flow chart of the program.

Figure 8.1

Flow chart of program

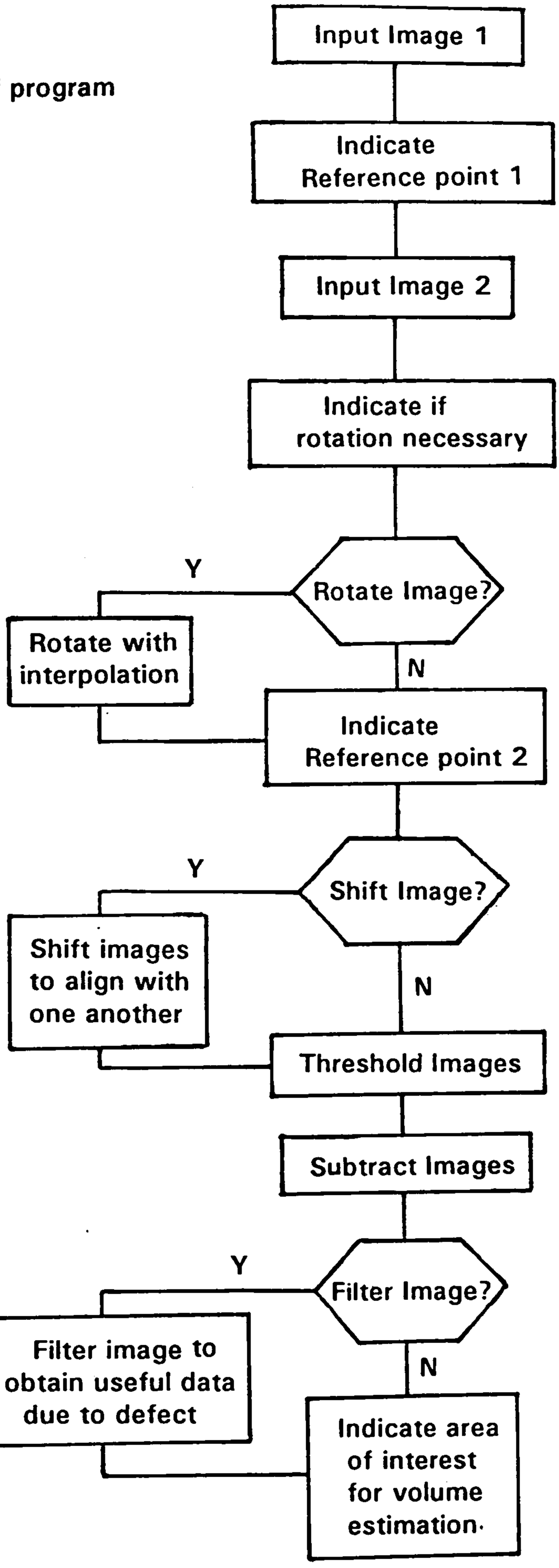

8.3 Discussion

A number of important points have been highlighted in this research work in the development of an inspection system and include:

i) The results obtained, following good re-alignment have percentage errors in volume determination of the order of 5%. It is felt that for the applications envisaged in section 1.4, this would be adequate. So, by this criterion the method may be considered successful.

With a common reference point on each image, the two samples may be easily aligned with one another, producing these successful results.

However, a problem still exists in ensuring that the fringes on each image align with one another. This is impossible to achieve, although it is possible to intelligently distinguish the data due to fringe non-alignment, from data due to any surface imperfection, within the subtracted image. As a consequence of a fringe misalignment, the appearance of the resulting subtracted image will consist of a number of columns of white pixels of significant width, distributed across part or the whole of the surface image.

A number of different methods of solving this problem were investigated, with the most successful involving the analysis of a line of data (within the direction of the columns of white pixels). By analysing lines of data throughout the image, data due to a surface imperfection may then be distinguished. Results of this row and column filter, presented in Chapter 6, are successful to degrees of varying magnitude. Depending upon the magnitude of the surface defect and displacement in the fringe misalignment, a number of conclusions may be

drawn. The filter is successful in distinguishing data due to misalignment, from data due to a surface imperfection, providing the magnitude of the imperfection is not small and the displacement not large. At which point in any case, the height data due to a surface defect would be lost. Acceptable results after filtering, for large defects and significant displacements, and for smaller defects with small displacements, have been found. The success of the filter is therefore dependent upon the magnitude and depth of the surface imperfection and magnitude of the misalignment involved. Ensuring that the misalignment is small, the filter would prove to be more successful, with acceptable results for a surface defect of any size. Therefore, precise relocation of the samples in unnecessary.

In addition, a change to alternative hardware will no doubt provide a significant improvement in the speed of operation and therefore time of operation. A near real-time inspection would therefore be a possibility.

ii) Accuracy in determining the set-up constants is essential (as proven in section 7.2) for an accurate inspection to be possible, with the angle parameter the most important constant. An error in determining this parameter would result in a significant error in the final result, particularly when the angle is large and the technique is at its most sensitive. However, the values for the angle and fringe period in setting up the system, are dependent upon the depth of any surface defect and therefore fringe modulation. The technique requires both these parameters to be such that the fringe shift within the subtracted image, is not greater than the fringe period. If this were not the case, a large error would result in the volume estimation, such as that demonstrated in one of the simulation results in Chapter 4.

Thus, to enable a range of surface imperfections, of varying size and depth, to be measured by this technique, a number of cameras and fringe projectors set at different angles would be ideal. Defects of significant depth could be accurately measured at a shallow angle, with defects of smaller depth at a greater angle.

iii) The problem of visual noise caused by the fluctuations in the lighting conditions may be minimised but not totally eliminated with the application of image averaging. The effect of the image averaging of the same scene, would be the averaging out of the only variable in that scene i.e. visual noise.

The alternative method investigated of pixel erosion within the subtracted image, is unsuitable since it irreversibly alters the image. The effect of thinning the number of white pixels within the image, will not only eliminate the background visual noise but also the edge data corresponding to the areas of any defect. A reduction of the apparent magnitude of the defect may therefore perhaps permit a defective item to pass through the system.

iv) The thresholding limiting value is an important but difficult feature which if incorrectly chosen, will produce an incorrect system result. As discussed earlier in Chapter (7.2), depending upon the thresholding volume chosen, the number of pixels may be above or below the true number related to a surface defect. In addition, difficulty is encountered in representing the thresholded data of a fringe boundary, the result of which is a quantising error. Results presented earlier in the error section 7.2, illustrate the importance of the thresholding limiting value, with the effect of lowering this value, producing an increase in the system error.

The conclusion of which is in producing good contrasting thresholded fringes upon the surface, the system error is small, producing acceptable results. Further investigation of this problem is undoubtedly required, for this problem to be resolved.

v) The surfaces and therefore items to be compared with one another, must be of similar reflectivity for a successful comparison to be possible. This is partly due to the difficulty in setting the correct thresholding limiting value for each image and therefore achieve a successful comparison. As a surface comparator, surfaces will have similar reflectivity, with the inspected component of the same material as its reference. In the case of the soap bar examples, similar coloured bars of soap can only be compared with one another. This due to the different light absorption properties exhibited by the different coloured soap bars.

vi) The adapted technique incorporating the use of a large fringe grating, which the item to be inspected is placed against, may prove to be a more suitable method for a real-time inspection system. The primary advantage of this technique concerns the fact that there is no requirement to relocate the item to be inspected and therefore filtering of the subtracted image. Thus, a real-time inspection system may be achieved.

However, there are disadvantages to this technique. These include the fact that this technique is no longer non-contact, a major advantage in minimising wear of the sensor and damage to the item being inspected. The requirement for the item to be inspected to be placed directly against the fringe grating, may cause damage to both the grating or item. In addition, the size of the grating required for a large item to be inspected may prove to be prohibitive. Finally, an absolute measurement is

obtained by this method, as compared to the original comparative method. Thus, difficulty may be encountered in the analysis of the result, since both defective and perfect samples will produce an absolute volumetric value.

This technique may prove to be successful depending upon the type of application the system is applied to.

vii) The large errors produced in the comparison of a rotated image with a reference image, indicate that rotation is not a viable solution. In rotating a fringe illuminated image, the image in addition with the fringes on its surface would rotate, making fringe alignment impossible. For a successful inspection, the fringes produced on the surface of the reference image, must be the same in relation to the fringes produced upon the gauged image. In utilising the adapted technique involving the use of a large fringe grating, this problem would be solved.

viii) The speed of the system may be improved by the use of alternative faster hardware, and the further development of the time-consuming steps in the technique. As described in the previous section, the most time consuming tasks involve the rotation of an image and the filtering of a subtracted image. Since the rotation step is now redundant, as a consequence of the magnitude of the error results, the filtering may be improved by adapting the filtering strategy. In addition, the transfer of the technique to faster hardware, will enable a near real-time inspection system to be viable. Similarly with the adapted technique a real-time inspection system may be achieved.

ix) The linear relationship investigated in section 5.2.4, as an alternative to avoid the problems associated with the accuracies required in determining the set-up constants, is not

a practical solution. This is due to the fact that good results are produced from the conventional method of inputting these set-up constants. The results produced with the sample relocated accurately or not, are more than acceptable.

8.4 Conclusions

Many important points have been highlighted in this research work on the development of an inspection system, from which a number of conclusions may be drawn. These include:

i) An inspection system, based on a combination of image subtraction and fringe projection, has been successful.

ii) The system achieves an accurate volume determination, particularly when the two images (and fringe patterns) are accurately aligned to one another. Reasonable results are still possible when these images and fringe patterns are misaligned, with the utilisation of a selective filtering scheme (the descriptions and results of which are shown in Chapters 5 and 6). Therefore precise relocation of the surfaces is not necessary. Care must be taken to ensure that the fringes produced on each image, are identical in orientation with respect to the surface and therefore each image.

iii) From the analysis of the theory, it has been shown that an accurate determination of the set-up constants is essential, for an accurate inspection/measurement to be possible.

iv) The angle parameter has been found to be the most important set-up constant that must be accurately determined. This is particularly important when the angle is large, when the technique is at its most sensitive, thus amplifying any error.

v) The choice of fringe period and angle are dependent upon the depth of any surface defect to be detected and therefore resulting fringe modulation.

vi) The visual noise due to the fluctuations in the lighting conditions can be minimised by applying the image averaging function within the software.

vii) The surfaces to be compared with one another, must be of similar reflectivity for a successful comparison to be possible.

viii) The thresholding limiting value must be such that, good quality and distinctive black and white fringes are produced, resulting in an accurate comparison.

ix) A very simple optical set-up is utilised in enabling large items to be compared at a reasonable cost. The projector used in this work was chosen, since a fringe pattern of uniform light intensity is produced.

x) The adapted technique comprising the use of a large fringe grating, which the item to be inspected is placed against, is a more suitable alternative for the development of a real-time inspection system. This is dependent upon the size and type of item that the system is to inspect.

xi) The linear relationship investigated in chapter 5.2.4, as an alternative to avoid the problems associated with the accuracies required in determining the set-up constants, is not a practical solution.

xii) The speed of the technique may only be improved by the use of alternative faster hardware and the further development of the most time consuming step in the technique, namely the filtering strategy to selectively distinguish useful data.

8.5 Recommendations For Future Work

With the feasibility of the technique established, there are a number of improvements necessary in enabling a practical instrument to be possible. Further work in developing the adapted method would be a more obvious approach to achieve a practical real-time instrument. This would avoid the problems of fringe alignment highlighted in Chapter 5 . The tasks remaining include:

i) Computer Hardware

The fundamental basis of the research work described in this thesis, comprises the image subtraction of two thresholded images (to highlight the difference and thus surface volume), with image averaging to minimise the visual noise, caused by the fluctuations in the lighting conditions. The problem exists in that the averaging and thresholding functions cannot be applied in combination, since the image processing system (ITI100) hardware will not enable this to occur. This is due to the fact that only one input look-up table (LUT) is available, and therefore for further development to be possible, the ability to perform both tasks together is desirable.

With the ever increasing improvement of the hardware available within the field of image processing, the development of this surface inspection system is probable. The development of this technique on a relatively dated and low cost system has shown the feasibility of this technique with further improvements necessary on different hardware. Moving to a new device will require some re-development of the analysis software, to make the most efficient use of the hardware. With faster hardware a near real-time system may be achieved with this technique, with the alternative adapted method a real-time possibility.

ii) Work on Algorithm

In developing the adapted method, additional alterations and improvements in the algorithm, are essential in enabling a real-time inspection system to be achievable. The necessity to pick reference points on both images, and to rotate and shift each image to align with a reference, would be redundant.

In addition, when incorporated on new hardware, the ability to average and threshold an input image, would require further alterations to the algorithm.